# INSIGHTS INTO THE PHOTOPHYSICAL REACTION COORDINATE OF $1^{\rm ST}$ ROW TRANSITION METAL CHROMOPHORES FROM VIBRATIONAL COHERENCES

By

Bryan Christopher Paulus

# A DISSERTATION

Submitted to
Michigan State University
in partial fulfillment of the requirements
for the degree of

 $Chemistry-Doctor\ of\ Philosophy$ 

2020

### **ABSTRACT**

# INSIGHTS INTO THE PHOTOPHYSICAL REACTION COORDINATE OF $1^{\rm ST}$ ROW TRANSITION METAL CHROMOPHORES FROM VIBRATIONAL COHERENCES

By

## Bryan Christopher Paulus

Controlling the processes which occur following absorption of photon is beneficial for any conceivable application which seeks to convert light into chemical potential. Transition metal chromophores often undergo ultrafast photoinduced transformations which involve significant nuclear motion. This intricate relationship between electronic and nuclear degrees of freedom suggests significant mixing of their wavefunctions and an interdependence of these molecular properties that can map onto the photophysical dynamics. In systems such as these, the rich dynamical information encoded in vibrational coherences can in principle provide unique insight into the nature of this coupling. Furthermore, this has the potential to provide subtle clues for how one could exert some degree of kinetic control through informed structural, compositional, and environmental modifications. This dissertation describes efforts to use excited state vibrational coherences to glean mechanistic information about ultrafast excited state decay in several first-row transition metal chromophore systems and, further, to exploit that information to reengineer the chromophore to alter the photophysical properties.

This dissertation begins by using ultrafast transient absorption measurements to provide an updated kinetic model for a series of chromium(III) tris-betadiketonate compounds. Following prompt  ${}^4T_2 \rightarrow {}^2E$  ISC to the lowest energy excited state, thermally activated back-intersystem crossing repopulates the  ${}^4T_2$  state which internally converts to the ground state on the  $\sim 1$  ps timescale. Steric bulk in the periphery of the molecule reduces the rate of internal conversion resulting in significantly different spectral evolution. Identical low frequency symmetric breathing modes with dephasing times ranging from  $\sim 200$ -2500 fs were identified in the  ${}^2E$  excited state of each molecule. The more rapid dephasing times are likely due to IVR. Similar methodology was then used to characterize the excited state dynamics in a structurally related series of cobalt(III) tris-betadiketonate compounds. Following ligand field excitation into the  ${}^1T_{1g}$  state, each

compound had essentially identical biphasic kinetics with ground state recovery occurring with a ~2 ps time constant from an excited state of  $(t_{2g})^5(e_g^*)$  electron configuration. Low frequency metal-ligand breathing modes similar to those observed in the chromium systems were observed with dephasing times consistently on the order of ~200 fs.

Finally, two methods to elongate MLCT lifetimes of iron(II) polypyridyl compounds were demonstrated. In the first, the vibrational modes which drive the ultrafast, sub-200 fs MLCT deactivation to the lower energy metal-centered excited states in a  $[Fe(cage)]^{2+}$  control molecule were identified by their coherent oscillations in a transient absorption experiment. These modes were subsequently hindered by incorporation of electronically benign copper(I) atoms to the  $N_4$  coordination environments in the periphery of the ligand scaffold resulting in a > 20-fold increase in the MLCT lifetime. In the final study, it was shown that the excited state properties of iron(II) polypyridyl type systems can be systematically and dramatically tuned by swapping out a single bidentate phenanthroline ligand of a  $[Fe(phen)_3]^{2+}$  control molecule with stronger-field cyanide or acyclic dicarbene ligands. This modular approach to tuning the kinetics resulted in a > 25-fold increase in the MLCT lifetime and a fundamentally different decay pathway.

### **ACKNOWLEDGMENTS**

I first want to thank Jim for allowing me into his group, giving me a cool project, funding my way for ACS and ICP trips, and allowing me to work on projects that I was interested in. Next, I would like to thank the previous McCusker group ultrafast laser members Eileen, Jennie, and Monica for not only teaching me how to use the laser and set up experiments but also for coming to the rescue when I couldn't fix things. I would also like to thank Hayden for coming along and taking the laser reigns. To all the synthesis lab members, thank you for all your advice and helping hands. Thank you for letting me borrow your various hand-prepared solutions to use in syntheses, and in several cases, making molecules that I could study with TA. I would further like to thank all McCusker group members for being willing to talk science, to read through my writings to make me sound less foolish, and for listening to my presentations to make me a better presenter. Finally, I would like to thank my family for always supporting me.

# TABLE OF CONTENTS

LIST OF TABLES	viii
LIST OF FIGURES	xi
KEY TO SYMBOLS AND ABBREVIATIONS	xxii
Chapter 1: Coherent Vibrational Dynamics of Inorganic Molecular Chromophores	1
1.1. Introduction	
1.2. Transition Metal Photophysical Properties	1
1.3. Transient Absorption Spectroscopy	
1.4. Coherences and Impulsive Vibrational Spectroscopy	
1.5. Content of This Dissertation	13
REFERENCES	14
Chapter 2: Electronic and Vibrational Excited State Dynamics in a Series of Cr(acac') <sub>3</sub> D	Derivatives 16
2.1. Introduction to Chromium(III)	16
2.2. Summary of Previous Results	19
2.3. Experimental Section	31
2.3.1. Synthesis of Cr(acac) <sub>3</sub> Derivatives	31
2.3.2. Computational Methods	33
2.3.3. Time Resolved Spectroscopic Methods	
2.4. Results and Discussion	43
2.4.1. Cr(acac) <sub>3</sub>	
$2.4.2. Cr(3-NO_2ac)_3$	62
2.4.3. Cr(3-Clac) <sub>3</sub>	65
2.4.4. Cr(3-Brac) <sub>3</sub>	
2.4.5. Cr(3-Iac) <sub>3</sub>	
2.4.6. Conclusions on 3-Substituted Cr(acac') <sub>3</sub> Compounds	
2.4.7. Effects of Increasing Steric Bulk	
2.4.8. Cr(HD) <sub>3</sub>	
2.4.9. Cr(DMHD) <sub>3</sub>	
2.4.10. Concluding Comments on Effects of Steric Bulk	
2.4.11. Cr(TMHD) <sub>3</sub>	
2.4.3. Cr(4-Cl-TMHD) <sub>3</sub>	
2.5. Concluding Comments on Cr(acac') <sub>3</sub> Systems	
APPENDICES	
Appendix 2.A. Crystal Structures	
Appendix 2.B. Dephasing Times of Common Solvent Modes	
Appendix 2.C. Fit of Cr(acac) <sub>3</sub> Raman Spectrum	
REFERENCES	120
Chapter 3: Excited State Dynamics of a Series of Co(acac') <sub>3</sub> Derivatives	
3.1. Introduction	
3.2. Summary of Previous Results	128
3.3. Experimental Methods	
3.3.1. Synthesis of Co(acac') <sub>3</sub> Compounds	
3.3.2. Computational Methods	132

3.3.3. Duschinsky Displacement Vector Calculations	1 . 2 4
3.3.4. Time Resolved Spectroscopic Methods	136
3.4. Results and Discussion	136
3.4.1. Co(acac) <sub>3</sub>	
$3.4.2. \text{ Co}(3-\text{Iac})_3$	
3.4.3. Co(TMHD) <sub>3</sub>	157
3.5. Concluding Thoughts on Co(acac') <sub>3</sub> Dynamics	
APPENDICES	
Appendix 3.A. NMR Spectra	
Appendix 3.B. Duschinsky Displacement Vector Calculation MATLAB Script	
REFERENCES	
Chapter 4: Geometric Control of Ultrafast Charge-Transfer Relaxation Dynamics in Fe(II)-Based	
Chromophores: Using Coherence to Inform Synthetic Design	178
4.1. Introduction	
4.2. Experimental Methods	
4.2.1. Synthesis	
4.2.2. Density Functional Theory Calculations	
4.2.3. Ultrafast Transient Absorption Spectroscopy	
4.3. Results and Discussion	
APPENDICES	
Appendix 4.A. Additional Transient Absorption Data on Compound 2	
Appendix 4.B. Reorganization Energy Calculation for [Fe(bpy) <sub>3</sub> ] <sup>2+</sup>	
Appendix 4.C. Additional Normal Mode Assignment for Compound 1	
Appendix 4.D. Results of Kinetic and Oscillatory Analyses on Each Individual Dataset	
REFERÊNCES	207
Chapter 5: A Modular Approach to Controlling Excited State Properties of Iron(II) Polypyridyls	211
5.1. Introduction	211
5.2. Experimental Methods	
	213
5.2.1. Synthesis and Characterization	
5.2.1. Synthesis and Characterization	213
· · · · · · · · · · · · · · · · · · ·	213 214
5.2.2. Ultrafast Transient Absorption Spectroscopy	213 214 215
5.2.2. Ultrafast Transient Absorption Spectroscopy	213 214 215
5.2.2. Ultrafast Transient Absorption Spectroscopy  5.3. Results and Discussion  5.3.1. Ground-State Properties of Compounds 1, 2, and 3  5.3.2. Excited State Dynamics of 1	213 214 215 216
5.2.2. Ultrafast Transient Absorption Spectroscopy  5.3. Results and Discussion  5.3.1. Ground-State Properties of Compounds 1, 2, and 3  5.3.2. Excited State Dynamics of 1  5.3.3. Excited State Dynamics of 2	213 214 215 215 219
5.2.2. Ultrafast Transient Absorption Spectroscopy  5.3. Results and Discussion  5.3.1. Ground-State Properties of Compounds 1, 2, and 3  5.3.2. Excited State Dynamics of 1  5.3.3. Excited State Dynamics of 2  5.3.4. Excited State Dynamics of 3	213 214 215 216 219 223
5.2.2. Ultrafast Transient Absorption Spectroscopy  5.3. Results and Discussion  5.3.1. Ground-State Properties of Compounds 1, 2, and 3  5.3.2. Excited State Dynamics of 1  5.3.3. Excited State Dynamics of 2  5.3.4. Excited State Dynamics of 3  5.4. Concluding Thoughts	213 214 215 216 219 223 228
5.2.2. Ultrafast Transient Absorption Spectroscopy  5.3. Results and Discussion  5.3.1. Ground-State Properties of Compounds 1, 2, and 3  5.3.2. Excited State Dynamics of 1  5.3.3. Excited State Dynamics of 2  5.3.4. Excited State Dynamics of 3  5.4. Concluding Thoughts  APPENDICES  Appendix 5.A. Singular Value Decomposition MATLAB Script for Full Spectrum TA An	213 214 215 216 219 223 228 229 alysis
5.2.2. Ultrafast Transient Absorption Spectroscopy  5.3. Results and Discussion  5.3.1. Ground-State Properties of Compounds 1, 2, and 3  5.3.2. Excited State Dynamics of 1  5.3.3. Excited State Dynamics of 2  5.3.4. Excited State Dynamics of 3  5.4. Concluding Thoughts  APPENDICES  Appendix 5.A. Singular Value Decomposition MATLAB Script for Full Spectrum TA An	213 214 215 216 219 223 228 229 alysis 230
5.2.2. Ultrafast Transient Absorption Spectroscopy  5.3. Results and Discussion 5.3.1. Ground-State Properties of Compounds 1, 2, and 3 5.3.2. Excited State Dynamics of 1 5.3.3. Excited State Dynamics of 2 5.3.4. Excited State Dynamics of 3  5.4. Concluding Thoughts  APPENDICES  Appendix 5.A. Singular Value Decomposition MATLAB Script for Full Spectrum TA An	213 214 215 216 219 223 228 229 alysis 230
5.2.2. Ultrafast Transient Absorption Spectroscopy  5.3. Results and Discussion 5.3.1. Ground-State Properties of Compounds 1, 2, and 3 5.3.2. Excited State Dynamics of 1 5.3.3. Excited State Dynamics of 2 5.3.4. Excited State Dynamics of 3  5.4. Concluding Thoughts  APPENDICES  Appendix 5.A. Singular Value Decomposition MATLAB Script for Full Spectrum TA An  Appendix 5.B. Simulated MLCT Spectra  Appendix 5.C. Global Fits of Full Spectrum TA Data	213214215216219223228229 alysis230233
5.2.2. Ultrafast Transient Absorption Spectroscopy  5.3. Results and Discussion  5.3.1. Ground-State Properties of Compounds 1, 2, and 3  5.3.2. Excited State Dynamics of 1  5.3.3. Excited State Dynamics of 2  5.3.4. Excited State Dynamics of 3  5.4. Concluding Thoughts  APPENDICES  Appendix 5.A. Singular Value Decomposition MATLAB Script for Full Spectrum TA An  Appendix 5.B. Simulated MLCT Spectra  Appendix 5.C. Global Fits of Full Spectrum TA Data  Appendix 5.D. Additional TA Data with Coherent Oscillations	213214215216219223229 alysis233234237
5.2.2. Ultrafast Transient Absorption Spectroscopy  5.3. Results and Discussion 5.3.1. Ground-State Properties of Compounds 1, 2, and 3 5.3.2. Excited State Dynamics of 1 5.3.3. Excited State Dynamics of 2 5.3.4. Excited State Dynamics of 3  5.4. Concluding Thoughts  APPENDICES  Appendix 5.A. Singular Value Decomposition MATLAB Script for Full Spectrum TA An Appendix 5.B. Simulated MLCT Spectra Appendix 5.C. Global Fits of Full Spectrum TA Data	213214215216219223229 alysis233234237
5.2.2. Ultrafast Transient Absorption Spectroscopy  5.3. Results and Discussion  5.3.1. Ground-State Properties of Compounds 1, 2, and 3  5.3.2. Excited State Dynamics of 1  5.3.3. Excited State Dynamics of 2  5.3.4. Excited State Dynamics of 3  5.4. Concluding Thoughts  APPENDICES  Appendix 5.A. Singular Value Decomposition MATLAB Script for Full Spectrum TA An  Appendix 5.B. Simulated MLCT Spectra  Appendix 5.C. Global Fits of Full Spectrum TA Data  Appendix 5.D. Additional TA Data with Coherent Oscillations  REFERENCES	213214215216219223228229 allysis230231237
5.2.2. Ultrafast Transient Absorption Spectroscopy  5.3. Results and Discussion  5.3.1. Ground-State Properties of Compounds 1, 2, and 3  5.3.2. Excited State Dynamics of 1  5.3.3. Excited State Dynamics of 2  5.3.4. Excited State Dynamics of 3  5.4. Concluding Thoughts  APPENDICES  Appendix 5.A. Singular Value Decomposition MATLAB Script for Full Spectrum TA An  Appendix 5.B. Simulated MLCT Spectra  Appendix 5.C. Global Fits of Full Spectrum TA Data  Appendix 5.D. Additional TA Data with Coherent Oscillations  REFERENCES	213214215216219223228229 alysis233234234
5.2.2. Últrafast Transient Absorption Spectroscopy  5.3. Results and Discussion  5.3.1. Ground-State Properties of Compounds 1, 2, and 3  5.3.2. Excited State Dynamics of 1  5.3.3. Excited State Dynamics of 2  5.3.4. Excited State Dynamics of 3  5.4. Concluding Thoughts  APPENDICES  Appendix 5.A. Singular Value Decomposition MATLAB Script for Full Spectrum TA An  Appendix 5.B. Simulated MLCT Spectra  Appendix 5.C. Global Fits of Full Spectrum TA Data  Appendix 5.D. Additional TA Data with Coherent Oscillations  REFERENCES  Chapter 6: Future Work  6.1. Introduction	213214215216219223228229 alysis230234234245245
5.2.2. Ultrafast Transient Absorption Spectroscopy  5.3. Results and Discussion  5.3.1. Ground-State Properties of Compounds 1, 2, and 3  5.3.2. Excited State Dynamics of 1  5.3.3. Excited State Dynamics of 2  5.3.4. Excited State Dynamics of 3  5.4. Concluding Thoughts  APPENDICES  Appendix 5.A. Singular Value Decomposition MATLAB Script for Full Spectrum TA An  Appendix 5.B. Simulated MLCT Spectra  Appendix 5.C. Global Fits of Full Spectrum TA Data  Appendix 5.D. Additional TA Data with Coherent Oscillations  REFERENCES  Chapter 6: Future Work	213214215216219223229 allysis230234237242245245

6.5. Modular Manipulation of Excited State Dynamics of Iron(II) Chromophores	249
REFERENCES	

# LIST OF TABLES

<b>Table 1.1.</b> Summary of the extinction coefficients, $\varepsilon$ , and oscillator strengths, $f$ , typically observed for various electronic transitions of transition metal complexes
<b>Table 2.1.</b> Summary of oscillatory components observed for variable excitation wavelength TA experiments conducted by Foszcz <sup>12</sup> on Cr(acac) <sub>3</sub> . Errors are reported as standard deviations of all the data listed in Foszcz's dissertation work.
<b>Table 2.2.</b> Summary of coherent vibrational modes of Cr(acac) <sub>3</sub> observed during TA experiments in various solvents. Reported IRFs are rounded to the nearest integer multiple of 5 fs
<b>Table 2.3.</b> Summary of the coherent vibrational modes of $Cr(3-NO_2ac)_3$ following $^4A_2 \rightarrow ^4T_2$ excitation. All measurements performed in Dioxane used 4 and 0.4 $\mu J$ pump and probe pulses respectively while the THF measurement employed 4.7 and 0.5 $\mu J$ pump and probe pulses. The dioxane and THF experiments had 40 and 35 fs IRFs respectively.
<b>Table 2.4.</b> Summary of observed coherent vibrational modes of Cr(3-Clac) <sub>3</sub> in toluene following excitation into the <sup>4</sup> T <sub>2</sub> state. The sub-100 cm <sup>-1</sup> oscillatory components picked up by the LPSVD fitting program were included for transparency, however, they are likely due to poor exponential fitting of the data and not to coherent vibrational motion. All experiments employed 4 and 0.4 μJ pump and probe pulses respectively with a 45 fs IRF.
<b>Table 2.5.</b> Summary of the coherent oscillations of Cr(3-Brac) <sub>3</sub> following excitation into the <sup>4</sup> T <sub>2</sub> state. Experimental parameters such as pump and probe wavelengths and pulse energies as well as IRF FWHMs are also included for each experiment.
<b>Table 2.6.</b> Summary of the coherent oscillations of Cr(3-Iac) <sub>3</sub> following 600 nm excitation into the <sup>4</sup> T <sub>2</sub> state. Each measurement employed 4 and 0.4 μJ pump and probe pulse energies respectively with a 40 fs IRF
<b>Table 2.7.</b> Summary of the oscillatory components observed for Cr(TMHD) <sub>3</sub> following excitation into the ${}^{4}T_{2}$ state across several solvents. Experimental details such as the IRF and pump and probe wavelengths and pulse energies are included for each experiment. Probe pulse energies were not measured when using a continuum probe and are labeled below as "na".
<b>Table 2.8.</b> Summary of coherent oscillations observed in TA data on Cr(4-Cl-TMHD) <sub>3</sub> following 600 nm excitation into the ${}^4T_2$ state while monitoring at 600 nm in dichloromethane. The sub-100 cm <sup>-1</sup> oscillatory components were included for transparency; however, it is likely that they arise from poor exponential fitting and do not truly represent coherent vibrational motion of the solute. Experimental details such as the IRF and the pump and probe pulse energies are included for each measurement98
Table 2.B.1. Frequencies and dephasing times of common solvent vibrational modes as determined from transient absorption spectroscopy.       118
<b>Table 3.1.</b> Summary of the observed kinetics in reference 8.    128
<b>Table 3.2.</b> Summary of kinetic components from single wavelength transient absorption experiments on Co(acac) <sub>3</sub> in acetonitrile following 600 nm excitation into the ${}^{1}T_{1g}$ state

<b>Table 3.3.</b> Summary of the coherent vibrational modes observed for Co(acac)3 in acetonitrile. Pump and probe pulse energies, E <sub>pu</sub> , and E <sub>pr</sub> , are provided for each experiment. The IRF was 40 fs for each experimen
<b>Table 3.4.</b> Comparison of the oscillation amplitude and the preexponential factor for the 510 fs kinetic component of Co(acac) <sub>3</sub> observed during TA experiments. Oscillation amplitudes and preexponential factors were either both directly acquired from LPSVD fits or separately acquired from an exponential fit to the data and the oscillation magnitude of the residual of the exponential fit
<b>Table 3.5.</b> Summary of kinetic components from single wavelength transient absorption experiments of $Co(3-Iac)_3$ in toluene following 600 nm excitation into the ${}^1T_{1g}$ state
<b>Table. 3.6.</b> Summary of the coherent vibrational modes for Co(3-Iac) <sub>3</sub> in toluene following 600 nm excitation into the ${}^{1}$ T <sub>1g</sub> excited state. All measurements had 40 fs IRF and employed 2.9 and 0.4 μJ pump and probe pulse energies respectively.
<b>Table 3.7.</b> Summary of kinetic components of Co(TMHD) <sub>3</sub> in DCM following 600 nm excitation 159
<b>Table 3.8.</b> Summary of coherent oscillations of Co(TMHD) <sub>3</sub> in DCM following 600 nm excitation159
Table 3.9. Summary of the kinetic components and coherent oscillations of each of the Co(acac') compounds investigated in this chapter.       160
<b>Table 4.1.</b> Summary of the coherent vibrational modes of [Fe(L)](PF <sub>6</sub> ) <sub>2</sub> (1) observed during TA experiments following 600 nm excitation in acetonitrile solution
<b>Table 4.2.</b> Summary of the coherent vibrational modes of [FeCu <sub>2</sub> (L)(PF <sub>6</sub> ) <sub>4</sub> (2) in different solvents. All errors are expressed as the standard deviation of multiple trials.
<b>Table 4.3.</b> Summary kinetic components of [FeCu <sub>2</sub> (L)] <sup>2+</sup> in various solvents and with PF <sub>6</sub> <sup>-</sup> and Bar <sup>F</sup> counteranions. Errors are expressed as standard deviations from multiple trials
<b>Table 4.D.1.</b> Coherent oscillatory components observed for individual TA datasets on [Fe(L)[(PF <sub>6</sub> ) <sub>2</sub> in acetonitrile solvent following 600 nm excitation
<b>Table 4.D.2.</b> Kinetic components and fit parameters for individual TA datasets on [FeCu <sub>2</sub> (L)](PF <sub>6</sub> ) <sub>4</sub> in various solvents following 600 nm excitation. A 7 ns kinetic component was locked in to describe the slow ground state recovery process and account for any baseline offset
<b>Table 4.D.3.</b> Coherent oscillatory components observed in individual TA datasets on [FeCu <sub>2</sub> (L)](PF <sub>6</sub> ) <sub>4</sub> in various solvents following 600 nm excitation. The observed sub-100 cm <sup>-1</sup> components are not expected to be physically meaningful.
<b>Table 4.D.4.</b> Kinetic components and fit parameters for individual TA datasets on [FeCu <sub>2</sub> (L)](Bar <sup>F</sup> ) <sub>4</sub> in various solvents following 600 nm excitation and while monitoring at 700 nm. A 7 ns kinetic componen was locked in and used to describe the slow ground state recovery process and account for any baseling offset.
Table 4.D.5. Results of individual kinetic fits of [Fe(L)](PF <sub>6</sub> ) <sub>2</sub> TA data following 600 nm excitation in acetonitrile solvent.       206
<b>Table 5.1.</b> Electrochemical and spectroscopic parameters of [Fe(phen) <sub>3</sub> ] <sup>2+</sup> (1), [Fe(phen) <sub>2</sub> (CN) <sub>2</sub> ] (2), and [Fe(phen) <sub>2</sub> (C <sub>4</sub> H <sub>10</sub> N <sub>4</sub> )] (3) collected by Karl Nielsen of the McCusker group

<b>Table 5.2.</b> Summary of the kinetic components of $[Fe(phen)_3](BF_4)_2$ (1), $[Fe(phen)_2(CN)_2]$ (2), and $[Fe(phen)_2(C_4H_{10}N_4)](PF_6)_2$ (3) in methanol solution.
<b>Table 5.D.1.</b> Summary of coherent oscillations of [Fe(phen) <sub>3</sub> ](BF <sub>4</sub> ) <sub>2</sub> (1) observed in TA experiments in methanol following 520 nm excitation. Experiments were conducted similarly in both wavelength regions, except that in the 610-630 nm region, several separate experiments were conducted individually at 610, 620, and 630 nm and the results of the LPSVD fits from each of these probe wavelengths were averaged together.
<b>Table 5.D.2.</b> Summary of the coherent oscillations of $[Fe(phen)_2(C_4H_{10}N_4)](PF_6)_2$ (3) in methanol and acetonitrile following 600 nm excitation. The presented results are from a single dataset for each probe wavelength and solvent. As such, no error bars in the form of a standard deviation are presented for these values.
<b>Table 5.D.3.</b> Summary of the kinetic components of [Fe(phen) <sub>2</sub> (C <sub>4</sub> H <sub>10</sub> N <sub>4</sub> )](PF <sub>6</sub> ) <sub>2</sub> ( <b>3</b> ) in methanol and acetonitrile following 600 nm excitation. Errors are reported as the standard deviation of multiple trials.

# LIST OF FIGURES

<b>Figure 1.1.</b> Jablonski diagram depicting various excited state processes including vibrational relaxation (VR), internal conversion (IC), intersystem crossing (ISC), fluorescence (FL), and phosphorescence (PH). Radiative transitions are shown as solid lines and nonradiative transitions are shown as dashed lines 3
<b>Figure 1.2.</b> Energy level diagram showing possible signals in a pump-probe transient absorption experiment including ground state bleach (GSB), excited state absorption (ESA) and stimulated emission (SE).
<b>Figure 1.3.</b> Illustration of the different ways pump-probe TA data can be viewed. In the 2-dimensional data set shown in (a) the entire transient spectrum is collected at each time delay. A vertical slice of this data (black) contains the differential absorption at a single wavelength across a series of time delays. This is illustrated in the black boxed kinetics trace of (b). A horizontal slice shown in red represents the transient spectrum at a specific pump-probe delay time and is shown in the red boxed spectrum (c) 6
<b>Figure 1.4.</b> Resonance as an analogy to coherence. The ground state wavefunction of benzene is a linear combination of multiple component wavefunctions
<b>Figure 1.5.</b> Generation of a coherent superposition state, or wavepacket, as a linear combination of oscillating wavefunctions.
<b>Figure 1.6.</b> Potential energy surface diagram depicting the process of forming a wavepacket on the ground electronic state.
<b>Figure 1.7.</b> Simulated wavepacket propagation on an excited state potential energy surface which (a) has the same force constant as the ground state, (b) has a different force constant than the ground state, (c) is anharmonic, and (d) is dissociative. The initial projected wavepacket is shown in red. Wavepackets that have propagated on the excited state surface are shown in dashed lines
<b>Figure 1.8.</b> (a) Effect of coherent vibrational motion on the entire transient absorption spectrum. Band oscillates according to the frequencies of the activated vibrations. (b) Manifestation of coherent vibrational motion on single wavelength TA measurements. Oscillatory features are superimposed upon the population dynamics. (c) Fourier transformation (blue) of oscillatory components of TA data results in a vibrational spectrum of the molecule. LPSVD fit of TA data provides not only frequencies of coherent vibrational modes but also their dephasing times.
<b>Figure 2.1.</b> Qualitative potential energy diagram representing the pertinent electronic states of $Cr(acac)_3$ . The ${}^2T_{1g}$ and ${}^2E$ potential energy surfaces have been merged into a single " ${}^2E$ " state for simplicity. The electron configurations in the 1-electron picture are represented for each state at right
<b>Figure 2.2.</b> Electron density distributions for the pertinent electronic ground and excited states of d <sup>3</sup> compounds in an O <sub>h</sub> ligand field. Distributions were calculated using the LIGFIELD program with the help of Jon Yarranton.
<b>Figure 2.3.</b> (left) Transient absorption spectrum of $Cr(acac)_3$ in acetonitrile solution at $\Delta t = 5$ ps (solid line) along with normalized absorption amplitudes obtained from single-wavelength nanosecond transient absorption data (red markers) collected in a 9:2 propionitrile/butyronitrile glass at 90 K. Close agreement between these two datasets suggests that $Cr(acac)_3$ is in the fully thermalized lowest energy excited state, the ${}^2E$ state, by $\Delta t = 5$ ps. (right) Transient absorption spectrum of $Cr(acac)_3$ over the course of the first 5

Society
<b>Figure 2.4.</b> (a) Single-wavelength kinetic trace of $Cr(acac)_3$ monitored at $592 \pm 2$ nm following 600 nm excitation in acetonitrile. An exponential increase in excited state absorbance ( $\tau = 320$ fs) was subtracted from the data to better illustrate the oscillatory component of the data. The solid line corresponds to a fit to two exponentially damped oscillatory components with frequencies and damping times of $164 \pm 20$ cm <sup>-1</sup> ( $\tau_{damp} = 70$ fs) and $75 \pm 25$ cm <sup>-1</sup> ( $\tau_{damp} = 1.6$ ps). (b) Density functional theory calculated vibrational mode on the ground electronic state. The excited state wavepacket was proposed to exhibit a similar motion to this $184$ cm <sup>-1</sup> calculated symmetric breathing mode. Figure reproduced from reference 10 with permission of the Royal Society of Chemistry.
<b>Figure 2.5.</b> (a) Transient absorption spectra of Cr(TMHD) <sub>3</sub> in dicloromethane following 633 nm excitation. (b) Single-wavelength kinetic trace collected at 450 nm and (c) 550 nm following 610 nm excitation. Solid lines represent single exponential fits (with $\tau_{\text{obs}} = 2.0 \pm 0.2$ ps and $1.6 \pm 0.2$ ps for (b) and (c) respectively). Figure reproduced from reference 10 with permission of the Royal Society of Chemistry
<b>Figure 2.6.</b> (a) Plot of the elements of the Duschinsky displacement vector for the distortion of the ground state geometry to ${}^{4}T_{2}$ state equilibrium geometry as a function of vibrational modes on the ground electronic state inset showing an overlay of these two geometries. (b) Time dependent populations calculated using wavepacket analysis. (c) Plot of the position expectation value as a function of time during wavepacket simulation (solid) and standard deviation (shaded). Reprinted with permissions from Reference 8 23
<b>Figure 2.7.</b> (a) Steady state (lower trace) and transient difference spectra (upper traces) following 400 nm excitation of Cr(acac) <sub>3</sub> in tetrachloroethylene. (b) Evolution of the 1521 cm <sup>-1</sup> bleach recovery ( $\nu$ C=C) following 400 nm excitation. Solid line corresponds to a biexponential fit with $\tau_1$ = 15 ps and $\tau_2$ = 760 ps. Inset superposes the bleach and the inverse of the excited state absorption feature at 1509 cm <sup>-1</sup> . The sharp feature at early time is part of the coherent artifact. Figure reprinted with permission from reference 13. © (2007) American Chemical Society.
<b>Figure 2.8.</b> (a) Time dependent shifting for $\nu$ CO and $\nu$ C=C stretching ESA bands of Cr(acac) <sub>3</sub> in tetrachloroethylene following ${}^4A_2 \rightarrow {}^4T_1$ (400 nm) and ${}^4A_2 \rightarrow {}^4LMCT$ (345 nm) excitation. (b) Time dependent narrowing of the for $\nu$ CO and $\nu$ CC ESA features. (c) Bleach recovery kinetics of the $\nu$ C=C stretching band following excitation into the 0 $\rightarrow$ 1 transition at 1521 cm <sup>-1</sup> with fit shown in red. The inset shows a comparison of the decay dynamics following excitation at various wavelengths. Data in inset are normalized to the value at 10 ps. Reprinted with with permission from reference 14. © (2015) American Chemical Society.
<b>Figure 2.9.</b> Simplified Energy level diagram for Cr(acac) <sub>3</sub> depicting the relaxation processes proposed in reference 14.
<b>Figure 2.10.</b> Bleach recovery dynamics of Cr(acac) <sub>3</sub> in tetrachloroethylene with experimental data (symbols) and simulated (solid lines) ground state populations. Reprinted with with permission from reference 14. © (2015) American Chemical Society
<b>Figure 2.11.</b> Early time full spectrum transient absorption data on (a) $Cr(3-Br-acac)_3$ , (b) $Cr(3-SCN-acac)_3$ , (c) $Cr(3-NO_2-acac)_3$ , and (d) $Cr(3-Ph-acac)_3$ following $^4A_2 \rightarrow ^4T_2$ excitation. Reproduced from data in Reference 15.
Figure 2.12. Representative OKE trace collected in methanol with 600 nm degenerate pump and probe.  The first half of the detect (block simples) was fit to a Gaussian to determine the EWHM of the IRE.

<b>Figure 2.13.</b> (a) Representative TA data exhibiting coherent oscillations (blue). The corresponding LPSVD fit (red) and exponential components acquired from LPSVD fit (black) are superimposed on the original dataset. The Residuals of each of these with respect to the raw data are shown above in red and black respectively. (b) Individual oscillatory components parsed out of raw data using LPSVD
<b>Figure 2.14.</b> Illustration of methodology used to systematically identify origin of coherent oscillations in TA data. TA data and corresponding LPSVD fits of (a) Cr(TMHD) <sub>3</sub> dissolved in benzene in a quartz cuvette, (b) neat benzene in a quartz cuvette, and (c) an empty quartz cuvette. (d) Superimposed LPSVD magnitude spectra normalized to the common peak at 500 cm <sup>-1</sup> .
<b>Figure 2.15.</b> Approximated impulsive windows for various IRFs
<b>Figure 2.16.</b> (a) Full spectrum transient absorption data on $Cr(acac)_3$ following ${}^4A_2 \rightarrow {}^4T_1$ (400 nm) excitation in acetonitrile. (b) Decay associated difference spectra (DADS) associated with the global fit of the data in (a). A 1 ns lifetime associated with the longtime offset was locked in but had no bearing on the value of the shorter time constant.
<b>Figure 2.17.</b> (a) Qualitative energy level diagram depicting the ground ${}^{4}A_{2}$ state ( $ A\rangle$ ), ${}^{2}E$ state ( $ E\rangle$ ), ${}^{4}T_{2}$ state ( $ T\rangle$ ), and charge transfer manifold ( $ C\rangle$ ) that the ${}^{2}E$ and ${}^{4}T_{2}$ states can be promoted to through resonance with the probe beam. (b) Double sided Feynman diagrams depicting stimulated emission (SE), ground state bleaching (GSB) and excited state absorption (ESA) processes. Following excitation, to the ${}^{4}T_{2}$ state, the system may evolve. Depending on the time delay between pump and probe, a population may exist in the ${}^{4}T_{2}$ or ${}^{2}E$ states. This relaxation pathway is denoted by a gray box. (c) The relationship between signal amplitude (third order response function) and transition dipole moments for relevant field interactions for SE, GSB, and ESA.
<b>Figure 2.18.</b> (a) Representative TA data on Cr(acac) <sub>3</sub> collected in acetonitrile following 600 nm excitation and monitoring at 592 nm. (b) Comparison of results of  FFT  (blue) and LPSVD (red) analyses of data from part a. (c) Analogous data collected while monitoring at 480 nm. (d) Comparison of  FFT  and LPSVD analyses for 480 nm probe data.
<b>Figure 2.19.</b> (a) Representative TA data on Cr(acac) <sub>3</sub> collected in tetrahydrofuran (THF) following 600 nm excitation while monitoring at the red edge of the excited state absorption feature. (b) Corresponding FFT and LPSVD analyses. (c) Analogous data collected in 1,4-dioxane and (d) corresponding  FFT  and LPSVD vibrational spectra. It is possible that the 271 cm <sup>-1</sup> band in part b is a vibrational mode of THF. The ~500 cm <sup>-1</sup> component in part d can be attributed to the glass of the cuvette
<b>Figure 2.20.</b> (a) TA data collected on an empty 1 mm glass cuvette. The observed coherent oscillations are assigned to ground state vibrational coherence in the cuvette itself. (b) Fast Fourier transform and LPSVD spectrum of the coherent oscillations of (a), showing a ~ 500 cm <sup>-1</sup> component
<b>Figure 2.21.</b> Resonance Raman spectra collected on neat THF (black) and $Cr(acac)_3$ (red). The solvent background was subtracted from the $Cr(acac)_3$ dataset. The 488 nm excitation source is resonant with the blue edge of the ${}^4A_2 \rightarrow {}^4T_2$ transition.
<b>Figure 2.22.</b> (a) Raman spectrum of neat tetrahydrofuran (blue) with 488 nm excitation source. A Lorentzian fit to a band centered at $913 \text{ cm}^{-1}$ (red) shows a FWHM of $12.9 \text{ cm}^{-1}$ corresponding to a dephasing time of $820 \pm 30 \text{ fs}$ . (b) TA data on neat THF with 600 nm excitation source and 584 nm probe (blue) along with LPSVD fit of the dataset (red). The average dephasing time measured with four datasets is $950 \pm 140 \text{ fs}$ .

**Figure 2.23.** Nuclear deformations associated with the 193 cm<sup>-1</sup> (a) and 461 cm<sup>-1</sup> (b) vibrational modes of

$\operatorname{Cr}(\operatorname{acac})_3$
<b>Figure 2.24.</b> Drawing of the Cr(acac') <sub>3</sub> derivatives to be studied in this report
<b>Figure 2.25.</b> Representative TA data on $Cr(3-NO_2ac)_3$ following 600 nm excitation into the ${}^4T_2$ state in 1,4 dioxane while monitoring a 4 nm slice of the probe spectrum at (a) 608 nm, (c) 600 nm, and (e) 592 nm FFT and LPSVD analyses corresponding to the (b) 608 nm, (d) 600 nm, and (f) 592 nm data sets 63
<b>Figure 2.26.</b> Nuclear deformation associated with the 150 cm <sup>-1</sup> vibrational mode of Cr(3-NO <sub>2</sub> ac) <sub>3</sub> 64
<b>Figure 2.27.</b> Absorption spectrum of Cr(3-Clac) <sub>3</sub> in dichloromethane.
<b>Figure 2.28.</b> (a) Early time full spectrum TA data on Cr(3-Clac) <sub>3</sub> in toluene following 600 nm excitation into the ${}^{4}T_{2}$ state. (b) Decay associated difference spectrum (DADS) associated with the global fit of the TA data to a sequential biexponential decay. The long-time offset was modeled by fixing a 1 ns exponential decay to describe the slower ground state recovery process. (c) Evolution associated difference spectra (EADS) associated with the global fit.
<b>Figure 2.29.</b> Representative single wavelength TA data on $Cr(3-Clac)_3$ in toluene following 600 nm excitation into the ${}^4T_2$ state while monitoring at (a) 490 nm, (b) 550 nm, and (c) 650 nm. The two blues wavelengths show ~1.2 ps fits while the 650 nm probe data may show additional dynamics
<b>Figure 2.30.</b> Representative TA traces and FFT and LPSVD analyses of coherent oscillations of Cr(3 Clac) <sub>3</sub> in toluene following excitation into the <sup>4</sup> T <sub>2</sub> state. Coherent oscillations were monitored at (a) 608 nm, (c) 600 nm, and (e) 592 nm. Corresponding FFT and LPSVD vibrational spectra are shown in (b), (d) and (f).
<b>Figure 2.31.</b> Nuclear deformations associated with the 149 cm <sup>-1</sup> vibrational mode of Cr(3-Clac) <sub>3</sub> 70
<b>Figure 2.32.</b> (a) Early time full spectrum TA data on Cr(3-Brac) <sub>3</sub> in toluene following 600 nm excitation into the <sup>4</sup> T <sub>2</sub> state. The 570-630 nm spectral region was omitted due to large contamination from pump scatter. (b) Decay associated difference spectrum (DADS) associated with the global fit of the TA data to a sequential biexponential decay. The long-time offset was modeled by fixing a 1 ns exponential decay to describe the slower ground state recovery process. (c) Evolution associated difference spectra (EADS) associated with the global fit.
<b>Figure 2.33.</b> Representative single wavelength TA traces collected on Cr(3-Brac) <sub>3</sub> in toluene following excitation into the <sup>4</sup> T <sub>2</sub> state and monitoring at (a) 490 nm, (b) 550 nm, and (c) 650 nm
<b>Figure 2.34.</b> Representative TA traces and FFT and LPSVD analyses of coherent oscillations of Cr(3-Brac) <sub>3</sub> in toluene following excitation into the <sup>4</sup> T <sub>2</sub> state. Coherent oscillations were monitored at (a) 608 nm and (c) 592 nm. Corresponding FFT and LPSVD vibrational spectra are shown in (b) and (d) 73
<b>Figure 2.35.</b> Nuclear deformations associated with the 123 cm <sup>-1</sup> vibrational mode of Cr(3-Brac) <sub>3</sub> 74
<b>Figure 2.36.</b> Absorption spectrum of Cr(3-Iac) <sub>3</sub> .
<b>Figure 2.37.</b> Crystal Structure of Cr(3-Iac) <sub>3</sub> collected by Sara Adelman and solved by Professor Richard Staples of Michigan State University.
<b>Figure 2.38.</b> (a) Early time full spectrum TA data on Cr(3-Iac) <sub>3</sub> in toluene following 600 nm excitation into the <sup>4</sup> T <sub>2</sub> state. (b) Decay associated difference spectra (DADS) associated with the global fit of the TA data

to a sequential biexponential decay. The long-time offset was modeled by fixing a 1 ns exponential decay to describe the slower ground state recovery process. (c) Evolution associated difference spectra (EADS) associated with the global fit. Distortions around 600 nm in the data, DADS, and EADS are due to residual pump scatter
<b>Figure 2.39.</b> Representative single wavelength TA data on $Cr(3-Iac)_3$ in toluene following 600 nm excitation into the ${}^4T_2$ state while monitoring at (a) 490 nm, (b) 550 nm, and (c) 650 nm
<b>Figure 2.40.</b> Representative TA traces and FFT and LPSVD analyses of coherent oscillations of $Cr(3-Iac)_3$ in toluene following excitation into the $^4T_2$ state. Coherent oscillations were monitored at (a) 608 nm, (c) 600 nm, and (e) 592 nm. Corresponding FFT and LPSVD vibrational spectra are shown in (b), (d), and (f).
<b>Figure 2.41.</b> Nuclear deformations associated with the 101 cm <sup>-1</sup> vibrational mode of Cr(3-Iac) <sub>3</sub> 80
<b>Figure 2.42.</b> Summary of the results on the 3-substituted Cr(acac') <sub>3</sub> series. Internal conversion lifetimes for Cr(acac) <sub>3</sub> and Cr(3-NO <sub>2</sub> ac) <sub>3</sub> were acquired from references 7 and 15 respectively
<b>Figure 2.43.</b> Depiction of the two possible mechanisms for excited state decay at early times in $Cr(TMHD)_3$ . Mechanism 1 involves a slow 1.8 ps ${}^4T_2 \rightarrow {}^2E$ ISC. Mechanism 2 involves a rapid equilibration of the ${}^4T_2$ and ${}^2E$ states. As the molecule begins to vibrationally cool the ${}^2E \leftrightarrow {}^4T_2$ equilibrium shifts to the left and results in a 1.8 ps ISC. IC within the quartet manifold can occur, although it is not the dominant source of population relaxation.
<b>Figure 2.44.</b> (a) Early time full spectrum TA data on $Cr(HD)_3$ in dichloromethane following 600 nm excitation into the ${}^4T_2$ state. (b) Decay associated difference spectra (DADS) associated with the global fit of the TA data to a sequential biexponential decay. The long-time offset was modeled by fixing a 1 ns exponential decay to describe the slower ground state recovery process. (c) Evolution associated difference spectra (EADS) associated with the global fit. Distortions in the transient spectrum near 600 nm are due to residual pump scatter.
<b>Figure 2.45.</b> Representative single wavelength TA data on $Cr(HD)_3$ in acetonitrile (a) and dichloromethane (b and c) following 600 nm excitation into the ${}^4T_2$ state while monitoring at (a) 490 nm, (b) 550 nm, and (c) 650 nm.
<b>Figure 2.46.</b> (a) Early time full spectrum TA data on $Cr(DMHD)_3$ in dichloromethane following 600 nm excitation into the $^4T_2$ state. (b) Decay associated difference spectra (DADS) associated with the global fit of the TA data to a sequential biexponential decay. The long-time offset was modeled by fixing a 1 ns exponential decay to describe the slower ground state recovery process. (c) Evolution associated difference spectra (EADS) associated with the global fit. Distortions in the transient spectrum near 600 nm are due to residual pump scatter.
<b>Figure 2.47.</b> Representative single wavelength TA data on Cr(DMHD) <sub>3</sub> in dichloromethane (a and b) and acetonitrile (c) following 600 nm excitation into the $^4T_2$ state while monitoring at (a) 490 nm, (b) 550 nm, and (c) 586 nm.
<b>Figure 2.48.</b> Early time full spectrum TA data on (a) Cr(acac) <sub>3</sub> , (b) Cr(HD) <sub>3</sub> , (c) Cr(DMHD) <sub>3</sub> , and (d) Cr(TMHD) <sub>3</sub> following excitation into the <sup>4</sup> T <sub>2</sub> excited state. Parts (a) and (d) were reproduced with data from references 7 and 15 respectively
<b>Figure 2.49.</b> Representative transient absorption data on Cr(TMHD) <sub>3</sub> in 1,4-dioxane following excitation into the <sup>4</sup> T <sub>2</sub> excited state while monitoring at (a) 592 nm and (c) 550 nm with corresponding vibrational

spectra (b and d) resulting from FFT and LPSVD analyses. 92
<b>Figure 2.50.</b> Representative transient absorption data on $Cr(TMHD)_3$ in tetrahydrofuran following excitation into the ${}^4T_2$ excited state while monitoring at (a) 568 nm and (c) 545 nm with corresponding vibrational spectra (b and d) resulting from FFT and LPSVD analyses. 93
<b>Figure 2.51.</b> Stacked plot of Raman data on $Cr(acac)_3$ and $Cr(TMHD)_3$ in THF with 488 nm excitation source in resonance with the blue edge of the ${}^4A_2 \rightarrow {}^4T_2$ absorption band
<b>Figure 2.52.</b> Nuclear deformations associated with the (a) 173 cm <sup>-1</sup> and (b) 249 cm <sup>-1</sup> experimentally observed coherent vibrational modes of Cr(TMHD) <sub>3</sub> .
<b>Figure 2.53.</b> (a) Early time full spectrum TA data on $Cr(4-Cl-TMHD)_3$ in dichloromethane following 600 nm excitation into the ${}^4T_2$ state. (b) Global fit of the TA data to a sequential biexponential decay. The long-time offset was modeled by fixing a 1 ns exponential decay to describe the ground state recovery process. (c) Decay associated difference spectra (DADS) and (d) Evolution associated difference spectra (EADS) associated with the global fit
<b>Figure 2.54.</b> (a) Representative single wavelength TA data on $Cr(4-Cl-TMHD)_3$ following 600 nm excitation into the ${}^4T_2$ state in dichloromethane. Time constants for the fits of specific data sets are included on the graph itself, however the average time constant measured across all datasets is $1.7 \pm 0.2$ ps. (b) Zoomed in portion of the 600 nm probe data shown in part a with exponential and LPSVD fits and (c) corresponding vibrational spectrum resulting from FFT and LSVD analyses. 97
<b>Figure 2.55.</b> Nuclear deformations associated with the 118 cm <sup>-1</sup> experimentally observed coherent oscillations of Cr(4-Cl-TMHD) <sub>3</sub> .
<b>Figure 2.56.</b> Summary of the frequencies and dephasing times of the low frequency symmetric breathing mode observed in each Cr(acac') <sub>3</sub> derivative
<b>Figure 2.A.1.</b> Crystal structure for Cr(DMHD) <sub>3</sub> that was collected by Sara Adelman and solved by Professor Richard Staples
<b>Figure 2.A.2.</b> Crystal structure for Cr(4-Cl-TMHD) <sub>3</sub> that was collected by Sara Adelman and solved by Professor Richard Staples. The structure is highly disordered but still shows the desired compound 117
<b>Figure 2.C.1.</b> Resonance Raman spectrum of $Cr(acac)_3$ in THF solution (blue) in the vicinity of the 455 cm <sup>-1</sup> solute mode. The 488 nm excitation source is resonant with the blue edge of the ${}^4A_2 \rightarrow {}^4T_2$ transition. A fit of the 455 cm <sup>-1</sup> band to a Lorentzian function with a polynomial background (red) shows a FWHM of $8.5 \pm 0.1$ cm <sup>-1</sup> corresponding to a dephasing time of $1.25 \pm 0.2$ ps
<b>Figure 3.1.</b> Series of cobalt complexes to be studied in this chapter
<b>Figure 3.2.</b> (a) Tanabe-Sugano diagram for Co(acac) <sub>3</sub> calculated by McCusker group Member Jonathan Yarranton using the dtansug program written by Professor Joshua Telser of Roosevelt University and using the Racah B and C interelectronic repulsion parameters from reference 5. The rightmost dashed line corresponds to the value of Dq presented in that paper and the left most dashed line corresponds better to the vertical transition energies presented therein. (b) Vertical transition energies acquired from reference 5. The <sup>5</sup> T <sub>2g</sub> band was not observed experimentally but calculated using the LIGFIELD program of reference 6. (c) Qualitative potential energy surface diagram based on the Tanabe-Sugano diagram in part a. (d) One-electron pictures of relevant electronic states.

<b>Figure 3.3.</b> (a) Transient absorption spectrum for an aqueous solution of [Co(tppn)](ClO <sub>4</sub> ) <sub>3</sub> following ~500 fs excitation at 314 nm. (b) Transient absorption data measured at 390 nm with a biexponential fit. Reprinted with permission from reference 8. © (1993) American Chemical Society
<b>Figure 3.4.</b> Potential energy surface diagram for the ${}^{1}T_{1g}$ , ${}^{3}T_{1g}$ , ${}^{5}T_{2g}$ and ${}^{1}A_{1g}$ states of $[Co(NH_{3})_{6}]^{3+}$ along the $\nu(a_{1g})$ vibrational coordinate. The ${}^{5}T_{2g}$ surface is depicted as several dashed lines to represent a range of possible positions and a solid line to represent the position with largest overlap with the relaxed ${}^{3}T_{1g}$ state. Digitized from data in reference 13.
<b>Figure 3.5.</b> Full spectrum transient absorption data on Co(acac) <sub>3</sub> in acetonitrile solution following excitation at (a) 365 nm, (b) 390 nm, (c) 650 nm, and (d) 580 nm. Transient absorption data averaged ± 5 nm from center wavelengths of (e) 710 nm and (f) 520 nm following 390 nm excitation. (h) and (g) represent analogous datasets following 365 nm excitation. Reprinted with permission from reference 4. © 2019 Ferrari, Satta, Palma, Di Mario, Catone, O'Keeffe, Xema, Prosperi, and Turchini
<b>Figure 3.6.</b> (a) A pictorial representation of a cross product between two vectors, <b>a</b> and <b>b</b> separated by angle $\theta$ . The cross product, $\mathbf{a} \times \mathbf{b}$ , is perpendicular to the plane that contains <b>a</b> and <b>b</b> . The vector, <b>n</b> , is a unit vector in the same direction as $\mathbf{a} \times \mathbf{b}$ . (b) A pictorial representation of the process by which each atom is projected onto the plane perpendicular to the unit vector determined by the sum of the mass weighted cross products of the position vectors and that contains the center of mass of the molecule. This is to eliminate extra contributions to the moment of inertia to ensure an accurate angle, $\theta$ , is calculated which is needed to rotate the structure to nullify the angular momentum between two geometries.
<b>Figure 3.7.</b> Ground state absorption spectrum of Co(acac) <sub>3</sub> in acetonitrile
<b>Figure 3.8.</b> (a) Transient absorption data from 460-610 nm for Co(acac) <sub>3</sub> in acetonitrile following 600 nm excitation into the ${}^{1}T_{1g}$ state. (b) Decay associated difference spectrum associated with a global fit to two sequentially decaying exponential kinetic components. (c) Evolution associated difference spectra for the two kinetic components extracted from a global fit of the dataset
<b>Figure 3.9.</b> Additional full spectrum transient absorption data on Co(acac) <sub>3</sub> in acetonitrile following 600 nm excitation.
<b>Figure 3.10.</b> Representative TA traces and FFT and LPSVD analyses of coherent oscillations of Co(acac) <sub>3</sub> in acetonitrile following 600 nm excitation into the ${}^{1}T_{1g}$ state. Kinetics were monitored at (a) 620 nm, (c) 600 nm, and (e) 580 nm using a probe beam with a spectrum centered at 600 nm. Insets show coherent oscillations at early times. Corresponding FFT and LPSVD vibrational spectra are shown in (b), (d), and (f).
<b>Figure 3.11.</b> (a) Transient absorption data on Co(acac) <sub>3</sub> measured at the peak of the high energy band of the transient spectrum at 520 nm following 600 nm excitation into the ${}^{1}T_{1g}$ state. The inset shows the coherent oscillations at early time and an LPSVD fit. (b) Corresponding LPSVD and FFT vibrational spectrum.
<b>Figure 3.12.</b> Plots of the calculated inner-sphere reorganization energy as a function of normal mode frequency for pertinent electronic transitions of $Co(acac)_3$ . (a) Plot of the reorganization energy for the ${}^3T_{1g}$ transition as a function of the frequencies of the vibrational modes of the ${}^3T_{1g}$ electronic excited state. (b) Plot of the reorganization energy for the ${}^5T_{2g} \rightarrow {}^1A_{1g}$ transition as a function of the frequencies of the vibrational modes of the ${}^5T_{2g}$ electronic excited state. Reorganization energies were calculated from the nuclear displacements of the Duschinsky displacement vectors for the corresponding electronic transitions.

<b>Figure 3.13.</b> Nuclear deformations associated with the (a) 162 cm <sup>-1</sup> , (b) 440 cm <sup>-1</sup> , and (c) 466 cm <sup>-1</sup> experimentally observed vibrational modes of Co(acac) <sub>3</sub>
<b>Figure 3.14.</b> Possible assignments for the 263 cm <sup>-1</sup> experimentally observed coherent vibrational mode of $Co(acac)_3$ along with the corresponding inner-sphere reorganization energies for each mode along the ${}^3T_{1g} \rightarrow {}^1A_{1g}$ reaction coordinate determined from the Duschinsky displacement vector
<b>Figure 3.15.</b> Ground state absorption spectrum of Co(3-Iac) <sub>3</sub> in toluene
<b>Figure 3.16.</b> Difference spectrum of Co(3-Iac) <sub>3</sub> in toluene before and after significant light exposure153
<b>Figure 3.17.</b> Full spectrum TA data on $Co(3\text{-Iac})_3$ in toluene following 600 nm excitation into the ${}^1T_{1g}$ state. The region from $\sim$ 570-640 nm was omitted due to contamination from pump scatter
<b>Figure 3.18.</b> Representative single wavelength TA traces and FFT and LPSVD analyses of coherent oscillations of $Co(3\text{-Iac})_3$ in toluene following 600 nm excitation into the ${}^1T_{1g}$ state. Kinetics were monitored at (a) 620 nm, (c) 600 nm, and (e) 580 nm using a probe beam with a spectrum centered at 600 nm. Insets show coherent oscillations at early times. Corresponding FFT and LPSVD vibrational spectra are shown in (b), (d), and (f). LPSVD contributions are omitted from the 580 nm probe data due to lack of solute oscillations.
<b>Figure 3.19.</b> DFT calculated symmetric breathing mode of $Co(3\text{-Iac})_3$ on (a) the $^1A_{1g}$ ground state, (b) the $^3T_{1g}$ lowest energy triplet excited state, and (c) the $^5T_{2g}$ lowest energy excited state of the system 156
<b>Figure 3.20.</b> Ground state absorption spectrum of Co(TMHD) <sub>3</sub> in dichloromethane solution
<b>Figure 3.21.</b> (a) Full spectrum TA data on Co(TMHD) <sub>3</sub> in DCM following 600 nm $^{1}A_{1g} \rightarrow {}^{1}T_{1g}$ excitation. Anomalies around 600 nm are due to excess pump scatter. (b) DADS associated with a global fit of the data to a single exponential kinetic component
<b>Figure 3.22.</b> (a) and (c) Single wavelength TA data on Co(TMHD) <sub>3</sub> in DCM following 600 nm $^1A_{1g} \rightarrow ^1T_{1g}$ excitation. (b) and (d) corresponding vibrational spectra from FFT and LPSVD analysis 159
<b>Figure 3.23.</b> Nuclear distortion associated with the coherent vibrational mode of Co(TMHD) <sub>3</sub> 160
<b>Figure 3.24.</b> (a) Two-level potential energy surface diagram with displaced minima for use in wavepacket calculation. Diabatic and adiabatic representations are shown as dashed and solid lines respectively. The initial gaussian wavepacket is placed at 0 Å on the upper surface and allowed to propagate. (b) Contour plot showing the sum of the amplitude of the corresponding wavepackets on both excited states in position space as a function of time. (c) Two-level potential energy surface diagram with nested potentials for use in wavepacket simulations. The initial gaussian wavepacket is placed at 0 Å on the upper surface. (d) Contour plot showing the sum of the amplitude of the corresponding wavepackets on both excited states. Despite continuously cycling population from one surface to the other, the wavepacket retains a well-defined phase relationship
Figure 3.A.1. NMR spectrum of Co(acac) <sub>3</sub> in CDCl <sub>3</sub> .
<b>Figure 3.A.2.</b> NMR spectrum of Co(3-Iac) <sub>3</sub> in deuterated toluene
Figure 3.A.3. NMR spectrum of Co(TMHD) <sub>3</sub> in CDCl <sub>3</sub> .
Figure 4.1 Drawing of cage ligand (L) used in this study

<b>Figure 4.2.</b> Single-crystal x-ray structures of the cations of (a) $[Fe(L)](PF_6)_2$ (1), (b) $[FeCu_2(L)](PF_6)_4$ (2), and (c) $[ZnCu_2(L)](PF_6)_4$ (3). The hydrogen atoms have been removed for clarity. For metal ions: red = Fe, green = Cu, light blue = Zn.
<b>Figure 4.3.</b> Ground state electronic absorption spectra of [Fe(L)](PF <sub>6</sub> ) <sub>2</sub> (1), [FeCu <sub>2</sub> (L)](PF <sub>6</sub> ) <sub>4</sub> (2), and [ZnCu <sub>2</sub> (L)](PF <sub>6</sub> ) <sub>4</sub> (3). The spectra were acquired at room temperature in CH <sub>3</sub> CN solutions
<b>Figure 4.4.</b> Femtosecond time-resolved absorption data of [Fe(L)](PF <sub>6</sub> ) <sub>2</sub> (1) acquired in CH <sub>3</sub> CN solution. (a) Full spectrum data collected over the first few ps following MLCT excitation at 600 nm. The anomalous features near 600 nm are due to scattered light from the excitation source. (b) Single wavelength kinetics trace monitored at 608 nm with LPSVD fit. (c) Resulting vibrational spectrum corresponding to the FFT of the residuals of an exponential fit (blue) and the oscillations extracted through LPSVD fitting (red). (d) Single wavelength kinetics trace monitored at 658 nm with LPSVD fit. (e) Vibrational spectrum of the kinetic data collected at 658 nm.
<b>Figure 4.5.</b> Spectroelectrochemical data on [Fe(L)] <sup>2+</sup> (1) collected by Sara Adelman
<b>Figure 4.6.</b> DFT calculated vector displacement diagrams of several of the coherently excited vibrational modes of [Fe(L)](PF <sub>6</sub> ) <sub>2</sub> (1)
<b>Figure 4.7.</b> Overlay of the Fe-N <sub>6</sub> region of $[Fe(L)](PF_6)_2$ (1) and $[FeCu_2(L)](PF_6)_4$ (2) crystal structures. The complex drawn with red bonds is complex 1 and the complex with purple bonds is complex 2189
<b>Figure 4.8.</b> Representative TA data on [FeCu <sub>2</sub> (L)](PF <sub>6</sub> ) <sub>2</sub> ( <b>2</b> ) in acetonitrile following 600 nm excitation while monitoring at (a) 700 nm and (c) 650 nm (blue) with fit to equation 4.1 (red) and inset showing LPSVD fit to equation 4.2. Corresponding vibrational spectra (b) and (d) resulting from LPSVD fit (red) and FFT of the residuals of the exponential fit (blue). The appearance of an additional peak in the low frequency region in the LPSVD spectrum in part d can be attributed to error in exponential fitting in the LPSVD program, likely arising from fitting a small portion of the overall data set
<b>Figure 4.9.</b> Representative TA data on [FeCu <sub>2</sub> (L)](PF <sub>6</sub> ) <sub>4</sub> ( <b>2</b> ) in (a) butyronitrile and (b) acetone following 600 nm excitation and monitoring at 700 nm with insets showing raw data (blue) and LPSVD fits (red) over the first few picoseconds. (c) and (d) show the vibrational spectra resulting from the FFT and LPSVD analyses of the data in butyronitrile and acetone respectively.
<b>Figure 4.10.</b> DFT calculated vector displacement diagrams of the coherent modes of <b>2</b> observed in this study.
<b>Figure 4.11.</b> Femtosecond time-resolved absorption spectra of [FeCu <sub>2</sub> (L)](PF <sub>6</sub> ) <sub>4</sub> (2) following 600 nm excitation in acetonitrile solution.
<b>Figure 4.12.</b> Representative datasets of [FeCu <sub>2</sub> (L)](Bar <sup>F</sup> ) <sub>4</sub> in (a) acetonitrile, (b) acetone, and (c) butyronitrile following 600 nm excitation while monitored at 700 nm
<b>Figure 4.13.</b> Plots of the calculated inner-sphere reorganization energy as a function of normal mode frequency for the ${}^5T_{2g} \rightarrow {}^1A_{1g}$ transitions of (a) $[Fe(L)]^{2+}$ and (b) $[FeCu_2(L)]^{4+}$ . The normal modes used are inherent to the ${}^5T_{2g}$ excited state. Reorganization energies were calculated from the nuclear displacements of the Duschinsky displacement vectors for the corresponding electronic transition
<b>Figure 4.A.1.</b> (a) TA data of [FeCu <sub>2</sub> (L)](PF <sub>6</sub> ) <sub>4</sub> ( <b>2</b> ) in acetonitrile while exciting at 600 nm and monitoring at 396 nm (blue) with LPSVD fit to equation 4.2 (red). (b) LPSVD vibrational spectrum (red) with corresponding FFT of the residuals to an exponential fit (blue)

<b>Figure 4.B.1.</b> Calculated reorganization energy for the ${}^5T_{2g} \rightarrow {}^1A_{1g}$ transition of $[Fe(bpy)_3]^{2+}$
<b>Figure 4.C.1.</b> DFT calculated vector displacement diagram of the 123 cm <sup>-1</sup> vibrational mode of [Fe(L)] <sup>2+</sup>
Figure 5.1. Qualitative potential energy surfaces for six-coordinate (a) iron(II) and (b) ruthenium(II) compounds
<b>Figure 5.2.</b> Radial distribution function for (a) the n = 3 orbitals of iron(II) and (b) the n = 4 orbitals of ruthenium(II)
<b>Figure 5.3.</b> Drawing of the three compounds investigated in this study
<b>Figure 5.4.</b> Ground state absorption spectra of $[Fe(phen)_3](BF_4)_2$ (1), $[Fe(phen)_2(CN)_2]$ (2), and $[Fe(phen)_2(C_4H_{10}N_4)](PF_6)_2$ (3), collected by Karl Nielsen of the McCusker group
<b>Figure 5.5.</b> (a) Full spectrum TA data on [Fe(phen) <sub>3</sub> ](BF <sub>4</sub> ) <sub>2</sub> (1) in methanol following 570 nm excitation. Irregularities at 570 nm can be attributed to uncorrected pump scatter. (b) First (black) and second (blue) right eigenvectors from SVD of full spectrum dataset with 970 ps single exponential fits (red). (c) EADS for the single kinetic component obtained from SVD analysis
<b>Figure 5.6.</b> Single wavelength kinetics traces collected on $[Fe(phen)_3](BF_4)_2$ (1) in methanol at 520 nm following 520 nm excitation. This particular dataset was fit to a $1250 \pm 150$ ps time constant with the error bar representative of this single dataset
<b>Figure 5.7.</b> Single wavelength kinetics trace collected on [Fe(phen) <sub>3</sub> ](BF <sub>4</sub> ) <sub>2</sub> (1) in methanol at 610 nm following 520 nm excitation. Inset includes a fast Fourier transform of the residuals of an exponential fit to the population dynamics (blue) overlaid with a vibrational spectrum produced via LPSVD of the TA data (red)
<b>Figure 5.8.</b> (a) Full spectrum TA data on [Fe(phen) <sub>2</sub> (CN) <sub>2</sub> ] (2) in methanol following 570 nm excitation. (b) First (black), second (green), and third (blue) right eigen vectors from SVD of 2 and a biexponential fit (red) of the first right eigenvector to 6.6 and 315 ps kinetic components. (c) Simulated excited state populations using the time constants acquired from the right eigenvector fits and assuming sequential decay dynamics as shown in equation 5.3. (d) EADS calculated for the two kinetic components using equation 5.2. The red (F1) and blue (F2) spectra correspond to the fast and slowly decaying species respectively.
<b>Figure 5.9.</b> (a) Representative TA data of [Fe(phen) <sub>2</sub> (CN) <sub>2</sub> ] (2) in methanol following 590 nm excitation and monitored at 550 nm in the center of the ground state bleach. (b) Representative TA data on <b>2</b> following 600 nm excitation and monitored at 590 nm, the red edge of the ground state bleach. The two data sets show different kinetics at early times.
<b>Figure 5.10.</b> Single wavelength kinetics trace of [Fe(phen) <sub>2</sub> (CN) <sub>2</sub> ] ( <b>2</b> ) monitored at 620 nm following 550 nm excitation. Oscillatory features near the coherent artifact can be attributed to vibrational coherences.
<b>Figure 5.11.</b> (a) Chirp corrected full spectrum TA data on $[Fe(phen)_2(C_4H_{10}N_4)](PF_6)_2$ (3) following 600 nm excitation in methanol. The region between 590 and 610 nm has been removed and interpolated to remove the contribution from excess pump scatter. (b) First four right eigenvectors from SVD of TA data of compound 3 with triexponential fits (red) to 0.15, 1.2, and 5.3 ps time constants. An inset is included to

highlight the dynamics over the first 10 ps. (c) Simulated excited state populations using the time constants

acquired from the right eigenvector fits and assuming sequential decay dynamics as shown in equation 5.4. (d) EADS calculated from the time constants measured from SVD analysis assuming sequential decay dynamics
<b>Figure 5.12.</b> Single wavelength kinetics traces on [Fe(phen) <sub>2</sub> (C <sub>4</sub> H <sub>10</sub> N <sub>4</sub> )](PF <sub>6</sub> ) <sub>2</sub> ( <b>3</b> ) in methanol monitored at (a) 650 nm abd (b) 550 nm following 600 nm excitation. Insets show first 5 ps and highlight observed coherent oscillations.
<b>Figure 5.B.1.</b> Simulated MLCT spectrum of (a) $[Fe(phen)_3]^{2+}$ (1), (b) $[Fe(phen)_2(CN)_2]$ (2), and (c) $[Fe(phen)_2(C_4H_{10}N_4)]^{2+}$ (3) in methanol, predicted by summing the oxidative and reductive spectra 233
<b>Figure 5.C.1.</b> (a) Chirp corrected global fit using OPTIMUS fitting software on full spectrum data of [Fe(phen) <sub>3</sub> ] <sup>2+</sup> (1) to a single 940 ps exponential kinetic component. (b) DADS from global fit of 1 full spectrum data. Since there was only a single kinetic component, the DADS is equivalent to the EADS
<b>Figure 5.C.2.</b> (a) Chirp corrected global fit using OPTIMUS fitting software on full spectrum data of [Fe(phen) <sub>2</sub> (CN) <sub>2</sub> ] (2) to two 5.5 ps and 290 ps exponential kinetic components. (b) DADS from the global fit. (c) EADS from the global fit assuming sequential decay dynamics
<b>Figure 5.C.3.</b> (a) Chirp corrected global fit using OPTIMUS fitting software on full spectrum data of $[Fe(phen)_2(C_4H_{10}N_4)](PF_6)_2$ (3) to three 0.12, 0.66, and 4.7 ps exponential kinetic components. (b) DADS from the global fit. (c) EADS from the global fit assuming sequential decay dynamics
<b>Figure 5.D.1.</b> (a) Early time TA data (blue) on [Fe(phen) <sub>3</sub> ](BF <sub>4</sub> ) <sub>2</sub> (1) in methanol monitored at 610 nm following 520 nm excitation. An exponential fit (red) and a LPSVD fit (black) are superimposed on the data. (b) FFT of the residual of the exponential fit of the 610 nm TA data (blue) and LPSVD vibrational spectrum (red). (c) Early time TA data (blue) of compound (1) monitored in the bleach region at 520 nm with exponential (red) and LPSVD (black) fits. (d) Corresponding FFT (blue) and LPSVD vibrational spectra.
<b>Figure 5.D.2.</b> (a) Early time TA data (blue) on [Fe(phen) <sub>2</sub> (C <sub>4</sub> H <sub>10</sub> N <sub>4</sub> )](PF <sub>6</sub> ) <sub>2</sub> ( <b>3</b> ) in methanol monitored at 550 nm following 600 nm excitation. Exponential fit (red) and LPSVD fit (black) are superimposed on the dataset. (b) Corresponding FFT of the residual of the exponential fit (blue) and LPSVD vibrational spectrum (red). (c) Analogous data monitoring at 650 nm and (d) corresponding FFT (blue) and LPSVD (red) vibrational spectra.
<b>Figure 5.D.3.</b> (a) Early time TA data (blue) on [Fe(phen) <sub>2</sub> (C <sub>4</sub> H <sub>10</sub> N <sub>4</sub> )](PF <sub>6</sub> ) <sub>2</sub> ( <b>3</b> ) in acetonitrile monitored at 550 nm following 600 nm excitation. Exponential fit(red) and LPSVD fit (black) are superimposed on the dataset. (b) Corresponding FFT of the residual of the exponential fit (blue) and LPSVD vibrational spectrum (red). (c) Analogous TA data while monitoring at 650 nm and (d) corresponding FFT (blue) and LPSVD (red) vibrational spectra.
<b>Figure 6.1.</b> Structures of proposed condensed macrocyclic cage ligands

## KEY TO SYMBOLS AND ABBREVIATIONS

acac: Acetylacetonate

acac': Generic acetylacetonate ligand

A<sub>exp</sub>: Amplitude of exponential decay

A<sub>v</sub>: Amplitude of oscillatory component

△A: Change in absorption

bISC: Back-intersystem crossing

bpy: 2,2'-Bipyridine

Calc.: Calculated

CDCl<sub>3</sub>: Deuterated chloroform

 $c_{gs}$ : Ground state concentration

DADS: Decay associated difference spectrum

daxial: Axial metal ligand bond length

deq: Equatorial metal ligand bond length

DFT: Density functional theory

DMHD: 2,6-Dimethyl-3,5-heptanedione

DSSC: Dye sensitized solar cell

 $E_a$ : Activation energy

EADS: Evolution associated difference spectrum

 $E_n$ : Energy of n<sup>th</sup> vibrational level

en: Ethylenediamine

ESA: Excited state absorption.

Exp.: Experimental

f: Oscillator strength

FFT: Fast Fourier transform

GSB: Ground state bleach

HD: 3,5-Heptanedione

I: Moment of inertia

IC: Internal conversion

IR: Infrared

IRF: Instrument response function

ISC: Intersystem crossing

ISRS: Impulsively stimulated Raman scattering

IVR: Intramolecular vibrational redistribution

K: Duschinsky displacement vector

k: Rate constant

*k<sub>b</sub>*: Boltzmann constant

 $k_{bISC}$ : Back-intersystem crossing rate constant

 $k_{IC}$ : Internal conversion rate constant

 $k_p$ : Phosphorescence rate constant

 $k_{VC}$ : Vibrational cooling rate constant

 $k_{VR}$ : Vibrational relaxation rate constant

L: Cage ligand

LMCT: Ligand to metal charge transfer

LPSVD: Linear predictive singular value decomposition

 $L^r$ : Matrix that diagonalizes the mass weighted Cartesian Hessian of the reactant geometry

 $\vec{L}$ : Angular momentum

M: Diagonal mass matrix

 $m_i$ : Mass of ith atom,

MLCT: Metal to ligand charge transfer

[MLCT<sub>a</sub>]: Initial MLCT excited state concentration

[MLCT<sub>b</sub><sup>cool</sup>]: Vibrationally cool MLCT state concentration

[MLCT<sub>b</sub><sup>hot</sup>]: Vibrationally excited MLCT state concentration

 $R_{nl}(r)$ : Probability density function

 $\overrightarrow{R_{l}}$ : Cartesian coordinate of ith reactant atom

 $\overrightarrow{R_i^p}$ : Cartesian coordinate of ith product atom

 $\Delta R$ : Cartesian displacement vector

SE: Stimulated emission

SOC: Spin-orbit coupling

SVD: Singular value decomposition

T(t): Time dependent effective temperature

T: Rotation matrix

t: Time

 $T_{l,elec}$ : Electronic population relaxation

 $T_{I,vib}$ : Vibrational population relaxation

 $T_1$ : Population relaxation time constant

 $T_2^*$ : Pure dephasing

 $T_2$ : Homogeneous dephasing time

TA: Transient absorption

TMHD: 2,2,6,6-Tetramethyl-3,5-heptanedione

 $T_x$ : Initial effective temperature

VC: Vibrational cooling

VR: Vibrational relaxation

△: Fluctuation magnitude

 $\Delta v$ . Full width at half maximum of Raman peak.

- $\Delta \tau$ . Dephasing time
- $\Lambda$ : Effective fluctuation frequency
- $\varepsilon$ : Extinction coefficient
- $\phi$ : Oscillation phase
- $\eta_i$ : Fraction of excited state population i
- $\lambda$ : Reorganization energy
- $\lambda$ : Wavelength
- $\sigma_{IRF}$ : Standard deviation of gaussian IRF
- $\theta$ : Angle
- $\tau$ . Time constant
- ω: Angular frequency
- ψ: Wavefunction

## Chapter 1: Coherent Vibrational Dynamics of Inorganic Molecular Chromophores

## 1.1. Introduction

This dissertation discusses the ultrafast photoinduced excited state dynamics in several different first-row transition metal molecular systems ranging from six coordinate chromium(III) and cobalt(III) betadiketonate complexes to iron(II) polypyridyl and carbene compounds. Much of this dissertation places a particular emphasis on characterizing the coherent vibrational dynamics occurring in each chromophore for the goal of using information from coherences to not only glean important dynamical information for excited state characterization but also to suggest ways in which synthetic modifications can alter important vibrational-electronic couplings to tune photophysical properties. In this work, the ultrashort timescales characteristic of impulsive vibrational dynamics as well as many excited state transformations necessitates experimental techniques with similarly short time resolution. As such, much of the work herein will utilize ultrafast transient absorption (TA) spectroscopy, which uses pulses of light on the order of a millionth of a billionth of a second to both induce and monitor excited state processes. In what follows, we will briefly discuss the basics of transition metal photophysical properties, transient absorption spectroscopy, and finally coherences and their manifestations in TA signals.

## 1.2. Transition Metal Photophysical Properties

Transition metal chromophores have numerous types of electronic transitions available to them including d-d and various types of charge transfer transitions. An excellent discussion of these topics can be seen in Figgis and Hitchman's book<sup>1</sup> and will briefly be summarized here. To start, the intensity or allowedness of electronic transitions depends on the transition moment integral, Q (equation 1.1), in which

$$Q = \langle \psi_1 | \mu | \psi_2 \rangle \tag{1.1}$$

 $\psi_1$  and  $\psi_2$  are the wavefunctions for the initial and final states and  $\mu$  is the dipole moment operator. A wavefunction itself is built of a product of multiple component wavefunctions as shown in equation 1.2.

$$\psi_{tot} = \psi_{orbital} \cdot \psi_{vib} \cdot \psi_{spin} \cdot \psi_{rot} \cdot \psi_{trans}$$
 1.2

This leads to several factors which can affect the magnitude of Q. First, if there is a change in the spin moment between the final and initial wavefunctions (i.e.  $\Delta S \neq 0$ ), then Q = 0. This spin selection rule says that an electronic dipole induced transition cannot induce a change in spin state. These forbidden transitions can become somewhat allowed by spin-orbit coupling interactions that intermix an amount of different spin character to the final or initial states involved in the transition. Nevertheless, this spin-selection rule results in substantial 100-1000-fold reductions in intensities relative to spin-allowed transitions. Despite their low intensity these transitions are an important aspect of spectroscopy in transition metal complexes, and have even been utilized in the ruby laser.<sup>2</sup>

Another important selection rule in the spectroscopy of transition metal compounds arises from orbital symmetry. Because the transition moment integral, Q, is performed over symmetric boundaries, this implies that Q=0 if the product  $\psi_1 \times \mu \times \psi_2$  is an odd function. Thus, since the dipole moment operator,  $\mu$ , is antisymmetric (ungerade) with respect to the inversion center of a system and is therefore an odd function, it follows that  $\psi_1$  and  $\psi_2$  must have opposite parity for the overall  $\psi_1 \times \mu \times \psi_2$  product to be an even function (gerade) and, by extension, to have a nonzero transition moment integral. Thus, for an electronic transition between two d orbitals (which are even functions) the integrand of the transition moment integral is an odd function and Q=0. These parity- or Laporte-forbidden transitions are quite weak, yet nevertheless give many transition metal compounds their color. The parity-selection rule can be overcome when a molecule lacks an inversion center. For example, in compounds of  $T_d$  symmetry, several of the d and p orbitals have the same irreducible representation, which allows for mixing and a relaxation of the Laporte-selection rule. Alternatively, since the wavefunction is a product of many component wavefunctions, a d-d transition may couple with an antisymmetric vibration to become vibronically allowed.

The last important electronic transition common to transition metal compounds are charge transfer transitions. The first type of charge transfer involves the transfer of an electron from a molecular orbital of high ligand orbital character to an orbital of high metal character. This ligand to metal charge transfer

**Table 1.1.** Summary of the extinction coefficients,  $\varepsilon$ , and oscillator strengths, f, typically observed for various electronic transitions of transition metal complexes.

Transition Type	$\varepsilon$ (M <sup>-1</sup> cm <sup>-1</sup> )	f
d-d, spin forbidden	0.1-1	$10^{-7}$ - $10^{-6}$
d- $d$ , spin allowed	10-100	$10^{-5}$ - $10^{-4}$
Charge Transfer	1000-10,000	$10^{-3}$ - $10^{-2}$

(LMCT) is common in systems with high energy, filled ligand bonding or nonbonding orbitals and relatively low energy unfilled orbitals localized on the metal center. Alternatively, the reverse can occur where an electron in a largely metal based molecular orbital is transferred to a largely ligand centered orbital. These metal to ligand charge transfer (MLCT) occur in low valent metal complexes with high-lying, populated metal centered orbitals and low-lying empty ligand-based orbitals. Because both charge transfer type transitions involve the gerade d orbitals of the metal and the ungerade p orbitals of the ligands, they are fully allowed and hence much more intense than d-d transitions. Likewise, ligand centered transitions are often between states of opposite parity, resulting in highly intense electronic transitions. A summary of the typical extinction coefficients and oscillator strengths for transitions commonly seen in transition metal complexes can be seen in Table 1.1.\(^1

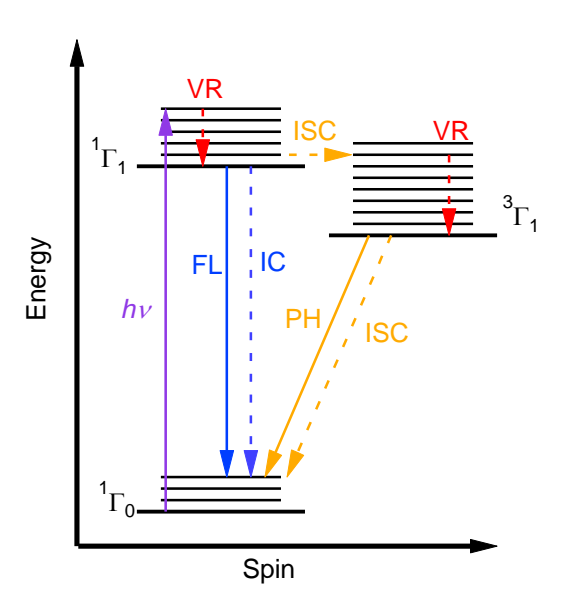


**Figure 1.1.** Jablonski diagram depicting various excited state processes including vibrational relaxation (VR), internal conversion (IC), intersystem crossing (ISC), fluorescence (FL), and phosphorescence (PH). Radiative transitions are shown as solid lines and nonradiative transitions are shown as dashed lines.

Following absorption of a photon, a molecule can undergo several types of photophysical processes to dissipate energy. A summary of these processes is shown in the Jablonski diagram in Figure 1.1. After the initial photoexcitation (shown in purple in Figure 1.1) a molecule is promoted from the ground electronic state to a higher energy excited state which is often of the same spin multiplicity as the ground state. In some cases, this also produces a vibrationally excited molecule which can dissipate this vibrational energy in two ways. The molecule can undergo vibrational cooling (VC) in which excess vibrational energy is dissipated towards the solvent bath, or intramolecular vibrational redistribution (IVR) could occur in which vibrational energy is spread from one vibrational mode to another. These are often referred to collectively as vibrational relaxation (VR) which is shown in red in Figure 1.1. Additionally, the excited molecule can convert to another state of the same spin multiplicity either radiatively in the case of fluorescence (FL) or nonradiatively via internal conversion (IC). During FL, excess energy is dissipated as electromagnetic radiation, whereas during IC excess energy is either converted to vibrational energy on the newly formed electronic state or dissipated as heat towards the solvent bath. Instead of converting to a new electronic state of similar spin, the molecule can also undergo a nonradiative transition to an excited state of different spin. This is referred to as intersystem crossing (ISC). Just like in the case of IC, ISC can dissipate thermal energy outwards towards the solvent bath or inwards to make a vibrationally excited state which can again undergo VR. Finally, the molecule can nonradiatively ISC to the ground state of different multiplicity or radiatively phosphoresce (PH). All these processes can be labelled collectively under the term photophysics. In addition to photophysical transformations, electromagnetic radiation can result in the formation of a new chemical species. This is referred to as photochemistry. The work performed in this dissertation will seek to avoid photochemical reactions to make analysis of the photophysical properties of each system easier to interpret.

## 1.3. Transient Absorption Spectroscopy

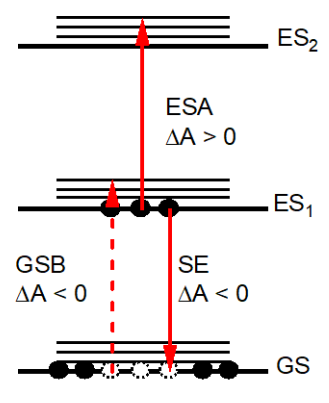
Due to the short timescales of many excited state processes, experiments need exceptionally short time resolution to track photoinduced dynamics in many systems. The work in this dissertation will employ pump-probe transient absorption (TA) spectroscopy. The basic premise of this experiment is to irradiate

the sample with an ultrashort laser pulse (pump) to create an excited state population in a small fraction of the molecules and subsequently, after a set time delay, interrogate the absorptive properties of the sample with a second weaker laser pulse (probe) by measuring its transmittance through the sample. By systematically varying the time delay between pump and probe pulses one can track the absorptive changes in the sample and in effect the excited state dynamics. Because the fraction of molecules that have been excited is generally quite small, the difference in absorbance between the sample that has been irradiated with the pump pulse and the sample that has not been pumped is measured. This can be described using equation 1.3 where  $I(\lambda,t)_{pumped}$  is the time dependent transmittance of the pumped sample and  $I(\lambda)_{unpumped}$  is

$$\Delta A(\lambda, t) = -\log\left(\frac{I(\lambda, t)_{pumped}}{I(\lambda)_{unpumped}}\right) = \sum_{i} \left[\varepsilon_{i}(\lambda) - \varepsilon_{GS}(\lambda)\right] \cdot b \cdot c_{GS} \cdot \eta_{i}(t)$$
1.3

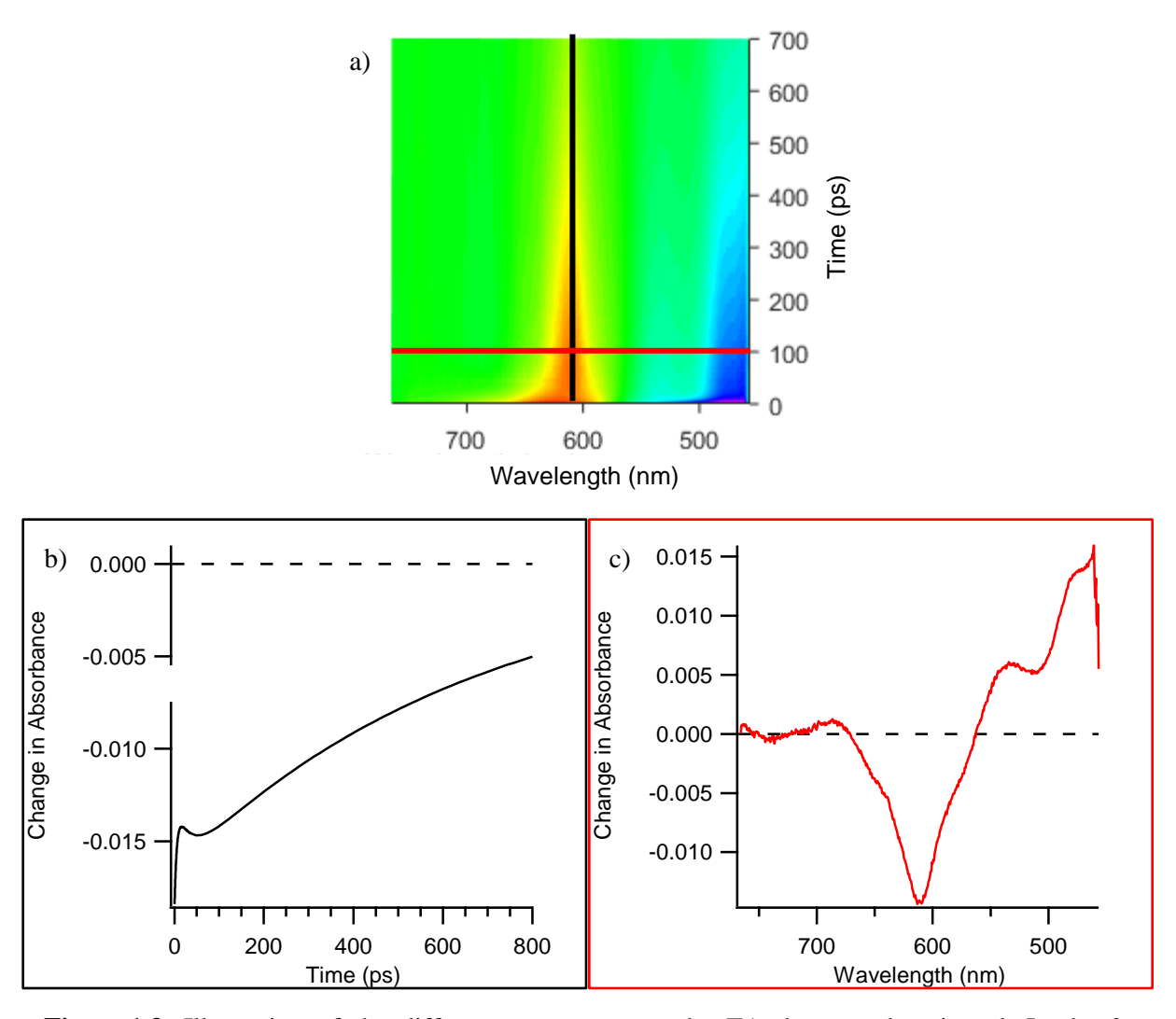
the transmittance before the pump pulse arrives. The magnitude of the signal is related to the difference between the extinction coefficients of the excited state,  $\varepsilon_i$ , and ground state,  $\varepsilon_{GS}$ , and also relates to the pathlength, b, the initial concentration of the chromophore,  $c_{GS}$ , and the time dependent fraction of the ith excited state population,  $\eta_i(t)$ .<sup>3,4</sup> It is clear from equation 1.3 that large amplitude transient signals arise when the extinction coefficients or cross-sections are very different between the ground and excited state.

Figure 1.2 shows an energy level diagram with possible signal contributions in a pump-probe transient absorption experiment. First, since the pump pulse reduces the number of absorbing molecules in



**Figure 1.2.** Energy level diagram showing possible signals in a pump-probe transient absorption experiment including ground state bleach (GSB), excited state absorption (ESA) and stimulated emission (SE).

the ground electronic state, then a probe pulse with frequencies overlapping the ground state absorption spectrum will experience a decrease in absorption. This is referred to as ground state bleach (GSB). Second, since a pump photon can create an excited state population, a probe photon can stimulate the molecule to emit a photon and return to the ground state. This stimulated emission (SE) results in a higher perceived transmittance and thus a more negative  $\Delta A$ . Finally, the probe pulse can induce an absorption from the populated excited state to another excited state. This excited state absorption (ESA) results in a decreased



**Figure 1.3.** Illustration of the different ways pump-probe TA data can be viewed. In the 2-dimensional data set shown in (a) the entire transient spectrum is collected at each time delay. A vertical slice of this data (black) contains the differential absorption at a single wavelength across a series of time delays. This is illustrated in the black boxed kinetics trace of (b). A horizontal slice shown in red represents the transient spectrum at a specific pump-probe delay time and is shown in the red boxed spectrum (c).

transmittance of the probe pulse and hence an increase in  $\Delta A$ . Each of these types of signal may or may not overlap spectrally. Thus, the total transient signal at a given wavelength may have contributions from multiple processes.

Transient absorption data can be viewed and collected in several ways as illustrated in Figure 1.3. In some cases a spectrally broad probe beam (often a white light continuum generated via self-phase modulation) is directed into a spectrometer following the sample to be dispersed across a multichannel detector so that the frequency resolved differential absorption spectrum can be measured across the entire probe spectrum at once. Collection of this data across multiple pump-probe delay times results in a dataset like the one shown in Figure 1.3a. A horizontal slice of this dataset shows the transient difference spectrum at a single pump-probe delay time as shown in the red boxed spectrum of Figure 1.3c. A vertical slice of this 2-dimensional dataset shows the change in absorption at a single wavelength as a function of time as shown in the black boxed dataset in Figure 1.3b. This data style may also be collected using a monochromator to select out a single slice of the entire probe spectrum to measure or by using a spectrally narrower probe beam.

## 1.4. Coherences and Impulsive Vibrational Spectroscopy

We will next discuss the concept of coherence and impulsive vibrational spectroscopy. Before diving right in, however, we can first utilize an analogous concept: the idea of resonance from organic chemistry.<sup>5</sup> Benzene for instance has two main resonance structures denoted by  $\psi_1$  and  $\psi_2$  in Figure 1.4.

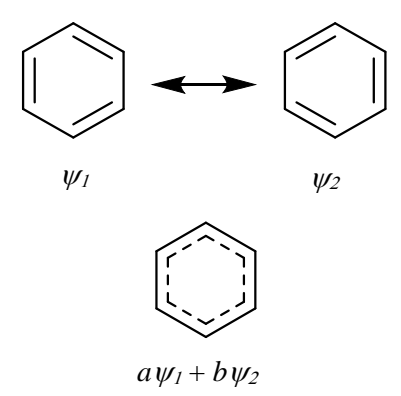


**Figure 1.4.** Resonance as an analogy to coherence. The ground state wavefunction of benzene is a linear combination of multiple component wavefunctions.

Neither of these two Kekulé structures correspond to the true wavefunction of benzene. Furthermore, the molecule is not flickering back and forth between them. The true wavefunction is a superposition or a linear combination of each Kekulé wavefunction:  $a\psi_1 + b\psi_2$ . Wavefunctions that are comprised of a linear combination of multiple component wavefunctions are commonly observed in transient absorption experiments. Ultrashort laser pulses with bandwidths that are broad enough to span multiple vibrational levels on an electronic excited state can excite several vibrational levels simultaneously. The resulting wavefunction is a linear combination of each of the constituent wavefunctions as shown in equation 1.4 where  $\psi(R,t)$  is the net

$$\psi(R,t) = \sum_{n} c_n \psi_n(R) \exp\left(\frac{-iE_n t}{\hbar}\right)$$

wavefunction,  $c_n$  is the population coefficient,  $\psi_n(R)$  is the wavefunction in of the nth vibrational level, and  $E_n$  is the energy of the nth vibrational level.<sup>6</sup> A pictorial representation of this can be seen in Figure 1.5, in which the net wavefunction, or wavepacket (blue), is the sum of each of the first five vibrational wavefunctions resulting in a much more localized amplitude in position space due to constructive and destructive interferences. The oscillatory nature of each wavefunction, originating from the exponential term in equation 1.4, shifts the interference pattern causing the wavepacket to migrate back and forth across the potential surface at the frequency of the activated vibration.

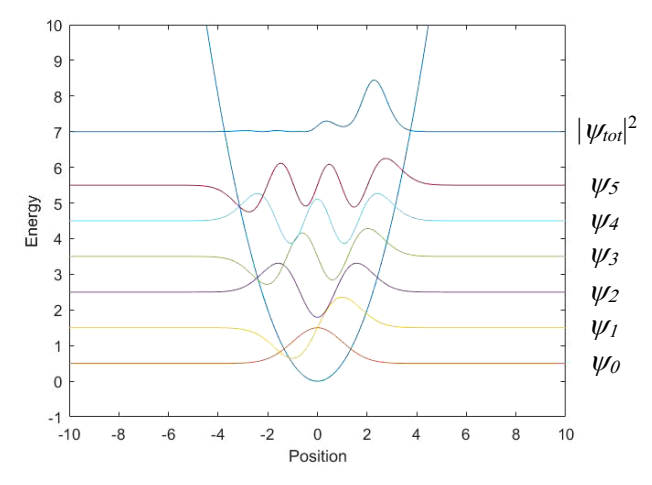


**Figure 1.5.** Generation of a coherent superposition state, or wavepacket, as a linear combination of oscillating wavefunctions.

Vibrational wavepackets, or coherences, can also be generated on the ground electronic state. To explain how, it is helpful to view the pump-probe TA experiment in terms of a three-field interaction with the sample. Excited state coherences are generated when the first two field interactions of the ultrashort pump pulse create an excited state population wavepacket which can oscillate back and forth across the excited state potential energy surface. Ground state vibrational coherences are generated when the first field interaction of the pump pulse generates an excited state polarization wavepacket and then, after some time delay, the second field interaction projects the wavepacket onto the ground state, displaced from its initial position.<sup>7</sup> This process is known as impulsively stimulated Raman scattering (ISRS).<sup>8</sup> The oscillation amplitude of these ground state wavepackets strongly depends on the ability of the excited state polarization wavepacket to propagate long enough to become significantly displaced from the hole on the ground state. When the pump pulse is too short this condition is not met and ground state vibrational features are not very significant.<sup>7</sup>

The curvature of a potential surface has an important role in the propagation of a wavepacket. To illustrate this a figure from the book *Coherent Vibrational Dynamics*<sup>7</sup> was reproduced by simulating a

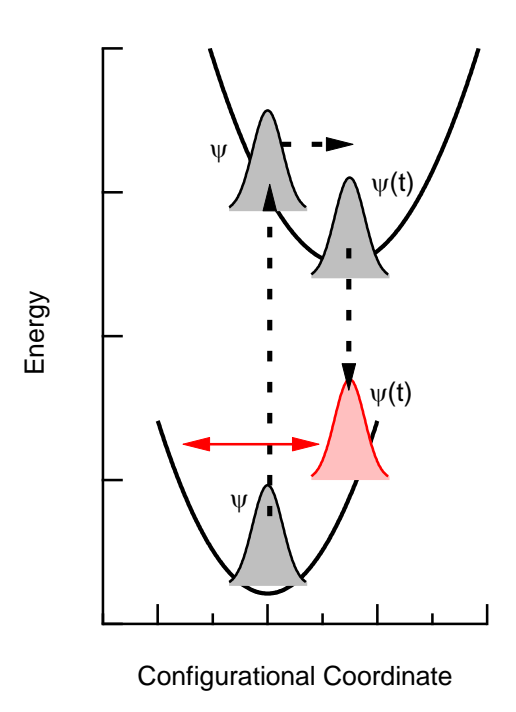


**Figure 1.6.** Potential energy surface diagram depicting the process of forming a wavepacket on the ground electronic state.

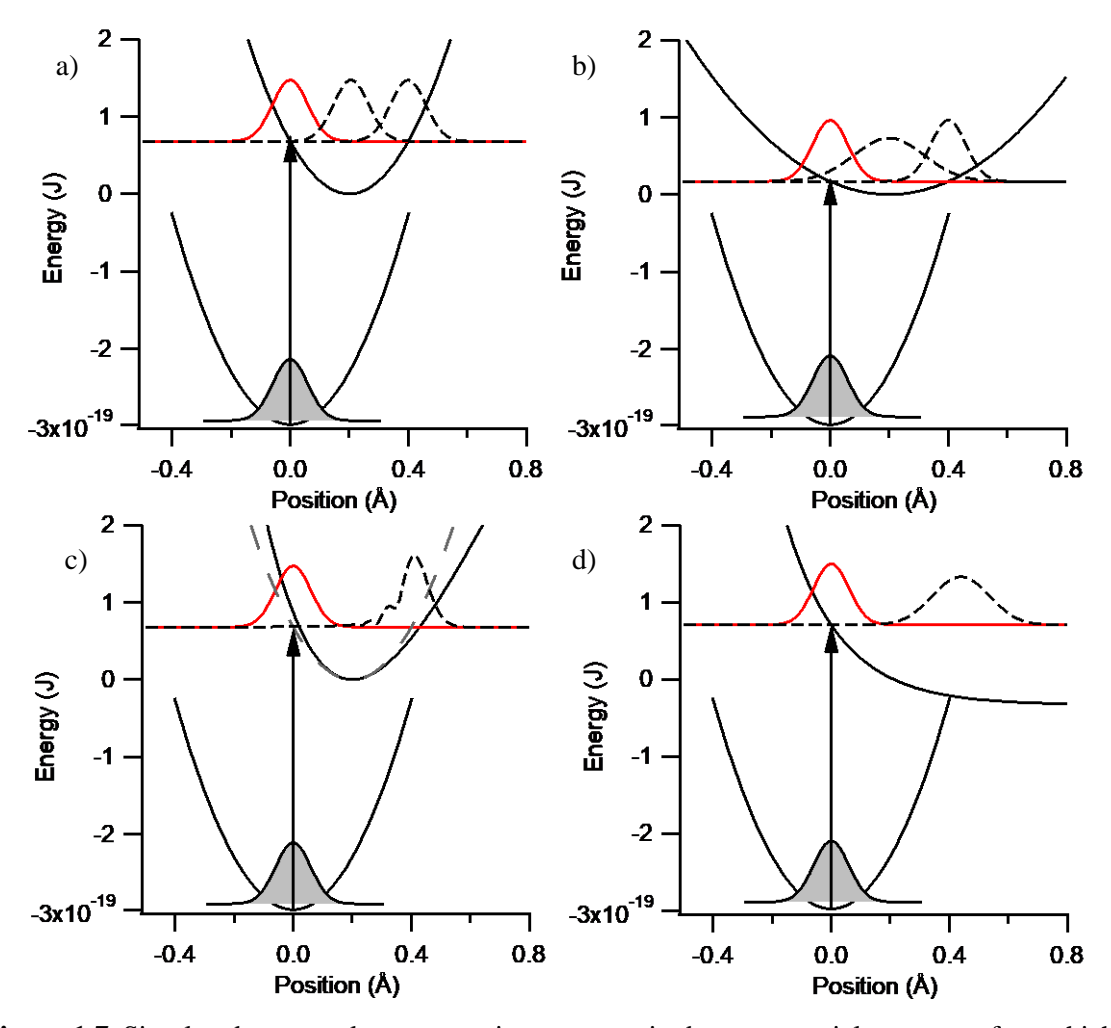


**Figure 1.7.** Simulated wavepacket propagation on an excited state potential energy surface which (a) has the same force constant as the ground state, (b) has a different force constant than the ground state, (c) is anharmonic, and (d) is dissociative. The initial projected wavepacket is shown in red. Wavepackets that have propagated on the excited state surface are shown in dashed lines.

wavepacket on several types of potential energy surfaces (Figure 1.7) using the split operator method<sup>9</sup> in a homebuilt MATLAB program. When the excited and ground state potential surfaces have the same curvature the wavepacket maintains its shape as it slides back and forth across the excited state surface (Figure 1.7a). In contrast, when the curvature is different between the final and initial states, the wavepacket expands or contracts according the forces experienced on the new potential surface (Figure 1.7b). For example, when the excited state has a smaller force constant, the restoring forces near the now flatter equilibrium geometry are insufficient to hold the wavepacket together so it spreads out. Then, at the turning point, the combination of positive momentum and a negative restoring force recompress the wavepacket

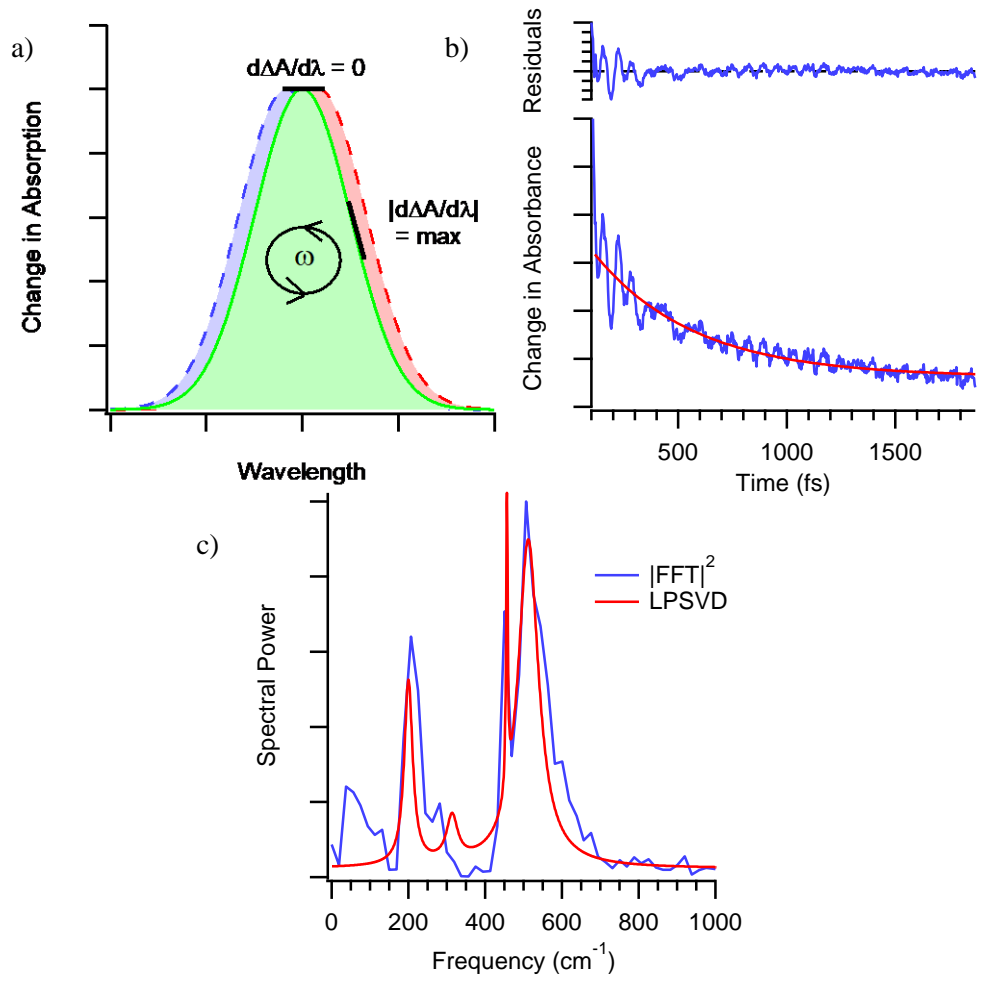


**Figure 1.8.** (a) Effect of coherent vibrational motion on the entire transient absorption spectrum. Band oscillates according to the frequencies of the activated vibrations. (b) Manifestation of coherent vibrational motion on single wavelength TA measurements. Oscillatory features are superimposed upon the population dynamics. (c) Fourier transformation (blue) of oscillatory components of TA data results in a vibrational spectrum of the molecule. LPSVD fit of TA data provides not only frequencies of coherent vibrational modes but also their dephasing times.

back to its original shape. In the anharmonic potential (Figure 1.7c), the different vibrational spacing at higher and lower energy portions of the potential surface cause nonuniform oscillation frequencies which "tilt" the wavepacket and cause it to breakup after a few oscillations.<sup>7</sup> Finally, a dissociative potential surface (Figure 1.7d) results in the migration of the wavepacket away from the Franck Condon position while spreading out.

The propagation of wavepackets has important photophysical ramifications, and can even, according to the time-dependent theory of spectroscopy, determine the absorption and emission spectrum

of a chromophore. 10 In a TA experiment, the migration of a wavepacket along a potential energy surface causes periodic modifications to the Franck-Condon factors for absorption or emission. This manifests as oscillatory components in the TA data that occur at the same frequency as the activated vibrations. This can be seen as a shifting of the transient spectrum to higher and lower wavelengths<sup>11</sup> as shown in Figure 1.8a. The amplitudes of these oscillations are dependent on the curvature of the transient absorption profile. Probing at the apex of the absorption feature where the derivative,  $d\Delta A/d\lambda$ , is zero tends to wash out oscillations, whereas probing at inflection points where the slope is largest tends to show the strongest oscillations. 12,13 Ground state vibrational coherences of the solvent bath can also lead to oscillatory features in TA data even when the probe is not resonant with an electronic transition. The synchronized vibrational motion of the solvent molecules induced by the pump pulse periodically modifies the refractive index and, in turn, the frequency content of the probe spectrum. 11 The resultant shifting of the probe spectrum to higher and lower frequencies induces an oscillating transmittance of the probe pulse at each wavelength across its spectrum. When performing single wavelength measurements as shown in Figure 1.8b, coherences of both the solvent and solute manifest as oscillations that are superimposed upon the population dynamics of the molecule. Fourier transformation of the isolated oscillatory components results in a vibrational spectrum of the system consisting only of the coherently activated vibrational modes. Additionally, using linear predictive singular value decomposition (LPSVD)<sup>14</sup> to fit the TA data to a summation of exponentially damped cosines as seen in equation 1.5, allows one to not only extract frequency information similar to a Fourier transform

$$S(t) = \sum_{i=1}^{n} A_i \exp\left(\frac{-t}{\tau_i}\right) \cos\left(2\pi \nu_i t + \phi_i\right)$$
1.5

analysis, but also the phase of the oscillation,  $\phi_i$ , its amplitude,  $A_i$ , and its dephasing time,  $\tau_i$ . The quantitative characterization of coherent nuclear motion afforded by LPSVD analysis then provides the experimenter with an intricate view of the coherent excited state dynamics just after absorption of a photon.

#### 1.5. Contents of This Dissertation

The work presented in the remainder of this dissertation discusses the ultrafast excited state dynamics in several different first-row transition metal chromophores, with an emphasis on characterizing and extracting dynamical information from excited state vibrational coherences. We begin in chapter 2 with a series of chromium(III) tris-betadiketonate compounds. A review of the relevant literature surrounding this class of chromophores is presented and an updated excited state deactivation mechanism is proposed to describe the dynamics in each molecule of the series. The coherent nuclear motion is characterized and used to help build the kinetic model.

In chapter 3, we will use transient absorption spectroscopy to characterize the excited state dynamics in a small, related series of cobalt(III) tris-betadiketonate compounds. The coherent nuclear motion will again be characterized to aid in describing the excited state dynamics of the system. Furthermore, the types of motion and their dephasing times will be compared with the structurally similar chromium systems.

The subsequent two chapters address two separate methods for extending the MLCT lifetime of iron(II) polypyridyl type complexes. First, in chapter 4 we seek to identify and disrupt the specific normal modes that drive the ultrafast MLCT deactivation in this class of compounds. By gleaning information from excited state vibrational coherences, a synthetic modification to hinder a specific subset of the 3N-6 normal modes of a control molecule is proposed which results in a dramatically altered MLCT lifetime. In chapter 5, we show that the photophysical properties of iron(II) chromophores can be systematically and modularly tuned by swapping a single bidentate polypyridyl ligand with stronger field cyanide or acyclic dicarbene ligands. This approach results in over an order of magnitude change in both the ground state recovery and MLCT lifetimes.

Finally, in chapter 6 of this dissertation we discuss possible future efforts in each of the areas investigated.

REFERENCES

#### REFERENCES

- (1) Figgis, B. N.; Hitchman, M. A. *Ligand Field Theory and Its Applications*; Wiley-VCH: New York, 2000.
- (2) Maiman, T. H. Stimulated Optical Radiation in Ruby. *Nature* **1960**, *187*, 493–494.
- (3) Berera, R.; van Grondelle, R.; Kennis, J. T. M. Ultrafast Transient Absorption Spectroscopy: Principles and Application to Photosynthetic Systems. *Photosynth. Res.* **2009**, *101*, 105–118.
- (4) Balzani, V.; Juris, A.; Ceroni, P. *Photochemistry and Photophysics: Concepts, Research, Applications*; Wiley-VCH: Weinheim, 2014.
- (5) Scholes, G. D.; Fleming, G. R.; Chen, L. X.; Aspuru-Guzik, A.; Buchleitner, A.; Coker, D. F.; Engel, G. S.; van Grondelle, R.; Ishizaki, A.; Jonas, D. M.; *et al.* Using Coherence to Enhance Function in Chemical and Biophysical Systems. *Nature* **2017**, *543*, 647–656.
- (6) Zewail, A. H. Femtochemistry: Atomic-Scale Dynamics of the Chemical Bond. *J. Phys. Chem. A* **2000**, *104*, 5660–5694.
- (7) De Silvestri, S.; Cerullo, G.; Lanzani, G. *Coherent Vibrational Dynamics*; CRC Press: Boca Raton, FL, 2008.
- (8) Ruhman, S.; Joly, A. G.; Nelson, K. A. Time Resolved Observations of Coherent Molecular Vibrational Motion and the General Occurrence of Impulsive Stimulated Scattering. *J. Chem. Phys.* **1987**, *86*, 6563–6565.
- (9) Al., F. E. Solution of the Schrodinger Equation by a Spectral Method. *J. Comput. Phys.* **1982**, *47*, 412–433.
- (10) Heller, E. J. The Semiclassical Way to Molecular Spectroscopy. *Acc. Chem. Res.* **1981**, *14*, 368–375.
- (11) Liebel, M.; Schnedermann, C.; Wende, T.; Kukura, P. Principles and Applications of Broadband Impulsive Vibrational Spectroscopy. *J. Chem. Phys. A* **2015**, *119*, 9506–9517.
- (12) Yang, T.-S.; Chang, M.-S.; Chang, R.; Hayashi, M.; Lin, S. H.; Vöhringer, P.; Dietz, W.; Scherer, N. F. Femtosecond Pump-Probe Study of Molecular Vibronic Structures and Dynamics of a Cyanine Dye in Solution. *J. Chem. Phys.* 1999, 110, 12070.
- (13) Pollard, W. T.; Decheimer, S. L.; Wang, Q.; Peteanu, L. A.; Shank, C. V.; Mathies, R. A. Theory of Dynamic Absorption Spectroscopy of Nonstationary States. 4. Application to 12-fs Impulsive Raman Spectroscopy of Bacteriorhodopsin. *J. Phys. Chem.* **1992**, *96*, 6147–6158.
- (14) Rosca, F.; Kumar, A. T. N.; Ye, X.; Sjodin, T.; Demidov, A. A.; Champion, P. M. Investigations of Coherent Vibrational Oscillations in Myoglobin. *J. Phys. Chem. A* **2000**, *104*, 4280–4290.

# Chapter 2: Electronic and Vibrational Excited State Dynamics in a Series of Cr(acac')<sub>3</sub> Derivatives 2.1. Introduction to Chromium(III)

Transition metal chromophores can often show stability across a wide range of oxidation states and the presence of many different types of excited states only adds to their unique utility towards photochemical and photophysical applications. Charge transfer excited states for example, which involve oxidation of the metal center and reduction of one of the ligands for metal to ligand charge transfer states or vice versa for ligand to metal charge transfer excited states, are of broad interest for use in electron transfer based applications such as dye sensitized solar cells and photoredox catalysis. Ligand field excited states, which essentially derive from redistribution of electrons amongst the valance *d*-orbitals of the metal center, are capable of redox chemistry<sup>1</sup> and are often also conducive to substitution and isomerization reactions due to the significant antibonding nature of some *d* orbitals.<sup>2</sup> Furthermore, in the case of chromium, these ligand field excited states are involved in the original ruby laser.<sup>3</sup>

To date, chromium chromophores are the most well studied out of any transition metal. Even as far back as 1857, the phosphorescent lifetimes of chromium compounds were measured by Becquerel and his phosphoroscope. Earlier yet, chromium's chromophoric reputation goes back to its discovery in 1798 by French chemist Nicholas Louis Vauquelin, who noticed the wide range of colors that the element could produce and hence named the newly discovered element chromium deriving from the Greek root *chroma* meaning color. More recent investigations, however, have likely been more inspired from chromium's use in the first laser, the ruby laser, by Theodore Maiman in 1960. Additionally, from a practical perspective,  $d^3$  chromium compounds have a number of convenient properties. The  $d^3$  electron configuration is relatively kinetically inert with respect to ligand substitution reactions, hus allowing a wealth of homoleptic octahedral chromium(III) compounds in the literature. These compounds are also often luminescent, providing a nice handle with which to investigate photophysical properties. Relative to other d-electron configurations, the electronic structure of chromium(III) compounds are quite simple as well, with a limited number of excited states to worry about while performing photophysical investigations.

In this work, the photophysical properties of Cr(acac)<sub>3</sub> and its electronically and sterically perturbed analogues will be investigated with regard to how nuclear motion maps onto the excited state decay mechanism as a function of electronic and steric perturbation. The Cr(acac)<sub>3</sub> molecular platform in particular has several properties that make it convenient to study, including the low quantum yield for photosubstitution reactions and the availability of high oscillator LMCT transitions from the excited electronic state that improve the signal amplitude for transient absorption experiments.<sup>7</sup> The electronic structure is simple as suggested earlier, with only a few electronic states involved in the photodynamics upon visible light excitation. While  $Cr(acac)_3$  is formally of  $D_3$  symmetry, it is often helpful to express its electronic states using O symmetry labels. The pertinent electronic states of Cr(acac)<sub>3</sub>, expressed using O symmetry labels and depicted using the 1 electron picture are presented in Figure 2.1. The ground electronic state  $({}^{4}A_{2})$  has a  $(t_{2g})^{3}$  electron configuration and consists of an electron of parallel spin occupying each of the three valence  $t_{2g}$  orbitals of chromium. The lowest energy excited states of Cr(acac)<sub>3</sub> are the <sup>2</sup>E and <sup>2</sup>T<sub>1</sub> states which both have the  $(t_{2g})^3$  electron configuration. The <sup>2</sup>E excited state involves an intraconfigurational spin-flip transition of one of  $t_{2g}$  electrons relative to the ground state, while the  ${}^{2}T_{1}$  state consists of one singly occupied  $t_{2g}$  orbital and one doubly occupied  $t_{2g}$  orbital on the metal center. Since these electronic states are close in energy and behave similarly to modifications in the ligand field strength, they are often referred to collectively as the <sup>2</sup>E state. This dissertation will similarly henceforth refer to both states collectively as the <sup>2</sup>E state. Because the <sup>2</sup>E state is isoconfigurational with the ground state, its energy is relatively insensitive to changes in the overall ligand field strength of the molecule. Due to the spin-flip nature of this transition, however, its energy is sensitive to the electron density on the metal center and the interelectronic repulsion, and thus can be tuned through nephelauxetic effects. Additionally, due to the intraconfigurational nature of the  ${}^4A_2 \rightarrow {}^2E$  transition, the geometries of these states are typically quite similar resulting in nested potential energy surfaces and narrow absorption and emission profiles. The <sup>4</sup>T<sub>2</sub> state has a  $(t_{2g})^2(e_g)^1$  electron configuration and because it involves the promotion of a  $t_{2g}$  electron to an  $e_g^*$ antibonding orbital, its energy relative to the ground electronic state is highly dependent on the energy gap between these orbital sets, i.e. the ligand-field strength of the molecule. Furthermore, since the  $e_g^*$  orbital

has substantial metal-ligand antibonding character, this results in significantly distorted geometries relative to the ground electronic state. Rather than a symmetric expansion across all Cr-O bonds, however, the spatial degeneracy of the  ${}^4T_2$  state dictates that a symmetry breaking distortion will occur to stabilize the complex according to the Jahn-Teller theorem. Quantum chemical calculations performed by Ando *et al.* have shown that for Cr(acac)<sub>3</sub> this results in an axial compression and equatorial expansion of the Cr-O bonds.<sup>8</sup>

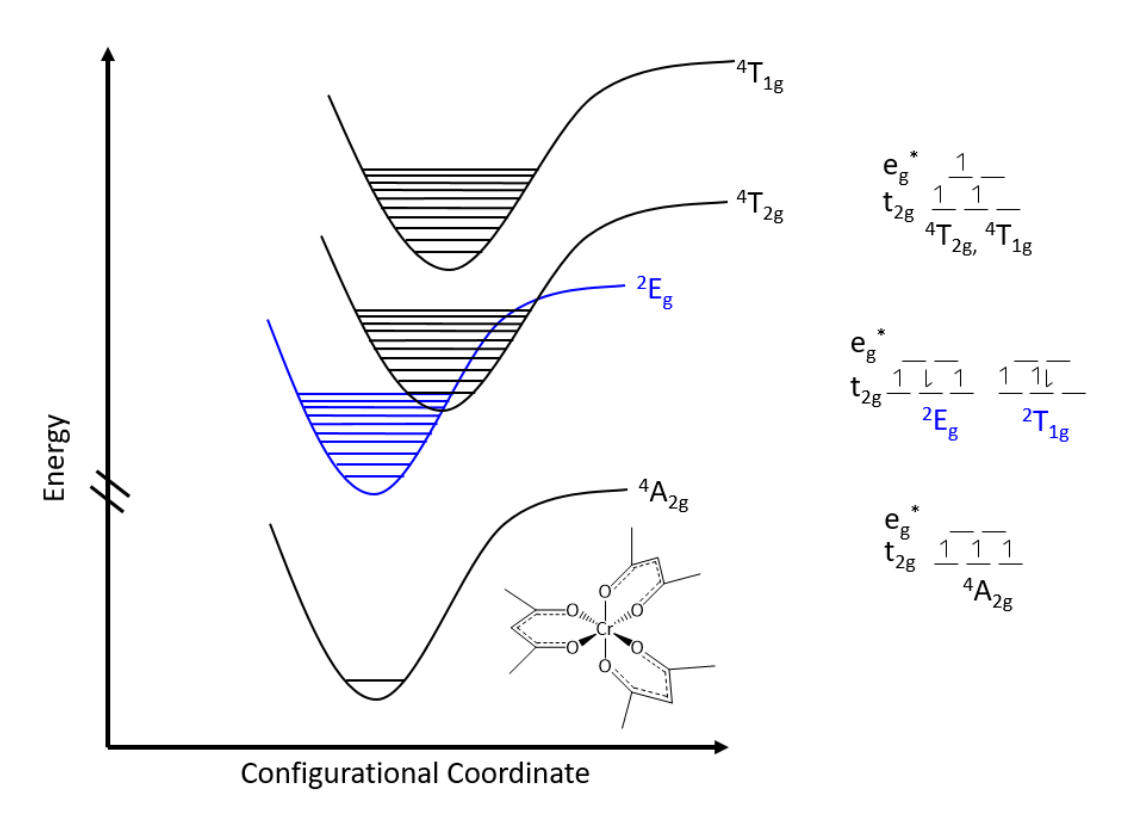


**Figure 2.1.** Qualitative potential energy diagram representing the pertinent electronic states of  $Cr(acac)_3$ . The  ${}^2T_{1g}$  and  ${}^2E$  potential energy surfaces have been merged into a single " ${}^2E$ " state for simplicity. The electron configurations in the 1-electron picture are represented for each state at right.

In reality, the electronic states depicted in Figure 2.1 cannot always be expressed perfectly in the one electron picture. To provide a more complete description of the wavefunctions for the pertinent electronic states of the  $d^3$  Cr(acac)<sub>3</sub>,the LIGFIELD program<sup>9</sup> was used with the help of Jon Yarranton to calculate the electron density distributions for each of the electronic states listed in Figure 2.1. The resulting electron density distributions are illustrated in Figure 2.2. Since the  $^2$ E and  $^2$ T<sub>1</sub> states result from intraconfigurational

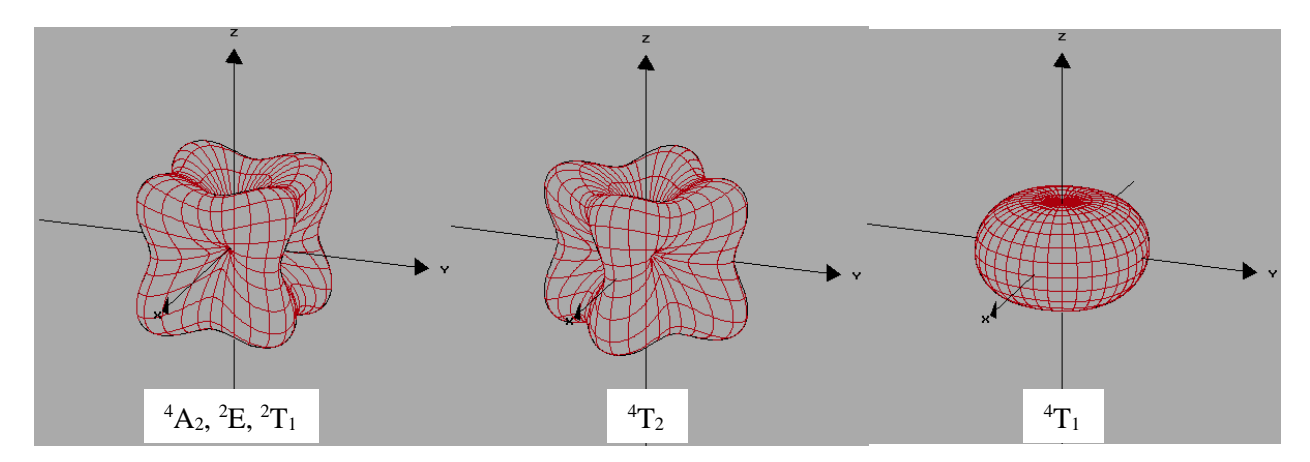


**Figure 2.2.** Electron density distributions for the pertinent electronic ground and excited states of d<sup>3</sup> compounds in an O<sub>h</sub> ligand field. Distributions were calculated using the LIGFIELD program with the help of Jon Yarranton.

transitions from the  ${}^4A_2$  ground state, each of these wavefunctions appear essentially identical. The  ${}^4T_2$  and  ${}^4T_1$  states, however, result from interconfigurational transitions from the  ${}^4A_2$  ground state and hence look quite different. The  ${}^4T_2$  state results from the promotion of a  $t_{2g}$  electron to an  $e_g*$  orbital. More specifically, this arises from one of three one-electron transitions  $(d_{xy} \rightarrow d_{x^2-y^2}, d_{xz} \rightarrow d_{z^2-x^2}, \text{ or } d_{yz} \rightarrow d_{z^2-y^2})$  which effectively cause a  $45^\circ$  rotation of the electron density about one the cartesian axes. The  ${}^4T_1$  state is more complex and arises from partial population of both of the  $e_g*$  set of orbitals. With partial population in each of the d-orbitals, the  ${}^4T_1$  electron density distribution is much more spherically symmetric relative to each of the electronic states discussed previously.

#### 2.2. Summary of Previous Results

The Cr(acac)<sub>3</sub> molecule has had a long history both within and outside of the McCusker group. We begin our summary of the photophysics of Cr(acac)<sub>3</sub> with the work of Juban *et al.* which represents the first photophysical investigation to study this molecule on ultrafast timescales.<sup>7</sup> Juban *et al.* used ultrafast and low temperature nanosecond visible pump visible probe spectroscopy as well as low temperature emission measurements to characterize the dynamics in this system. The narrow emission feature presented within this work as well as the congruence between the low temperature ns TA spectrum with the TA spectrum collected at 5 ps, unequivocally showed the <sup>2</sup>E state has formed by 5 ps and is the lowest energy electronic state from which the ~700 ps room temperature ground state recovery occurs. The apparent narrowing of

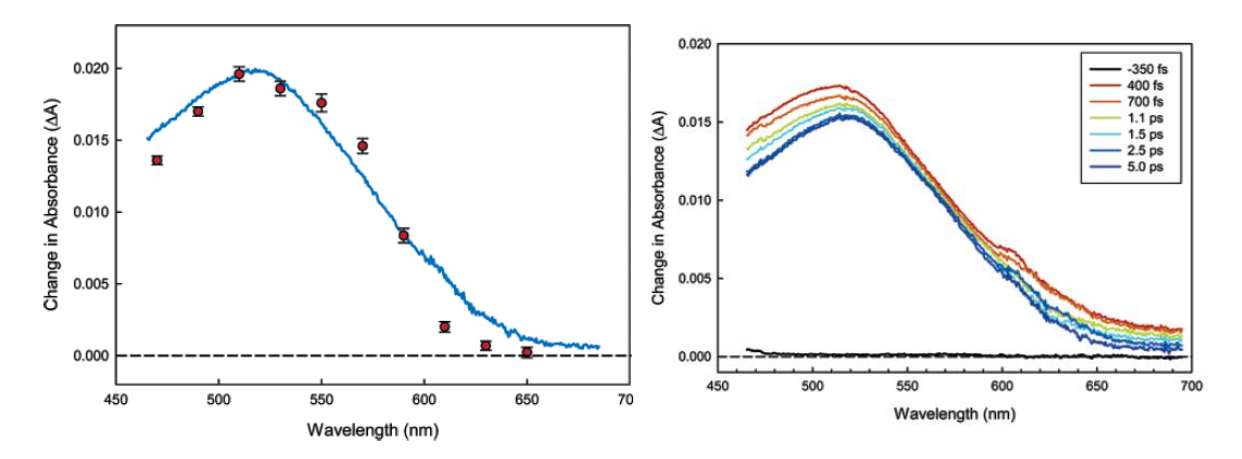


**Figure 2.3.** (left) Transient absorption spectrum of  $Cr(acac)_3$  in acetonitrile solution at  $\Delta t = 5$  ps (solid line) along with normalized absorption amplitudes obtained from single-wavelength nanosecond transient absorption data (red markers) collected in a 9:2 propionitrile/butyronitrile glass at 90 K. Close agreement between these two datasets suggests that  $Cr(acac)_3$  is in the fully thermalized lowest energy excited state, the  ${}^2E$  state, by  $\Delta t = 5$  ps. (right) Transient absorption spectrum of  $Cr(acac)_3$  over the course of the first 5 ps following 625 nm excitation. Reprinted with permission from reference 7. © (2005) American Chemical Society.

the TA spectrum (Figure 2.3) with a time constant of 1.1 ps was assigned to vibrational cooling on the  ${}^{2}\text{E}$  state and a lower limit for the rate of  ${}^{4}\text{T}_{2} \rightarrow {}^{2}\text{E}$  ISC was assigned as  $k > 1 \times 10^{13} \text{ s}^{-1}$  ( $\tau < 100 \text{ fs}$ ) based on their instrument response function. Interestingly, the time constant for this fast, 1.1 ps, process was found to be invariant with respect to excitation energy, however the magnitude for the decay was found to increase as excitation energy increased. At the time, this was rationalized based on the wider range of absorptions available from a higher lying vibrational level than a lower lying vibrational level.

A follow up study performed by Joel Schrauben and Kevin Dillman on the Beck group laser system at Michigan State University attempted to leverage the shorter laser pulses of that system to observe the  ${}^4T_2 \rightarrow {}^2E$  ISC event in  $Cr(acac)_3$ . He instead observed a rapidly damped 164 cm<sup>-1</sup> wavepacket on the excited electronic state (Figure 2.4a). Since coherent oscillations were observed well after the ISC event occurred, these wave packets were said to have been generated on the initially populated  ${}^4T_2$  surface and survived the ISC to the  ${}^2E$  state. Furthermore, it was hypothesized that the rapid dephasing time was an indicator that the observed vibrational mode was intricately involved in the ISC dynamics. Given that the electronic state on which the wavepacket was initially formed exhibited a significant expansion of the Cr-O bond distance, it was proposed that the observed mode was similar to the 184 cm<sup>-1</sup> symmetric breathing mode of the ground

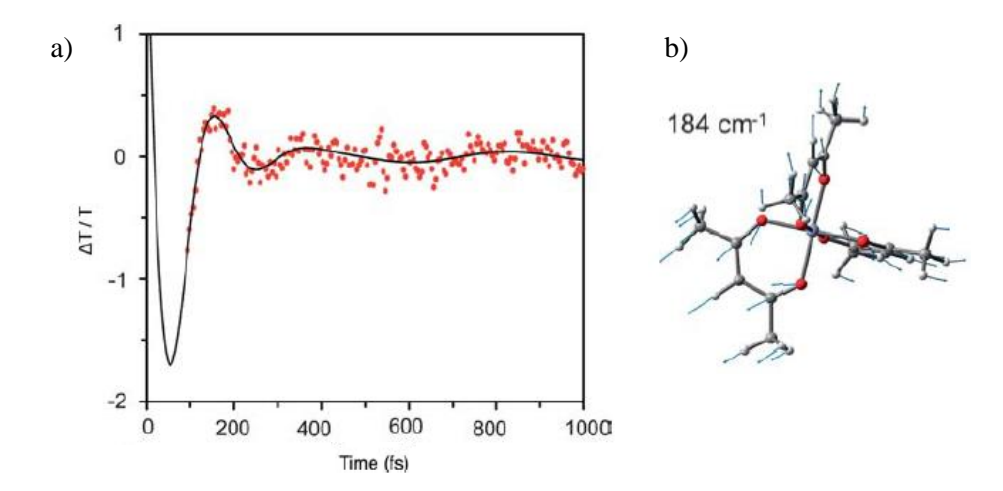


**Figure 2.4.** (a) Single-wavelength kinetic trace of  $Cr(acac)_3$  monitored at  $592 \pm 2$  nm following 600 nm excitation in acetonitrile. An exponential increase in excited state absorbance ( $\tau = 320$  fs) was subtracted from the data to better illustrate the oscillatory component of the data. The solid line corresponds to a fit to two exponentially damped oscillatory components with frequencies and damping times of  $164 \pm 20$  cm<sup>-1</sup> ( $\tau_{damp} = 70$  fs) and  $75 \pm 25$  cm<sup>-1</sup> ( $\tau_{damp} = 1.6$  ps). (b) Density functional theory calculated vibrational mode on the ground electronic state. The excited state wavepacket was proposed to exhibit a similar motion to this 184 cm<sup>-1</sup> calculated symmetric breathing mode. Figure reproduced from reference 10 with permission of the Royal Society of Chemistry.

state as calculated from density functional theory calculations (Figure 2.4b). Upon inspection of motions inherent to this 184 cm<sup>-1</sup> calculated mode and several other low frequency modes, it was observed that many of these normal modes involved significant distortion of the Cr-O bonds coupled with large amplitude motions of the periphery methyl groups. It was subsequently hypothesized that disruption of this mode via synthetic modifications to make the peripheral groups more sterically encumbered would result in changes to the photophysics of the compound. To test this hypothesis, the methyl groups were replaced with t-butyl groups. Instead of a slight narrowing of the spectrum as observed for  $Cr(acac)_3$ , the TA spectrum of the  $Cr(TMHD)_3$  compound (Figure 2.5) exhibited a decay in the bluer portion of the excited state absorption region and a concomitant rise in the redder portion of the ESA region with an average time constant of 1.8  $\pm$  0.4 ps and representing a significant change to the overall spectral profile. Based on the principle that vibrational relaxation should not result in a significant overall change to the visible transient difference spectrum,  $^{11}$  these results were interpreted to depict a change in electronic state implying a 1.8 ps  $^4T_2 \rightarrow ^2E$  ISC. This represents a significant reduction to the ISC rate relative to the parent  $Cr(acac)_3$  molecule and

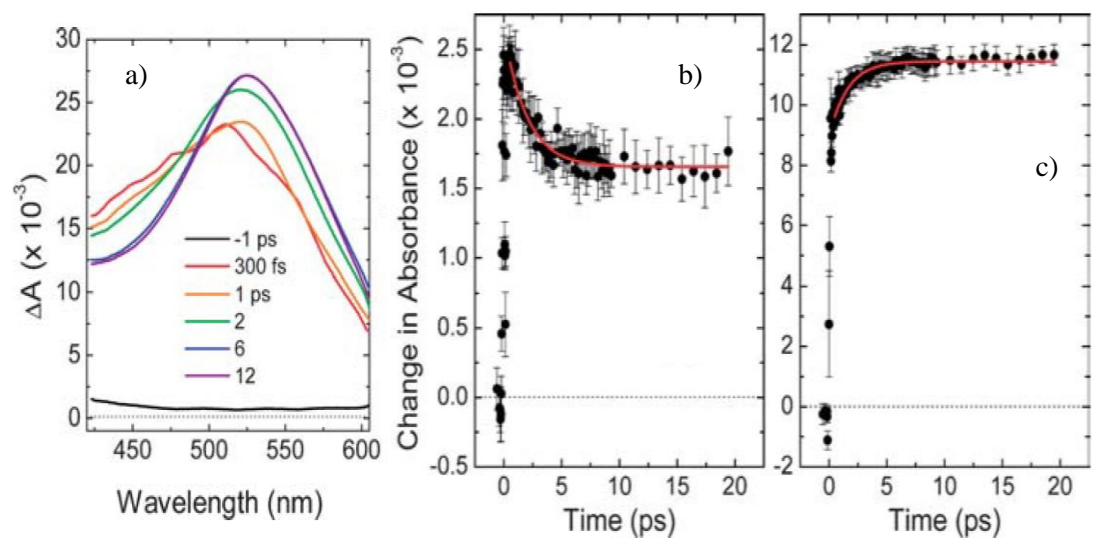


**Figure 2.5.** (a) Transient absorption spectra of  $Cr(TMHD)_3$  in dicloromethane following 633 nm excitation. (b) Single-wavelength kinetic trace collected at 450 nm and (c) 550 nm following 610 nm excitation. Solid lines represent single exponential fits (with  $\tau_{obs} = 2.0 \pm 0.2$  ps and  $1.6 \pm 0.2$  ps for (b) and (c) respectively). Figure reproduced from reference 10 with permission of the Royal Society of Chemistry.

seems to support the hypothesis that the rapid dephasing time of the 164 cm<sup>-1</sup> mode is indicative that the nuclear motion occurring during this vibration is somehow involved in and perturbed by the intersystem crossing process and that synthetic modifications inspired by the identification of these rapidly dephased modes can lead to altered photophysics. These results are seminal to both the work presented in the dissertation of Dr. Eileen Foszcz<sup>12</sup> which will be summarized shortly and the bulk of the work presented in this dissertation in which the veracity of these claims will be investigated and this approach will be applied in an effort to tailor the photophysics of a different chemical system.

The next advance in the understanding of the photophysics of Cr(acac)<sub>3</sub> came from the computational work of Ando *et al.*<sup>8</sup> This group calculated the geometries of the ground and lowest energy quartet excited state. After approximating the <sup>2</sup>E geometry as the ground state geometry they were able to calculate the displacement of each normal mode of the <sup>2</sup>E state required to distort the complex from the lowest energy geometry of the <sup>2</sup>E state to the lowest energy geometry of the <sup>4</sup>T<sub>2</sub> state. In other words, they calculated the Duschinsky displacement vector (Figure 2.6). This in turn allowed the group to construct a one-dimensional linear reaction coordinate describing the least motion path between the geometries of the <sup>2</sup>E and <sup>4</sup>T<sub>2</sub> states. By calculating the potential energy surfaces for the pertinent doublet and quartet excited

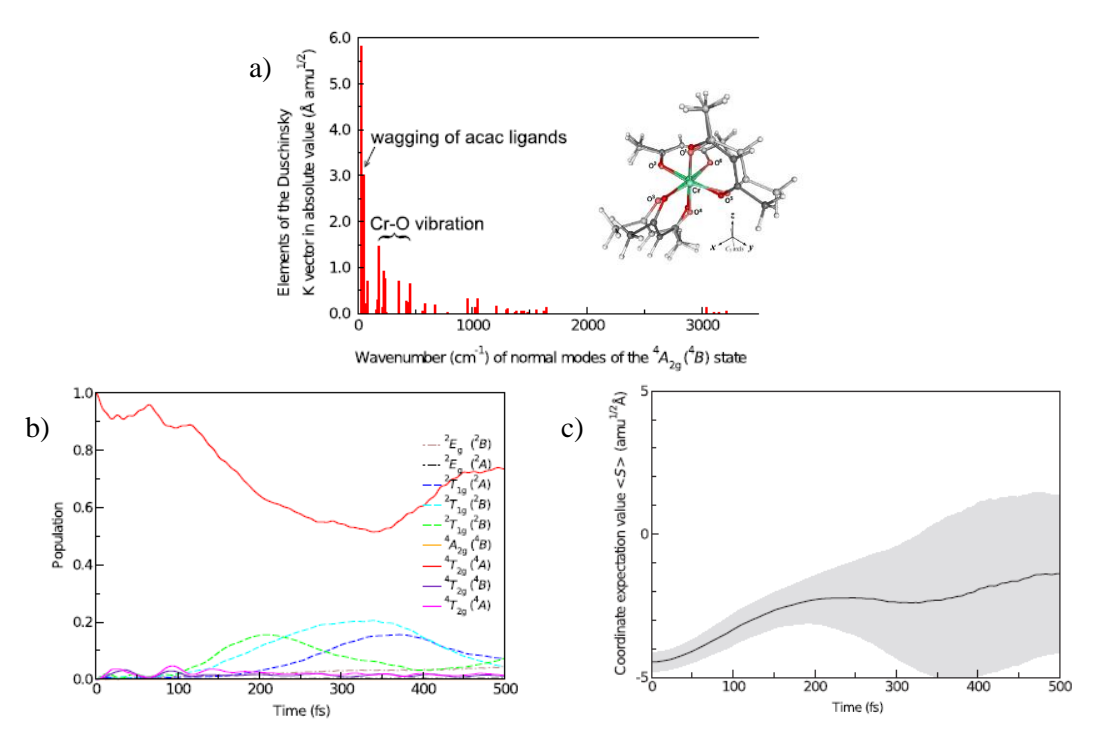


**Figure 2.6.** (a) Plot of the elements of the Duschinsky displacement vector for the distortion of the ground state geometry to  ${}^{4}T_{2}$  state equilibrium geometry as a function of vibrational modes on the ground electronic state inset showing an overlay of these two geometries. (b) Time dependent populations calculated using wavepacket analysis. (c) Plot of the position expectation value as a function of time during wavepacket simulation (solid) and standard deviation (shaded). Reprinted with permission from Reference 8.

states as well as SOC constants along this reaction coordinate the group was able to then perform wavepacket simulations to model the excited state dynamics. These simulations had shown  $\sim 40$  % of the  $^4T_2$  population transfer to the doublet manifold within 250 fs, in large part due to the curve crossing and large spin orbit coupling between the  $^4T_2$  and  $^2T_1$  states. Interestingly these simulations show a relatively compact standard deviation of the expectation value of the position along this one-dimensional coordinate during the first  $\sim 200$  fs and then a subsequent ballooning of this standard deviation suggesting a broadening or dephasing of the wavepacket, consistent with the short dephasing times measured for the symmetric breathing mode observed by Schrauben<sup>10</sup>, Foszcz<sup>12</sup>, and work described later in this dissertation. It is also noteworthy that this simulation shows a significant  $^4T_2$  population remaining by 300 fs which does not match with the interpretations of the ultrafast work conducted by Juban and McCusker.<sup>7</sup> While this may be effected by the lack of an internal conversion pathway within the doublet manifold, and only using a single nuclear coordinate, it may hint at a nuance in the photophysical properties of Cr(acac)<sub>3</sub>.

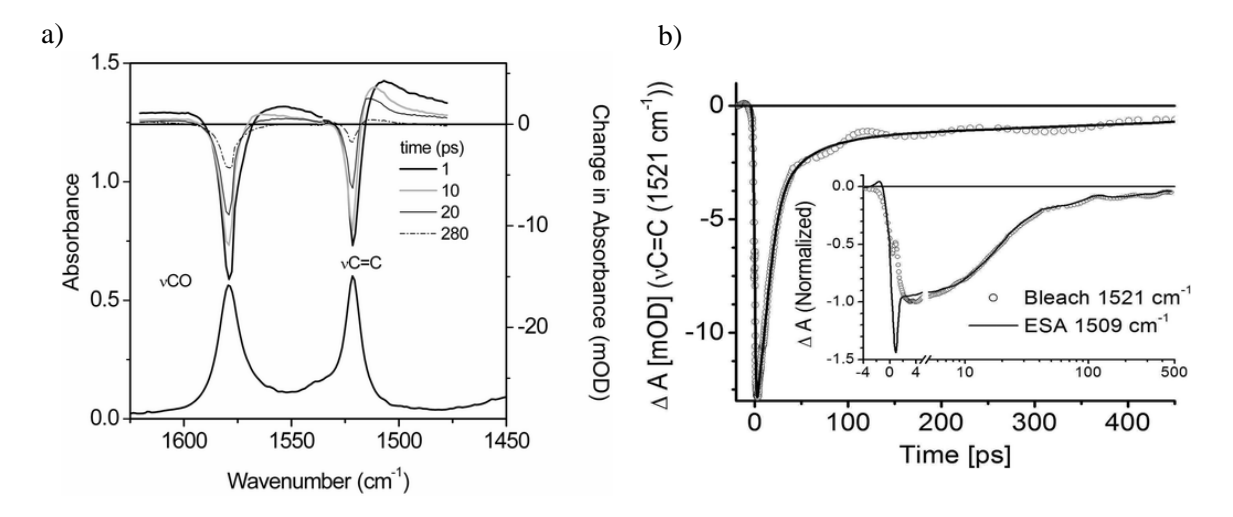


**Figure 2.7.** (a) Steady state (lower trace) and transient difference spectra (upper traces) following 400 nm excitation of  $Cr(acac)_3$  in tetrachloroethylene. (b) Evolution of the 1521 cm<sup>-1</sup> bleach recovery ( $\nu C=C$ ) following 400 nm excitation. Solid line corresponds to a biexponential fit with  $\tau_1 = 15$  ps and  $\tau_2 = 760$  ps. Inset superposes the bleach and the inverse of the excited state absorption feature at 1509 cm<sup>-1</sup>. The sharp feature at early time is part of the coherent artifact. Figure reprinted with permission from reference 13. © (2007) American Chemical Society.

The next series of works conducted by Kunttu and coworkers, <sup>13,14</sup> used ultrafast time resolved infrared spectroscopy to investigate the electronic relaxation pathways of Cr(acac)<sub>3</sub> through the lens of vibrational dynamics. In the first study, <sup>13</sup> Kunttu and coworkers excited at 400 nm into the higher energy <sup>4</sup>T<sub>1</sub> band of Cr(acac)<sub>3</sub> and performed transient absorption studies while monitoring across the  $\nu$ CO and  $\nu$ C=C stretching bands (Figure 2.7). Biphasic bleach recovery was observed with time constants of 15 and 760 ps. The slow, 760 ps, kinetic component was assigned as ground state recovery from the relaxed <sup>2</sup>E state which matches well with the ~800 ps ground state recovery measured by Juban and McCusker. <sup>7</sup> The 15 ps process which produces 70-85 % of the ground state recovery is ascribed to ISC back to the quartet manifold, likely initially to the <sup>4</sup>T<sub>2</sub> state. This 15 ps process was unobserved in the visible probe TA data of Juban and McCusker.

The next study by Kunttu and coworkers<sup>14</sup> sought to further clarify the details of the excited state dynamics of Cr(acac)<sub>3</sub>. From the work of Juban and McCusker,<sup>7</sup> it was already known that excitation into the <sup>4</sup>T<sub>2</sub>, <sup>4</sup>T<sub>1</sub>, and <sup>4</sup>LMCT excited states results in sub-100 fs decay to the <sup>2</sup>E state and that by 100 ps decay was exclusively from the <sup>2</sup>E state. Kunttu and coworkers sought to describe the details of the dynamics

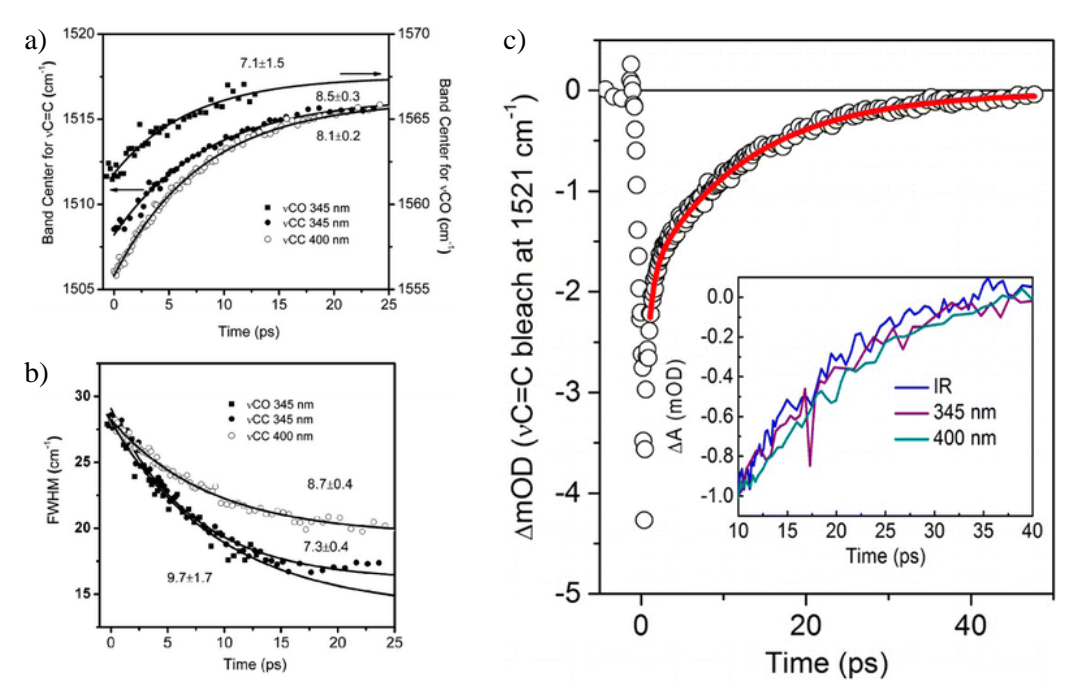


**Figure 2.8.** (a) Time dependent shifting for  $\nu$ CO and  $\nu$ C=C stretching ESA bands of Cr(acac)<sub>3</sub> in tetrachloroethylene following  $^4A_2 \rightarrow ^4T_1$  (400 nm) and  $^4A_2 \rightarrow ^4LMCT$  (345 nm) excitation. (b) Time dependent narrowing of the for  $\nu$ CO and  $\nu$ CC ESA features. (c) Bleach recovery kinetics of the  $\nu$ C=C stretching band following excitation into the  $0 \rightarrow 1$  transition at 1521 cm<sup>-1</sup> with fit shown in red. The inset shows a comparison of the decay dynamics following excitation at various wavelengths. Data in inset are normalized to the value at 10 ps. Reprinted with permission from reference 14. © (2015) American Chemical Society.

between these times by invoking a more detailed analysis of time resolved infrared data both after infrared and electronic excitation and to fit the data to an updated kinetic model. By analysis of the time dependent shifting and narrowing of the excited state absorption for both the  $\nu$ CO and  $\nu$ C=C stretching bands for  $^4$ LMCT (345 nm) and  $^4$ T<sub>1</sub> (400 nm) excitation, a consistent 7-10 ps time constant was observed that was assigned to vibrational relaxation on the excited electronic state (Figure 2.8). Following this shifting and narrowing process, the ESA band kinetics were similar to the bleach. The difference between this 7-10 ps lifetime and the 15 ps bleach recovery was ascribed to a bottleneck state in the electronic decay cascade. Additionally, by monitoring bleach recovery dynamics following infrared excitation of the fundamental  $\nu$ CO and  $\nu$ C=C stretching transitions, a 12 ps kinetic component was observed that is representative of the vibrational relaxation rate on the ground electronic state as well as a  $\sim$  300-700 fs component that was assigned as intramolecular vibrational redistribution (IVR). Given this 12 ps lifetime for vibrational cooling

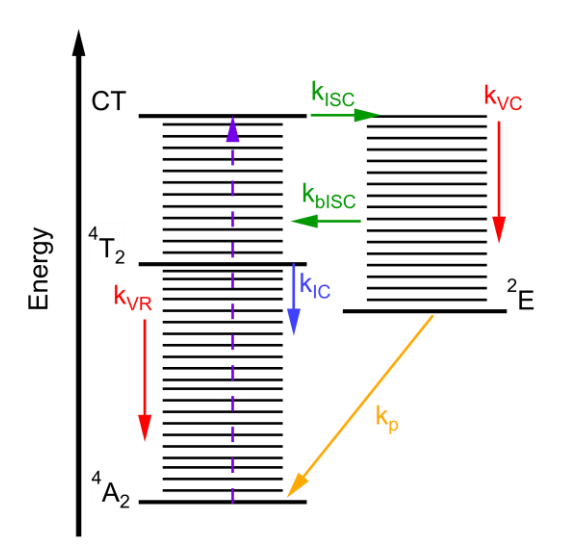


**Figure 2.9.** Simplified Energy level diagram for Cr(acac)<sub>3</sub> depicting the relaxation processes proposed in reference 14.

on the ground electronic state and the superposable bleach recovery dynamics at longer timescales for IR and electronic excitation (Figure 2.8c inset), it was proposed that ground state recovery following electronic excitation was limited by vibrational relaxation on the ground electronic state and that the difference between the rates following IR and electronic excitation could be attributed to additional electronic contribution to the decay process.<sup>14</sup>

With the above insights, Kunttu and coworkers, <sup>14</sup> proposed the kinetic model depicted in Figure 2.9 and described mathematically by the set of differential equations in equation 2.1.

$$\frac{d\left[{}^{2}E\right]}{dt} = -\left(k_{bISC} + k_{p}\right)\left[{}^{2}E\right] = -\left(A\exp\left(\frac{-E_{a}}{k_{b}T(t)}\right) + k_{p}\right)\left[{}^{2}E\right]$$
2.1a

$$\frac{d\left[{}^{4}T_{2}\right]}{dt} = k_{bISC}\left[{}^{2}E\right] - k_{IC}\left[{}^{4}T_{2}\right] = A\exp\left(\frac{-E_{a}}{k_{b}T(t)}\right)\left[{}^{2}E\right] - k_{IC}\left[{}^{4}T_{2}\right]$$
2.1b

$$\frac{d\left[{}^{4}A_{2}^{hot}\right]}{dt} = k_{IC}\left[{}^{4}T_{2}\right] - k_{VR}\left[{}^{4}A_{2}^{hot}\right]$$
2.1c

$$\frac{d\left[{}^{4}A_{2}\right]}{dt} = k_{VR}\left[{}^{4}A_{2}^{hot}\right] + k_{p}\left[{}^{2}E\right]$$
2.1d

In this model, the initial  ${}^4T_2 \rightarrow {}^2E$  ISC is considered prompt so that all the excess energy is converted directly to vibrational energy on the  ${}^2E$  state, consistent with the conclusion of the initial ultrafast work of Juban and McCusker that ISC is kinetically competitive with vibrational relaxation on the  ${}^4T_2$  state. Since the lifetime of the  ${}^2E$  state exhibits an Arrhenius behavior, this can be described by a thermally activated back-intersystem crossing (bISC) to the  ${}^4T_2$  state governed by the time dependent effective temperature of the  ${}^2E$  state population, T(t), described in equation 2.2. and the activation energy,  $E_a$ .

$$T(t) = 298K + (T_x - 298K)\exp(-k_{VC}t)$$
 2.2

The time dependent effective temperature is a function of the initial effective temperature of the  ${}^{2}E$  state population,  $T_x$ , and the vibrational cooling rate constant,  $k_{VC}$ . At high intramolecular temperatures, the  ${}^{2}E$  state population can undergo efficient bISC to the  ${}^{4}T_2$  state and subsequently undergo IC to the ground electronic state according to  $k_{IC}$ . At this point, the hot  ${}^{4}A_2$  population undergoes vibrational relaxation according to  $k_{VR}$  to reform a fully relaxed ground state. Phosphorescence from the  ${}^{2}E$  state was included in the model with  $k_p$ , however the slow relative rate has little impact on the model at room temperature. It should be noted that with lower effective temperatures, the bISC process is significantly less efficient, supporting the differences in the observations between the lower energy excitations of Juban and McCusker<sup>7</sup> and the higher energy excitations of Kunttu and coworkers<sup>14</sup>.

The kinetic model described above was able to simulate the bleach recovery dynamics well for both  ${}^{4}A_{2} \rightarrow {}^{4}T_{1}$  and  ${}^{4}A_{2} \rightarrow {}^{4}LMCT$  excitation (Figure 2.10) and yielded  $E_{a} = 23.0 \text{ kJ mol}^{-1}$ ,

 $A=2.9 \times 10^{13}$  s<sup>-1</sup> (1/ $A \sim 35$  fs), and  $k_{IC}=0.64 \times 10^{12}$  s<sup>-1</sup> ( $\tau_{IC}=1.56$  ps). Interestingly the 1.56 ps time constant for internal conversion from the  ${}^4T_2$  state, matches well with the 1.1 ps time constant observed in the earlier visible pump probe work of Juban and McCusker<sup>7</sup> which was assigned to vibrational relaxation on the  ${}^2E$  state suggesting a misassignment for this kinetic component. While the comparison between the interpretations of Juban<sup>7</sup> and Kunttu<sup>13,14</sup> are made more difficult by the use of different solvents and excitation energies, it is compelling to consider the merits of both and how each interpretation would affect the conclusions drawn in other bodies of work on Cr(acac)<sub>3</sub>, namely those of Joel Schrauben whose work

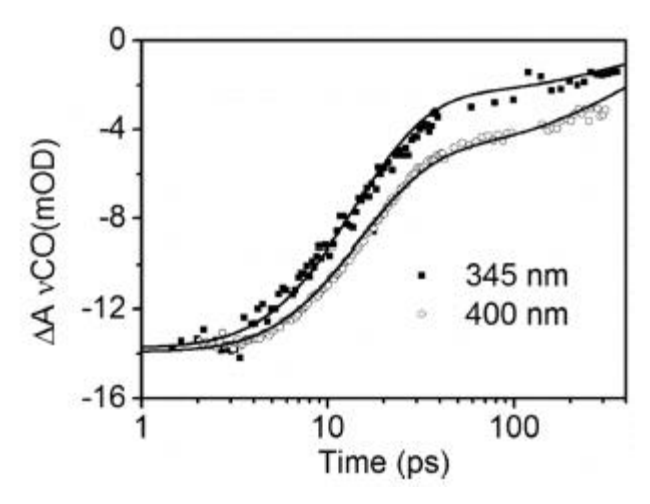


**Figure 2.10.** Bleach recovery dynamics of Cr(acac)<sub>3</sub> in tetrachloroethylene with experimental data (symbols) and simulated (solid lines) ground state populations. Reprinted with permission from reference 14. © (2015) American Chemical Society.

was published prior to these discoveries. 10,15 For the moment, we will leave the question of which interpretation has more merit and the subsequent implications to be addressed with the results shown later in this chapter.

It seems also necessary to pause and reflect on the rapid, ~300-700 fs component that was observed by Kunttu and coworkers<sup>14</sup> following infrared excitation and assigned to IVR. This fast component was observed on the ground electronic state in each of Cr(acac)<sub>3</sub>, Al(acac)<sub>3</sub> and Fe(acac)<sub>3</sub> as well as in different solvents, strongly suggesting it is inherent to the M(acac)<sub>3</sub> structure. Interestingly, although the magnitude of this component was significant in both the vCO and vC=C modes studied, it also varied between them, showing that the observation of IVR is vibrational mode dependent. Finally, this rapid ~300 fs IVR process seems also likely to result in dephasing of any vibrational coherences of these normal modes thus raising questions about the hypothesis presented in the work of Schrauben *et al.* that short dephasing times are an indicator for vibronic mixing of the nuclear and electronic degrees of freedom. These questions will be discussed alongside the results presented in this dissertation shortly.

In addition to observing coherent oscillations in the excited state of Cr(acac)<sub>3</sub>, Joel Schrauben also investigated the ultrafast dynamics of a series of Cr(acac)<sub>3</sub> analogues involving substitutions either in the 3 position of the acac backbone or at each of the methyl groups in the periphery of the molecule.<sup>15</sup> Early time

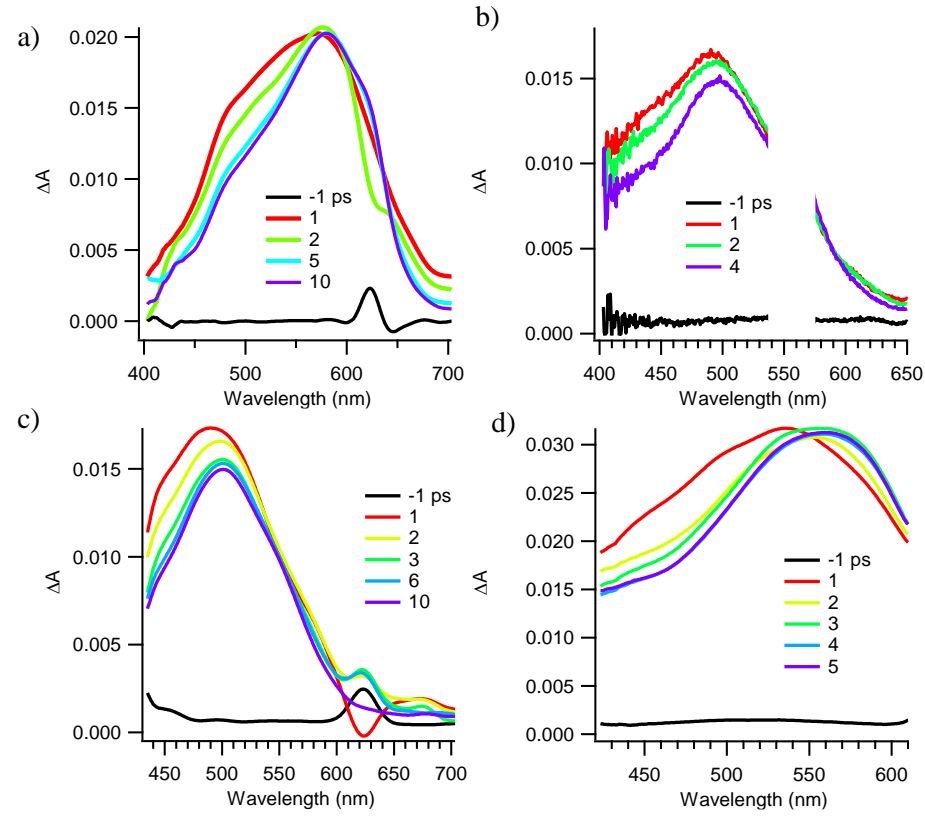


**Figure 2.11.** Early time full spectrum transient absorption data on (a)  $Cr(3-Br-acac)_3$ , (b)  $Cr(3-Br-acac)_3$ , (c)  $Cr(3-NO_2-acac)_3$ , and (d)  $Cr(3-Ph-acac)_3$  following  $^4A_2 \rightarrow ^4T_2$  excitation. Reproduced from data in Reference 15.

full spectrum TA data on several 3-substituted  $Cr(acac)_3$  molecules are shown in Figure 2.11. Schrauben's work had shown that each of the 3-substituted compounds behaved very similarly to the parent  $Cr(acac)_3$  compound, exhibiting a 1-2 ps decay in the blue edge of the spectrum that was described as a narrowing and redshift of the excited state absorption feature. Given the similarity between these spectral changes and those observed for the unsubstituted compound, these 1-2 ps kinetic components were also assigned to vibrational relaxation on the  $^2E$  excited state. While it was acknowledged that the exaggerated shifting observed for the phenyl-substituted derivative (Figure 2.11 d) could be interpreted in several ways such as being reflective of  $^4T_2 \rightarrow ^2E$  ISC, it was ultimately attributed to a rotation of the phenyl group. Attempts were made at investigating the rotationally hindered mesityl substituted compound although was incomplete by the time Joel graduated. Given that these data were collected prior to the work of Kunttu and

**Table 2.1.** Summary of oscillatory components observed for variable excitation wavelength TA experiments conducted by Foszcz<sup>12</sup> on Cr(acac)<sub>3</sub>. Errors are reported as standard deviations of all the data listed in Foszcz's dissertation work.

Oscillation Frequency, cm <sup>-1</sup>									
	70 (13)	111 (11)	187 (11)	221 (8)	256 (7)	282 (4)	333 (8)	457 (9)	553 (15)
Oscillation Damping Time, fs									
	240	2300	580	340	2300	160	580	1200	650
	(250)	(2900)	(400)	(140)	(3000)	(160)	(700)	(1200)	(560)

coworkers, <sup>14</sup> which claimed a back-intersystem crossing decay mechanism, these assignments may benefit from further consideration.

The final body of work to be summarized comes from previous McCusker group member, Eileen Foszcz. 12 Foszcz's work attempted to investigate the influence of excitation wavelength on the observed vibrational coherences of Cr(acac)<sub>3</sub> and Cr(TMHD)<sub>3</sub>. Despite the ~3000 cm<sup>-1</sup> range in excitation wavelength applied across the  ${}^4A_2 \rightarrow {}^4T_2$  absorption band, for Cr(acac)<sub>3</sub> and Cr(TMHD)<sub>3</sub> no significant differences in the oscillatory components were observed, both with respect to frequency and damping times. A summary of the observed oscillatory components of the Cr(acac)<sub>3</sub> datasets are presented in Table 2.1. It should be noted that a ~500 cm<sup>-1</sup> component has been omitted from Table 2.1 since it will be shown shortly that this oscillatory component does not originate from Cr(acac)<sub>3</sub>. An important observation from the results of this body of work is that among the numerous oscillatory components listed, the 187 and 457 cm<sup>-1</sup> modes appear most robustly throughout the collection of data sets and are easily assigned to metal ligand stretching modes, with the 187 cm<sup>-1</sup> mode resembling the DFT calculated mode from the work of Schrauben et al. 10 Interestingly the frequency and dephasing time for this mode are significantly different between both bodies of work. Given the better frequency matching of the 187 cm<sup>-1</sup> average collected by Fosczcz, <sup>12</sup> it is likely that this is more correct. The substantially slower dephasing time observed by Foszcz for this mode raise questions about the hypotheses proposed in Schrauben's work as well. The large standard error in several of the presented damping times, however, make this difficult to speculate on. If two of the ~ps damping times observed for the 187 cm<sup>-1</sup> mode are deemed as outliers as was proposed by Foszcz, the average damping time is reduced to ~420 fs. These standard deviations and differences between the two studies highlight the difficulty in acquiring reproducible data with this experiment and sample. Furthermore, in

addition to the difficulties already inherent to this experimental technique, the low solubility of Cr(TMHD)<sub>3</sub> in acetonitrile, a solvent which exhibits relatively minor background oscillatory signal, prompted Foszcz to attempt to monitor coherent oscillations in dichloromethane, which exhibits large amplitude oscillatory components that mask those attributable to the solute.

Despite the numerous investigations into  $Cr(acac)_3$  and its synthetic derivatives, there seems to be several open questions regarding the photophysics of this set of compounds. First, the nature of the ~1 ps process must be identified. Several studies by previous McCusker group members,  $^{7,10,15}$  have assigned this as vibrational relaxation in the  $^2E$  state, whereas Kunttu and coworkers  $^{14}$  suggest this is  $^4T_2 \rightarrow ^4A_2$  ground state recovery preceded by thermally activated back-intersystem crossing. Next, we must address the question of which vibrational modes are coherently active in  $Cr(acac)_3$  and its derivatives and how these synthetic modifications affect which vibrational modes are observed and their influence on the photophysical dynamics. Furthermore, we must attribute each of these vibrational modes to specific electronic states. Finally, we will attempt to address the question of whether dephasing times can be an indicator for involvement of a given vibrational mode in the reaction coordinate for a photophysical process. Each of these questions will be addressed in the subsequent work of this dissertation.

# 2.3. Experimental Section

# 2.3.1. Synthesis of Cr(acac)<sub>3</sub> Derivatives

i. tris(2,4-pentanediono)chromium(III), Cr(acac). Cr(acac)<sub>3</sub> was prepared according to the procedure of Schrauben.<sup>15</sup>

ii. tris(3-chloro-2,4-pentanediono)chromium(III), Cr(3-Clac)<sub>3</sub>. Cr(3-Cl-ac)<sub>3</sub> was prepared from Cr(acac)<sub>3</sub> according to the method of Collman *et al.*<sup>16</sup> Anal. calcd. for C<sub>15</sub>H<sub>18</sub>O<sub>6</sub>Cl<sub>3</sub>Cr (452.64 g mol<sup>-1</sup>): C 39.8, H 4.0, N 0; found: C 40.88, H 4.01, N 0.20.

iii. tris(3-bromo-2,4-pentanediono)chromium(III), Cr(3-Brac)<sub>3</sub>. Cr(3-Brac)<sub>3</sub> was synthesized previously by Joel Schrauben. <sup>15</sup>

- iv. tris(3-iodo-2,4-pentanediono)chromium(III), Cr(3-Iac)<sub>3</sub>. Cr(3-Iac)<sub>3</sub> was prepared from Cr(acac)<sub>3</sub> according to the method of Collman *et al.*<sup>16</sup> Anal. calcd. for C<sub>15</sub>H<sub>18</sub>O<sub>6</sub>I<sub>3</sub>Cr (726.99 g mol<sup>-1</sup>): C 24.8, H 2.5, N 0; found: C 25.08, H 2.58, N 0.085. Crystal structure included in appendix.
- v. tris(3-nitro-2,4-pentanediono)chromium(III), Cr(3-NO<sub>2</sub>ac)<sub>3</sub>. Cr(3-NO<sub>2</sub>ac)<sub>3</sub> was synthesized previously by Joel Schrauben. <sup>15</sup>
- vi. tris(3,5-heptanediono)chromium(III), Cr(HD)<sub>3</sub>. Cr(HD)<sub>3</sub> was synthesized in a manner similar to Cr(acac)<sub>3</sub> but with slight modification.<sup>15</sup> Heptanedione (4.116 g) was added to a round bottom flask with CrCl<sub>3</sub>·6H<sub>2</sub>O (2.854 g), urea (19.897 g), and 100 mL of DI water followed by another 100 mL DI water. Solution was refluxed for 16 h and cooled to room temperature before filtering on glass frit while washing with a copious amount of water. Remaining solid was dissolved in acetone and filtered into a separate container and then filtered again through a silica plug with acetone eluent. The solvent was evaporated and then sample was dissolved in a small amount of chloroform, washed with brine, extracted into chloroform and dried over MgSO<sub>4</sub>. Solvent was evaporated off to afford a purple product.
- vii. tris(2,6-dimethyl-3,5-heptanediono)chromium(III), Cr(DMHD)<sub>3</sub>. Cr(DMHD)<sub>3</sub> was prepared in a manner similar to Cr(acac)<sub>3</sub> but with slight modification. <sup>15</sup> CrCl<sub>3</sub>·6H<sub>2</sub>O (0.424 g), dimethylheptanedione (2.790 g), and urea (0.752 g) were added to a 50 mL round bottom flask followed by 10 mL 1,4-dioxane and 9 mL DI water and brought to reflux for 22 h. Solid was collected via vacuum filtration subsequently filtered through a neutral alumina plug with acetone eluent. Solvent was evaporated to afford a purple product. Crystal structure is included in appendix.

viii. tris(2,2,6,6-tetramethyl-3,5-heptanediono)chromium(III), Cr(TMHD)<sub>3</sub>. Cr(TMHD)<sub>3</sub> was prepared according to the procedure of Schrauben. <sup>15</sup>

ix. tris(4-chloro-2,2,6,6-tetramethyl-3,5-heptanediono)chromium(III), Cr(4-Cl-TMHD)<sub>3</sub>. Cr(4-Cl-TMHD)<sub>3</sub> was prepared from Cr(TMHD)<sub>3</sub> from a slightly modified method of Collman *et all*.<sup>16</sup> To a suspension of Cr(TMHD)<sub>3</sub> (0.596 g) in glacial acetic acid, n-chlorosuccinimide (6.045 g) was added with vigorous stirring in four parts separated by a few minutes each. Solution was then allowed to stir another 30 min before being filtered over celite and washed with copious amounts of water, sat. NaHCO<sub>3(aq)</sub>,

sat. Na<sub>2</sub>S<sub>2</sub>O<sub>3(aq)</sub>, and then more water. Pulled solid into new filter flask with DCM then evaporated solvent and recrystallized from hexanes to afford green product. Crystal structure included in appendix.

#### **2.3.2.** Computational Methods

All calculations were performed with Gaussian 09 software<sup>17</sup> on the Michigan State University High Performance Computing Center servers. Previously optimized geometries for Cr(acac)<sub>3</sub> and Cr(TMHD)<sub>3</sub> calculated by former McCusker group member, Eileen Foszcz<sup>12</sup>, were used as starting geometries for Cr(acac)<sub>3</sub> and Cr(TMHD)<sub>3</sub> ground state optimizations, and all subsequent optimizations for the various Cr(acac)<sub>3</sub> derivatives were started from one of these geometries. Optimizations were performed using the unrestricted B3LYP functional, 6-311G\*\* basis set, tight convergence criteria, and a polarizable continuum model for the solvent. Calculations for Cr(3-Iac)<sub>3</sub> were unique in that the LANL2DZ basis set was used. Choice of solvent used for the polarizable continuum model had little effect on the results in the frequency region of interest. Cr(acac)<sub>3</sub>, Cr(HD)<sub>3</sub>, and Cr(DMHD)<sub>3</sub> calculations were performed in acetonitrile, Cr(TMHD)<sub>3</sub> was performed in tetrahydrofuran, Cr(3-Clac)<sub>3</sub>, Cr(3-Iac)<sub>3</sub>, and Cr(4-ClTMHD)<sub>3</sub> were performed in dichloromethane, Cr(3-Brac)<sub>3</sub> was performed in toluene, and Cr(3-NO<sub>2</sub>ac)<sub>3</sub> was performed in acetone with solvent choice in part inspired by solubilities of the various compounds and the solvents used for TA experiments. Mass weighted vector displacement diagrams of each pertinent vibrational mode were created in the Visual Molecular Dynamics program.<sup>18</sup>

#### 2.3.3. Time Resolved Spectroscopic Methods

Our ultrafast transient absorption spectroscopy setup has been described in detail previously. <sup>12,19</sup> A Ti:sapphire oscillator (Coherent: Mantis) provides a ~400 mW, 80 MHz seed beam centered at ~800 nm for use in a regenerative amplifier (Coherent: Legend Elite) with a 527 nm Nd:YLF pump (Coherent: Evolution) producing a 1 KHz pulse train of approximately 35 fs 1 mJ pulses at 800 nm. This output is split using a 70/30 beam splitter with the higher energy portion used to pump a two-stage optical parametric amplifier (OPA) (Coherent: OperA Solo) to generate a visible pump beam which is used as the excitation source during the transient absorption experiment. This pump beam is again split with a 90:10 beam splitter with the lower energy portion being used as a probe beam for degenerate pump-probe experiments. The

remaining 30% of the 800 nm output from the regenerative amplifier is either used to pump a second OPA (Coherent: Opera Solo) to generate a probe beam for single wavelength nondegenerate pump-probe experiments or used to make a white light continuum by attenuating the power and focusing  $\sim$ 1  $\mu$ J pulses into a 3 mm sapphire window. This white light continuum can again be used for single wavelength nondegenerate pump-probe experiments or a large swath of the continuum can be measured using full spectrum measurements. Group velocity dispersion for each OPA output is corrected using a folded prism compressor. Pump-probe delay is adjusted by routing the pump OPA output into a computer-controlled translation stage (Aerotech). Pump and probe polarizations are set to  $\sim$ 54.7° relative to each other to eliminate anisotropic contributions to the signal and focused into a 1 mm quartz cuvette containing the sample. The pump pulse energies were set in the range of 2-5  $\mu$ J and the signal was checked for linearity by halving the pump power using a variable neutral density filter wheel. Probe pulse energies were set to roughly 1/10th of the pump.

During single wavelength measurements, the pump beam was passed through a 446 Hz mechanical chopper. A monochromator (Jarrell Ash: MonoSpec 18; 1200 groove/mm grating, blaze 500 nm) was placed after the sample and used to select a 3.8 nm FWHM slice of the probe beam spectrum to be measured on an amplified silicon photodiode (Thor laboratories: PDA55). The center wavelength of this slice of the probe spectrum is specified for each single wavelength TA trace. A reference beam is produced from a reflection of the probe beam off a microscope slide cover slip inserted into the beam path prior to the sample. This reference beam is measured on another amplified silicon photodiode and attenuated with neutral density filters and an iris until its intensity matches that of the signal beam. Both the signal and reference beams are coupled to a lock-in amplifier (Stanford Research: SR810) which is synchronized to the chopper modulating the pump beam. Connection of the lock-in amplifier to a data acquisition card allows the signal to be converted from analogue to digital. A data workup program written in LabView by previous McCusker group members converts the data to a change in absorbance.

During full spectrum measurements the white light continuum probe was collimated and subsequently focused into the sample using spherical mirrors. A lens placed after the sample was then used

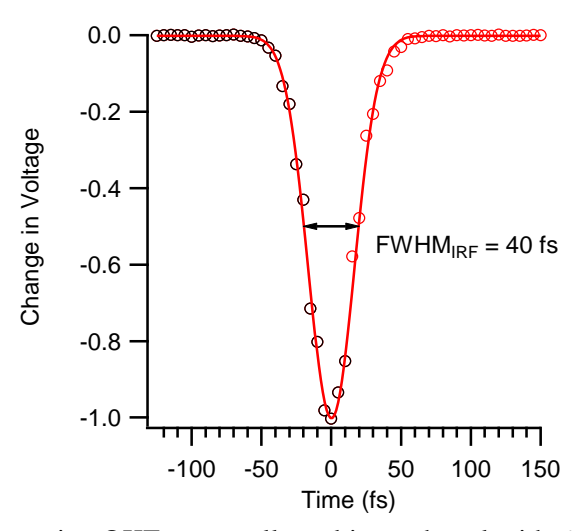


**Figure 2.12.** Representative OKE trace collected in methanol with 600 nm degenerate pump and probe. The first half of the dataset (black circles) was fit to a Gaussian to determine the FWHM of the IRF.

to focus the transmitted continuum probe into a liquid light guide which was coupled to a spectrometer (Spex 270 M) with 1 mm entrance slits. A grating (300 grooves/mm; blaze 600 nm) within the spectrometer dispersed the probe beam onto a diode array detector (Hamamatsu: HC233-0900; C5964 NMOS, 1x512 pixel array) affording a roughly 300 nm spectral window. Data is acquired using a LabView program written by previous McCusker group members. The program first collects "Dark Counts" by measuring the pump beam scatter reaching the detector in the absence of the probe beam. Next, a background is collected by measuring the signal with both pump and probe incident on the sample at negative time delay. This effectively measures the transmitted spectrum in the absence of excited state dynamics. A LabView program subsequently subtracts the dark counts spectrum to account for pump scatter. Data collection then proceeds by moving the pump delay line and measuring the transmitted intensity and dividing by the background signal.

In this chapter all single wavelength TA experiments used to measure coherent oscillations employed degenerate pump and probe beams except when the specified probe wavelength was 480 nm, in which case a white light continuum was used as the probe source. Single wavelength measurements employing a white light continuum probe were also used to measure the kinetics of several systems at 490, 550, and 650 nm. The instrument response function (IRF) for single wavelength kinetics traces was

determined from the optical Kerr effect (OKE) in methanol by fitting the early half of the signal to a Gaussian and extracting the full width at half maximum.<sup>20</sup> An example dataset is shown in Figure 2.12. To set up an OKE experiment, a polarizer is placed between the sample and the monochromator and set such that the transmitted polarization is 90° off the probe polarization. Since the polarizer blocks all the light reaching the signal photodiode, the reference photodiode is blocked during the experiment. The experiment is conducted by monitoring the intensity at the signal photodiode while scanning pump probe delay times from shortly before to shortly after the time at which the pump and probe pulses overlap in the sample. When both pump and probe are overlapped in the sample, the induced birefringence rotates the polarization of the probe beam and allows a small fraction to transmit through the polarizer to the detector. This response is a result of two types of contributions: electronic and nuclear. The essentially instantaneous electronic response results from the distortion of electron clouds of the molecules experiencing the intense electric field. The nuclear response arises from the reorientation of molecules to align in the direction of the electric field. The transient birefringence arising from the nuclear response decays as the molecules spontaneously rotate back to equilibrium positions.<sup>21</sup> When this reorientational motion is slow, a tail can be seen on the latter half of the OKE trace. Methanol's short-lived nuclear response makes it ideal for quantifying the duration of pump-probe overlap in the sample. For this reason, the IRF of single wavelength measurements will be quantified using OKE measurements performed in methanol as opposed to the solvent used to dissolve the sample of interest. In addition to the OKE measurement, a cross-correlation experiment can be performed in the same solvent used in the sample of interest to characterize the TA signals not due to the solute. The cross-correlation setup is similar to the OKE experiment except that the polarizer between the sample and monochromator is removed and the signal and reference photodiode signals in the absence of the pump beam are nonzero and matched. During full spectrum measurements, the IRF and dispersion are measured by collecting TA data on the neat solvent and then used to chirp correct the sample with solute.

Full spectrum datasets were often globally fit using the free to download OPTIMUS<sup>22</sup> fitting software developed by Dr. Chavdar Slavov of Goethe University in Frankfurt. This program allowed for chirp correction, fitting of the coherent artifact, and fitting of the population dynamics to a series of

exponential decay functions convolved with the IRF. One additional useful feature was the ability to calculate decay associated difference spectra (DADS). These plotted the amplitude of each exponential component as a function of wavelength to produce a spectrum that describes spectral changes arising from each kinetic component. The evolution associated difference spectra (EADS) could be calculated for cases of sequential decay dynamics as well. These plot the effective spectrum of transient species and are also useful for characterizing the excited state dynamics.

Single wavelength data was fit in the Igor pro program. Population dynamics were fit to a summation of exponential functions, with only enough exponential functions to adequately describe the data. These fits were started after the point where the coherent artifact of the neat solvent was found to return to baseline. A fast Fourier transform (FFT) was then performed on the residuals of this fit to produce a magnitude spectrum. No zero-padding, artificial resampling of the datapoints, or spectral window functions were used in the FFT analysis. The FFT was thus effectively performed using a rectangular window spanning from the initial residual point to the last point of the residuals which still had a constant time spacing. Additionally, oscillatory components were fit using a linear predictive singular value decomposition (LPSVD) program written in MATLAB originally by Dr. Andrey Demidov and Paul Champion<sup>23</sup> and edited by Dan Roscioli of the Beck group at Michigan State University. This program fits the data to a series of exponentially damped cosinusoids as shown in equation 2.3.

$$S(t) = \sum_{i=1}^{n} A_i \exp\left(\frac{-t}{\tau_i}\right) \cos\left(2\pi \nu_i t + \phi_i\right)$$
 2.3

This program allows the user to fit population dynamics using zero frequency components as well as extract exponentially damped oscillations. Additionally, by making use of the Fourier relationship between damping time and width in the frequency domain, the LPSVD program makes a vibrational spectrum that corelates to the LPSVD fit in the time domain. This LPSVD vibrational spectrum is then normalized and compared with the normalized FFT of the residuals of a fit of the population dynamics to help ground the result of a mathematical fit to reality.

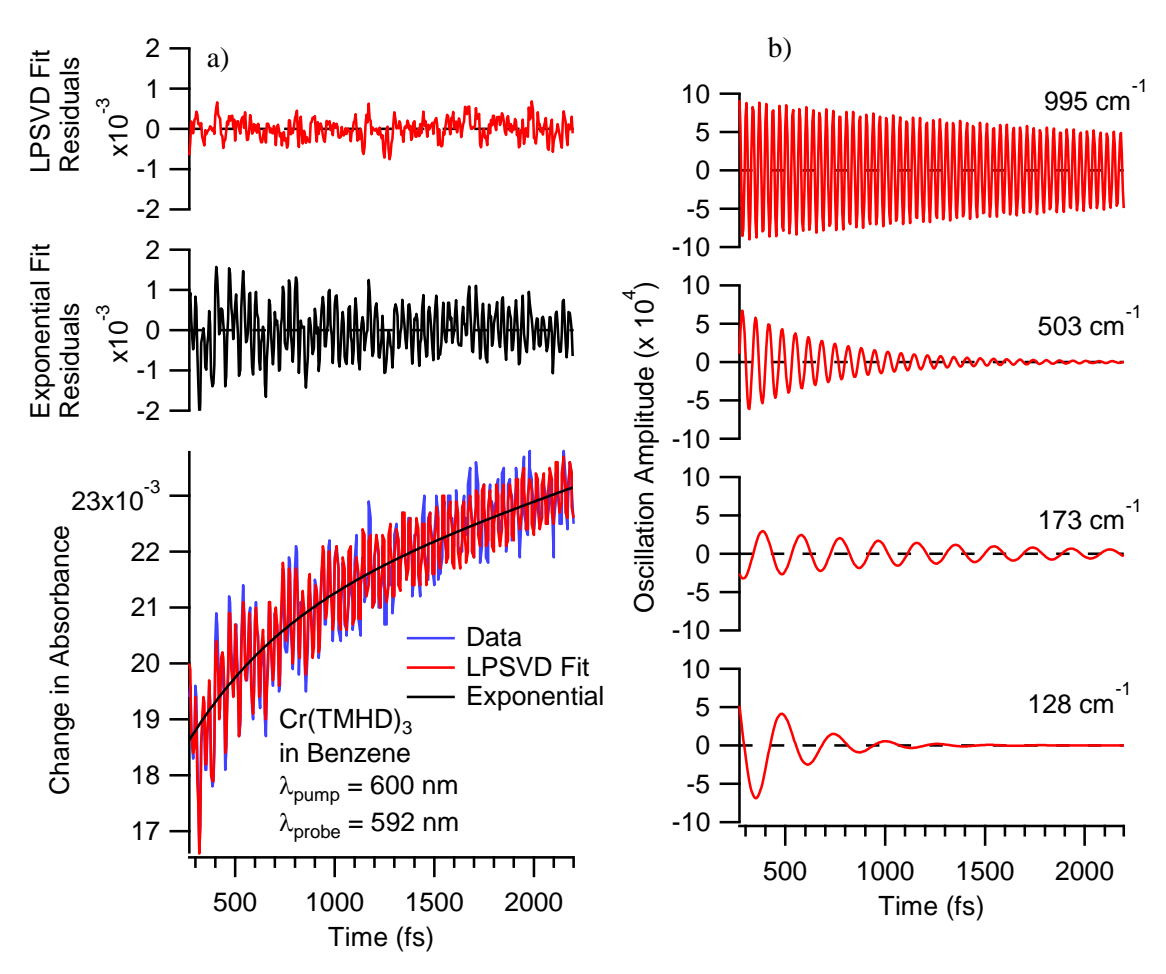


**Figure 2.13.** (a) Representative TA data exhibiting coherent oscillations (blue). The corresponding LPSVD fit (red) and exponential components acquired from LPSVD fit (black) are superimposed on the original dataset. The Residuals of each of these with respect to the raw data are shown above in red and black respectively. (b) Individual oscillatory components parsed out of raw data using LPSVD.

To illustrate the SVD portion of the LPSVD process, we can perform LPSVD on the TA data on Cr(TMHD)<sub>3</sub> in benzene in a 1 mm quartz cuvette with a 40 fs IRF featured in Figure 2.13a. In addition to an exponential rise, this data exhibited numerous oscillatory components. The LPSVD program is able to decompose the dataset into a linear combination of exponentially damped cososines as described in equation 2.3. The exponential kinetics of the system are modeled as zero-frequency components and are shown as the black line superimposed on the data in Figure 2.13a. The difference between the complete data and this exponential component contains the remaining oscillatory components as seen in the black residuals of Figure 2.13a. These oscillations are further decomposed into several frequency components

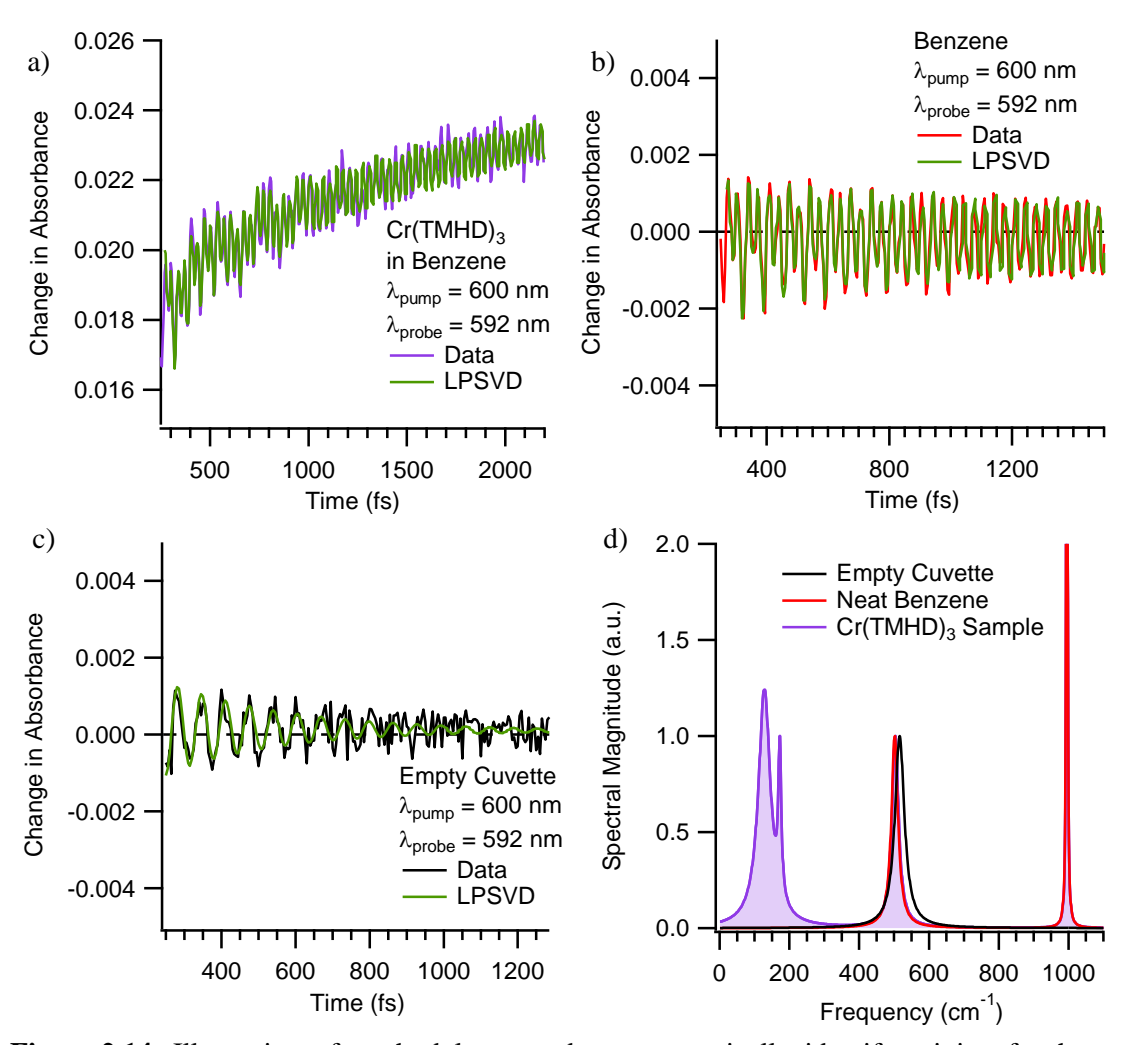


**Figure 2.14.** Illustration of methodology used to systematically identify origin of coherent oscillations in TA data. TA data and corresponding LPSVD fits of (a) Cr(TMHD)<sub>3</sub> dissolved in benzene in a quartz cuvette, (b) neat benzene in a quartz cuvette, and (c) an empty quartz cuvette. (d) Superimposed LPSVD magnitude spectra normalized to the common peak at 500 cm<sup>-1</sup>.

each with their own exponential damping times (Figure 2.13b). The sum of each of these oscillatory and exponential components gives the total LPSVD fit shown in red, superimposed upon the data in Figure 2.13a. The residuals of this fit contains unaccounted for oscillatory components (if any) and noise, although it can be warped if the exponential fitting is significantly off.

Once an LPSVD fit is obtained, the next step is to identify the origin of each of the oscillatory components of the dataset. The numerous possible sources of coherent oscillations in a TA experiment can make the complete assignment of coherences a difficult task. To alleviate some of this difficulty, control studies are performed on the neat solvent and, in some cases, the empty cuvette, in addition to the

experiment conducted on the sample of interest. By analyzing the frequency content of each of these data sets separately (either via FFT or LPSVD) the data can be compared for common oscillatory components. An example of this is shown in Figure 2.14 for the same dataset shown in Figure 2.13. Here, TA data along with LPSVD fits are shown for Cr(TMHD)<sub>3</sub> in benzene, neat benzene, and an empty quartz cuvette. Comparison of the frequency domain spectra in Figure 2.14d clearly shows an approximately 500 cm<sup>-1</sup> mode that is common to each dataset indicating it likely originates from the quartz cuvette. Similarly, the overlap of the 995 cm<sup>-1</sup> peak in the samples with and without solute (but not in the empty cuvette) clearly indicate that this is a mode of the the solvent. This type of assignment can often also be supported by looking at tables of vibrational modes for common solvents or by performing DFT frequency calculations. In the present case, we can readily assign the 995 cm<sup>-1</sup> mode to the strongly Raman active symmetric ring stretch mode of benzene. Finally the two additional lower frequency modes seen only for the non controll data must originate from the solute itself. In this example it does not seem as though a coherently active mode of the solute overlaps with a background frequency, however this is not always the case. In such cases it can be helpful to perform a similar experiment in a solvent with different frequency vibrations. If the mode still appears when the solute is in the newly chosen solvent but not in the new solvent control, it is likely that the solute does have a mode at that frequency. One could also, in theory, subtract the solvent response from the TA data on the sample of interest and observe if there is still frequency content in the region in question. This second method was not performed in the work of this dissertation. Nevertheless, we see that by performing careful control experiments every time experimental conditions are altered, one can relatively confidently identify vibrational modes of the solute.

When deciding how to set up the data collection parameters, several important factors were considered. Since the coherent oscillations observed in this work are often of relatively low amplitude, it is necessary to have a high signal to noise ratio to acquire reliable LPSVD fits. For control experiments on neat solvents with little additional background signals, this can be achieved in relatively few scans. For the work presented in this dissertation solvent control experiments were the result of at least 4 averaged scans. Data on the actual sample of interest was collected over a substantially longer period of time with a

minimum of 8 scans and often greater than 20 or 30. The individual scans were compared and any scans which showed a significant reduction to the signal magnitude or shifting of the coherent artifact were removed before averaging. Since both the LPSVD program and a general FFT require constant spacing between datapoints in the time domain, experiments were conducted such that the early time portions had constant time steps. When population dynamics were significantly slower than the oscillatory decay kinetics, both a high-density region of points at earlier times and a lower density of points were collected thereafter to adequately capture both the oscillatory and exponential kinetics. Typically, oscillations were fit over the first 2-3 ps of data (over which time the data would be collected with constant time spacing between data points), however in some instances, data was collected such that larger amounts of time could be fit. Typically, only compounds with longer dephasing times required more than 2-3 ps worth of data to perform a vibrational analysis on. For compounds with rapid dephasing times, collecting data over the first 2 ps should be more than enough since the oscillations will be completely damped out over most of this time. When collecting data for vibrational analysis, step distances of between 4 and 10 fs were used depending on the sample, its kinetics, and the length of time that needed to be collected to get a good LPSVD fit. The Nyquist frequency for each of these sampling rates is well above 1000 cm<sup>-1</sup> insuring that all the oscillatory components described in this dissertation are as adequately sampled as physically allowable. The resolution of the non-zero-padded FFT spectra presented in this chapter is typically between 5 and 20 cm<sup>-1</sup> depending on the step distance in the time domain and the number of datapoints included in the FFT. The resolution in the frequency domain could have been improved by up to a factor of 2 by zeropadding the data enough to double the number of datapoints, 24 however, this was not performed because the FFT was meant only to provide a qualitative sense of the frequency content of the data with the LPSVD analysis providing more quantitative results.

The duration of the IRF has an important influence on the ability to observe coherent oscillations in the time domain. It is rather intuitive that as the IRF becomes longer, the ability to observe periodic modulations to TA signal from vibrational coherences become diminished. Ground state vibrational coherences also have the additional caveat that they require sufficient time delay between the first and

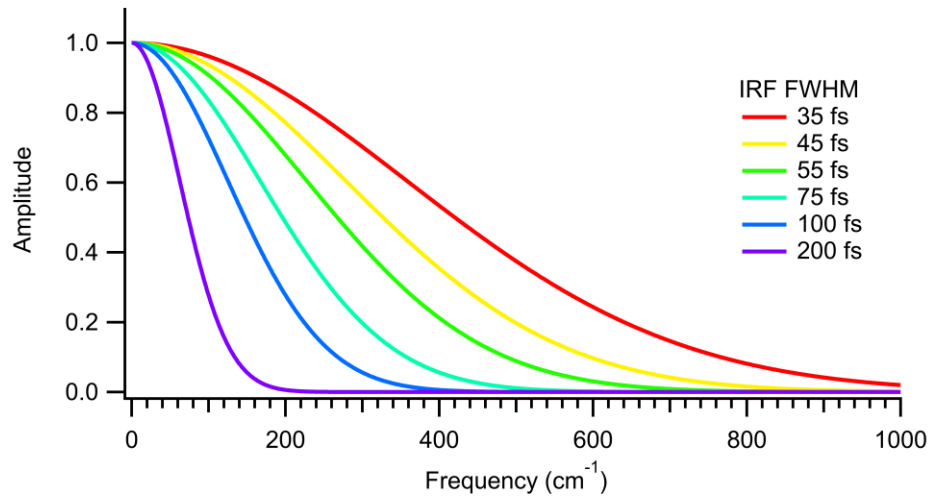


**Figure 2.15.** Approximated impulsive windows for various IRFs.

second field interactions of the pump pulse to show significant modulation amplitude. Ignoring this caveat for ground state vibrational coherences, we can get an idea of the so-called impulsive window describing the range of observable frequencies by convolving a gaussian IRF with a cosine function. The amplitude of the resulting oscillatory function is proportional to  $\exp(-\sigma_{IRF}^2\omega^2/2)$ , where  $\sigma_{IRF}$  is the standard deviation of the IRF and  $\omega$  is the angular frequency of the vibration.<sup>25</sup> It should be noted that an identical result can be obtained by simply taking the Fourier transform of the gaussian IRF. A simulation of the impulsive window for various IRFs can be seen in Figure 2.15. The specific IRFs in this chapter varied depending on the pump probe combination and the wavelength region of each. As described above the vast majority of the coherence data presented in this chapter are from degenerate pump probe TA experiments where the probe beam is a replica of the pump pulse generated in a beam splitter. When these pump and probe pulses were generated via second harmonic of the signal (i.e. when the center of the pump spectrum was between 580 and 700 nm) the IRF was roughly 45 fs with slight fluctuations on the order of 10 fs from one experimental to another. The McCusker group laser system produces its shortest laser pulses in this wavelength region and, as such, much of the experiments in this dissertation seeking to observe coherent oscillations employed laser pulses in this wavelength range. In contrast, degenerate pump probe experiments employing sum frequency of the idler (~570-530 nm) or sum frequency of the signal (~520-460 nm) had significantly longer IRFs which were roughly 70 fs. Experiments using a white light continuum probe had an IRF of roughly

100-160 fs. Whether using an IRF of ~45 fs or ~75 fs, the impulsive windows simulated in Figure 2.15 show that vibrational frequencies of 200 cm<sup>-1</sup> or less should be reliably visible in TA experiments. It is interesting to note that many of the datasets presented in this chapter show relatively high frequency solvent vibrational modes despite, according to the approximated impulsive windows in Figure 2.15, having significant, or in some circumstances, enormous attenuation factors. It is unknown to this author why exactly these modes are so reproducibly visible in the following TA data; however it may be a result of the intense electric fields of the laser pulses used in these experiments and the high Raman activity of the observed vibrational modes.

Ground state absorption spectra were collected on a Varion Cary 50 UV-vis spectrometer before and after TA experiments to check for sample degradation. Samples were made to have an absorbance between 0.2 and 0.8 at the center wavelength of the pump spectrum in a 1-mm pathlength cuvette. Instead of creating a blank for each ground state absorption measurement, the spectrometer was zeroed with nothing in the sample holder then an absorption spectrum was measured. The baseline offset at ~800 nm, a region in which ground state absorption was absent, was subtracted from the rest of the data set to approximate the actual absorption of the sample.

#### 2.4. Results and Discussion

# 2.4.1. Cr(acac)<sub>3</sub>

Addressing the Question of the Nature of the 1 ps Process

One of the open questions raised during the summary of the previous results on  $Cr(acac)_3$  was the nature of the excited state decay mechanism. Initial ultrafast visible transient absorption experiments conducted by Juban had assigned a ~1 ps narrowing and redshifting of the transient spectrum to vibrational relaxation on the  ${}^2E$  excited state following unobserved, ultrafast  ${}^4T_2 \rightarrow {}^2E$  ISC. ${}^7$  These conclusions were made in part based on the qualitative retention of the bandshape as well as the increased decay amplitude in the wings of the ESA spectrum following lower wavelength excitation. Kunttu and coworkers used a combination of IR pump IR probe and visible pump IR probe experiments to arrive at a mechanism involving impulsive  ${}^4T_2 \rightarrow {}^2E$  ISC followed by thermally activated bISC and ~1 ps  ${}^4T_2 \rightarrow {}^4A_2$  IC, with

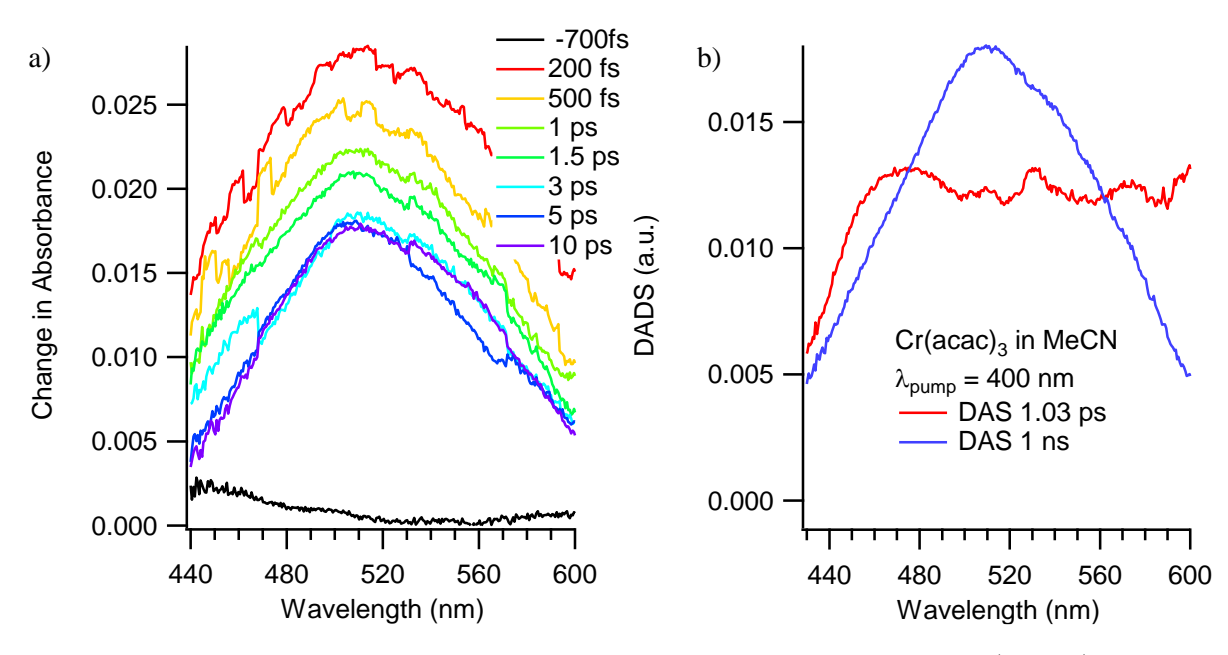


**Figure 2.16.** (a) Full spectrum transient absorption data on  $Cr(acac)_3$  following  ${}^4A_2 \rightarrow {}^4T_1$  (400 nm) excitation in acetonitrile. (b) Decay associated difference spectra (DADS) associated with the global fit of the data in (a). A 1 ns lifetime associated with the longtime offset was locked in but had no bearing on the value of the shorter time constant.

~7 ps vibrational relaxation on the <sup>2</sup>E state. <sup>13,14</sup> The interpretations within these two studies are in conflict and should be addressed before progressing to the focus of this work regarding the information that can be obtained from vibrational coherences and their dephasing times. While the comparison of these two studies is complicated by the different solvents used in each study as well as the vastly different energies associated with the initially generated excited states (conceivably opening the door to additional decay pathways), the increased sensitivity of the IR probe to vibrational dynamics suggests that the 7-10 ps vibrational relaxation time observed by Kunttu and coworkers is more plausible than the ~1 ps time constant assigned using a visible probe which is considerably less diagnostic or selective towards vibrational dynamics.

In addition to a retrospective comparison of the two above interpretations,<sup>7,14</sup> we can gain further evidence for which kinetic model is most appropriate by repeating the experiment of Kunttu and coworkers<sup>14</sup> with a visible probe beam, thus allowing for a more direct comparison of the physical observables. Figure 2.16a shows full spectrum TA data on Cr(acac)<sub>3</sub> following 400 nm excitation into the <sup>4</sup>T<sub>1</sub> state, similar to what was performed by Kunttu. Decay associated difference spectra (DADS) associated with a global fit of the dataset using OPTIMUS fitting software<sup>22</sup> can be seen in Figure 2.16b. The 1 ps time

constant extracted with this fit is consistent with both Juban's work involving the lowest energy spinallowed excitation into the <sup>4</sup>T<sub>2</sub> state while using a visible probe, as well as Kunttu's <sup>14</sup> work involving excitation into the higher energy <sup>4</sup>T<sub>1</sub> state and use of an infrared probe. Given the agreement between all three of these experiments, it is highly likely that the same process is being monitored. Initial examination of the TA data in Figure 2.16 shows a general decrease in intensity of the ESA spectrum while retaining the overall band shape. Closer inspection of the 1 ps DADS, however, shows a flat decay amplitude from ~460 nm to the edge of the probe window at 600 nm. Given that the <sup>2</sup>E state is formed in less than 100 fs,<sup>7</sup> and that the spectral evolution following 400 nm excitation does not resemble spectral narrowing, we can unequivocally say that the 1 ps process does not represent vibrational relaxation on the <sup>2</sup>E state. Thus, since ISC has already occurred, and the observed spectral evolution is not associated with vibrational relaxation, then the most likely origin of the spectral evolution is a net loss of excited state population. Furthermore, because the 1 ps DADS does not resemble the spectrum of the <sup>2</sup>E state represented by the spectrum at 10 ps, we can say that the TA data in Figure 2.16a do not show the loss of the <sup>2</sup>E state population exclusively. The presence of an additional excited state population can thus be inferred. This means that the spectrum of a quartet excited state, most likely the lowest energy <sup>4</sup>T<sub>2</sub> excited state, is superimposed upon the <sup>2</sup>E state spectrum at early times, consistent with the formation of a rapid equilibrium as seen in Kunttu's kinetic model.<sup>14</sup> The large amplitude decay across the entire spectrum suggests that at high excitation energy (low excitation wavelength), the <sup>4</sup>T<sub>2</sub> state serves to effectively siphon <sup>2</sup>E state population and direct recovery of the ground electronic state. The diminished amplitude of the decay following lower energy  ${}^4A_2 \rightarrow {}^4T_2$ excitation, <sup>7</sup> is consistent with a less efficient thermally activated bISC.

From the above analysis, it was shown that the most likely excited state decay mechanism in  $Cr(acac)_3$  at early times following excitation into the quartet manifold involves impulsive ISC to the  $^2E$  state followed by thermally activated bISC to the  $^4T_2$  state and IC to the ground state. The portion of the  $^2E$  state population that remains trapped following vibrational relaxation, then decays at a much slower timescale dependent on the temperature of the surrounding bath. It stands to reason that since many of the 3-substituted  $Cr(acac')_3$  derivatives shared very similar kinetics and spectral evolution as the unsubstituted

parent molecule, that each of these derivatives and the unsubstituted Cr(acac)<sub>3</sub> undergo a similar decay pathway. Extending these interpretations to the more sterically encumbered derivatives such as Cr(TMHD)<sub>3</sub>, however, requires more caution. The spectral evolution for Cr(TMHD)<sub>3</sub> (Figure 2.5) involves a decay of the ESA at ~465 nm with a concomitant rise centered around ~525 nm. Given the LMCT nature of the excited state absorption, the extinction coefficient for the ESA feature at 525 nm is likely several orders of magnitude larger than that for the Laporte forbidden ground state absorption, hence we can still say that the observed dynamics do not exclusively represent repopulation of the ground electronic state as this would result in a net decrease in  $\Delta A$ . Furthermore, the significant changes to the absorption profile suggest that vibrational relaxation is not a primary factor causing the observed spectral changes. Thus, a significant portion of the spectral evolution must be due to a change in electronic state, specifically, formation of the lowest energy, <sup>2</sup>E, excited state. This result could be achieved in two ways. In the first option, the initial  ${}^4T_2 \rightarrow {}^2E$  ISC event could be slowed relative to  $Cr(acac)_3$  and the observed 1.8 ps process could be the first and only change in excited state population that occurs. This route would require a moderately slower IC rate relative to Cr(acac)<sub>3</sub> as well as a substantially slower ISC rate. An alternative route may involve a rapid  ${}^4T_2 \rightarrow {}^2E$  ISC and subsequent bISC (similar to Cr(acac)<sub>3</sub>) with a less efficient IC to recover the electronic ground state. If the <sup>4</sup>T<sub>2</sub> population cannot efficiently undergo IC, then it must continue to decay back to the lowest energy <sup>2</sup>E excited state as the excess thermal energy is dissipated. At present, given the lack of information it is difficult to determine which mechanism better describes the dynamics of Cr(TMHD)<sub>3</sub>. One way to experimentally gain more insight into which mechanism has more merit may be a variable excitation wavelength experiment. Since the second mechanism involves a thermally activated bISC, then the variable excitation energy should modulate the amount of  ${}^{4}T_{2}$  population formed from bISC and by extension the amount of conversion to the <sup>2</sup>E state as the system vibrationally cools. The first mechanism, however, does not predict any difference in the net amplitude change as a function of excitation energy. A further discussion of these possible mechanisms will be continued again later in this chapter.

# Observation and Interpretation of Coherent Oscillations

As discussed in the summary of previous investigations into Cr(acac)<sub>3</sub>, Schrauben's work<sup>10</sup> had proposed the notion that dephasing times that are intermediate between the sub-100 fs dephasing times of electronic coherences<sup>26,27</sup> and the often reported as ~ps dephasing times of purely vibrational coherences<sup>24,27–31</sup> may serve as an indicator for vibronic mixing and involvement of a particular vibrational mode in an ultrafast photophysical process. Furthermore, it was proposed that the identification of these vibrational modes with short dephasing times, could help inspire synthetic modifications that could alter the photophysical properties of the system. Much of the remainder of the discussion in this chapter will seek to address these claims and to further understand the role of nuclear motion in the excited state evolution of Cr(acac)<sub>3</sub> and its derivatives. Specifically, an attempt will be made to (1) identify the coherently active vibrational modes of Cr(acac)<sub>3</sub>, (2) assign each of these vibrational modes to a specific electronic state, (3) quantify the dephasing times of each vibrational mode, (4) identify the origin of the dephasing mechanisms, and (5) address the merit of the of the hypothesis that short dephasing times can be indicative of involvement of specific vibrational modes in an ultrafast transformation. To achieve this, coherent vibrational modes will be observed as outlined in section 2.3.3.

In much of the following report, coherent oscillations in TA data will be analyzed to provide information on excited state dynamics. Because there are many mechanisms by which a coherence can be created in a sample during a pump-probe transient absorption experiment, it is important to assess the specific origin of each oscillatory component carefully. One can often exploit the disparity of time scales for dephasing between purely electronic and purely vibrational coherences to identify the type of coherence being monitored, i.e. electronic or vibrational. Electronic coherences typically dephase on sub-100 fs timescales, <sup>26,27</sup> whereas vibrational coherences can require several picoseconds to completely dephase. <sup>24,28–30</sup> In the system of interest, oscillations persist from several hundreds of femtoseconds to several picoseconds, <sup>10,12</sup> excluding purely electronic coherences as a likely component of the signal. This leaves three possible origins for the oscillatory components in the data: (1) ground state vibrational coherence in

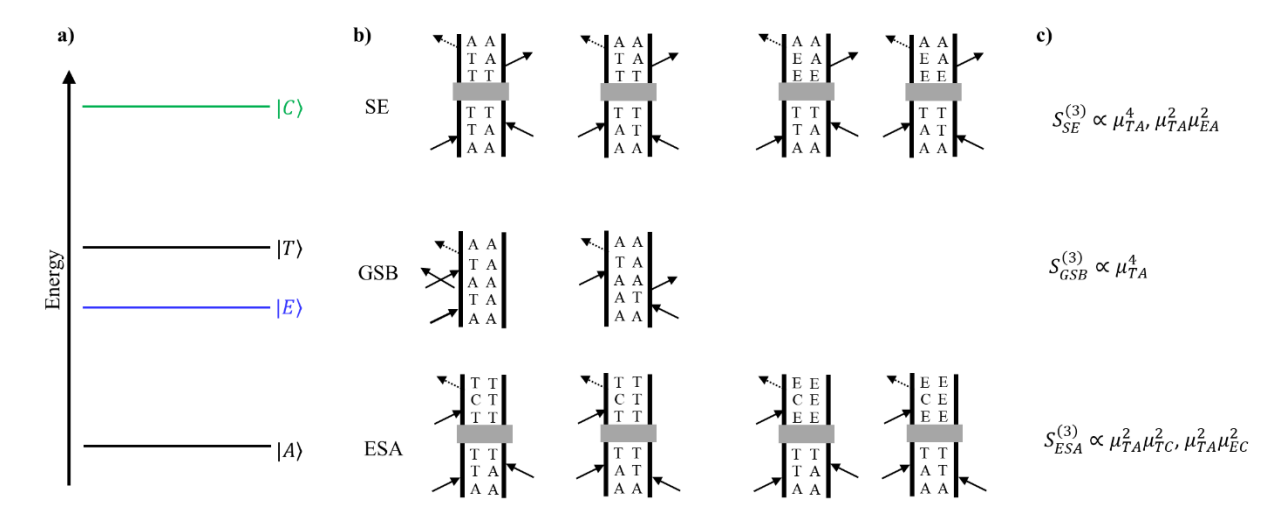


**Figure 2.17.** (a) Qualitative energy level diagram depicting the ground  ${}^4A_2$  state ( $|A\rangle$ ),  ${}^2E$  state ( $|E\rangle$ ),  ${}^4T_2$  state ( $|T\rangle$ ), and charge transfer manifold ( $|C\rangle$ ) that the  ${}^2E$  and  ${}^4T_2$  states can be promoted to through resonance with the probe beam. (b) Double sided Feynman diagrams depicting stimulated emission (SE), ground state bleaching (GSB) and excited state absorption (ESA) processes. Following excitation, to the  ${}^4T_2$  state, the system may evolve. Depending on the time delay between pump and probe, a population may exist in the  ${}^4T_2$  or  ${}^2E$  states. This relaxation pathway is denoted by a gray box. (c) The relationship between signal amplitude (third order response function) and transition dipole moments for relevant field interactions for SE, GSB, and ESA.

the solvent, (2) ground state vibrational coherence in the solute, or (3) vibrational coherence in the excited electronic state of the solute. In general, a vibrational coherence can be created in the ground state of the solvent or solute via impulsive stimulated Raman scattering (ISRS). The solvent contribution can often simply be identified by performing the pump-probe experiment on neat solvent or performing a frequency domain Raman experiment.

Discerning the nature of the solute coherence is in general more difficult. For this, it is helpful to consult the Feynman diagrams seen in Figure 2.17 depicting stimulated emission (SE), ground state bleaching (GSB) and excited state absorption (ESA) processes. It should be noted that the mechanism by which ground state vibrational coherence in the solute is generated (ISRS) can be grouped with GSB. The magnitude of the signal from each of these processes is a function of the probability of each necessary field interaction occurring, which is proportional to the transition dipole moment of the transition it induces. In the system of interest, both SE and GSB involve transitions solely between ligand field states, either between the  ${}^4A_2$  and  ${}^4T_2$  states or the  ${}^4A_2$  and  ${}^2E$  states. Due to the Laporte forbidden, and in some cases,

spin forbidden nature of these transitions, the transition dipole moments are particularly small. Transitions between the  $^2$ E or  $^4$ T<sub>2</sub> states and the charge transfer manifold, however, should exhibit a substantially larger transition dipole owing to the spin and parity allowed nature of these transitions. Thus, it is clear that the amplitude of ESA signal will be much greater than for SE or GSB. Furthermore, we can acquire a rough estimate of the magnitude of this disparity by approximating the squared transition dipole moments for the  $^4$ A<sub>2</sub>  $\leftrightarrow$   $^4$ T<sub>2</sub> and the ligand field  $\leftrightarrow$  charge transfer manifold transitions from the ground state extinction coefficients of Cr(acac)<sub>3</sub> ( $\sim$ 100 L mol<sup>-1</sup> cm<sup>-1</sup>)<sup>7</sup> and [Fe(bpy)<sub>3</sub>]<sup>2+</sup> ( $\sim$ 10,000 L mol<sup>-1</sup> cm<sup>-1</sup>)<sup>32</sup> respectively. From the third order response functions listed in Figure 2.17, these values imply that the ESA signal is approximately 100-fold larger than those for GSB or SE! This is further supported by the observation that the TA spectrum for the systems of interest are positive throughout the visible spectrum. <sup>7,10,15</sup> Consequently, the only means by which we can monitor vibrational coherence of the solute in this system is by excited state absorption, i.e. any observable coherence in Cr(acac)<sub>3</sub> or its derivatives must be in an electronic excited state.

Now that we have established the nature of the signals that will be observed during a transient absorption experiment, it is important to address the mechanisms by which coherences dephase. In the optical Bloch picture, dephasing occurs by population relaxation ( $T_I$ ) and pure dephasing ( $T_2^*$ ) caused by random environmental fluctuations that cause a loss of phase information. The contributions of these two processes to the observed homogenous dephasing time ( $T_2$ ) are additive as seen in equation 2.4:

$$\frac{1}{T_2} = \frac{1}{2} \left( \frac{1}{T_{1,a}} + \frac{1}{T_{1,b}} \right) + \frac{1}{T_2^*}$$
 2.4

Where  $T_{l,a}$  and  $T_{l,b}$  are the population relaxation times of the states involved in the coherence. Vibrational coherences typically show dephasing times on the order of picoseconds<sup>24,28–30</sup> and in solution phase this is often dominated by pure dephasing processes.<sup>33</sup> It is often observed that excited state vibrational coherences dephase faster than their ground state analogues due to either higher anharmonicity of the potential surface or an increased density of states leading to faster population relaxation. An alternative view of coherences involves their description as localized wave packets. In this picture, dephasing can in part be thought of as

**Table 2.2.** Summary of coherent vibrational modes of Cr(acac)<sub>3</sub> observed during TA experiments in various solvents. Reported IRFs are rounded to the nearest integer multiple of 5 fs.

$\lambda_{pu},nm \\ (E_{pu},\mu J)$	$\begin{array}{c} \lambda_{pr},nm \\ (E_{pr},\mu J) \end{array}$	IRF, fs	Solvent	Frequency, cm <sup>-1</sup> (Damping Time, fs)				
600 (3)	592 (0.3)	45	MeCN				286 (119)	462 (1142)
600 (5)	592 (0.3)	50	MeCN	98 (512)	192 (412)			463 (487)
600 (3.5) <sup>a</sup>	592 (0.3) <sup>a</sup>	50	MeCN	83 (376)				458 (1887)
600 (3.5) <sup>b</sup>	592 (0.3) <sup>b</sup>	50	MeCN		195 (411)	242 (1074)		
600 (3)	592 (0.3)	50	MeCN		203 (418)	, ,		462 (665)
600 (3)	592 (0.3)	60	MeCN		200 (404)		314 (300)	457 (2146)
600 (3)	592 (0.3)	60	MeCN		193 (283)			458 (1180)
600 (3)	480 (na)	160	MeCN	102 (265)	189 (435)		303 (348)	468 (736)
600 (3)	480 (na)	100	MeCN		185 (342)	239 (250)		457 (359)
600 (3)	480 (na)	75	MeCN	98 (374)				457 (1460)
600 (3)	592 (0.3)	45	Dioxane		205 (332)			461 (774)
600 (3)	480 (na)	100	Dioxane		175 (266)		295 (358)	, ,
600 (3)	595 (0.3)	50	THF		208 (261)		271 (12,900) <sup>c</sup>	458 (1320)
600 (3)	592 (0.3)	50	THF		187 (228)			477 (1260)
600 (4.8)	586 (0.5)	40	THF		186 (90)			460 (1359)
580 (4.4)	592 (0.5)	45	THF					458 (1051)
560 (5)	546 (0.5)	65	THF		187 (645)			
Average Frequency, cm <sup>-1</sup>				95	193	241	300	461
Standard Deviation, cm <sup>-1</sup>				8	9	2	12	6
Average Damping Time, fs				380	350	660	280	1130
Standard Deviation, fs				100	130	580	110	500

<sup>(</sup>a) Experiment performed with parallel pump and probe polarizations. (b) Experiment performed with perpendicular pump and probe polarizations. (c) This dephasing time was significantly larger than the remainder of the values in the series and thus was deemed as an outlier and not used to calculate an average.

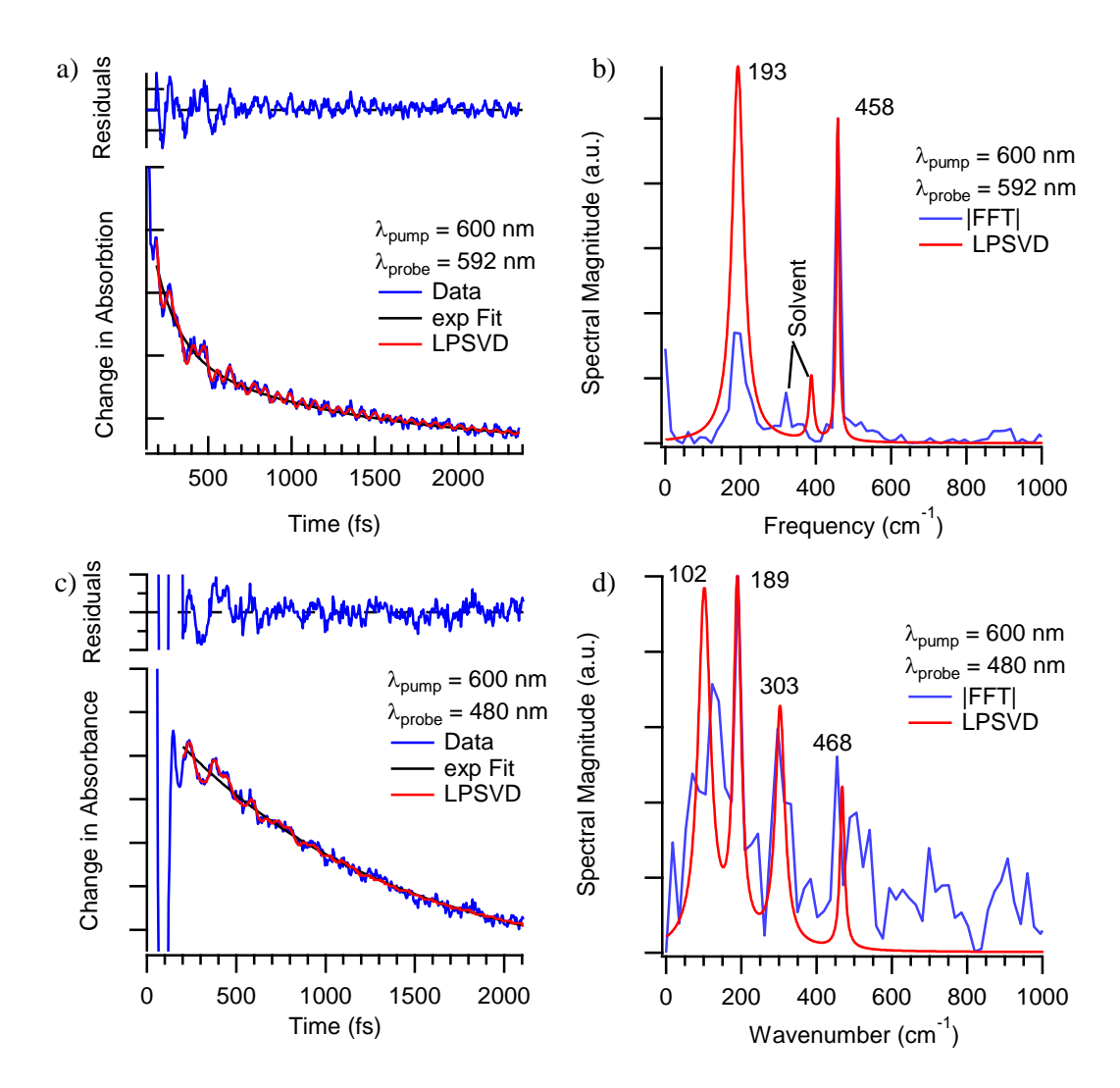


**Figure 2.18.** (a) Representative TA data on Cr(acac)<sub>3</sub> collected in acetonitrile following 600 nm excitation and monitoring at 592 nm. (b) Comparison of results of |FFT| (blue) and LPSVD (red) analyses of data from part a. (c) Analogous data collected while monitoring at 480 nm. (d) Comparison of |FFT| and LPSVD analyses for 480 nm probe data.

a spatial dispersion of the wave packet. This can occur in a highly anharmonic portion of the potential surface or as a result of multiple population transfer and back-transfer events between potential surfaces.

The vibrational coherences of  $Cr(acac)_3$  and their corresponding dephasing times following  ${}^4A_2 \rightarrow {}^4T_2$  excitation, were monitored using transient absorption spectroscopy. Studies were conducted in acetonitrile, 1,4-dioxane, and tetrahydrofuran while probing on the red and blue edges of the excited state absorption feature. The results are summarized in Table 2.2 and show good agreement with the previous results collected by Foszcz. <sup>12</sup> Inspection of the data in Table 2.2 show that both the frequencies observed

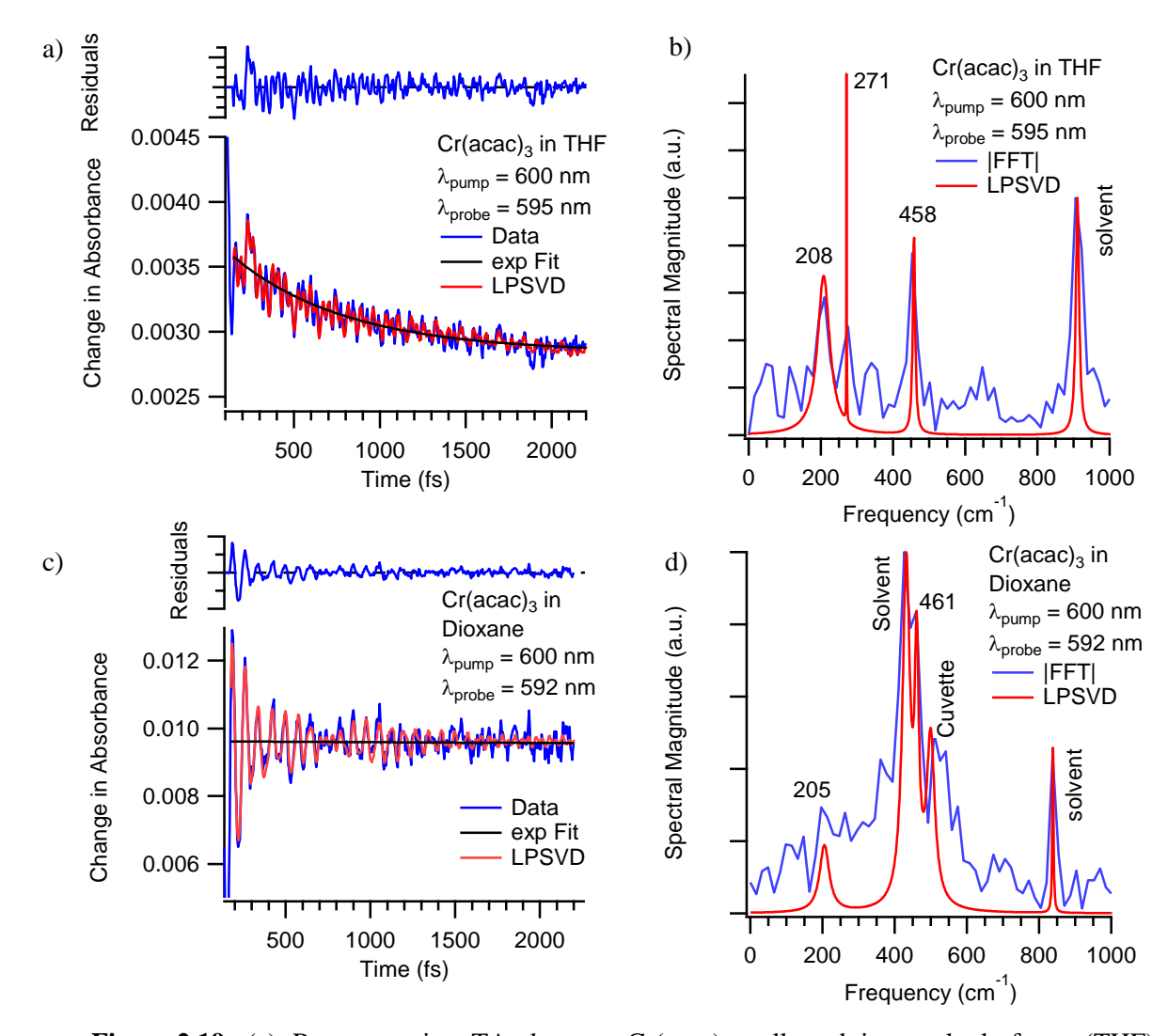


**Figure 2.19.** (a) Representative TA data on Cr(acac)<sub>3</sub> collected in tetrahydrofuran (THF) following 600 nm excitation while monitoring at the red edge of the excited state absorption feature. (b) Corresponding FFT and LPSVD analyses. (c) Analogous data collected in 1,4-dioxane and (d) corresponding |FFT| and LPSVD vibrational spectra. It is possible that the 271 cm<sup>-1</sup> band in part b is a vibrational mode of THF. The ~500 cm<sup>-1</sup> component in part d can be attributed to the glass of the cuvette.

and their corresponding dephasing times are relatively insensitive to both the probe wavelength and the choice of solvent and hence were combined when reporting averages and error bars. Representative datasets in acetonitrile can be seen in Figure 2.18 and in 1,4-dioxane and tetrahydrofuran in Figure 2.19. It is important to note that a ~500 cm<sup>-1</sup> oscillatory component with a ~200 fs damping time was observed in several datasets irrespective of the solvent used. In Foszcz's work, <sup>12</sup> a similarly rapidly damped ~500 cm<sup>-1</sup> oscillatory component was observed and assigned as a vibrational mode of Cr(acac)<sub>3</sub>. Because DFT

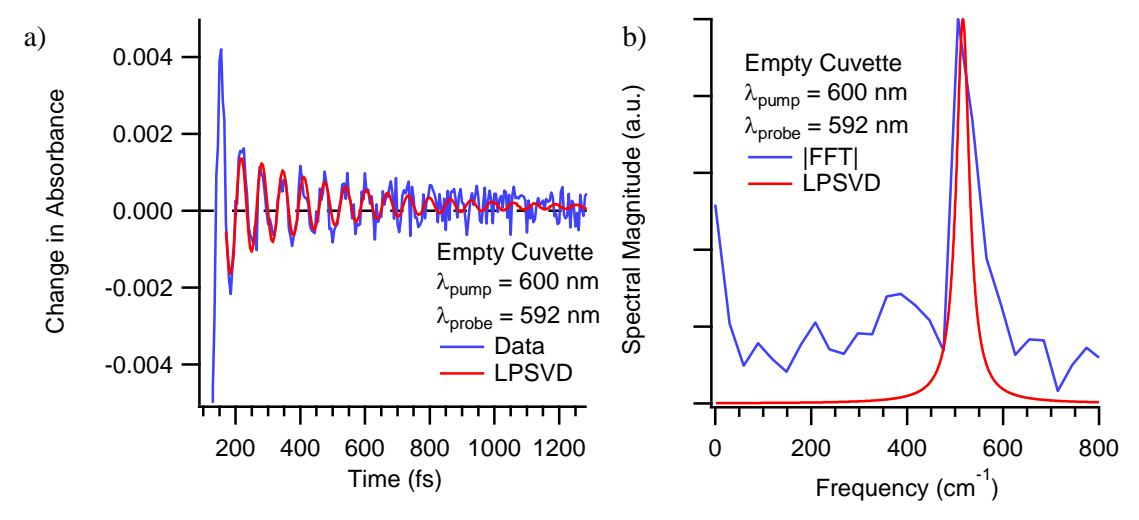


**Figure 2.20.** (a) TA data collected on an empty 1 mm glass cuvette. The observed coherent oscillations are assigned to ground state vibrational coherence in the cuvette itself. (b) Fast Fourier transform and LPSVD spectrum of the coherent oscillations of (a), showing a  $\sim$  500 cm<sup>-1</sup> component.

calculations on the ground electronic state did not show any frequencies around 500 cm<sup>-1</sup> this was assigned to a vibrational mode on the  ${}^4T_2$  excited state. TA data collected on an empty glass cuvette (Figure 2.20), however, show a ~500 cm<sup>-1</sup> oscillatory component, prompting a reassignment of this mode to vibrational coherence in the cuvette itself generated by off-resonant impulsively stimulated Raman scattering. Work by Furukawa and coworkers also show an intense Raman band in the range of 400-600 cm<sup>-1</sup> of silica based glasses that is assigned to a stretching/bending mode across bridging Si-O-Si oxygens.<sup>34</sup> It should also be noted that the 271 cm<sup>-1</sup> mode in the THF dataset in Table 2.2. and Figure 2.19 may be due to a vibrational mode of the solvent. Both DFT calculations and frequency domain Raman experiments on neat THF show a vibrational mode in this frequency region.

In addition to the 270cm<sup>-1</sup> and 500 cm<sup>-1</sup> modes discussed above, a cautionary note should also be placed upon the 95 cm<sup>-1</sup> frequency listed in Table 2.2. Given the presence of multiple oscillatory components superimposed on population dynamics in this system, it can often be difficult to acquire a perfect exponential fit of the data. Typically, incorrectly fit exponential decays show a fit line that oscillates both above and below the data itself appearing as a low frequency oscillatory component. Additionally, given that this mode is damped out at a similar timescale to the period of the oscillation, it may be the case

that this component was picked up by the LPSVD program to compensate for a poor exponential fit at early times. Because of the ambiguities associated with sub-100 cm<sup>-1</sup> oscillatory components, it is sometimes recommended to ignore them or take extra care to ensure exponential fitting is accurate.<sup>35</sup>

In addition to the difficulties associated with the often low-amplitude of the oscillatory features associated with vibrational coherences in a TA spectrum, the numerous sources of oscillatory components to the data sets as outlined above highlight the need for caution when interpreting results. As such, the remainder of the discussion will focus on vibrational modes that appear most robustly in the data. Inspection of Table 2.2. clearly indicates that the 193 and 461 cm<sup>-1</sup> vibrational modes appear most routinely, and hence will be the focus of analysis.

The lower frequency  $193 \text{ cm}^{-1}$  mode observed here is likely a more accurate value of the frequency observed originally by Schrauben<sup>10</sup> and shows good agreement with the value obtained by Foszcz<sup>12</sup>. The dephasing time observed in this study  $(350 \pm 130 \text{ fs})$  is also significantly longer than reported originally  $(70 \text{ fs})^{10}$ , however it is still substantially shorter than the ~ps dephasing times typically thought of for vibrational coherences. The 461 cm<sup>-1</sup> mode, on the other hand, shows a dephasing time  $(1130 \pm 500 \text{ fs})$  that fits well with traditional values for vibrational co herences. The observation of these modes in the TA experiments is complemented by their inclusion in the resonance Raman spectrum featured in Figure 2.21

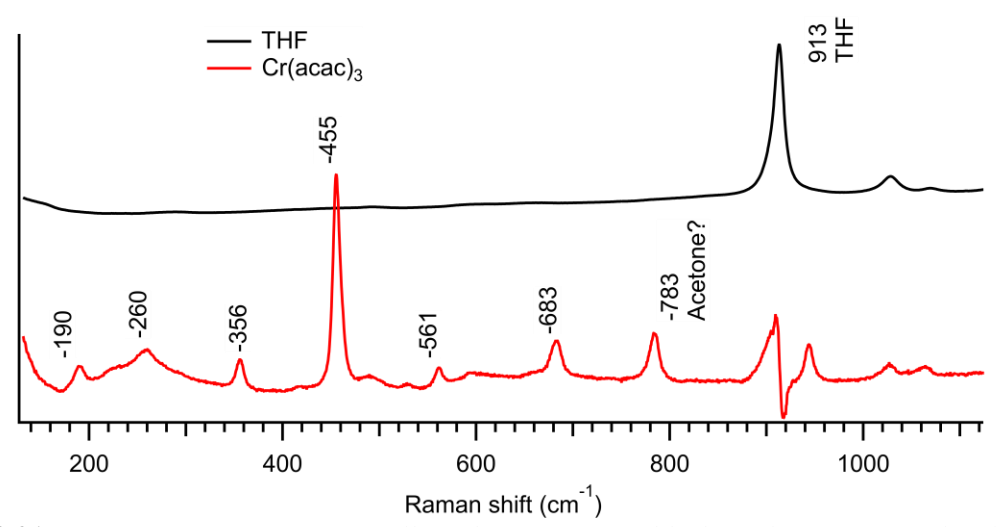


**Figure 2.21.** Resonance Raman spectra collected on neat THF (black) and  $Cr(acac)_3$  (red). The solvent background was subtracted from the  $Cr(acac)_3$  dataset. The 488 nm excitation source is resonant with the blue edge of the  ${}^4A_2 \rightarrow {}^4T_2$  transition.

which was collected on the Proshlyakov group instrument at Michigan State University by professor Proshlyakov.. By tuning the excitation source in the Raman experiment to be in resonance with the  ${}^4A_2 \rightarrow {}^4T_2$  absorption band, the ground state vibrational modes that are coupled to that transition will be selectively enhanced. Because these modes are strongly coupled to the interconfigurational  ${}^4A_2 \rightarrow {}^4T_2$  transition, it makes sense that they may also be coupled to the interconfigurational  ${}^4T_2 \leftrightarrow {}^2E$  transitions.

We can gain further insight into the dephasing mechanisms for the vibrational modes of Cr(acac)<sub>3</sub> by looking at the linewidth of the peaks in the resonant Raman spectrum. The linewidth of the peaks in the Raman spectra are linked to vibrational dephasing times via a Fourier transform relationship resulting in the relationship shown in equation 2.5.

$$\Delta v \Delta \tau = \frac{1}{\pi}$$
 2.5

where  $\Delta v$  is the full width at half maximum of the fit to the Raman peak and  $\Delta \tau$  is the dephasing time for that mode. The lineshape is often described using Kubo's stochastic lineshape theory. This assumes that the distribution of solvent environments from which the oscillator can be found induce a gaussian spread in vibrational frequency. The fluctuation of the vibrational energy gap can then be described by two parameters, a fluctuation magnitude,  $\Delta$ , and an effective fluctuation frequency,  $\Delta$ . The corresponding lineshape function becomes (equation 2.6)

$$g(t) = \left(\frac{\Delta}{\Lambda}\right)^{2} \left[\exp(-\Lambda t) + \Lambda t - 1\right]$$
 2.6

with coherence decay described as  $\exp[-g(t)]$ . When fluctuations are slow relative to the fluctuation magnitude,  $\exp[-g(t)]$  is approximately gaussian and inhomogeneously broadened, thus containing little dynamical information. In the fast modulation limit  $(\Lambda \gg \Delta)$  where thermal fluctuations rapidly allow each oscillator to sample the distribution of frequencies, the coherences decay exponentially as an ensemble producing a Lorentzian lineshape.<sup>36,37</sup> In the present experiment the ~460 cm<sup>-1</sup> peak in the Cr(acac)<sub>3</sub> Raman spectrum fits well to a Lorentzian lineshape despite being convolved with a estimated ~4.2 cm<sup>-1</sup> square wave pulse due to the experimental setup. Because of this, the fast modulation limit, i.e. exponential

coherence decay, is likely a reasonable approximation. A Lorentzian can also be fit to the  $\sim 190 \text{ cm}^{-1}$  peak, however the smaller amplitude of the signal in concert with the jagged background make it more difficult to get a reliable width. The homogeneous dephasing times ( $T_2$ ) for coherences produced in the Raman and TA experiments can now be described more specifically using the form seen in equation 2.4. Since the Raman experiment produces a coherence between the first excited vibrational level and a nondecaying ground state, the homogeneous dephasing time is described as seen in equation 2.7.

$$\frac{1}{T_2} = \frac{1}{2T_1} + \frac{1}{T_2^*}$$
 2.7

The form of the homogeneous dephasing relation for excited state coherence in our system requires some slight modification due to the additional sources of population decay present within this system. Here, coherences may decay from both electronic and vibrational population relaxation. Furthermore, since the excitation transition is Laporte-forbidden and because the initial excited state is strongly displaced relative to the ground state, it requires that each portion of the superposition state is initially vibrationally excited. If we assume a uniform vibrational and electronic relaxation time for each vibronic level, the homogeneous dephasing time for excited state vibrational coherences in our system can be described by equation 2.8,

$$\frac{1}{T_2} = \frac{1}{T_{1,elec}} + \frac{1}{T_{1,vib}} + \frac{1}{T_2^*}$$
 2.8

where  $T_{1,elec}$  and  $T_{1,vib}$  describe electronic and vibrational population relaxation times respectively.

With equations 2.7 and 2.8 in hand, we can now begin to parse out the origins of dephasing for the vibrational modes of Cr(acac)<sub>3</sub> by comparing dephasing times of the ground state vibrational modes obtained with the frequency domain, Raman, experiment and the dephasing times measured on an excited electronic state obtained with the time domain, TA, experiment. Before proceeding, however, it is worthwhile to test how well the frequency and time domain experiments agree. To do this, we can compare the ground state dephasing time of a solvent vibrational mode calculated from the linewidth in the Raman spectrum and measured directly using TA. Figure 2.22 illustrates this approach with the 913 cm<sup>-1</sup> symmetric ring breathing mode of tetrahydrofuran. A Lorentzian fit to the peak in the Raman spectrum shows a FWHM

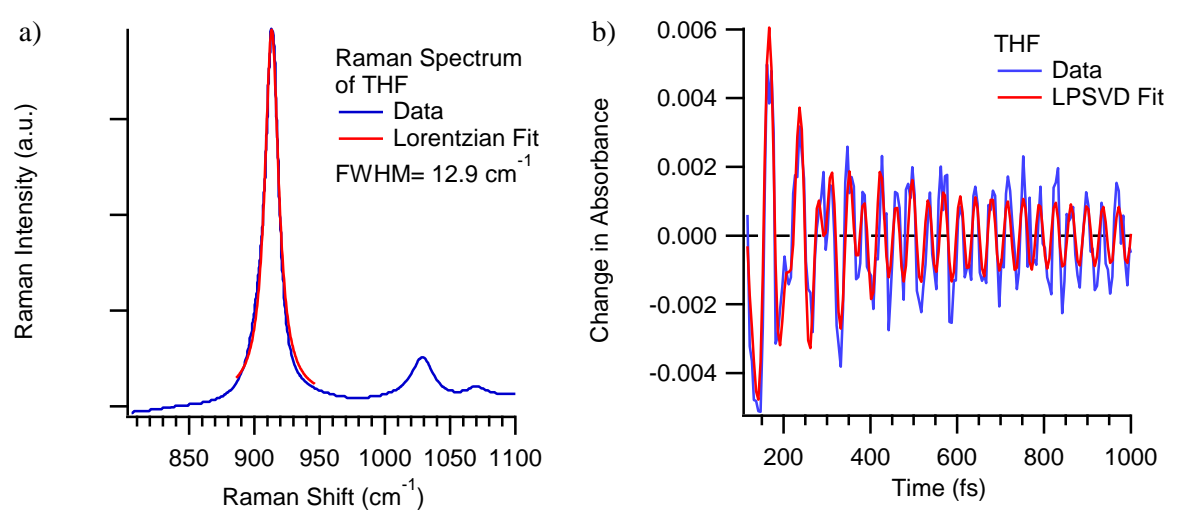


**Figure 2.22.** (a) Raman spectrum of neat tetrahydrofuran (blue) with 488 nm excitation source. A Lorentzian fit to a band centered at 913 cm<sup>-1</sup> (red) shows a FWHM of 12.9 cm<sup>-1</sup> corresponding to a dephasing time of  $820 \pm 30$  fs. (b) TA data on neat THF with 600 nm excitation source and 584 nm probe (blue) along with LPSVD fit of the dataset (red). The average dephasing time measured with four datasets is  $950 \pm 140$  fs.

of  $12.9 \pm 0.4$  cm<sup>-1</sup> corresponding to a dephasing time of  $820 \pm 30$  fs according to equation 2.5. In the time domain, dephasing times in the neat solvent for a  $913 \pm 6$  cm<sup>-1</sup> oscillatory component were  $950 \pm 140$  fs. While dephasing times are not perfectly in sync between the time and frequency domain measurements, they are still within error of each other and suggest that this approach may be valid for a sufficiently well resolved peak in the Raman spectrum.

With the method established, we can begin investigating the dephasing mechanism of the 461 cm<sup>-1</sup> mode of Cr(acac)<sub>3</sub> with ~1 ps damping time (Table 2.2). Due to the differences in kinetic assignments between the initial ultrafast visible pump visible probe experiments conducted by the McCusker group<sup>7</sup> and the visible pump IR probe experiments performed by Kunttu and coworkers<sup>13,14</sup> we must proceed with some degree of caution. Although it has been established that the kinetic model described by Kunttu and coworkers is most likely the more appropriate model, it can still be beneficial to see how the current results fit into both kinetic models. Thus, the following analyses will be based on several different permutations of kinetic assignments between these studies. First, we consider the case in which vibrational relaxation in the doublet excited state is described by a 1.1 ps time constant as assigned originally by the McCusker group (Case 1). Here, the agreement between the dephasing time observed in the TA experiment

and the vibrational relaxation time suggest that dephasing in the excited state is largely determined by vibrational relaxation and further that the electronic population relaxation corresponding to  ${}^{2}E \rightarrow {}^{4}A_{2}$ conversion on the nanosecond timescale and pure dephasing do not significantly contribute. The comparable  $1.25 \pm 0.02$  ps homogeneous dephasing time suggested by the  $8.5 \pm 0.1$  cm<sup>-1</sup> Raman linewidth for this mode (Figure 2.C.1) and the differences in equations 2.7 and 2.8, however, suggest that either the pure dephasing time significantly decreases or that the vibrational relaxation time approximately halves (i.e. that vibrational relaxation in the ground electronic state becomes faster). Both scenarios are considered unlikely. In the second case to consider (Case 2), we will use the vibrational relaxation time constants measured by Kunttu and coworkers<sup>14</sup> using the more structurally sensitive IR probe. Here, we use vibrational relaxation times of 7 and 12 ps for the excited and ground electronic states respectively and an electronic relaxation time on the order of a nanosecond describing  ${}^{2}E \rightarrow {}^{4}A_{2}$  conversion. Again, in this scenario,  $T_{1,elec}$  is too large to contribute to the observed dephasing time in the excited electronic state. Here, the slower vibrational relaxation implies that the bulk of the dephasing occurs via  $T_2^*$  with a time constant of 1.3 ps in agreement with the standard observation that most dephasing in liquids is due to pure dephasing.<sup>33</sup> Furthermore, this agrees well with the 1.2 ps dephasing time calculated for the Raman experiment using the same  $T_2^*$  as determined above and a 12 ps vibrational relaxation time and it also matches the  $1.25 \pm 0.02$  ps dephasing time determined experimentally from the Raman linewidth. Because of this, Case 2 seems to by a likely hypothesis. Finally, in Case 3, we must consider the alternative assignment for the 1.1 ps kinetic component suggested by the Kunttu group 14 and corroborated with the full spectrum dataset shown in the previous section to be  ${}^{4}T_{2} \rightarrow {}^{4}A_{2}$  IC. Here, we will again assume 7 and 12 ps vibrational relaxation times in the excited and ground states respectively. In this scenario, we must consider the possibility of coherence loss due to fast electronic population relaxation from the 1.1 ps IC. The inclusion of this as a significant relaxation pathway implies that the bulk of the dephasing seen for this mode in the TA experiment is due to  $T_{l,elec}$  from IC and that the pure dephasing is much slower as is the case for Case 1. This again yields similar problems when comparing to the Raman estimated dephasing time as in Case 1 and thus suggests that IC is not a very prevalent decay pathway following excitation into

the  ${}^4T_2$  state. Case 2 is thus considered the most likely evaluation of the dephasing mechanism for this vibrational mode, namely the bulk of the dephasing is due to 1.3 ps pure dephasing processes within the  ${}^2E$  excited state.

In principle, a similar analysis can be conducted on the ~190 cm<sup>-1</sup> vibrational mode. Due to the significantly lower amplitude of this peak in the Raman spectrum and the significant distortion of the spectral shape from the background signal, the conclusions from this analysis would be tentative at best. Attempts to fit this feature to a Lorentzian profile resulted in a  $10.1 \pm 0.9$  cm<sup>-1</sup> FWHM corresponding to a  $1.05 \pm 0.1$  ps dephasing time. While the results of this fitting are included for the sake of transparency, an analysis is omitted due to the potential errors associated with the fitting process.

Next, using density functional theory (DFT) calculations, we can start to acquire a better idea of the nature of each vibrational mode observed in the TA experiments and further define the type of motions active during the ISC process. It is important to reiterate that the vibrational modes in Cr(acac)<sub>3</sub> are predominantly sampled from the <sup>2</sup>E state which has the same electron configuration as the ground state and as such, is expected to have similar vibrational frequencies. The vibrational modes calculated for the ground electronic state should thus serve as an adequate substitute for vibrational modes in the excited state of Cr(acac)<sub>3</sub> and simplify the calculations. On the basis of frequency matching the 193 cm<sup>-1</sup> and 461 cm<sup>-1</sup>

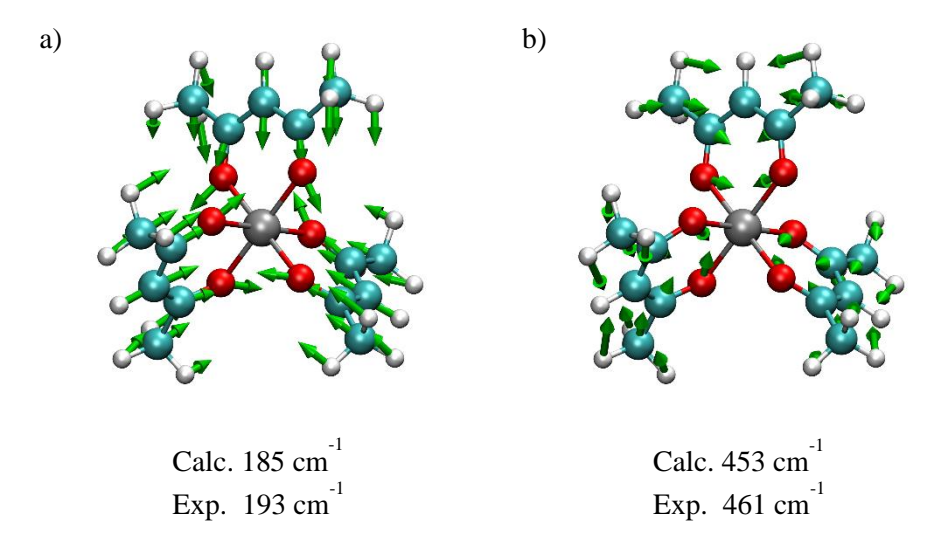


**Figure 2.23.** Nuclear deformations associated with the 193 cm<sup>-1</sup> (a) and 461 cm<sup>-1</sup> (b) vibrational modes of Cr(acac)<sub>3</sub>.

modes can be assigned to the pair of metal-ligand bond stretching vibrations calculated at 185 and 453 cm<sup>-1</sup> (Figure 2.23). Given the sigma antibonding character of the initially generated <sup>4</sup>T<sub>2</sub> state and the significant displacement along these types of coordinates on the  ${}^{4}T_{2} \rightarrow {}^{2}E$  trajectory it also makes intuitive sense that these modes involve significant distortion of the metal-ligand bond distance. These also match the assignments from Schrauben<sup>10</sup> and Foszcz<sup>12</sup> for these vibrational modes. In the lower frequency 193 cm<sup>-1</sup> mode the entire ligand pushes toward the metal center while the two oxygen atoms splay outwards. In the 461 cm<sup>-1</sup> mode, each ligand compresses to make a smaller footprint and decrease the bite angle of the ligand. The distance between the metal center and the central carbon atom on each acac ligand is largely unchanged. Furthermore, because neither of these vibrational modes involve the oxygen atoms moving directly towards the metal center, but rather involve the change in bight angle to some degree, there is also a small torsional element to each of these vibrational modes. The simplest way to view this torsional element is to view each vibrational mode along the  $C_3$  rotation axis as shown in Figure 2.23. If a triangle is formed with each of the three oxygen atoms nearest to the observer at a vertex and a separate triangle is formed with the three oxygen atoms furthest from the observer, it can be seen from the displacement vectors that the oxygen atoms that form each triangle are displaced such that each triangle is rotated in a different direction, i.e. the triangles are rotated so that they approach eclipsing. This torsional element is likely a result of tethering the oxygen atoms together.

It seems likely that a twisting motion would be effective in relaxing the Laporte selection rule and thus enhance the efficiency of an interconfigurational d-d transition. Indeed, evidence of the importance of torsional motion in transition metal complexes has been observed in several systems. Endicott and coworkers have shown trigonal twisting distortions to facilitate  ${}^2E \rightarrow {}^4A_2$  ISC in octahedral Cr(III) complexes.  ${}^{38,39}$  Additionally, Purcell has proposed that Bailar and Ray-Dutt twisting deformations may be involved in the racemization dynamics of  $[Fe(phen)_3]^{2+}$  (where phen = 1,10-ortho-phenanthroline) by expediting  ${}^1A_1 \leftrightarrow {}^5T_2$  ISC.  ${}^{40}$  These results were supported theoretically by Vanquickenborne and Pierloot who used the angular overlap model to show Bailar and Ray-Dutt twisting motions are coupled to spin state conversion in strong field six coordinate Fe(II) species  ${}^{41}$  and experimentally by McCusker  ${}^{et}$   ${}^{al}$   ${}^{42}$  who

showed that  ${}^{1}A_{1} \leftrightarrow {}^{5}T_{2}$  conversion is tied to mobility about the  $C_{3}$  rotation axis in a series of Fe(II) spin crossover compounds. Finally, Hörner and coworkers have shown that both trigonal twisting and ligand breathing motions are coupled to the  ${}^{1}A_{1} \leftrightarrow {}^{5}T_{2}$  conversion in constrained spin crossover Fe(II) systems.  ${}^{43}$  Conclusions on  $Cr(acac)_{3}$ 

The previous two sections focusing on Cr(acac)<sub>3</sub> have answered several of the open questions brought up at the end of the summary of previous results. By analysis of the visible pump visible probe TA data following 400 nm excitation into the high energy <sup>4</sup>T<sub>1</sub> state, it was shown that vibrational relaxation is not occurring with a 1 ps time constant as was originally reported by the McCusker group,<sup>7</sup> but rather a mechanism proposed by Kunttu and coworkers<sup>14</sup> involving back-intersystem crossing followed by internal conversion is more appropriate. Two coherently active symmetric metal-ligand bond stretching vibrations were observed in single wavelength TA data following excitation into the <sup>4</sup>T<sub>2</sub> excited state. The 461 cm<sup>-1</sup> mode with 1130 fs dephasing time was shown to dephase by a pure dephasing mechanism on the <sup>2</sup>E excited state. The following sections will seek to clarify what effects various substitutions on the acac ligand have on the photophysical dynamics following excitation into the <sup>4</sup>T<sub>2</sub> excited state with an emphasis on characterizing the coherent nuclear motions of each compound. This work will first investigate the dynamics of a series of Cr(acac<sup>3</sup>)<sub>3</sub> derivatives which have been substituted in the 3-position of the acac backbone. Presumably, since substitutions in this position can couple into the pi-system of the acac ligand,

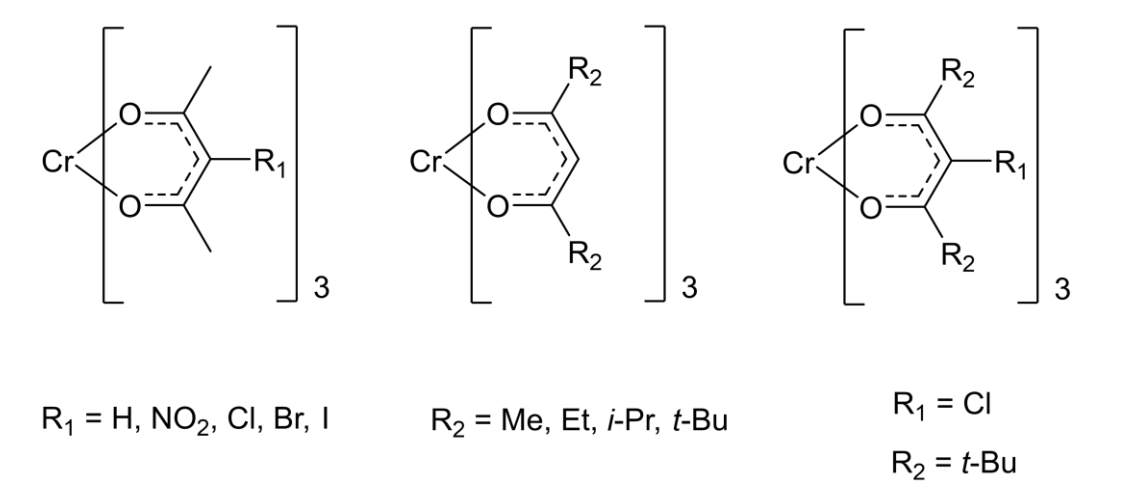


**Figure 2.24.** Drawing of the Cr(acac')<sub>3</sub> derivatives to be studied in this report.

this should afford a glimpse into the effect of electronic perturbations to the coherently active vibrational modes in this system. Additionally, since the report of Schrauben  $et\ al.^{10}$  proposed that the sterically encumbered t-butyl substitution had major photophysical ramifications, a series of increasingly sterically hindered molecules, building up to the t-butyl substituted acac will be studied. Finally, a molecule with both an electronic and a steric perturbing substitution will be investigated. A full list of the molecules studied in this chapter can be seen in Figure 2.24.

3-Substituted Derivatives of Cr(acac)<sub>3</sub>

# 2.4.2. Cr(3-NO<sub>2</sub>ac)<sub>3</sub>

The photophysical characterization of  $Cr(3-NO_2ac)_3$  was conducted in the dissertation work of previous McCusker group member Joel Schrauben<sup>15</sup> and the full spectrum transient absorption data from his work can be seen in Figure 2.11. The 1.65 ps narrowing and shifting of the transient spectrum was originally assigned to vibrational relaxation on the  $^2E$  state, however in light of the more recent work of Kunttu and coworkers<sup>14</sup> conducted after Joel's initial investigation and the results discussed above, we can reassign this as  $^4T_2 \rightarrow ^4A_2$  IC following bISC from the  $^2E$  state similar to the mechanism described for the unsubstituted parent compound. The remainder of the discussion for this compound will be centered around the coherent vibrational dynamics. The coherent vibrational modes of  $Cr(3-NO_2ac)_3$  are summarized in Table 2.3, with example datasets shown in Figure 2.25. Interestingly, now only a single coherent vibrational

**Table 2.3.** Summary of the coherent vibrational modes of  $Cr(3-NO_2ac)_3$  following  ${}^4A_2 \rightarrow {}^4T_2$  excitation. All measurements performed in Dioxane used 4 and 0.4  $\mu J$  pump and probe pulses respectively while the THF measurement employed 4.7 and 0.5  $\mu J$  pump and probe pulses. The dioxane and THF experiments had 40 and 35 fs IRFs respectively.

Pump (probe), nm	Solvent	Frequency, cm <sup>-1</sup> (Damping Time, fs)
600 (608)	Dioxane	151 (178)
600 (600)	Dioxane	153 (182)
600 (600)	Dioxane	146 (192)
600 (600)	Dioxane	151 (203)
600 (592)	Dioxane	149 (184)
600 (592)	Dioxane	145 (193)
600 (592)	THF	154 (171)
Average Frequency	, cm <sup>-1</sup>	150
Standard Deviation,	, cm <sup>-1</sup>	3
Average Damping Ti	ime, fs	186
Standard Deviation	n, fs	11

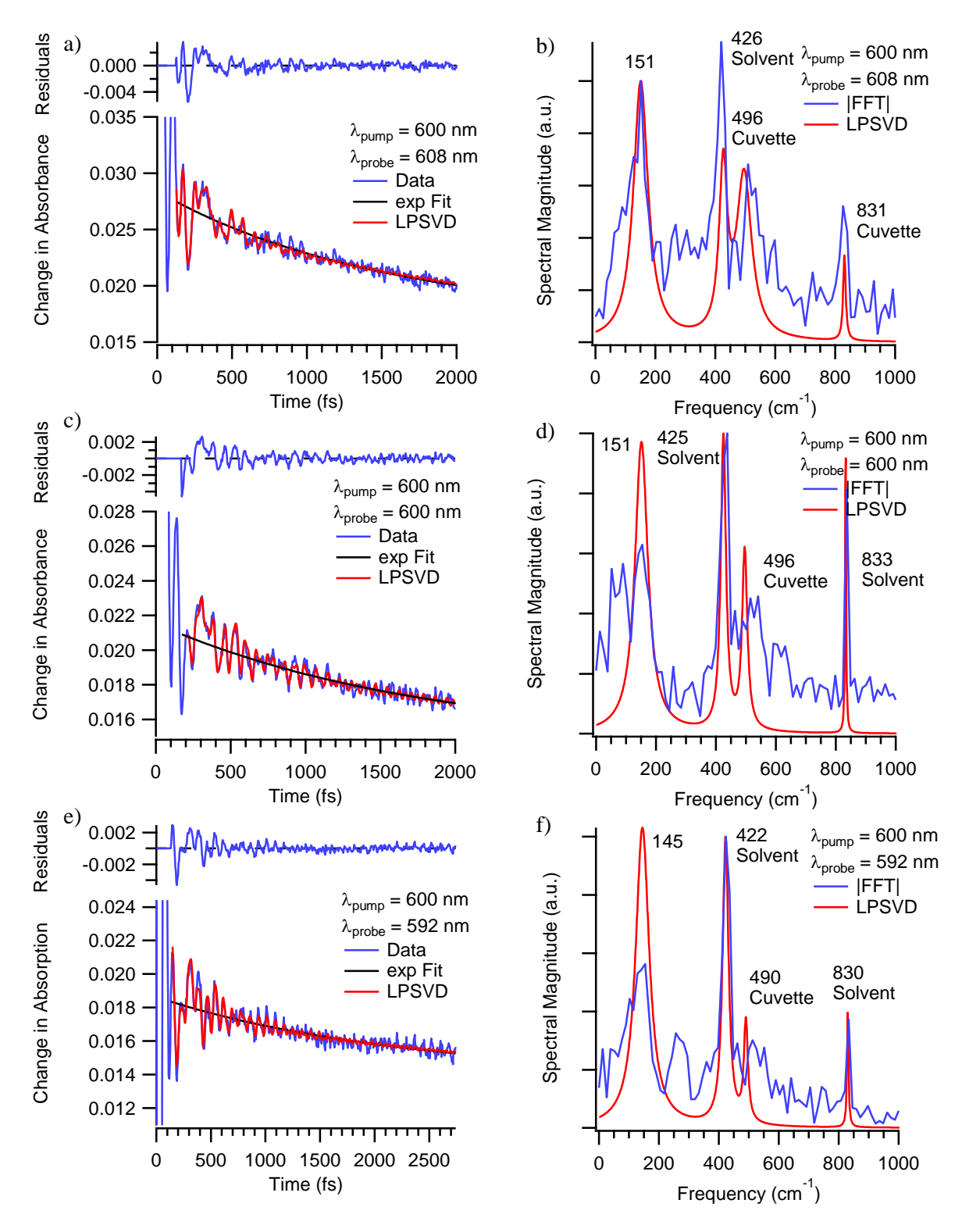


**Figure 2.25.** Representative TA data on  $Cr(3-NO_2ac)_3$  following 600 nm excitation into the  ${}^4T_2$  state in 1,4-dioxane while monitoring a 4 nm slice of the probe spectrum at (a) 608 nm, (c) 600 nm, and (e) 592 nm. FFT and LPSVD analyses corresponding to the (b) 608 nm, (d) 600 nm, and (f) 592 nm data sets.

mode is observed with a 150 cm<sup>-1</sup> frequency and 186 fs dephasing time, the latter of which is much shorter than the 350 fs dephasing time of the low frequency, 193 cm<sup>-1</sup> mode, of Cr(acac)<sub>3</sub>. At this point it is difficult to speculate why this might be so. The rapid dephasing time observed both here and in the parent Cr(acac)<sub>3</sub> molecule certainly fit with the hypothesis that rapid dephasing times may indicate involvement of a vibrational mode in an ultrafast change in electronic state, however there is simply not enough evidence at present to confirm this. It is just as plausible that this mode undergoes rapid intramolecular vibrational redistribution similar to what was observed for Cr(acac)<sub>3</sub> by Kunttu and coworkers.<sup>14</sup> In this light, the faster dephasing time here could be rationalized in terms of the loose bolt effect<sup>44</sup>. Here, the nitro group may be expected to rattle and rapidly dissipate energy akin to a loose bolt on a moving part of a machine. At this point, both explanations seem plausible, so any further judgement must wait until more evidence is gained from the other substituted Cr(acac')<sub>3</sub> systems.

To visualize the 150 cm<sup>-1</sup> mode of  $Cr(3-NO_2ac)_3$  we can again turn to density functional theory calculations. In the parent  $Cr(acac)_3$  we were able to confirm that the 461 cm<sup>-1</sup> mode was observed in the  $^2E$  excited state and could only speculate that the 193 cm<sup>-1</sup> mode was as well. Given that the  $^2E$  excited state and the  $^4A_2$  ground state have the same  $(t_{2g})^3$  orbital population, the geometry and vibrational frequencies are likely very similar between the two states. Thus, the frequency calculation for this compound was

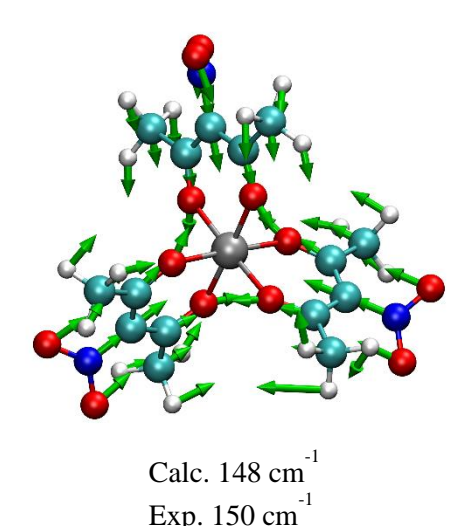
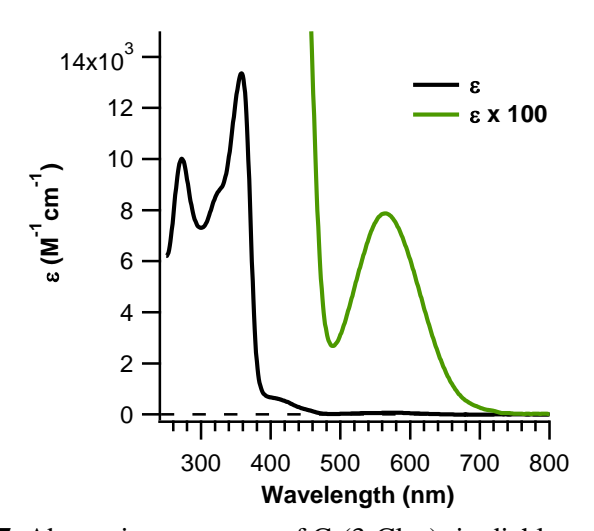


Figure 2.26. Nuclear deformation associated with the 150 cm<sup>-1</sup> vibrational mode of Cr(3-NO<sub>2</sub>ac)<sub>3</sub>.

performed on the ground electronic state for ease of computation. These calculations reveal a 148 cm<sup>-1</sup> metal ligand stretching vibration in good agreement with the  $150 \pm 4$  cm<sup>-1</sup> frequency observed in the TA experiments. A picture of this vibrational mode can be seen in Figure 2.26. This vibrational mode is essentially identical to the 193 cm<sup>-1</sup> mode of the Cr(acac)<sub>3</sub> control molecule suggesting that this particular vibration is essential for producing the geometric changes associated with  ${}^4T_2 \leftrightarrow {}^2E$  conversion.

#### 2.4.3. Cr(3-Clac)<sub>3</sub>



**Figure 2.27.** Absorption spectrum of Cr(3-Clac)<sub>3</sub> in dichloromethane.

Cr(3-Clac)<sub>3</sub> forms light brown needle like crystals. The ground state absorption spectrum for this compound can be seen in Figure 2.27. The  ${}^4A_2 \rightarrow {}^4T_2$  absorption band (564 nm, 79 M<sup>-1</sup>cm<sup>-1</sup>) is only slightly redshifted from the 560 nm maximum in Cr(acac)<sub>3</sub>, <sup>15</sup> consistent with the increased  $\pi$ -basicity of the chlorosubstituted ligand raising the energy of the  $t_{2g}$  orbital set and thus marginally decreasing the ligand field strength of the compound by ~125 cm<sup>-1</sup>. Based on analogous assignments on Cr(acac)<sub>3</sub>, the bands centered at 272 and 358 nm can be assigned to an intraligand  $\pi \rightarrow \pi^*$  transition and a LMCT type transition respectively. <sup>15</sup>

Early time full spectrum TA data on  $Cr(3-Clac)_3$  following 600 nm excitation into red edge of the  ${}^4A_2 \rightarrow {}^4T_2$  ground state absorption band can be seen in Figure 2.28 along with the decay associated difference spectra (DADS) and evolution associated difference spectra (EADS) resulting from a global fit of the full spectrum data to a sequential biexponential decay using OPTIMUS fitting software. This data

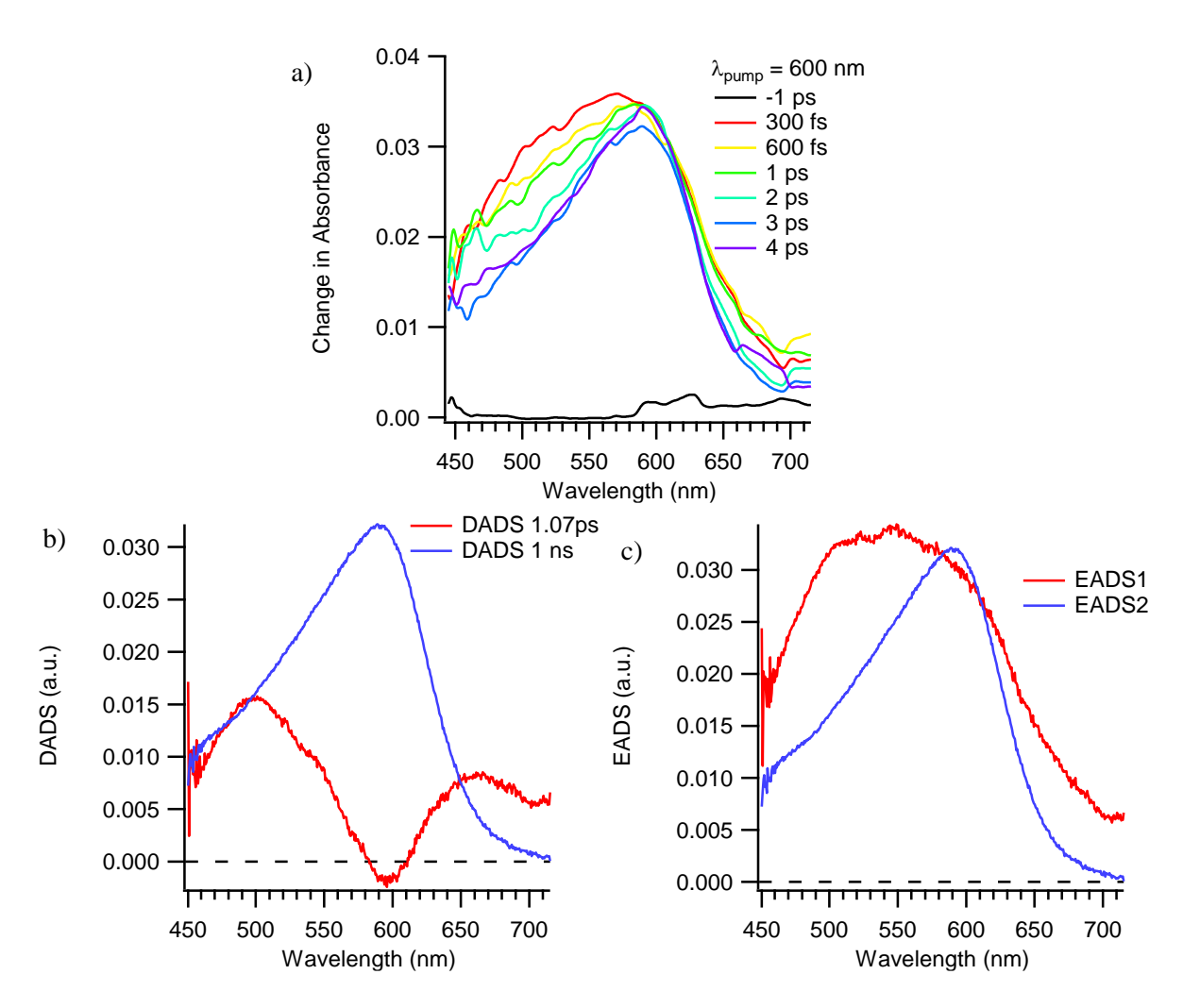


**Figure 2.28.** (a) Early time full spectrum TA data on  $Cr(3-Clac)_3$  in toluene following 600 nm excitation into the  ${}^4T_2$  state. (b) Decay associated difference spectrum (DADS) associated with the global fit of the TA data to a sequential biexponential decay. The long-time offset was modeled by fixing a 1 ns exponential decay to describe the slower ground state recovery process. (c) Evolution associated difference spectra (EADS) associated with the global fit.

set shows a clear decay in the blue and red edges of the transient absorption band similar to what was observed for the unsubstituted  $Cr(acac)_3$  parent molecule. Global fitting of the data to two sequentially decaying kinetic components reveals a 1.07 ps kinetic component responsible for the spectral changes at early times (Figure 2.28 b), again similar to what was observed for  $Cr(acac)_3$ . Given the similar kinetics and observations between the two compounds, the ~1.1 ps kinetic component of  $Cr(3-Clac)_3$  can also be assigned primarily to  ${}^4T_2 \rightarrow {}^4A_2$  IC following ISC and bISC. The EADS, describing the transient spectra before and after the 1.1 ps process is complete, can be seen in Figure 2.28 c. EADS2 resembles the transient

spectrum at longer delays and hence shows the spectrum of the <sup>2</sup>E excited state. At early times, there is an equilibrium between the <sup>2</sup>E and <sup>4</sup>T<sub>2</sub> states and hence EADS1 is representative of a superposition of the transient spectra of the <sup>2</sup>E and <sup>4</sup>T<sub>2</sub> excited states. EADS1 is also quite flat, reminiscent of the DADS observed following 400 nm excitation of Cr(acac)<sub>3</sub>, supporting the assessment that both excited state populations are present at early times.

Single wavelength datasets can be seen in Figure 2.29. Here, the datasets probing at 490 and 550 nm, representing the blue edge of the transient absorption band, show an average time constant of 1.24  $\pm$  0.07 ps, in good agreement with the full spectrum fit and quite similar to the time constant observed in

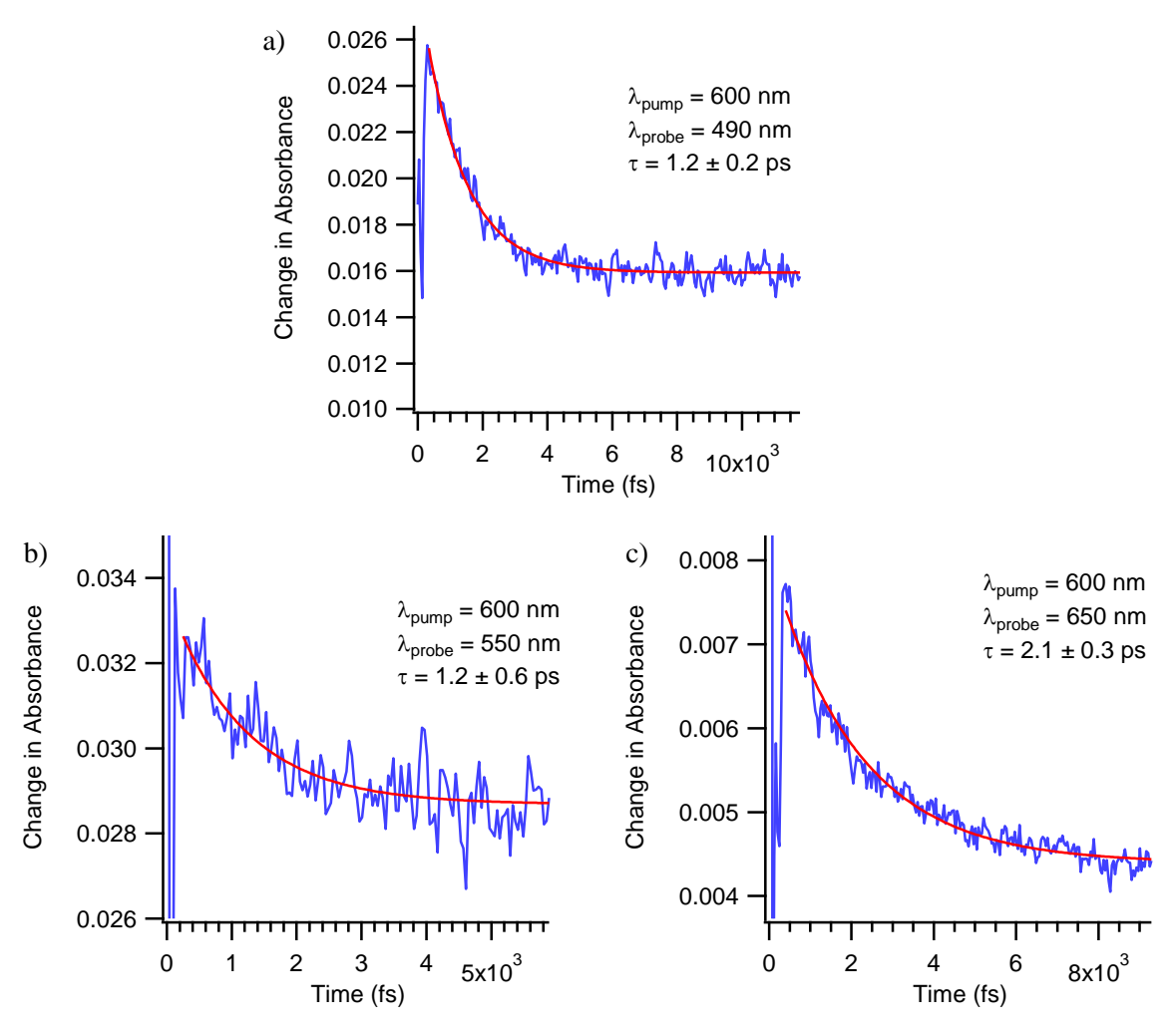


**Figure 2.29.** Representative single wavelength TA data on  $Cr(3-Clac)_3$  in toluene following 600 nm excitation into the  ${}^4T_2$  state while monitoring at (a) 490 nm, (b) 550 nm, and (c) 650 nm. The two bluer wavelengths show ~1.2 ps fits while the 650 nm probe data may show additional dynamics.

the unsubstituted Cr(acac)<sub>3</sub> compound. A single exponential fit of the 650 nm probe data (Figure 2.29 c) showed a longer time constant compared to the other two probe wavelength regions. A biexponential fit of the data looked better and gave 850 fs and 4.8 ps time constants which are reminiscent of the internal conversion and vibrational cooling time constants of Cr(acac)<sub>3</sub>, however considering the quality of the data, it is difficult to say whether a biexponential fit is appropriate. Given the larger amplitude decay in the bluer portion of the spectrum, however, the time constants observed at 490 nm and 550 nm are likely more representative of the timescale for IC.

Coherent oscillations of Cr(3-Clac)<sub>3</sub> were observed in a similar manner as the previously studied compounds. A summary of the results collected in toluene can be seen in Table 2.4 and representative datasets can be seen in Figure 2.30. The low frequency modes that were picked up during the LPSVD analysis of two of the datasets in Table 2.4 were included for the sake of transparency, however, it is expected that they are present to correct for poor exponential fitting of the LPSVD program and do not represent anything physically meaningful. Additionally, a 449 cm<sup>-1</sup> oscillatory component was observed in a single dataset. It is possible that this corresponds to a vibrational mode reminiscent of the 461 cm<sup>-1</sup> mode of Cr(acac)<sub>3</sub>, however, since it was only observed once, it is not worth spending too much time speculating over. Clearly the most robustly observed vibrational mode of these data is the 149 cm<sup>-1</sup> mode with 1100 fs

**Table 2.4.** Summary of observed coherent vibrational modes of  $Cr(3-Clac)_3$  in toluene following excitation into the  ${}^4T_2$  state. The sub-100 cm<sup>-1</sup> oscillatory components picked up by the LPSVD fitting program were included for transparency, however, they are likely due to poor exponential fitting of the data and not to coherent vibrational motion. All experiments employed 4 and 0.4  $\mu$ J pump and probe pulses respectively with a 45 fs IRF.

Pump (probe)	Frequency, cm <sup>-1</sup> (Damping Time, fs)					
600 (608)			144 (873)	449 (581)		
600 (608)	45 (-13640)	93 (5450)	150 (953)			
600 (600)	65 (32560)		149 (1100)			
600 (600)			150 (1224)			
600 (592)			151 (1426)			
600 (592)			149 (1015)			
600 (584)			151 (1100)			
Average Frequency, cm <sup>-1</sup>			149			
St	andard Deviation, cm	2				
	Average Damping, fs	1100				
	Standard Deviation, fs	180				

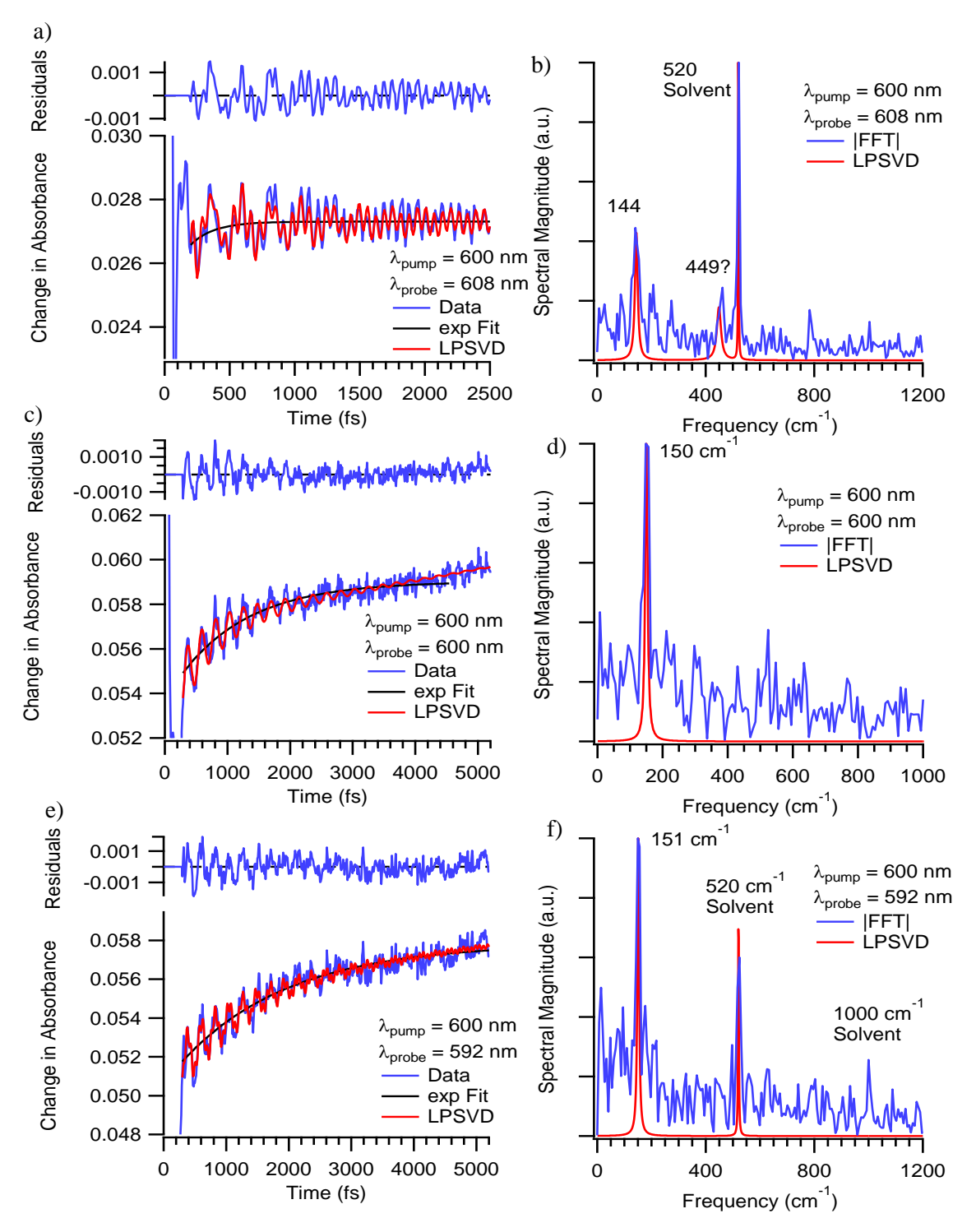
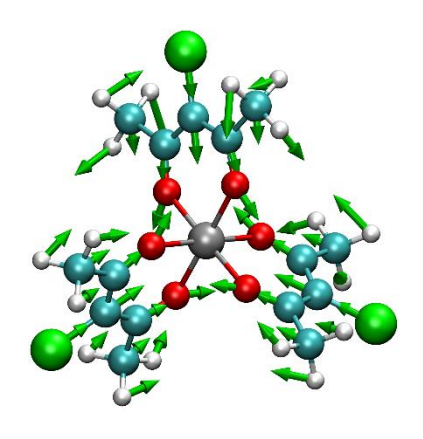


**Figure 2.30.** Representative TA traces and FFT and LPSVD analyses of coherent oscillations of Cr(3-Clac)<sub>3</sub> in toluene following excitation into the  ${}^{4}T_{2}$  state. Coherent oscillations were monitored at (a) 608 nm, (c) 600 nm, and (e) 592 nm. Corresponding FFT and LPSVD vibrational spectra are shown in (b), (d), and (f).



Calc: 153 cm<sup>-1</sup> Exp: 149 cm<sup>-1</sup>

**Figure 2.31.** Nuclear deformations associated with the 149 cm<sup>-1</sup> vibrational mode of Cr(3-Clac)<sub>3</sub>.

dephasing time. DFT frequency calculations on the ground electronic state show a 153 cm<sup>-1</sup> symmetric metal ligand breathing mode (Figure 2.31) similar to the 193 cm<sup>-1</sup> mode observed for Cr(acac)<sub>3</sub>. It is interesting that each of the three compounds discussed thus far appear to exhibit identical excited state decay mechanisms with the same coherent nuclear motion yet there is a wide range of dephasing times. This suggests that the dephasing times may not be as strong of an indicator of the involvement of a vibrational mode in an ultrafast photophysical transformation as was suggested by the hypothesis derived from Joel Schrauben's work. A more complete discussion of the implications of these dephasing times will be provided after the presentation of each of the 3-substituted compound results

# 2.4.4. Cr(3-Brac)<sub>3</sub>

General photophysical characterizations of Cr(3-Brac)<sub>3</sub> were conducted in the dissertation work of Joel Schrauben,<sup>15</sup> and the early time full spectrum TA data from his work can be seen in Figure 2.11a. As such, only work pertaining to the early time dynamics of this compound will be reported here. To start, another full spectrum TA dataset was obtained, which can be seen in Figure 2.32a with the DADS and EADS resulting from a sequential biexponential global fit using OPTIMUS<sup>22</sup> fitting software. The TA data are qualitatively similar to that collected by Joel on the same compound (Figure 2.11a)<sup>15</sup> and the TA data on Cr(acac)<sub>3</sub> (Figure 2.3).<sup>7</sup> Additionally, the global fit returned a ~1 ps kinetic component responsible for

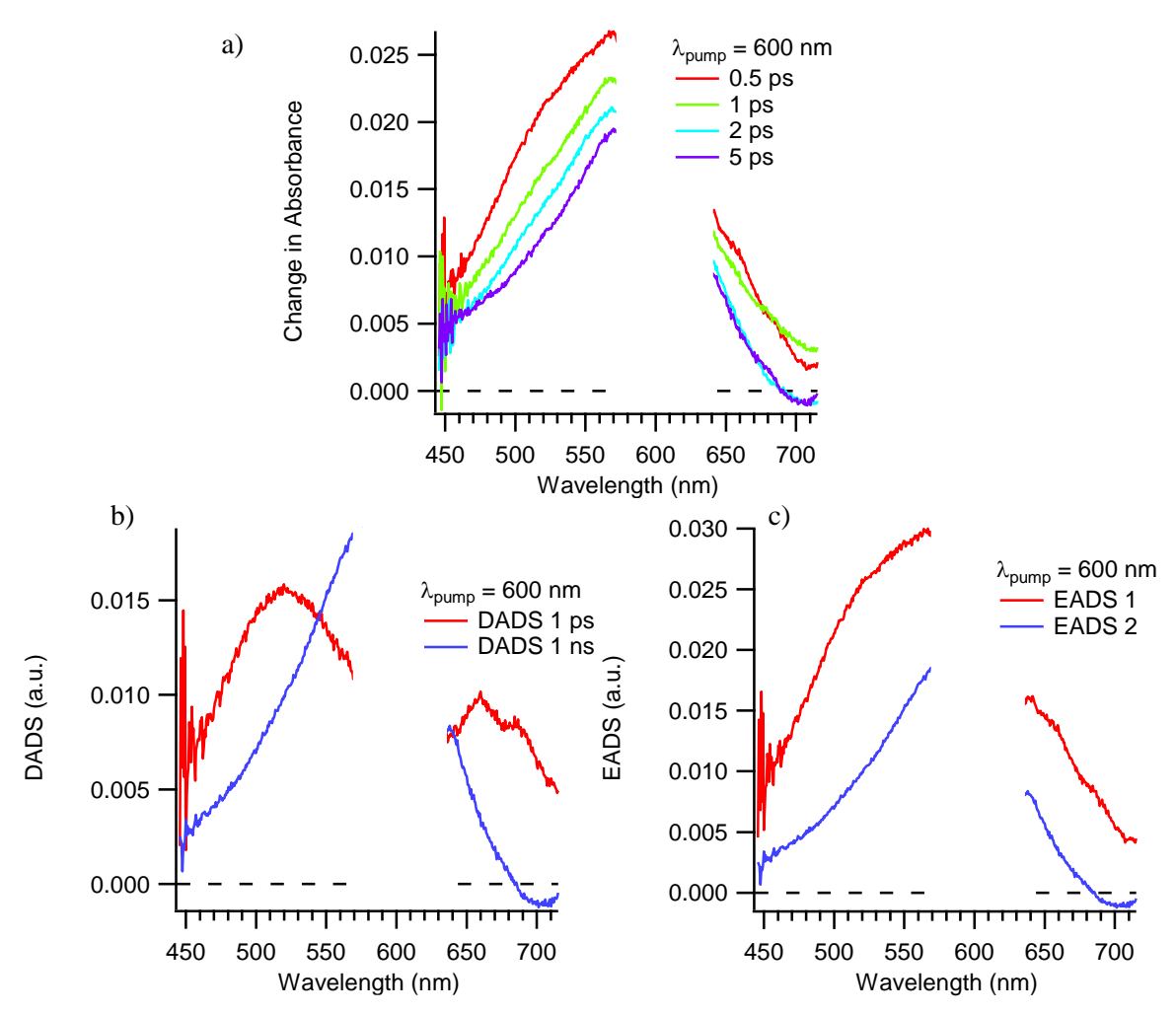


**Figure 2.32.** (a) Early time full spectrum TA data on Cr(3-Brac)<sub>3</sub> in toluene following 600 nm excitation into the <sup>4</sup>T<sub>2</sub> state. The 570-630 nm spectral region was omitted due to large contamination from pump scatter. (b) Decay associated difference spectrum (DADS) associated with the global fit of the TA data to a sequential biexponential decay. The long-time offset was modeled by fixing a 1 ns exponential decay to describe the slower ground state recovery process. (c) Evolution associated difference spectra (EADS) associated with the global fit.

the decay in the blue and red edges of the transient absorption spectrum. It is again evident from the qualitatively identical spectral evolution and kinetics that  $Cr(3-Brac)_3$  undergoes a similar decay mechanism as the  $Cr(acac)_3$  parent molecule involving rapid ISC/bISC and that the ~1 ps kinetic component can be attributed laregely to  ${}^4T_2 \rightarrow {}^4A_2$  IC.

In addition to the full spectrum dataset just discussed, the kinetics were also investigated using single wavelength measurements to get a more precise view of the time constants associated with excited state decay. Representative datasets can be seen in Figure 2.33. While the fits on the blue edge of the

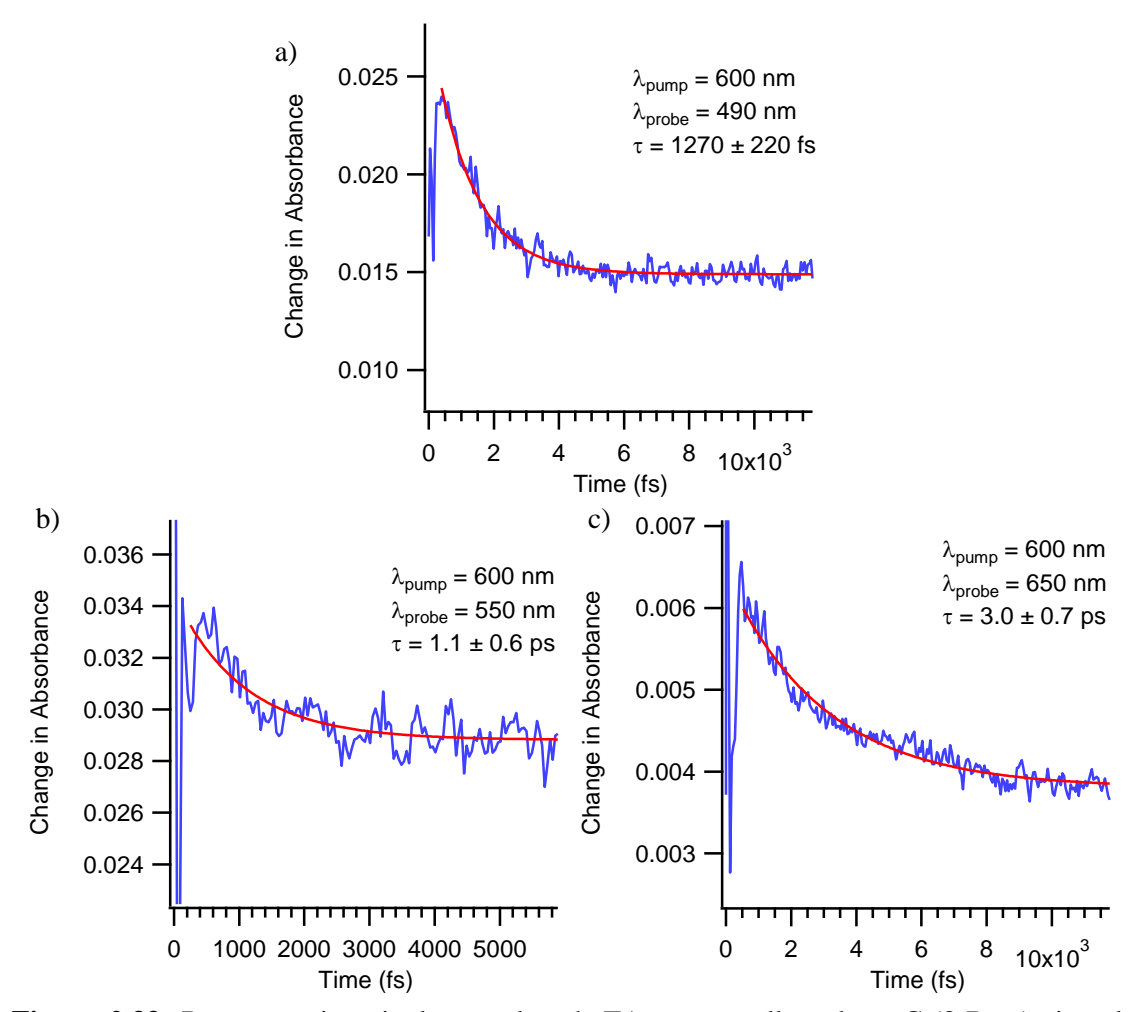


**Figure 2.33.** Representative single wavelength TA traces collected on  $Cr(3-Brac)_3$  in toluene following excitation into the  ${}^4T_2$  state and monitoring at (a) 490 nm, (b) 550 nm, and (c) 650 nm.

transient spectrum show similar time constants, the fit of the 650 nm probe data shows a time constant that is quite different and a does not match the data as well. A biexponential fit of the 650 nm data (not shown) produces a better fit to the data and produces ~1 and 6 ps time constants similar to the internal conversion and vibrational relaxation time constants measured for  $Cr(acac)_3$ .<sup>14</sup> Just like in the  $Cr(3-Clac)_3$  650 nm probe dataset (Figure 2.29c) it may be the case that more than one process is contributing to the spectral evolution here. Without higher quality data in this region, however, it is difficult to say with certainty, thus the 650 nm probe datasets will not be included in the averaging. The average time constant for  ${}^4T_2 \rightarrow {}^4A_2$  IC measured at 490 nm and 550 nm probe wavelengths is  $1.2 \pm 0.1$  ps, which is again, very similar to each of the previously discussed members of the series.

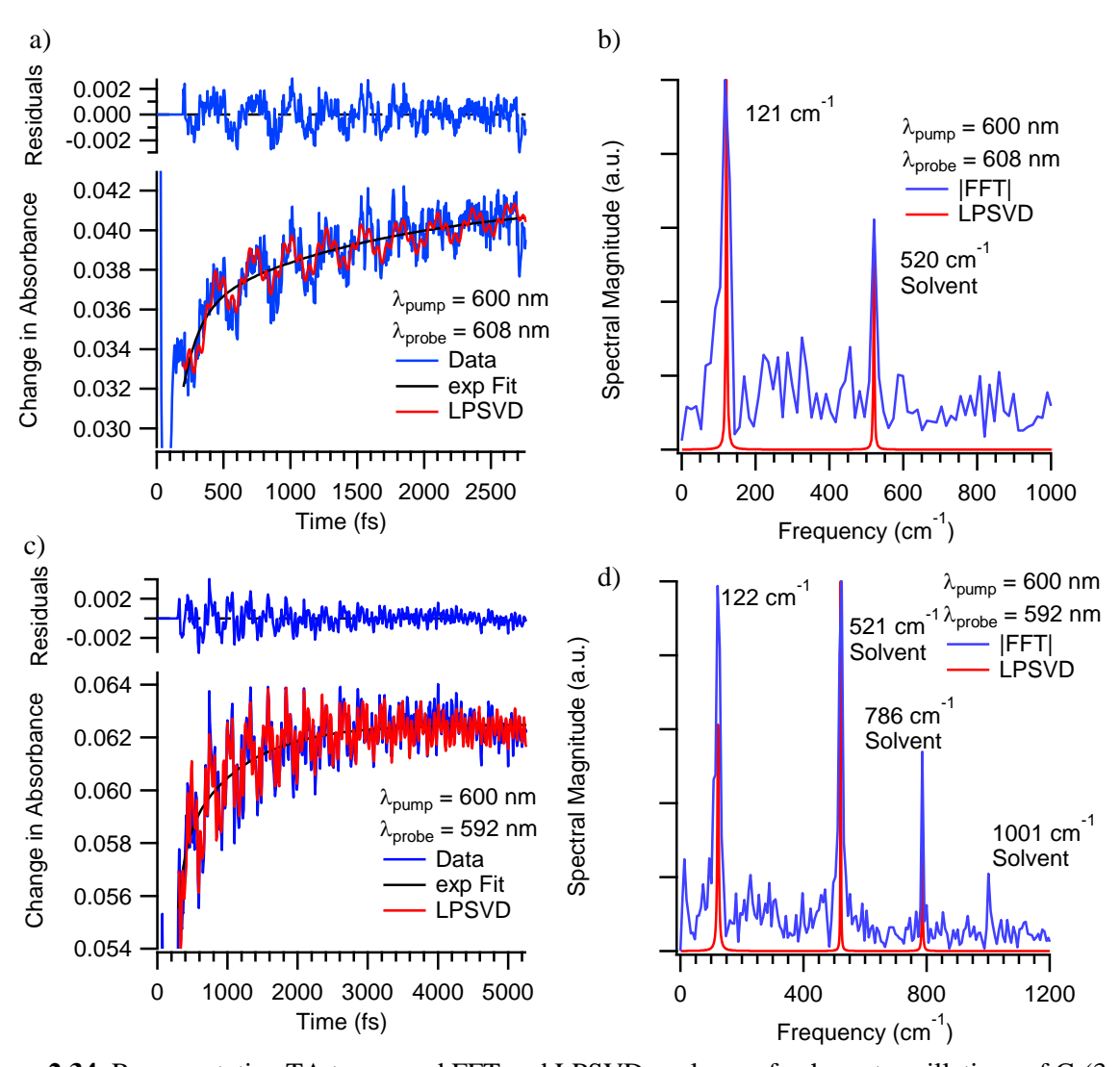
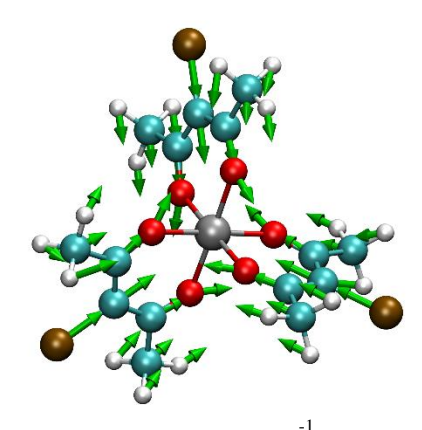


**Figure 2.34.** Representative TA traces and FFT and LPSVD analyses of coherent oscillations of  $Cr(3-Brac)_3$  in toluene following excitation into the  ${}^4T_2$  state. Coherent oscillations were monitored at (a) 608 nm and (c) 592 nm. Corresponding FFT and LPSVD vibrational spectra are shown in (b) and (d).

Next, we can turn to the coherent dynamics of  $Cr(3-Brac)_3$ . Table 2.5 summarizes the coherent vibrational modes of  $Cr(3-Brac)_3$  observed in toluene and dichloromethane following 600 nm excitation into the  ${}^4T_2$  state. In addition, representative datasets can be seen in Figure 2.34. Both show a single solute-attributable oscillation with a  $123 \pm 1$  cm<sup>-1</sup> frequency and a  $2.5 \pm 0.3$  ps dephasing time. DFT calculations on the ground electronic state show a 122 cm<sup>-1</sup> symmetric breathing mode (Figure 2.35) akin to the low frequency mode observed in the  $Cr(acac)_3$  control molecule.

**Table 2.5.** Summary of the coherent oscillations of  $Cr(3-Brac)_3$  following excitation into the  ${}^4T_2$  state. Experimental parameters such as pump and probe wavelengths and pulse energies as well as IRF FWHMs are also included for each experiment.

$\lambda_{pu}$ , nm (E <sub>pu</sub> , $\mu$ J)	$\lambda_{pr}$ , nm (E <sub>pr</sub> , $\mu$ J)	IRF, fs	Solvent	Frequency, cm <sup>-1</sup> (Damping Time, fs)
600 (4.7)	608 (0.5)	35	Toluene	121 (2780)
600 (5)	608 (0.5)	45	Toluene	122 (1390)
600 (3.3)	600 (0.4)	55	Toluene	125 (2580)
600 (4.7)	592 (0.5)	35	Toluene	123 (2450)
600 (3.3)	592 (0.4)	55	Toluene	122 (2040)
600 (3.3)	600 (0.4)	55	DCM	123 (2920)
600 (5)	600 (0.4)	40	DCM	122 (3610)
Av	verage Frequency,	123		
St	andard Deviation,	1		
Ave	erage Damping Tir	2500		
S	Standard Deviation	300		



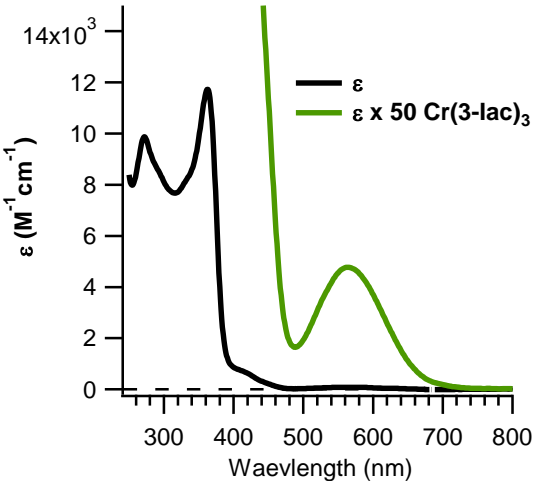
Calc: 122 cm Exp: 123 cm

Figure 2.35. Nuclear deformations associated with the 123 cm<sup>-1</sup> vibrational mode of Cr(3-Brac)<sub>3</sub>.

On an experimental note, this compound tended to crash out where the laser hit the sample. None of the presented results are expected to be greatly affected, however, care had to be taken to prevent a buildup of precipitate reducing the amount of light transmitted through the sample. This was achieved by careful consideration of how many data points to include in each scan as well as physically translating the cuvette after each scan.

## 2.4.5. $Cr(3-Iac)_3$

 $Cr(3\text{-Iac})_3$  forms light brown needle like crystals. The ground state absorption spectrum for this compound can be seen in Figure 2.36. The  ${}^4A_2 \rightarrow {}^4T_2$  absorption band (564 nm, 95  $M^{\text{-1}}\text{cm}^{\text{-1}}$ ) is redshifted



**Figure 2.36.** Absorption spectrum of Cr(3-Iac)<sub>3</sub>.

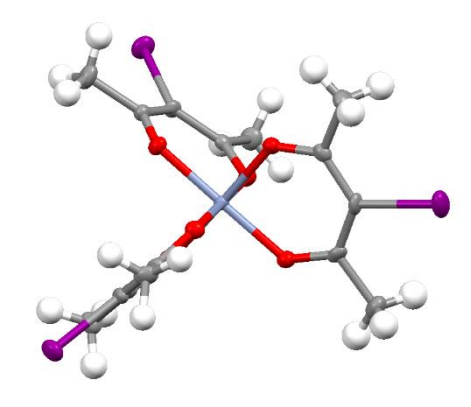


**Figure 2.37.** Crystal Structure of Cr(3-Iac)<sub>3</sub> collected by Sara Adelman and solved by Professor Richard Staples of Michigan State University.

from the 560 nm maximum of  $Cr(acac)_3$  by the same amount as the  $Cr(3\text{-Clac})_3$  analogue. Given the similarity in the remaining spectral features to those in  $Cr(3\text{-Clac})_3$ , we can again assign the bands centered at 272 and 363 nm to an intraligand  $\pi \to \pi^*$  transition and an LMCT type transition respectively. The redshift of the LMCT transition relative to the chloro-substituted derivative suggest that the iodo-group is a better  $\pi$ -donor. A crystal structure of  $Cr(3\text{-Iac})_3$  was also obtained (Figure 2.37.) and solved by group member Sara Adelman and Professor Richard Staples of Michigan State University. The coordinates can be found in the appendix.

Early time full spectrum TA data on  $Cr(3\text{-Iac})_3$  following 600 nm excitation into the red edge of the  $^4A_2 \rightarrow ^4T_2$  ground state absorption band can be seen in Figure 2.38 along with the decay associated difference spectra (DADS) and evolution associated difference spectra (EADS) resulting from a global fit of the full spectrum data to a sequential biexponential decay using OPTIMUS fitting software. This dataset again exhibits a decay in the blue edge of the spectrum similar to  $Cr(acac)_3$  and its derivatives that have already been discussed. The less apparent decay on the red edge of the spectrum is likely due to the smaller amplitude decay in that wavelength region in conjunction with the lower stability of the white light continuum in that wavelength region. Nevertheless, a decay on the red edge of the transient spectrum can be observed when using the more precise single wavelength measurements (Figure 2.39). Before

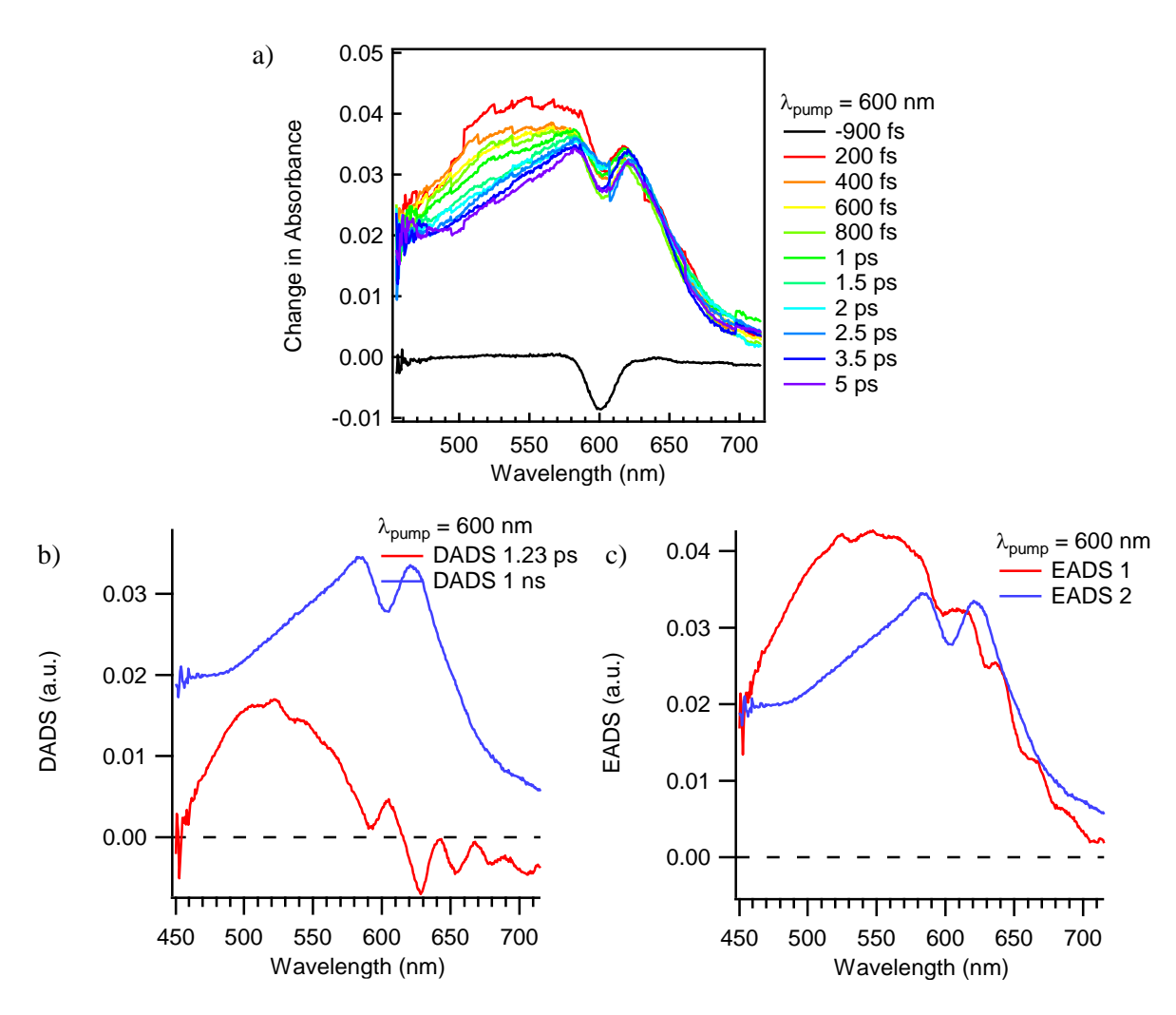


**Figure 2.38.** (a) Early time full spectrum TA data on  $Cr(3\text{-Iac})_3$  in toluene following 600 nm excitation into the  ${}^4T_2$  state. (b) Decay associated difference spectra (DADS) associated with the global fit of the TA data to a sequential biexponential decay. The long-time offset was modeled by fixing a 1 ns exponential decay to describe the slower ground state recovery process. (c) Evolution associated difference spectra (EADS) associated with the global fit. Distortions around 600 nm in the data, DADS, and EADS are due to residual pump scatter.

progressing to the single wavelength data, however, it is worth noting the 1.2 ps decay acquired from the global fit of the full spectrum TA data (Figure 2.38) which qualitatively matches both the unsubstituted  $Cr(acac)_3$  control molecule and each of its 3-substituted derivatives discussed previously. Like these other compounds, this 1.2 ps decay process can readily be assigned to  ${}^4T_2 \rightarrow {}^4A_2$  IC following equilibration of the  ${}^4T_2$  and  ${}^2E$  states.

Next, in search of a more precise measurement of the kinetics following  ${}^4A_2 \rightarrow {}^4T_2$  excitation, single wavelength experiments were performed. Representative datasets are shown in Figure 2.39 in which

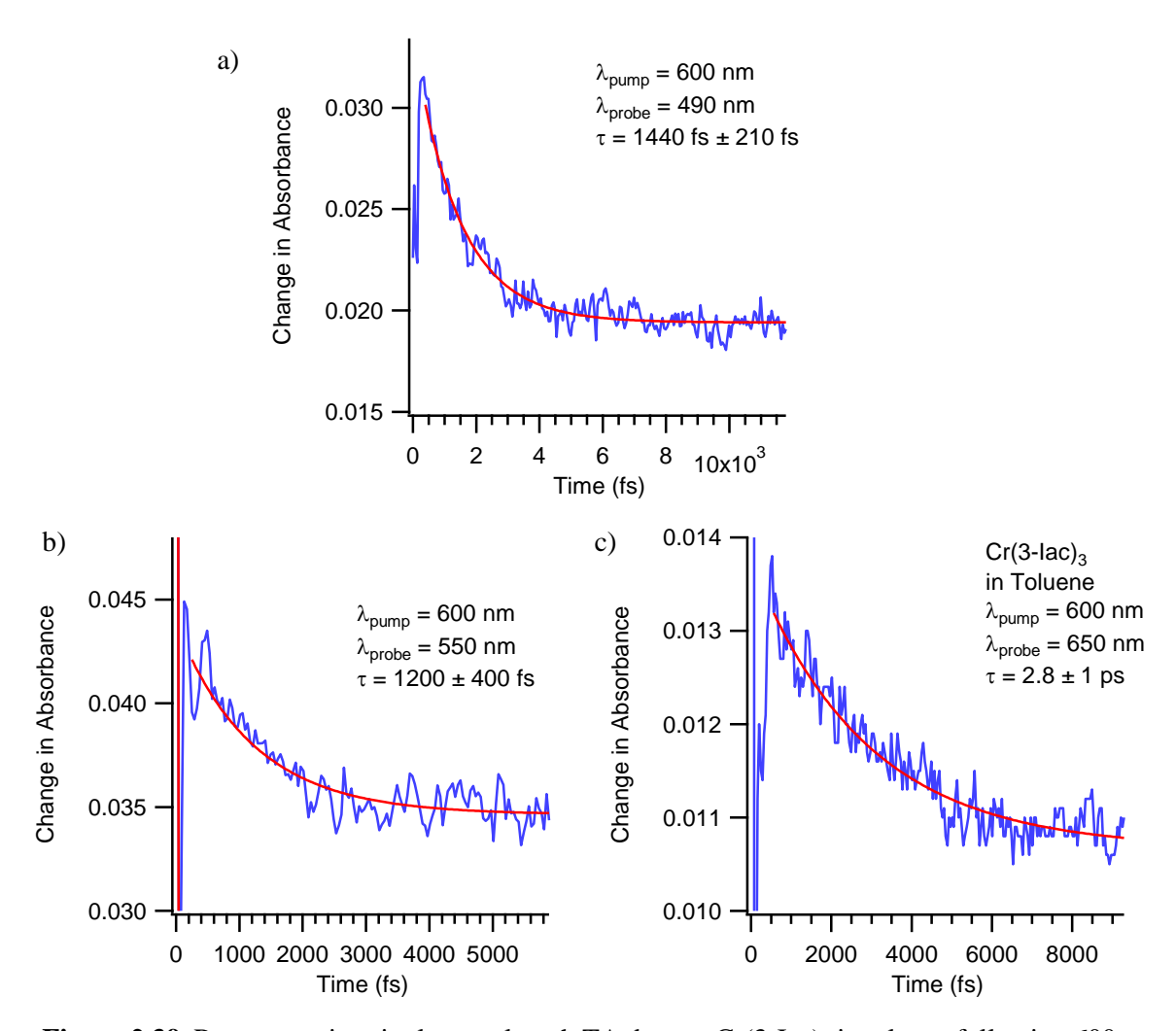


**Figure 2.39.** Representative single wavelength TA data on  $Cr(3-Iac)_3$  in toluene following 600 nm excitation into the  ${}^4T_2$  state while monitoring at (a) 490 nm, (b) 550 nm, and (c) 650 nm.

the decay was monitored on the blue and red wings of the transient spectrum. We again see that the kinetics measured on the blue edge of the transient spectrum appear somewhat different than on the kinetics measured on the red edge at 650 nm which appear slower. This situation was present for each of the halogen derivatives presented earlier. We will thus continue to ignore the kinetics monitored at 650 nm and report a time constant derived from the average of the 490 nm and 550 nm experiments. This results in a  $1.3 \pm 0.1$  ps time constant for  ${}^4T_2 \rightarrow {}^4A_2$  IC in good agreement with the results of the global fit of the full spectrum dataset and qualitatively similar to the remainder of the Cr(acac')<sub>3</sub> systems discussed thus far.

With an idea of the kinetics for population relaxation in hand we can next turn to the coherent vibrational dynamics in Cr(3-Iac)<sub>3</sub>. Table 2.6 summarizes the coherent oscillations of Cr(3-Iac)<sub>3</sub> following

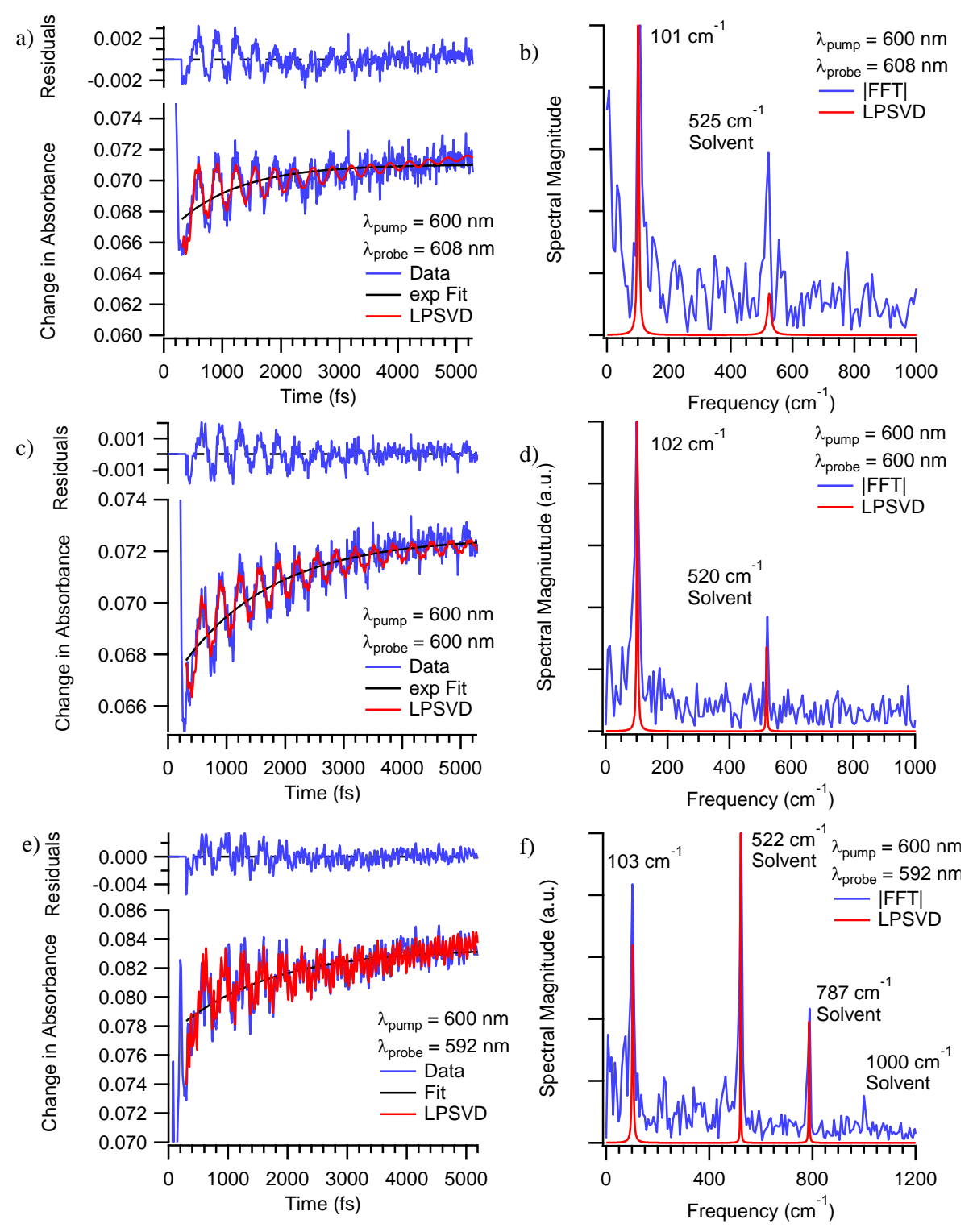


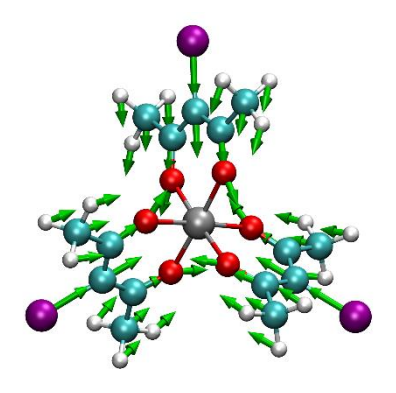
**Figure 2.40.** Representative TA traces and FFT and LPSVD analyses of coherent oscillations of  $Cr(3-Iac)_3$  in toluene following excitation into the  ${}^4T_2$  state. Coherent oscillations were monitored at (a) 608 nm, (c) 600 nm, and (e) 592 nm. Corresponding FFT and LPSVD vibrational spectra are shown in (b), (d), and (f).

**Table 2.6.** Summary of the coherent oscillations of  $Cr(3-Iac)_3$  following 600 nm excitation into the  ${}^4T_2$  state. Each measurement employed 4 and 0.4  $\mu J$  pump and probe pulse energies respectively with a 40 fs IRF.

Probe, nm	Probe, nm Solvent		Frequency, cm <sup>-1</sup> (Damping Time, fs)			
615	Toluene	55 (2060)	103 (3450)	204 (1420)		
608	Toluene		101 (1800)			
608	Toluene		100 (1780)			
600	Toluene		102 (2520)			
600	Toluene		103 (3090)			
592	Toluene		102 (2130)	181 (200)		
592	Toluene		103 (2020)			
600	DCM		96 (2190)			
Average Free	quency, cm <sup>-1</sup>	101				
Standard Dev	viation, cm <sup>-1</sup>	2				
Average Dam	ping Time, fs	2400				
Standard De	eviation, fs	600				

600 nm excitation into the  ${}^4T_2$  state and Figure 2.40 shows representative datasets. Clearly, the primary coherently active vibrational mode is a  $101 \pm 2$  cm<sup>-1</sup> vibration with a  $2.4 \pm 0.6$  ps dephasing time. This is readily apparent in the TA data provided in Figure 2.40 as a large amplitude oscillation that lasts for several picoseconds. On two occasions the LPSVD program picked up additional frequencies that were not observed in the neat solvent control experiment. Given the irreproducibility of these values it is highly unlikely that they correspond to actual solute vibrational modes. The 55 cm<sup>-1</sup> oscillatory component obtained during one experiment is likely due to poor exponential fitting of the LPSVD program. It is also possible that the ~200 cm<sup>-1</sup> component is a weakly Raman active out of plane bending mode of the methyl group of the toluene solvent.

We can again turn to density functional theory calculations to gain insight into the nature of this coherently active vibrational mode. And, just like the previous members of the 3-substituted series of  $Cr(acac')_3$  compounds, we can take advantage of the similarity of the electron distribution between the  $^4A_2$  and  $^2E$  ground and excited states and perform the frequency calculations on the more computationally accessible ground electronic state. The resulting  $102 \text{ cm}^{-1}$  calculated symmetric breathing mode (Figure 2.41) shows excellent agreement with the experimental  $101 \pm 1 \text{ cm}^{-1}$  frequency and is consistent with the vibrational modes observed for every member of the series thus far.



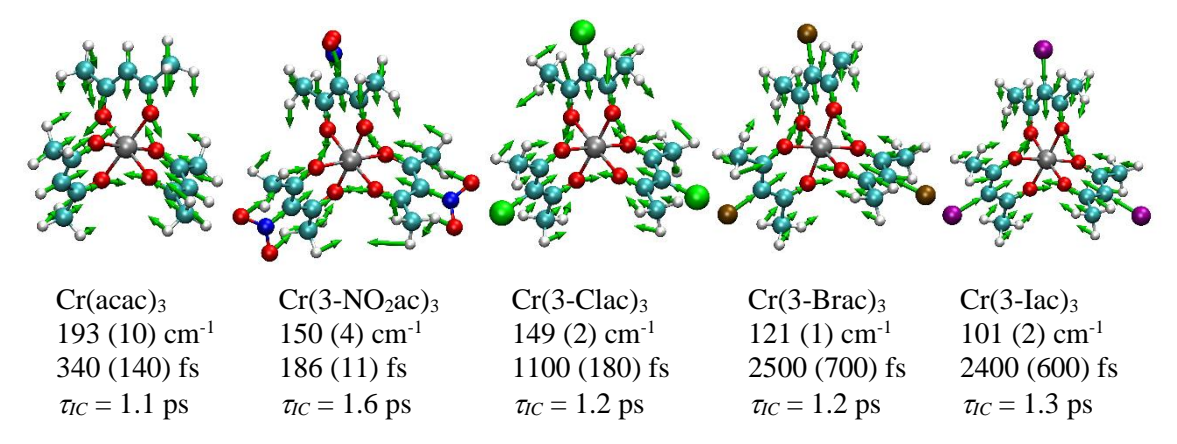
Calc: 102 cm Exp: 101 cm

Figure 2.41. Nuclear deformations associated with the 101 cm<sup>-1</sup> vibrational mode of Cr(3-Iac)<sub>3</sub>.

On an experimental note, Cr(3-Iac)<sub>3</sub> had the tendency to crash out of solution where the laser hit. As such, care was taken when deciding the number of data points in each scan to prevent a significant buildup of precipitate reducing the transmission of the probe beam through the sample. The cuvette was also translated after each scan when performing these experiments. Additionally, the sample was observed to decompose after a while as the solution began to turn brown. This was marked by an absorption feature growing in at ~500 nm that is likely a result of a dissociated iodine species. Given the excellent agreement between the calculated and experimental frequencies and the observation that the halogen atoms seem to dramatically and systematically change the vibrational frequency from ~190 cm<sup>-1</sup> in unsubstituted Cr(acac)<sub>3</sub> to ~101 cm<sup>-1</sup> in Cr(3-Iac)<sub>3</sub>, it is expected that this decomposition is not effecting the results shown here to any significant degree and that the observed oscillatory component can be attributed entirely to Cr(3-Iac)<sub>3</sub>.

#### 2.4.6. Conclusions on 3-Substituted Cr(acac')<sub>3</sub> compounds

Now that the results on each member of the 3-substituted  $Cr(acac')_3$  series has been shown, we can gain further insight by comparing the results on each compound. First, it is clear by the qualitatively similar spectral evolution across the series that the excited state decay mechanism is identical for each member, i.e. that following excitation into the  ${}^4T_2$  state, the molecule rapidly undergoes ISC to the doublet manifold followed by bISC to create a quasi-equilibrium between the  ${}^4T_2$  and  ${}^2E$  states and the  ${}^4T_2$  population can



**Figure 2.42.** Summary of the results on the 3-substituted Cr(acac')<sub>3</sub> series. Internal conversion lifetimes for Cr(acac)<sub>3</sub> and Cr(3-NO<sub>2</sub>ac)<sub>3</sub> were acquired from references 7 and 15 respectively.

undergo IC to reform the ground electronic state with a time constant of  $\sim 1$  ps. This further illustrates the insensitivity of the decay mechanism with respect to synthetic modifications.

Perhaps unsurprisingly, given the identical decay mechanisms across this series of 3-substituted  $Cr(acac^*)_3$  compounds, the coherent vibrational mode that is active in each compound is the same type of metal ligand breathing mode (Figure 2.42), which, due to the tethering of the oxygen atoms, results in a small torsional element as well. When comparing the dephasing times across this series to the IC time constants, we can gain important information regarding the electronic state that these vibrational modes are active on. From the Feynman diagrams discussed in section 2.4.1 we know that the coherences sampled during the TA experiments must be from an electronic excited state ( $^4T_2$  or  $^2E$ ). Given that the internal conversion time constant is smaller than the dephasing time for the heavier halogen-substituted derivatives then we can say unequivocally that this vibrational mode is not sampled from the  $^4T_2$  state and that all of the coherently active vibrational modes (including the 461 cm $^{-1}$  mode of the control molecule discussed earlier) are sampled in the  $^2E$  excited state. This is further supported by the good agreement between experiment and theory while using the  $^4A_2$  ground state (a proxy for the  $^2E$  state) for frequency calculations. Additionally, these results again indisputably disprove the vibrational relaxation assignment for the  $\sim 1$  ps process originally assigned by Juban and McCusker $^7$  as vibrational relaxation would result in dephasing of this mode and, according to equation 2.8, could not be faster than the observed vibrational dephasing.

We can next bring our attention to the main question driving this body of work: can dephasing times be an indicator for involvement of a vibrational mode in an ultrafast photophysical transformation. It is clear that <sup>2</sup>E state population is present at early times in each compound implying an ultrafast ISC. Yet, there also exists a wide range of dephasing times for the same vibrational mode across the series (200-2500 fs) suggesting that the ISC rate and the dephasing times observed here are uncorrelated and further that dephasing times are a poor indicator for involvement in an ultrafast photophysical transformation in this system. It is important to stress, however, that this represents a single counter example and that this does not mean that in all cases electronic state changes cannot result in vibrational dephasing. The burden of proof of this statement has not been met by this body of results. In fact, it may be the case that ISC does act to dephase these modes to some degree depending on the time constant for ISC and the vibrational period. It could very well be the case that the ISC is so fast relative to the slow vibrational periods of the heavier halogen derivatives that it is effectively instantaneous. It is easy to envision, however, that the shorter period of the 193 cm<sup>-1</sup> mode of the unsubstituted Cr(acac)<sub>3</sub>, may result in ISC events at staggered times across the ensemble, effectively causing dephasing. Given that the dephasing time for each of these modes is slower than the ISC time, this would suggest that if ISC is resulting in any dephasing, it does not result in the complete dephasing of the vibrational coherence and that additional factors must be at play. Unfortunately, without further evidence, it is impossible to know for certain at present. Indeed, intramolecular vibrational redistribution is also a plausible explanation for the short dephasing time in this system. Kunttu and coworkers<sup>14</sup> have already observed a ~300-700 fs IVR component in the ground electronic state of Cr(acac)<sub>3</sub>, Al(acac)<sub>3</sub>, and Fe(acac)<sub>3</sub> suggesting that rapid IVR may be inherent to the M(acac)<sub>3</sub> molecular structure. The sensitivity of the magnitude of IVR observed in that study to the vibrational frequency may also explain the wide range of dephasing times across the series shown here. However, without further evidence, we cannot say with certainty what exactly causes dephasing in this vibrational mode.

## 2.4.7. Effects of Increasing Steric Bulk

We have just established that the excited state decay mechanism of the  $Cr(acac')_3$  system is relatively insensitive with respect to synthetic modifications and that each of the 3-substituted  $Cr(acac')_3$  compounds undergo the same decay mechanism. We can now turn our attention to the effect of increased steric bulk in the periphery of the molecule such as with the  $Cr(TMHD)_3$  molecule first studied on ultrafast timescales by Schrauben. The transient difference spectrum for this compound (Figure 2.5) exhibited a  $\sim 1.8$  ps rise centered around 525 nm with a concomitant decay around 465 nm, which, based on the earlier discussion in section 2.4.1, we know is a manifestation of  ${}^4T_2 \rightarrow {}^2E$  ISC. It was rationalized that this could occur in one of two ways. In Case 1, we have a similar mechanism as the original one proposed by Schrauben. Following  ${}^4A_2 \rightarrow {}^4T_2$  excitation, the molecule slowly trickles down to the  ${}^2E$  state with a 1.8 ps time constant necessitating a slower  ${}^4T_2 \rightarrow {}^4A_2$  internal conversion rate relative to the  $Cr(acac)_3$  control molecule and more importantly a more than 18-fold increase in the ISC lifetime. This latter point on the remarkable change in the ISC lifetime seems somewhat unrealistic given earlier insensitivity of the decay

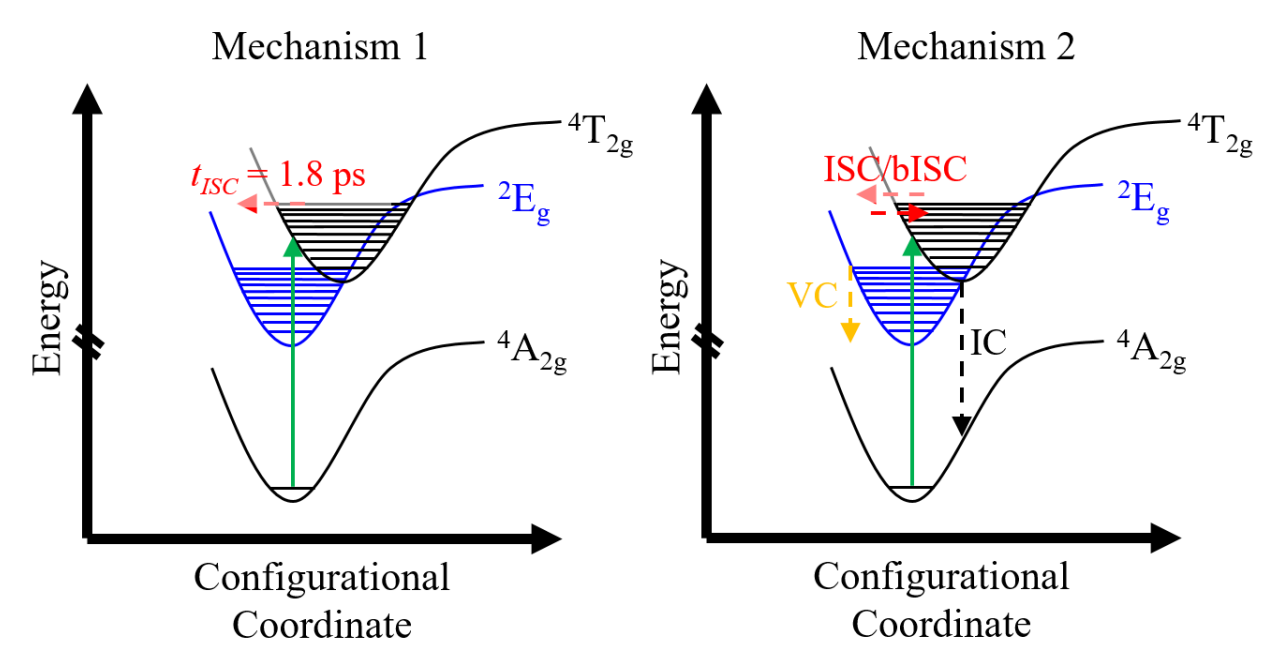


**Figure 2.43.** Depiction of the two possible mechanisms for excited state decay at early times in  $Cr(TMHD)_3$ . Mechanism 1 involves a slow 1.8 ps  ${}^4T_2 \rightarrow {}^2E$  ISC. Mechanism 2 involves a rapid equilibration of the  ${}^4T_2$  and  ${}^2E$  states. As the molecule begins to vibrationally cool the  ${}^2E \leftrightarrow {}^4T_2$  equilibrium shifts to the left and results in a 1.8 ps ISC. IC within the quartet manifold can occur, although it is not the dominant source of population relaxation.

mechanism to synthetic modifications of the  $Cr(acac')_3$  backbone. In the alternative proposed mechanism, Case 2,  $Cr(TMHD)_3$  behaves very similar to the  $Cr(acac)_3$  parent molecule. Following  ${}^4A_2 \rightarrow {}^4T_2$  excitation, the molecule undergoes rapid  ${}^4T_2 \rightarrow {}^2E$  ISC followed by rapid thermally activated  ${}^2E \rightarrow {}^4T_2$  bISC to create a quasi-equilibrium between these two states. If the IC from the  ${}^4T_2$  state is slowed relative to  $Cr(acac)_3$  then as the molecule vibrationally cools the thermally activated bISC from the doublet manifold will eventually become slower than the ISC from the  ${}^4T_2$  state resulting a net  ${}^4T_2 \rightarrow {}^2E$  ISC being observed. This mechanism implies that the primary difference between  $Cr(acac)_3$  and  $Cr(TMHD)_3$  is the slower IC from the  ${}^4T_2$  state. A summary of these two possible mechanisms for excited state decay in  $Cr(TMHD)_3$  at early times can be seen in Figure 2.43.

It seems that the major difference between these two mechanisms lies in the ISC rate. If Mechanism 1 is truly active then this implies a substantial reduction in the ISC rate relative to Cr(acac)<sub>3</sub>, whereas if Mechanism 2 is correct then the differences between Cr(acac)<sub>3</sub> and Cr(TMHD)<sub>3</sub> are much more subtle, primarily focused on the IC rate from the  ${}^4T_2$  state. To determine which of these mechanisms is most appropriate we can slowly build up to the Cr(TMHD)<sub>3</sub> compound and watch for changes in the dynamics. If a substantial change in the ISC rate is truly occurring this should be observed clearly in the progression of compounds depicted in Figure 2.24. In the following sections, we will thus investigate the dynamics in Cr(HD)<sub>3</sub> and Cr(DMHD)<sub>3</sub> and compare them to what is known about Cr(acac)<sub>3</sub> and Cr(TMHD)<sub>3</sub> to create a physical model that represents the dynamics in all systems.

## 2.4.8. Cr(HD)<sub>3</sub>

Transient absorption data on Cr(HD)<sub>3</sub> at early times in dichloromethane following 600 nm excitation can be seen in Figure 2.44. Although the data is a bit noisy there is a clear decay on the blue edge of the transient spectrum with no obvious rising feature indicating that there is no major shift in the ISC lifetime in this compound. Global fitting of the full spectrum dataset using the OPTIMUS fitting software,<sup>22</sup> reveals a 3 ps decay in both the red and blue edges. Overall, the spectral evolution appears very similar to Cr(acac)<sub>3</sub>, thus we can assign the 3 ps process to internal conversion from the <sup>4</sup>T<sub>2</sub> state.

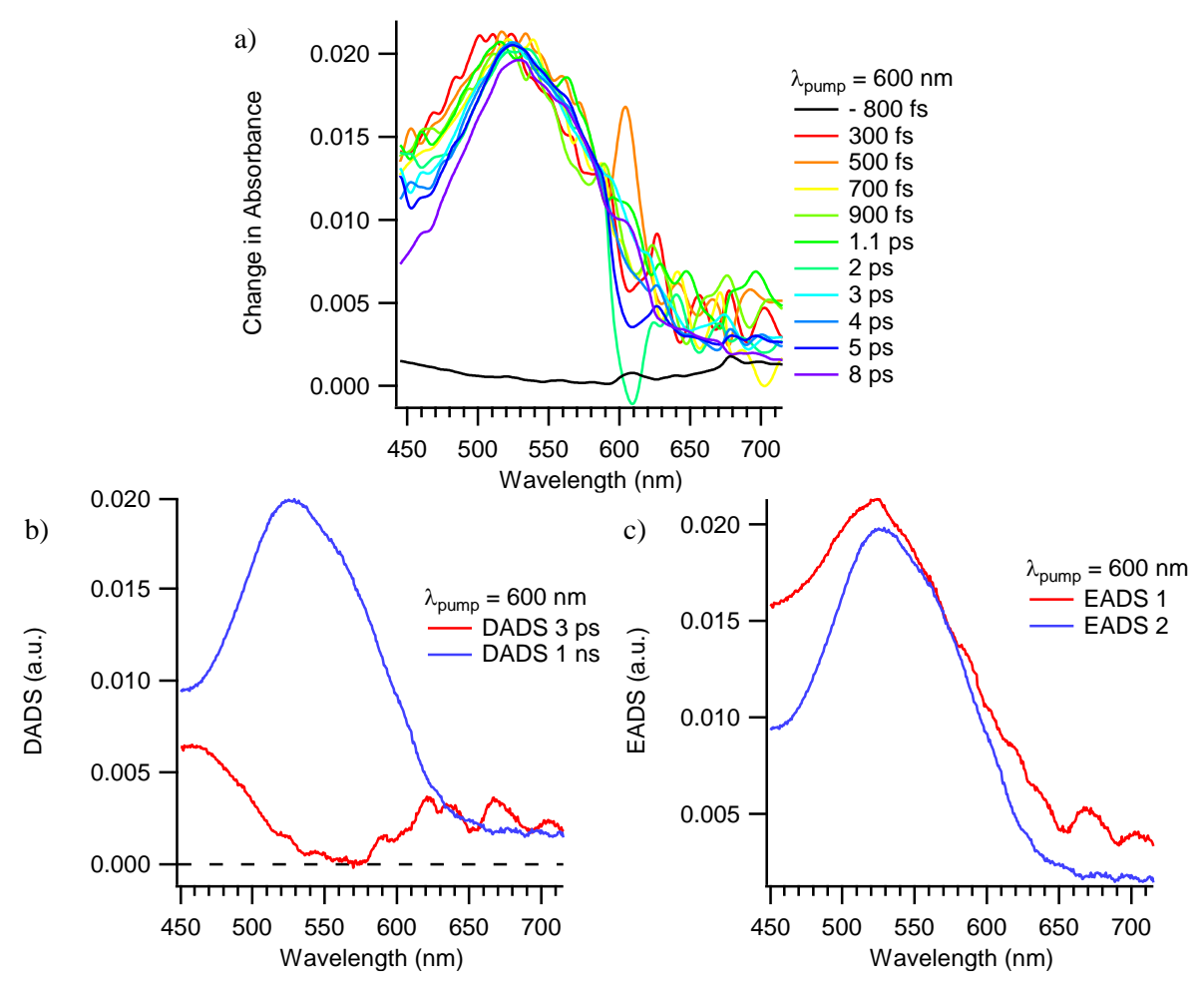


**Figure 2.44.** (a) Early time full spectrum TA data on  $Cr(HD)_3$  in dichloromethane following 600 nm excitation into the  ${}^4T_2$  state. (b) Decay associated difference spectra (DADS) associated with the global fit of the TA data to a sequential biexponential decay. The long-time offset was modeled by fixing a 1 ns exponential decay to describe the slower ground state recovery process. (c) Evolution associated difference spectra (EADS) associated with the global fit. Distortions in the transient spectrum near 600 nm are due to residual pump scatter.

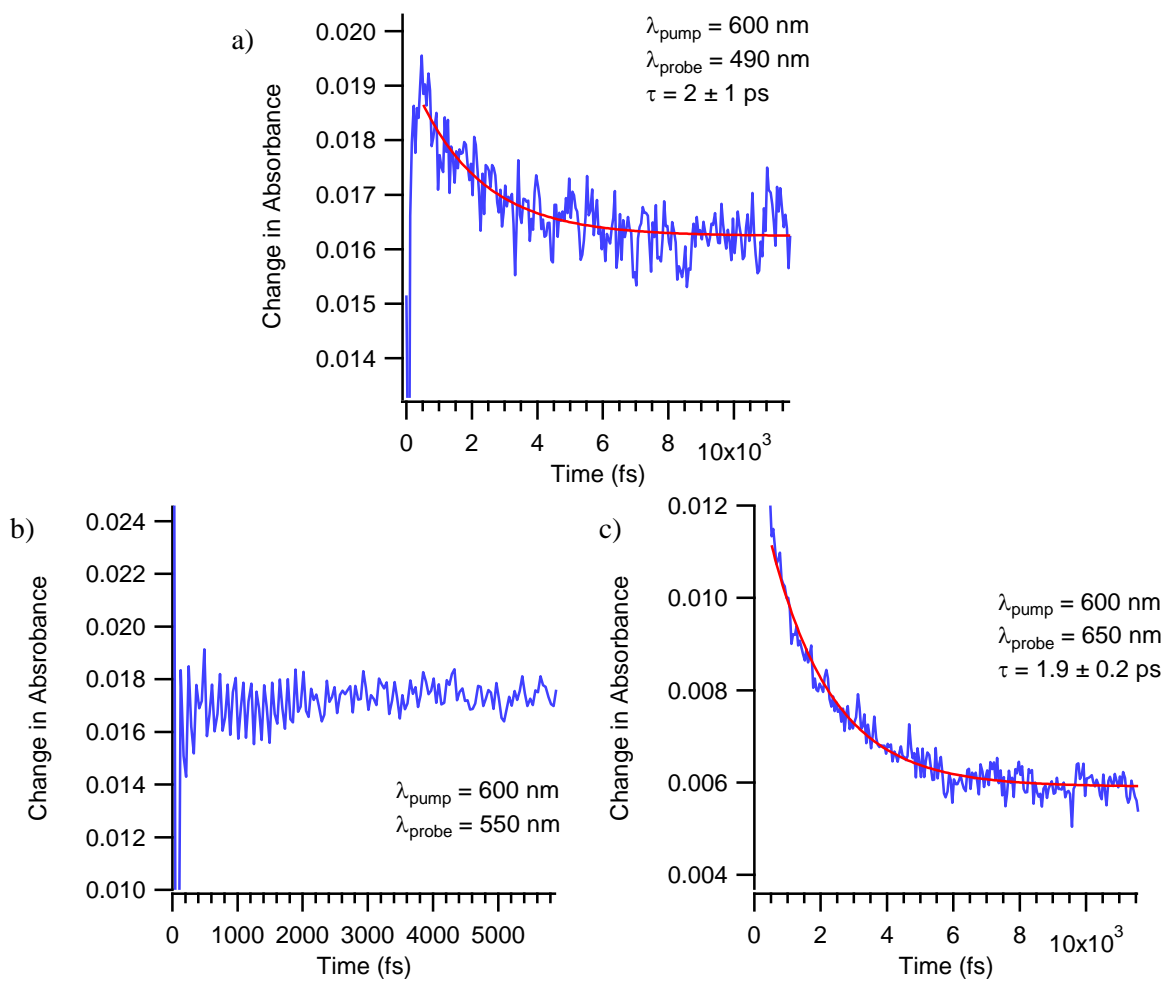


**Figure 2.45.** Representative single wavelength TA data on  $Cr(HD)_3$  in acetonitrile (a) and dichloromethane (b and c) following 600 nm excitation into the  ${}^4T_2$  state while monitoring at (a) 490 nm, (b) 550 nm, and (c) 650 nm.

We can acquire a more precise estimate of the IC lifetime by performing single wavelength TA experiments on  $Cr(HD)_3$  (Figure 2.45). These datasets qualitatively match the full spectrum datasets showing a  $1.7 \pm 0.4$  ps decay on both the red and blue edges of the transient spectrum, assigned as internal conversion from the  ${}^4T_2$  state. Unfortunately, no coherence of the solute was observed in this system, although it is likely that the same low frequency metal ligand stretching mode is active in this system as well (predicted to be  $\sim 182$  cm<sup>-1</sup> by DFT calculations). It is interesting to note that the IC lifetime in this compound is longer than in  $Cr(acac)_3$ , which was one of the required kinetic changes to achieve both Mechanisms 1 and 2 described earlier.

#### 2.4.9. Cr(DMHD)<sub>3</sub>

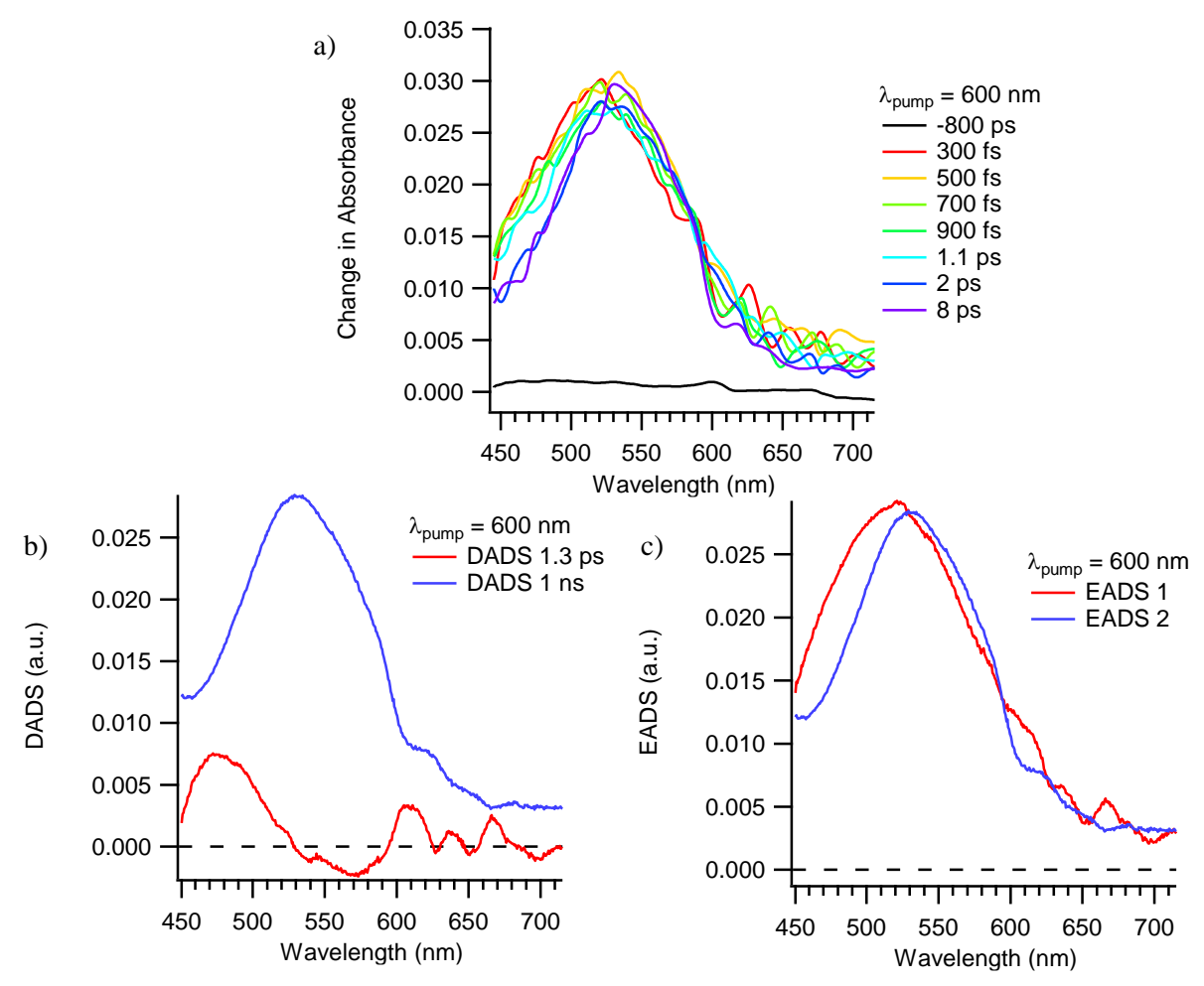


**Figure 2.46.** (a) Early time full spectrum TA data on Cr(DMHD)<sub>3</sub> in dichloromethane following 600 nm excitation into the  ${}^{4}T_{2}$  state. (b) Decay associated difference spectra (DADS) associated with the global fit of the TA data to a sequential biexponential decay. The long-time offset was modeled by fixing a 1 ns exponential decay to describe the slower ground state recovery process. (c) Evolution associated difference spectra (EADS) associated with the global fit. Distortions in the transient spectrum near 600 nm are due to residual pump scatter.

Full spectrum transient absorption data on  $Cr(DMHD)_3$  at early times in dichloromethane following 600 nm excitation into the  ${}^4T_2$  state can be seen in Figure 2.46. Although the data is noisy, there is a clear decay in the blue edge of the spectrum and what appears to be a slight rise between ~550-590 nm. A global fit of the dataset to a biexponential decay reveals 1.3 ps kinetic component which, according to the negative feature in the DADS, results in a slight rise between ~530-590 nm. This is also shown in the EADS. If this concomitant rise is truly present then this means  $Cr(DMHD)_3$  is behaving similarly to the slightly more sterically encumbered  $Cr(TMHD)_3$  compound.

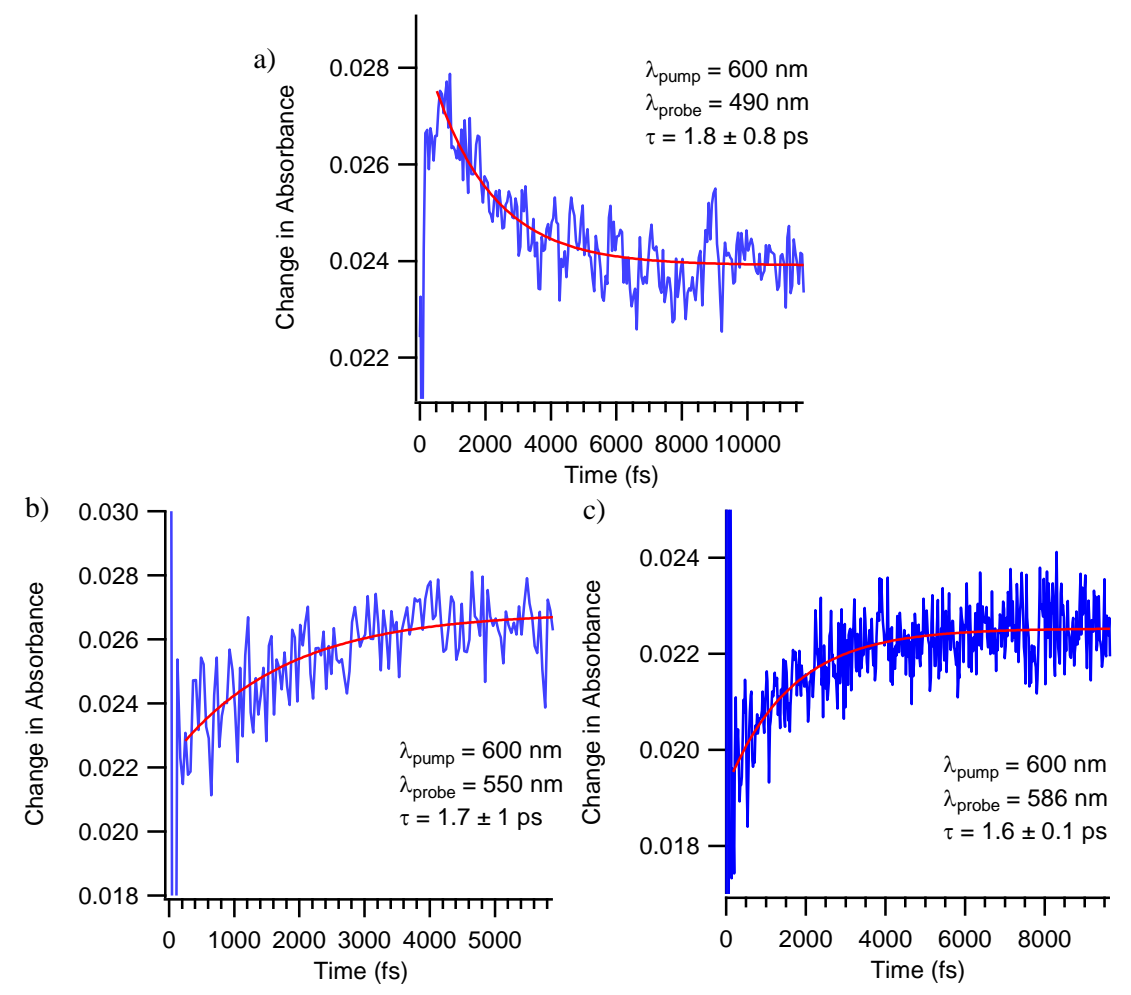


**Figure 2.47.** Representative single wavelength TA data on  $Cr(DMHD)_3$  in dichloromethane (a and b) and acetonitrile (c) following 600 nm excitation into the  ${}^4T_2$  state while monitoring at (a) 490 nm, (b) 550 nm, and (c) 586 nm.

To confirm these spectral features and to gain a better idea of the time constants associated with them, single wavelength measurements were performed on  $Cr(DMHD)_3$  to monitor the kinetics at the red and blue edges and at the center of the transient spectrum (Figure 2.47.). The single wavelength datasets reveal a decay on the blue edge of the transient spectrum at 490 nm with concomitant rising features at the center (550 nm) and red edges of the spectrum (586 nm), each with similar time constants (1.7  $\pm$  2 ps). The single wavelength datasets thus confirm the qualitative spectral changes observed in Figure 2.46 and by extension show that  $Cr(DMHD)_3$  behaves similar to  $Cr(TMHD)_3$  in terms of both spectral evolution and kinetics ( $\tau_{Cr(TMHD)3} = 1.8 \text{ ps})^{10}$ . Coherent vibrational modes of  $Cr(DMHD)_3$  were unable to be observed.

### 2.4.10. Concluding Comments on Effects of Steric Bulk

We can now assess which of the two excited state decay mechanisms outlined in section 2.4.7 is most appropriate when steric bulk is added to the periphery of the acac ligand. In the first possible mechanism, steric bulk causes a drastic increase in the lifetime for  ${}^{4}T_{2} \rightarrow {}^{2}E$  ISC and a slight increase in the lifetime for IC from the <sup>4</sup>T<sub>2</sub> state. The second possible mechanism is very similar to that for the unsubstituted Cr(acac)<sub>3</sub> molecule. Upon excitation to the <sup>4</sup>T<sub>2</sub> state, the molecule rapidly forms a quasiequilibrium between the <sup>2</sup>E and <sup>4</sup>T<sub>2</sub> states. As the system dissipates excess vibrational energy the efficiency of thermally activated bISC from the  ${}^2E$  state is diminished resulting in a shift of the  ${}^2E \leftrightarrow {}^4T_2$  equilibrium to the left and the observation of ISC from the <sup>4</sup>T<sub>2</sub> state. The only substantive change relative to Cr(acac)<sub>3</sub> is the slightly slower IC from the <sup>4</sup>T<sub>2</sub> state. We can parse out which of these excited state decay mechanisms is most realistic by comparing spectral evolution seen in the early time full spectrum data for each compound in Figure 2.48 including data on Cr(acac)<sub>3</sub> and Cr(TMHD)<sub>3</sub> collected by Eric Juban<sup>7</sup> and Joel Schrauben<sup>10,15</sup> respectively. We've already seen from the 3-substituted series that the excited state decay mechanism in Cr(acac')<sub>3</sub> is relatively insensitive to synthetic modifications. Furthermore, comparison of each of the datasets in Figure 2.48 shows only very subtle changes throughout the steric series, giving no indication of a quantum leap in the ISC lifetime. It is thus highly unlikely that the excited state decay mechanism (Mechanism 1) first proposed by Schrauben correctly describes the dynamics in this series of compounds. Mechanism 2, however, can describe the dynamics in every member in both the 3-substituted and steric-bulk acac series discussed thus far with small changes to the internal conversion lifetime. This modulation of the IC lifetime as a function of steric bulk is supported by the slower IC time constant observed for Cr(HD)<sub>3</sub> relative to the Cr(acac)<sub>3</sub> control molecule. Addition of another set of methyl groups to the periphery if the molecule is enough to make the shift in the  ${}^{2}E \leftrightarrow {}^{4}T_{2}$  equilibrium outpace the IC from the <sup>4</sup>T<sub>2</sub> state. This mechanism also makes intuitive sense when considering the vibrational overlap between relevant electronic states. For example, small changes in the geometry of the <sup>4</sup>T<sub>2</sub> state would not be expected to significantly alter the presumably abundant vibrational overlap with the <sup>2</sup>E electronic state and hence shouldn't significantly alter the rate of ISC. Small alterations of the equilibrium position of the <sup>4</sup>T<sub>2</sub> state as

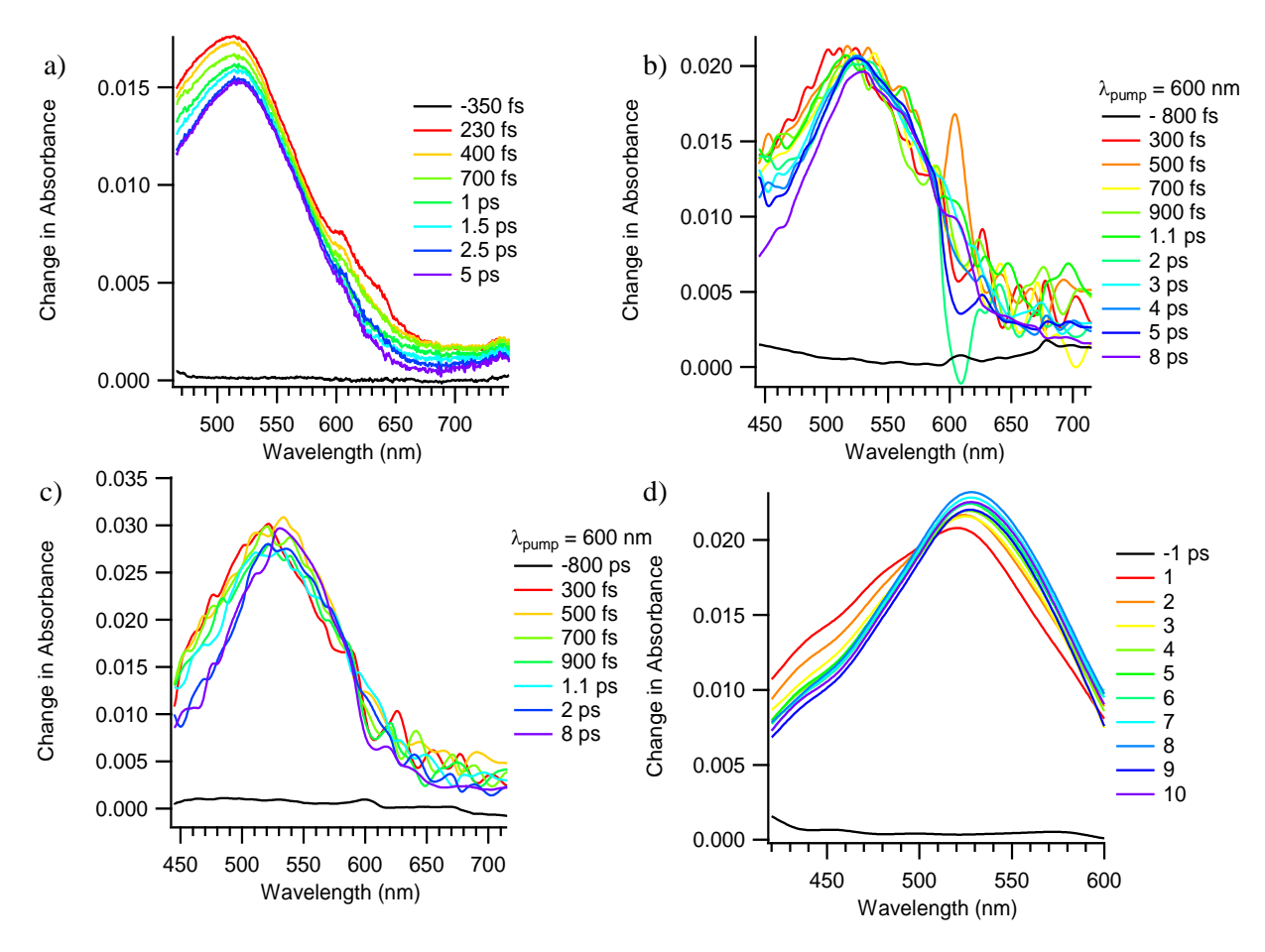


**Figure 2.48.** Early time full spectrum TA data on (a)  $Cr(acac)_3$ , (b)  $Cr(HD)_3$ , (c)  $Cr(DMHD)_3$ , and (d)  $Cr(TMHD)_3$  following excitation into the  ${}^4T_2$  excited state. Parts (a) and (d) were reproduced with data from references 7 and 15 respectively.

a result of increased steric encumbrance, however, would be expected to modulate the sparser vibrational overlap with the <sup>4</sup>A<sub>2</sub> ground state and in effect modify the IC rate.

## 2.4.11. Cr(TMHD)<sub>3</sub>

The previous section has just illustrated the decay mechanism of Cr(TMHD)<sub>3</sub>, and the kinetics of this compound have already been investigated. <sup>10,15</sup> This work will thus focus on characterizing the coherent vibrational motion of Cr(TMHD)<sub>3</sub>. A summary of the oscillatory components observed during TA experiments on Cr(TMHD)<sub>3</sub> can be seen in Table 2.7 with representative datasets in 1,4-dioxane andtetrahydrofuran shown in Figures 2.49 and 2.50 respectively. Frequencies bellow 100 cm<sup>-1</sup> were not reported as they were likely due to poor exponential fitting or poor signal stability. Furthermore, many of the values in Table 2.7 have large error bars arising from the low magnitude of the oscillatory signal, the

**Table 2.7.** Summary of the oscillatory components observed for  $Cr(TMHD)_3$  following excitation into the  ${}^4T_2$  state across several solvents. Experimental details such as the IRF and pump and probe wavelengths and pulse energies are included for each experiment. Probe pulse energies were not measured when using a continuum probe and are labeled below as "na".

$\lambda_{pu}, nm$ $(E_{pu}, \mu J)$	$\lambda_{pr}$ , nm $(E_{pr}, \mu J)$	IRF, fs	Solvent	Freque			quency, cm <sup>-1</sup> (Damping Time, fs)			
600 (3)	592 (0.3)	45	Dioxane		166 (683)					
600 (3)	592 (0.3)	45	Dioxane	115 (543)	168 (6102) <sup>a</sup>		246 (485)	285 (1609)		
600 (2)	592 (0.2)	45	Dioxane	124 (542)	,		, ,	,		
600 (2)	592 (0.2)	45	Dioxane	137 (1485)		221 (1028)				
600 (2.8)	592 (0.3)	40	Dioxane	, ,	162 (840)					
600 (3)	480 (na)	100	Dioxane		157 (1221)					
600 (3)	480 (na)	125	Dioxane		201 (138)					
600 (3)	480 (na)	165	Dioxane	122 (606)	177 (175)		256 (428)			
560 (3)	550 (0.3)	50	Dioxane		168 (431)		244 (929)			
520 (5)	514 (0.4)	75	Dioxane		177 (327)			298 (882)		
600 (3)	592 (0.3)	45	Benzene	128 (255)	173 (1052)					
600 (3)	595 (0.3)	50	THF	111 (373)		221 (229)			346 (1026)	
600 (3)	592 (0.3)	50	THF				242 (396)			
600 (3)	592 (0.3)	45	THF		186 (1639)		245 (2387)		323 (2199)	372 (1151)
600 (3)	592 (0.3)	50	THF	139 (499)						
600 (5)	584 (0.5)	35	THF		162 (1371)					
600 (3)	480 (na)	165	THF	126 (1143)	195 (383)		256 (820)			
580 (5)	568 (0.5)	45	THF		162 (559)					
560 (3)	550 (0.3)	50	THF		172 (638)					
560 (5)	545 (0.5)	55	THF		177 (855)		252 (1242)			
560 (5)	546 (0.5)	65	THF		166 (734)	209 (3928)				375 (995)
520 (5)	508 (0.5)	70	THF		174 (1300)	197 (769)				
Average Frequency, cm <sup>-1</sup>				125	173	212	249	292	335	374
Standard Deviation, cm <sup>-1</sup>			10	12	11	6	9	16	2	
Average Damping, fs			680	770	1490	960	1250	1600	1070	
Standard Deviation, fs			420	450	1660	700	510	830	110	

a. The slow nature of this decay coupled with the additional oscillatory components present made it difficult for the LPSVD program to get a reasonable dephasing time for this vibrational mode. This value was thus excluded from the averaging process.

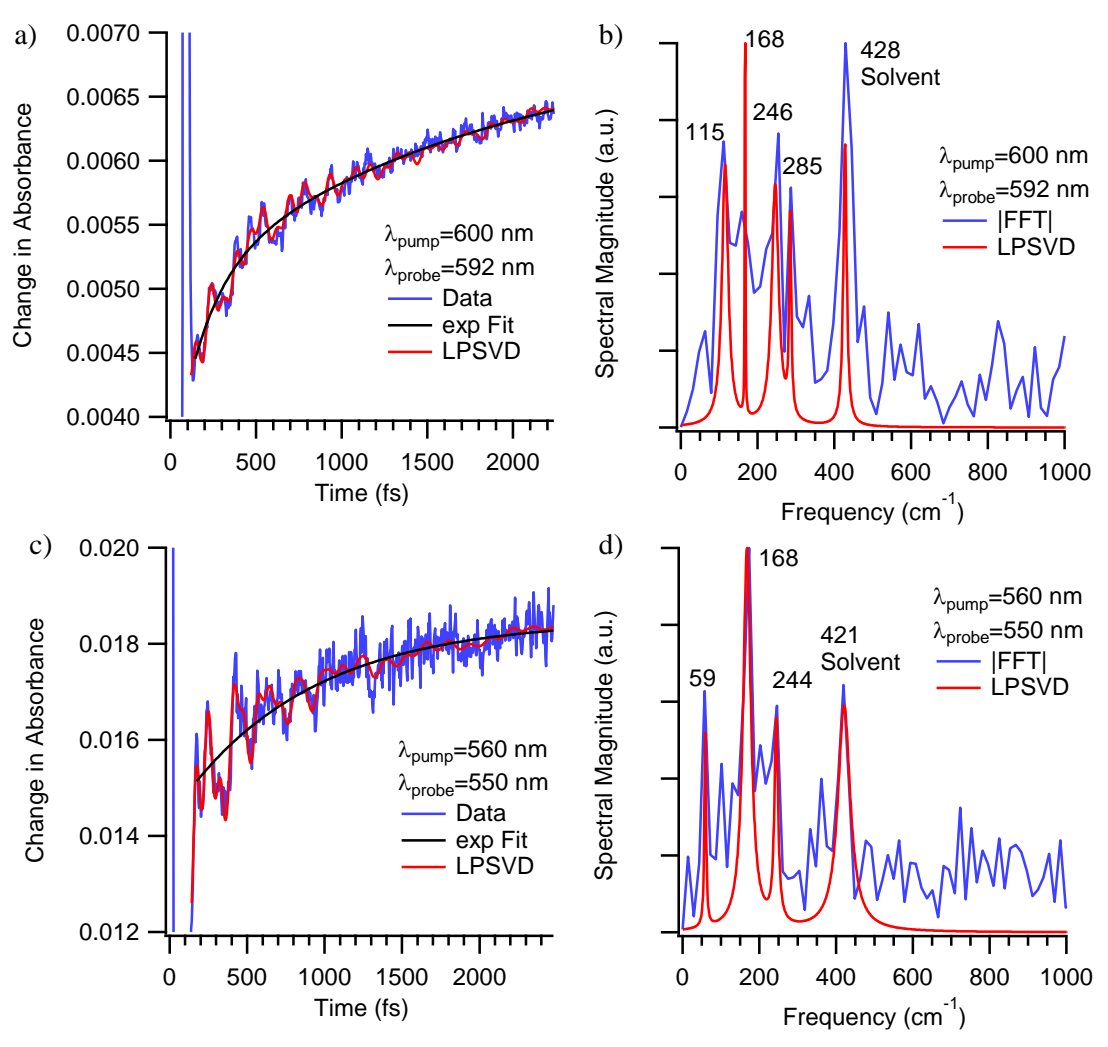


**Figure 2.49.** Representative transient absorption data on Cr(TMHD)<sub>3</sub> in 1,4-dioxane following excitation into the  ${}^{4}T_{2}$  excited state while monitoring at (a) 592 nm and (c) 550 nm with corresponding vibrational spectra (b and d) resulting from FFT and LPSVD analyses.

presence of oscillatory background signals from the solvent, and a generally congested vibrational spectrum. Given the consistently low number of vibrational modes observed for each of the other Cr(acac')<sub>3</sub> derivatives (i.e. mostly only the low frequency symmetric breathing mode) it is likely that several of the frequencies extracted from LPSVD analyses are simply experimental artifacts and not attributable to anything physically meaningful. Inspection of Table 2.7 shows that the 125, 173, and 249 cm<sup>-1</sup> frequencies appear most frequently across the provided datasets and thus are most likely to actually represent excited state vibrational coherences. To gain more insight into the legitimacy of these vibrational modes we can use the resonance Raman spectrum of Cr(TMHD)<sub>3</sub> shown in Figure 2.51. Since the 125 cm<sup>-1</sup> feature from

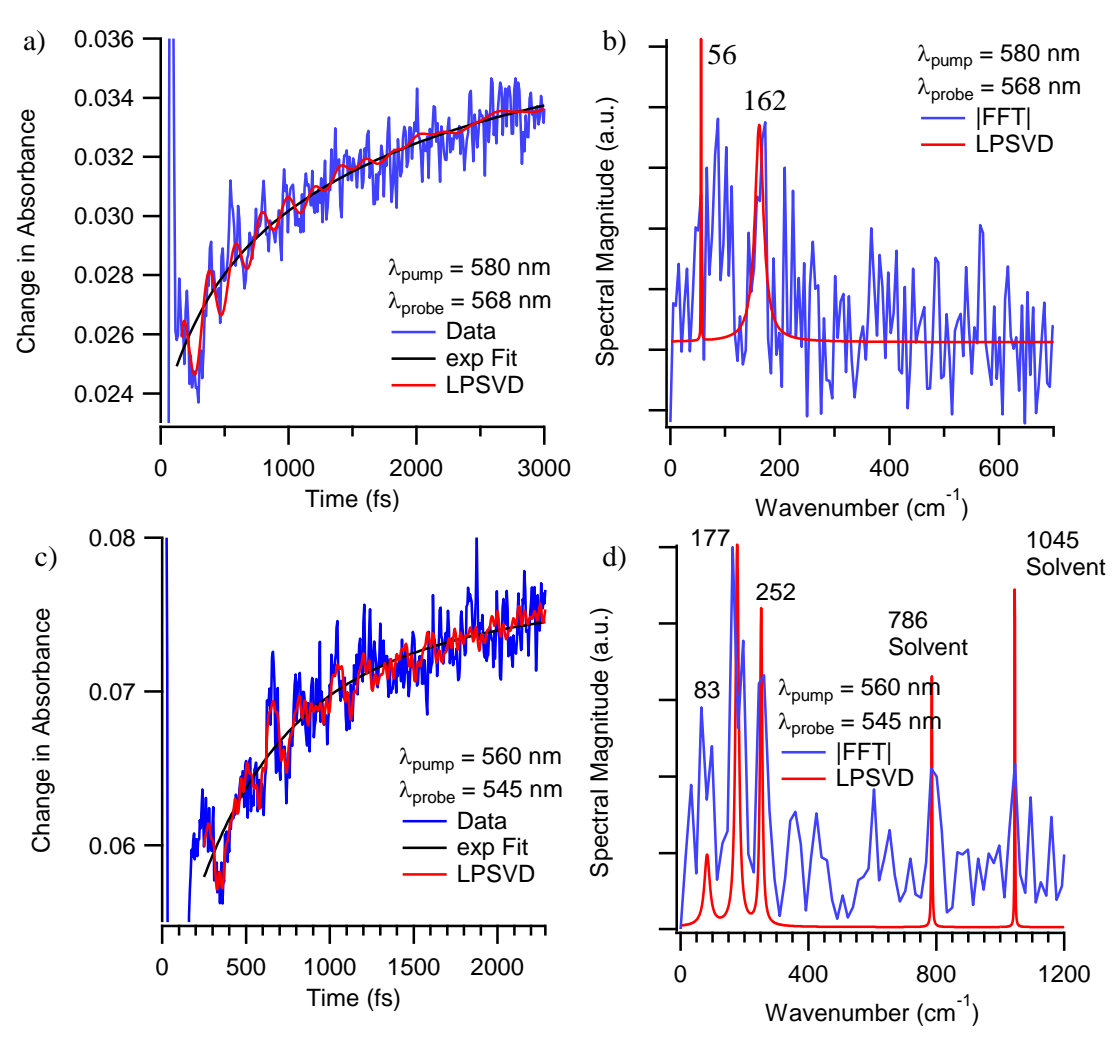


**Figure 2.50.** Representative transient absorption data on  $Cr(TMHD)_3$  in tetrahydrofuran following excitation into the  ${}^4T_2$  excited state while monitoring at (a) 568 nm and (c) 545 nm with corresponding vibrational spectra (b and d) resulting from FFT and LPSVD analyses.

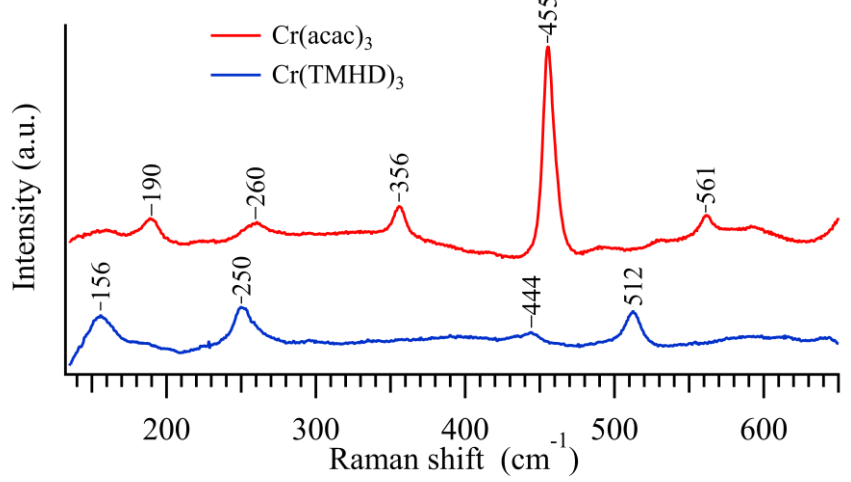


**Figure 2.51.** Stacked plot of Raman data on  $Cr(acac)_3$  and  $Cr(TMHD)_3$  in THF with 488 nm excitation source in resonance with the blue edge of the  ${}^4A_2 \rightarrow {}^4T_2$  absorption band.

Table 2.7 is too close to the Rayleigh line, its presence in the Raman spectrum of Figure 2.51 could not be confirmed or denied. Considering the large error bars on the 173 (12) cm<sup>-1</sup> mode it seems that this could be attributed to the 156 cm<sup>-1</sup> peak in the Raman spectrum. The 249 cm<sup>-1</sup> mode, on the other hand is in good agreement with the 250 cm<sup>-1</sup> peak observed in the Raman data. The 212, 292, 335, and 374 cm<sup>-1</sup> frequencies observed in the TA data, however, do not have corresponding peaks in the Raman spectrum. While this could be a symptom of selection rules, it seems unlikely given the irregularity of their occurrence in the TA data that they arise from coherences of Cr(TMHD)<sub>3</sub>. The 212, 292, 335, and 374 cm<sup>-1</sup> oscillatory components are thus assigned as experimental artifacts.

Now that the 125, 173, and 249 cm<sup>-1</sup> frequencies observed during TA experiments on Cr(TMHD)<sub>3</sub> have been shown to possibly be legitimate vibrational modes, the nuclear deformations associated with these modes can be characterized with DFT calculations. We can first assign the 173 cm<sup>-1</sup> experimental frequency to a calculated 162 cm<sup>-1</sup> symmetric breathing mode (Figure 2.52) that is essentially identical to the vibrational mode observed for each of the Cr(acac')<sub>3</sub> derivatives studied thus far. While the frequency matching between the 173 (12) cm<sup>-1</sup> experimental and 162 cm<sup>-1</sup> calculated frequencies is not very good, the calculated mode does fall within the error bars. This is also in good agreement with the 156 cm<sup>-1</sup> peak in the resonance Raman spectrum (Figure 2.51). Assigning the 249 cm<sup>-1</sup> vibrational mode is more complicated

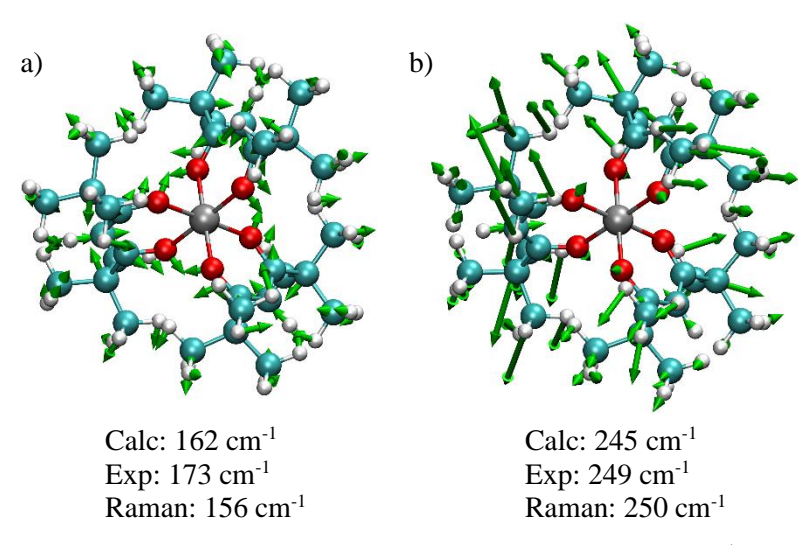


**Figure 2.52.** Nuclear deformations associated with the (a) 173 cm<sup>-1</sup> and (b) 249 cm<sup>-1</sup> experimentally observed coherent vibrational modes of Cr(TMHD)<sub>3</sub>.

given the density of states in this frequency region and the lack of precedent to compare to. Nevertheless, this mode is tentatively assigned to a 245 cm<sup>-1</sup> calculated vibrational mode (Figure 2.52) which exhibits a symmetric compression of the TMHD ligands towards the metal center concomitant with each oxygen atom splaying outwards in the plane of the ligand backbone. This particular motion was chosen in consideration of the symmetry of the mode (and the lack thereof in several of the other modes in this frequency region) as well as the calculated Raman activity of this mode. While the selection rules for Raman, resonance Raman, and excited state coherent vibrational modes observable in this TA experiment are all likely different, we have seen that every observable coherent vibrational mode in this system thus far has been highly symmetric and Raman active. We can thus make the assumption that this holds for the experimental 249 cm<sup>-1</sup> mode as well given that it is also observed in the resonance Raman spectrum (Figure 2.51). While this vibrational mode is somewhat similar to the symmetric breathing mode that has been present in many of the other Cr(acac')3 derivatives, this mode exhibits a bit more emphasis on distortion of the periphery of the molecule as opposed to distortion of the primary coordination sphere. It may be the case that the additional atoms in this molecule result in several different flavors of this type of motion appearing at different frequency regions. Finally, the 125 (10) cm<sup>-1</sup> mode again falls in a region of high density of vibrational states. With no precedent, large error bars, and no obvious way to assess the viability of each of these candidate modes, no assignment will be made here.

When comparing the dephasing times of the low frequency symmetric breathing mode across the Cr(acac')<sub>3</sub> series, it can be seen that the more sterically encumbered Cr(TMHD)<sub>3</sub> exhibits dephasing times (770 fs) that are intermediate between the unsubstituted Cr(acac)<sub>3</sub> (340 fs) and halogenated Cr(3-Clac)<sub>3</sub> (1100 fs) compounds. While it was established that the dephasing times in this system are not very informative with regards to contribution to an electronic state change, it may yet be enlightening to further probe why the dephasing times are changing across this series of compounds. Apart from Cr(3-NO<sub>2</sub>ac)<sub>3</sub> the dephasing time increased as the vibrational frequency decreased. This may suggest a correlation between the vibrational frequency and the susceptibility of a normal mode to dephasing via excited state dynamics or hint at a subtle relationship between the collection of vibrational frequencies of a molecule and the rate

of IVR. To investigate this we can study one more molecule, Cr(4-Cl-TMHD)<sub>3</sub> which should have a reduced vibrational frequency of the symmetric breathing mode relative to Cr(TMHD)<sub>3</sub>.

#### 2.4.12. Cr(4-Cl-TMHD)<sub>3</sub>

The goal of this section is to characterize the early time ultrafast dynamics of Cr(4-Cl-TMHD)<sub>3</sub> and to glean more information on the origin of dephasing in these types of systems. As such the discussion will largely focus on these endeavors. The crystal structure information is shown in the appendix and was collected by McCusker group member Sara Adelman and solved by Professor Richard Staples of Michigan State University.

The early time full spectrum TA data on  $Cr(4-Cl-TMHD)_3$  in DCM following excitation into the  ${}^4T_2$  state is shown in Figure 2.53a. While this dataset is unfortunately quite noisy, the global fit

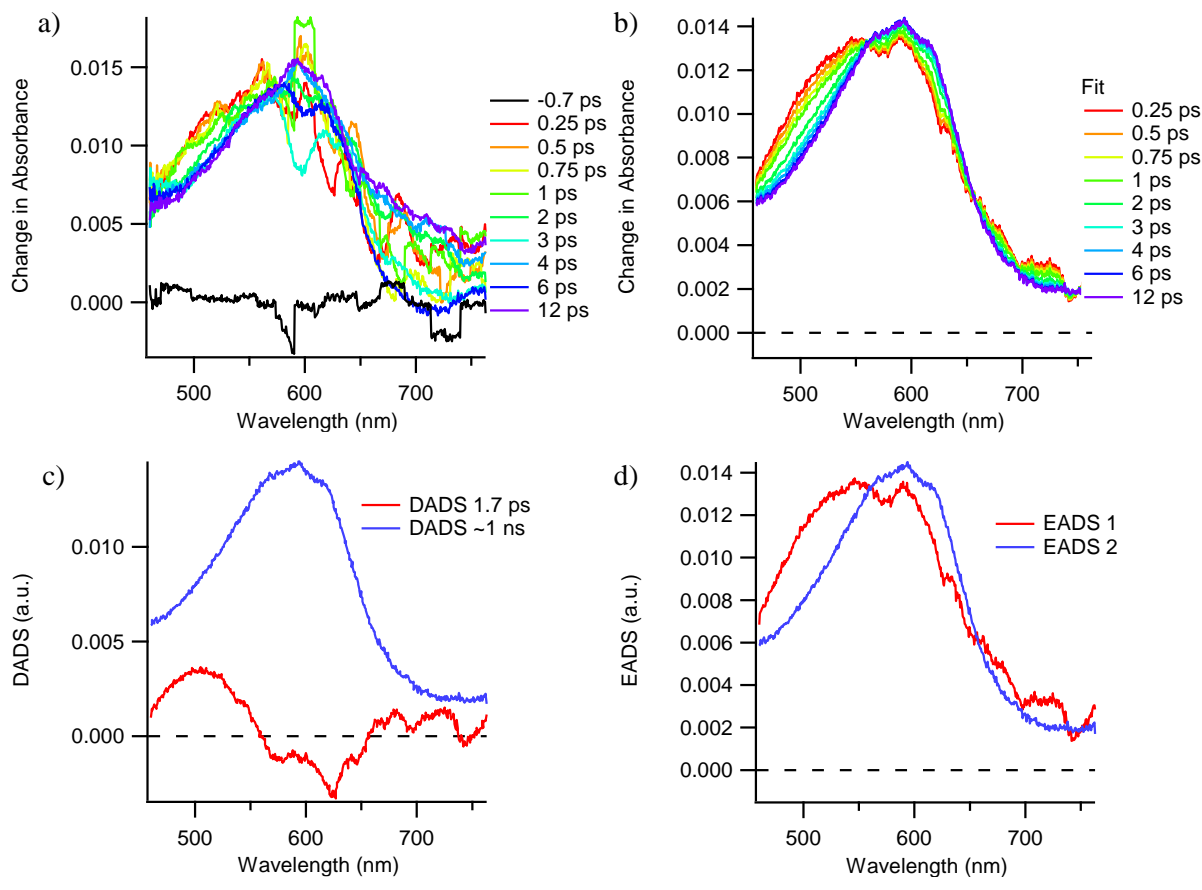


**Figure 2.53.** (a) Early time full spectrum TA data on  $Cr(4-Cl-TMHD)_3$  in dichloromethane following 600 nm excitation into the  ${}^4T_2$  state. (b) Global fit of the TA data to a sequential biexponential decay. The long-time offset was modeled by fixing a 1 ns exponential decay to describe the ground state recovery process. (c) Decay associated difference spectra (DADS) and (d) Evolution associated difference spectra (EADS) associated with the global fit.

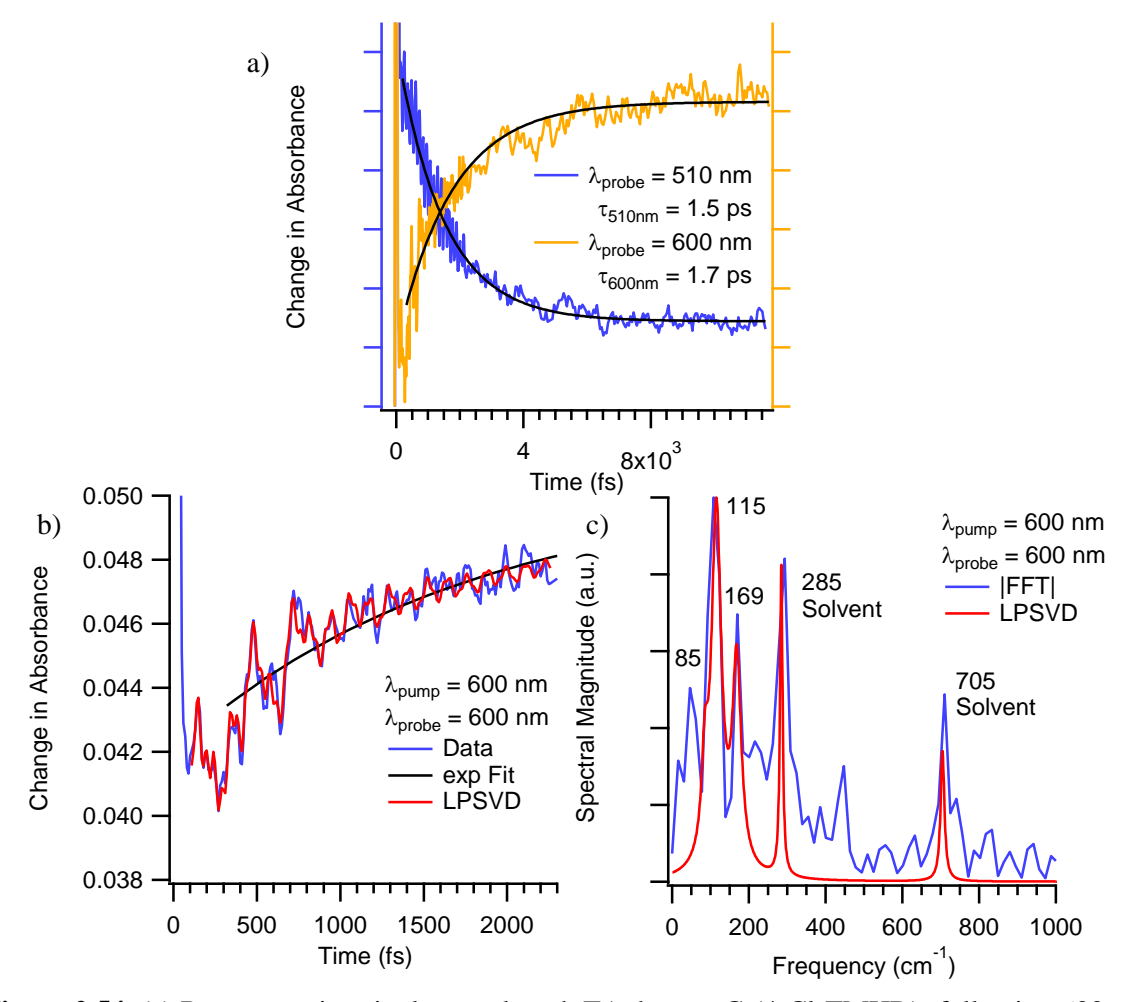


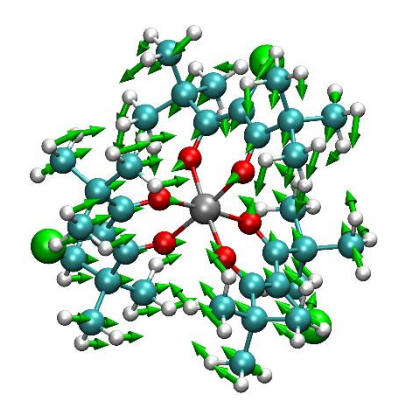
**Figure 2.54.** (a) Representative single wavelength TA data on  $Cr(4-Cl-TMHD)_3$  following 600 nm excitation into the  ${}^4T_2$  state in dichloromethane. Time constants for the fits of specific data sets are included on the graph itself, however the average time constant measured across all datasets is 1.7  $\pm$  0.2 ps. (b) Zoomed in portion of the 600 nm probe data shown in part a with exponential and LPSVD fits and (c) corresponding vibrational spectrum resulting from FFT and LSVD analyses.

(Figure 2.53b) cleans up nicely and seams to closely resemble the spectral evolution of  $Cr(TMHD)_3$  in Figure 2.48d. The fit reveals a 1.7 ps kinetic component which exhibits a decay in the blue edgeof the transient spectrum with a concomitant rise from ~550-650 nm, which is again similar to  $Cr(TMHD)_3$  in terms of kinetics and spectral evolution. These spectral features are confirmed in single wavelength datasets (Figure 2.54a) showing a rising feature in the red edge of the transient spectrum at 600 nm and a concomitant decaying feature in the blue edge of the spectrum at 510 nm and an average time constant of  $1.7 \pm 0.2$  ps. The early time kinetics of  $Cr(4-Cl-TMHD)_3$  are thus essentially identical to those of  $Cr(DMHD)_3$  ( $1.7 \pm 0.2$  ps) and  $Cr(TMHD)_3$  (1.8 ps)<sup>10</sup>.

**Table 2.8.** Summary of coherent oscillations observed in TA data on  $Cr(4-Cl-TMHD)_3$  following 600 nm excitation into the  ${}^4T_2$  state while monitoring at 600 nm in dichloromethane. The sub-100 cm<sup>-1</sup> oscillatory components were included for transparency; however, it is likely that they arise from poor exponential fitting and do not truly represent coherent vibrational motion of the solute. Experimental details such as the IRF and the pump and probe pulse energies are included for each measurement.

$E_{pu}(E_{pr}), \mu J$	IRF, fs	Free	quency, cm <sup>-1</sup> (Damping	Time, fs)
2.2 (0.3)	55	48 (279)	120 (478)	153 (235)
3.6 (0.4)	45	85 (529)	115 (342)	169 (381)
Average Frequency, cm <sup>-1</sup>		67	118	161
Standard Deviation, cm <sup>-1</sup>		26	4	11
Average Damp	oing Time, fs	400	400	300
Standard De	viation, fs	200	100	100

In addition to confirming the qualitative spectral evolution of Cr(4-Cl-TMHD)<sub>3</sub>, the single wavelngth datasets also showed coherent oscillations supperimposed on the population dynamics (Figure 2.54b) which were analysed with FFT and LPSVD techniques (Figure 2.54c). A summary of these preliminary results can be seen in Table 2.8. It should be noted that the sub-100 cm<sup>-1</sup> oscillatory components presented in Table 2.8 likely do not actually represent coherent vibrational motion of Cr(4-Cl-TMHD)<sub>3</sub> but rather an artifact of poor exponential fitting of the LPSVDS program. It is readilly apparent from each of the Cr(acac')<sub>3</sub>derivatives thus far that one of these modes is likely a symmetric breathing mode. This is confirmed by DFT calculations showing a calculated 118 cm<sup>-1</sup> symmetric breathing mode (Figure 2.55) in excellent agreement with the experimental results. Unfortunately, the high degree of uncertainty in the



Calc: 118 cm<sup>-1</sup> Exp: 118 cm<sup>-1</sup>

**Figure 2.55.** Nuclear deformations associated with the 118 cm<sup>-1</sup> experimentally observed coherent oscillations of Cr(4-Cl-TMHD)<sub>3</sub>.

161 cm<sup>-1</sup> component coupled with the high density of states in that frequency region precludes any definitive assignment of that mode. Additional TA experiments are needed to narrow the selection of possible vibrational modes before any meaningful assignment can be made.

We can now turn our attention to the dephasing time of the low frequency symmetric breathing mode. In the 3-substituted series of Cr(acac')<sub>3</sub> compounds it was observed that halogen substitution served to both reduce the vibrational frequency of the symmetric breathing mode and extend the dephasing time. Replacement of the methyl groups in the periphery of the structure with bulkier t-Butyl groups was also shown to decrease the vibrational frequency while increasing the dephasing time relative to the Cr(acac)<sub>3</sub> control molecule. This trend prompts the question of whether there is an inverse relationship between the vibrational frequency (and by extension the vibrational period) and the susceptibility of a vibrational mode to be dephased by excited state evolution or if there is a more subtle relationship between the collection of vibrational frequencies of a molecule and its IVR rate. Until now, it seemed that Cr(3-NO2ac)3 which exhibited a similar frequency to Cr(3-Clac)<sub>3</sub> yet a shorter dephasing time than Cr(acac)<sub>3</sub> was the only outlier to the trend of increased dephasing times concomitant with lower vibrational frequencies. Now, however, the Cr(4-Cl-TMHD)<sub>3</sub> results affords several additional comparisons. First, when comparing the ~190 cm<sup>-1</sup> mode of Cr(acac)<sub>3</sub> with 380 fs damping time to this 118 cm<sup>-1</sup> mode of Cr(4-Cl-TMHD)<sub>3</sub> with 400 fs damping time, we see there is a drastic reduction in frequency with essentially no change in dephasing time, which suggests that there is no inverse relationship between dephasing and vibrational frequency that is active in this system. Furthermore, when comparing the Cr(4-Cl-TMHD)<sub>3</sub> results with the ~160 cm<sup>-1</sup> mode (770 fs dephasing time) of the unchlorinated Cr(TMHD)<sub>3</sub> compound, we see a decrease in the dephasing time upon a decrease in the vibrational frequency further disproving the above hypothesis. This thus points to a more complicated relationship between the dephasing of this mode and its vibrational frequency, whereby the rate of dephasing is dictated by the relative energies of the symmetric breathing mode and the accepting vibrational modes that are excited via IVR.

#### 2.5. Concluding Comments on Cr(acac')<sub>3</sub> Systems

The work presented in this chapter has built both upon the works of previous McCusker group members<sup>7,10,12,15</sup> and other research groups<sup>8,13,14</sup> to build a comprehensive photophysical model of the excited state dynamics of Cr(acac)<sub>3</sub> and it's 3-substituted and more sterically encumbered derivatives. These results show that following excitation into a quartet excited state, a rapid quasi-equilibrium is established between the  ${}^2E$  and  ${}^4T_2$  excited states. This equilibrium is perturbed by  ${}^4T_2 \rightarrow {}^4A_2$  IC with a rate that is modulated by steric bulk in the periphery of the molecule, and by vibrational cooling which shifts the <sup>2</sup>E  $\leftrightarrow$   $^4T_2$  equilibrium to the left. A previous assignment of 1.1 ps vibrational relaxation<sup>7</sup> on the  $^2E$  state of Cr(acac)<sub>3</sub> was disproven separately using an analysis of full spectrum TA data following higher energy excitation into the <sup>4</sup>T<sub>1</sub> excited state; analysis of the resonance Raman linewidth and the dephasing time of the 461 cm<sup>-1</sup> mode of Cr(acac)<sub>3</sub>; and by the excited state dephasing times observed in various Cr(acac')<sub>3</sub> derivatives exceeding the previously proposed vibrational cooling time constant. This ~1 ps process was then reassigned to internal conversion from the <sup>4</sup>T<sub>2</sub> state. It was also consistently shown that the same low frequency symmetric metal-ligand stretching vibration is active in each Cr(acac')<sub>3</sub> compound studied. The unsubstituted Cr(acac)<sub>3</sub> compound also exhibited an additional coherent metal-ligand stretching mode at 461 cm<sup>-1</sup>. Both of these normal modes were attributed to the <sup>2</sup>E excited state on the basis of low oscillator strength preventing the observation of wavepackets on the ground electronic state during TA experiments; similar dephasing times in the excited state measured by TA and on the ground state extracted by an analysis of the Raman linewidth; and damping times that were slower than the internal conversion from the <sup>4</sup>T<sub>2</sub> state. Finally, this work addressed the proposition that short dephasing times can be an indicator for involvement of specific vibrational modes in an ultrafast electronic state change. Observation of dephasing times of the same vibrational mode that varied from ~200 fs to 2.5 ps with no observable change in the ultrafast ISC rate suggested that in this system, dephasing times are a rather poor indicator for involvement in the ultrafast ISC. Furthermore, the subtle patterns in dephasing times in relation to vibrational frequencies suggests that IVR may be contributing to the observed dephasing in this system and that its efficiency is dependent on the relative energies of the 3N-6 vibrational modes of the molecule. A summary of the frequencies and

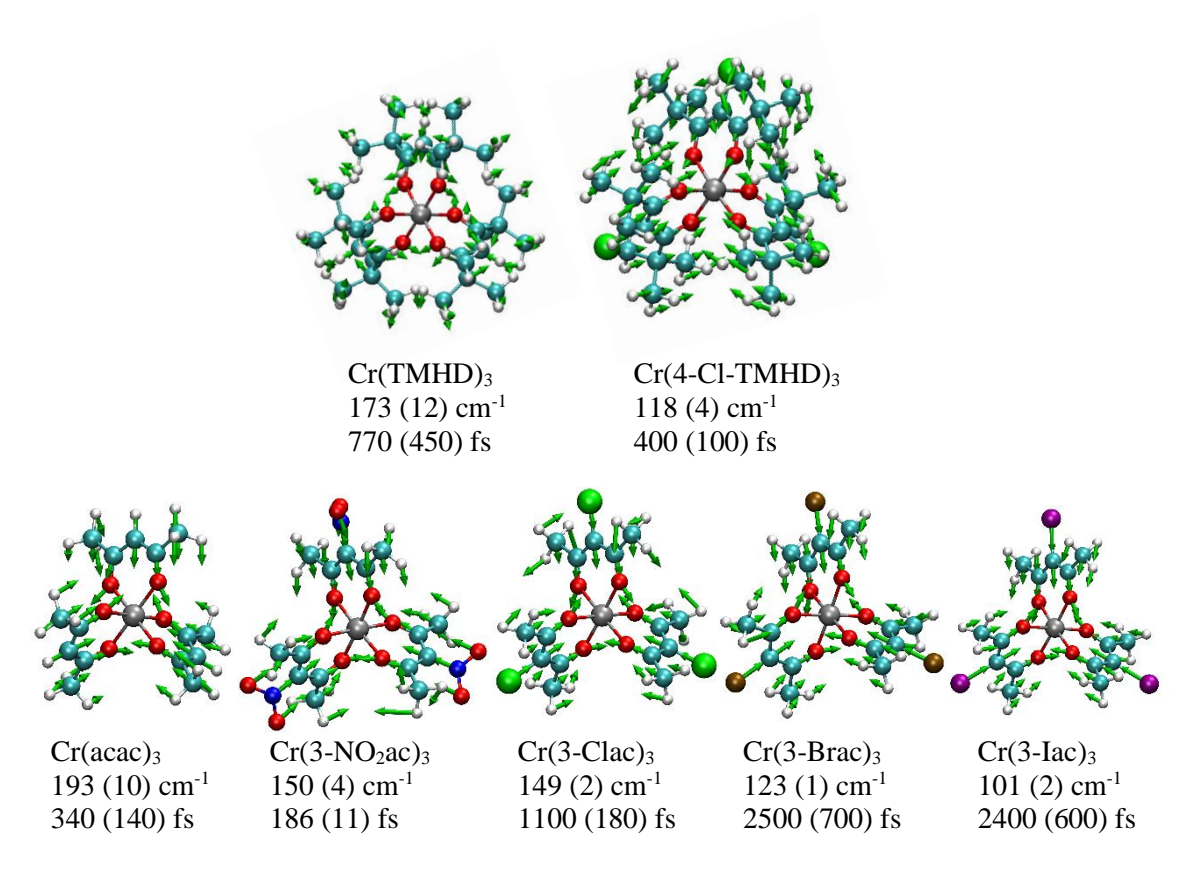


**Figure 2.56.** Summary of the frequencies and dephasing times of the low frequency symmetric breathing mode observed in each Cr(acac')<sub>3</sub> derivative.

dephasing times of the low frequency symmetric breathing mode observed in each complex can be seen in Figure 2.56.

Further studies on the  $Cr(acac)_3$  system may benefit from variable temperature and variable excitation wavelength measurements. It was proposed in the work of Kunttu and coworkers<sup>14</sup> that relaxation from the  ${}^2E$  excited state at long times followed an Arrhenius relationship resulting from thermally activated bISC to the  ${}^4T_2$  state from which ground state recovery could occur via  ${}^4T_2 \rightarrow {}^4A_2$  IC. If so then variable temperature experiments on the set of compounds studied here could provide thermodynamic properties to help describe the  ${}^2E \leftrightarrow {}^4T_2$  equilibrium which may be useful for a more complete quantitative modeling of the excited state dynamics. These results could be combined with variable excitation wavelength experiments that introduce a range of different effective internal temperatures of the  $Cr(acac')_3$  system which in turn determine the quantum yield of ground state recovery at early times due to IC within the

quartet manifold. The combination of these two sets of experiments may provide enough information to accurately and quantitatively describe the excited state dynamics in this class of compounds.

**APPENDICES** 

#### Appendix 2.A. Crystal Structures

The following is the PDB file for the crystal structure of Cr(3-Iac)<sub>3</sub>.

```
HEADER CSD ENTRY sla bcp2005
CRYST1 12.8403 10.1064 16.2581 90.00 105.04 90.00
          0.077880 0.000000 0.020928
                                      0.000000
SCALE1
SCALE2
          0.000000 0.098947 0.000000
                                      0.000000
SCALE3
          0.000000 0.000000 0.063690
                                      0.000000
HETATM
          1 I001 UNK
                           4.300 0.876 -0.286 1.00 2.22
                                                           I
ANISOU
         1 I001 UNK
                          324 290 231 -15
                                             -45
                                                  -92
HETATM 2 I002 UNK
                           5.954 8.926 3.495 1.00 2.11
                       1
ANISOU 2 I002 UNK
                               147 349
                                         -46
                      1
                          304
                                              -13
                                                   56
                                                         I
                           5.373 1.115 9.099 1.00 2.60
HETATM 3 I003 UNK
                                                           I
ANISOU 3 I003 UNK
                      1
                               256
                                    207
                                         -52
                                              -60
                                                         I
                          526
                                                   65
                            5.363 3.587 4.269 1.00 1.08
                                                           Cr
HETATM 4 Cr04 UNK
                       1
ANISOU 4 Cr04 UNK
                      1
                          156
                               105
                                   151
                                           7
                                             -10
                                                   -2
                                                        Cr
HETATM 5 0005 UNK
                            4.062 2.238 3.734 1.00 1.45
                                                           0
                       1
                                         -32
ANISOU 5 0005 UNK
                       1
                           176
                                159
                                     215
                                               27
                                                    -2
                                                         O
                            6.695 4.929 4.763 1.00 1.50
HETATM 6 0006 UNK
                                                            O
                           206
                                     225
                                                   -7
ANISOU 6 O006 UNK
                       1
                                141
                                           4
                                              -44
                                                        0
HETATM 7 0007 UNK
                       1
                            4.387 3.794 5.945 1.00 1.58
                                                            O
ANISOU 7 0007 UNK
                       1
                           244
                                180
                                     177
                                          41
                                                   -9
                                                        O
                                                6
HETATM 8 0008 UNK
                            4.297 5.001
                                        3.439 1.00 1.51
                                                            O
ANISOU 8 0008 UNK
                       1
                                159
                                     228
                                           0
                                              -45
                                                   13
                                                         0
                            6.447 2.192 5.114 1.00 1.57
HETATM 9 0009 UNK
                       1
                                                            O
ANISOU 9 0009 UNK
                                175
                                   207
                                          28
                                                        O
                       1
                           216
                                               -1
                                                   -7
HETATM 10 O00A UNK
                        1
                             6.269 3.361 2.558 1.00 1.50
                                                            0
ANISOU 10 O00A UNK
                        1
                            180
                                187
                                      202
                                          -34
                                                 5
                                                    -25
                                                          0
HETATM 11 C00B UNK
                             5.745 6.848 3.764 1.00 1.30
                                                            C
                            229
                                 90 177
                                         -17
ANISOU 11 C00B UNK
                                                    34
                                               11
HETATM 12 COOC UNK
                             4.573 6.233 3.277 1.00 1.33
                        1
                                                            C
ANISOU 12 COOC UNK
                                140 161
                                           12
                                                -3
                                                     9
                                                         C
                       1
                                                            C
HETATM 13 C00D UNK
                             3.919 1.640 2.627 1.00 1.36
                                                          \mathbf{C}
ANISOU 13 COOD UNK
                            139
                                140
                                     236
                                           28
                                               -45
                                                     -2
HETATM 14 COOE UNK
                             6.761 6.159 4.459 1.00 1.26
                                                            C
                        1
ANISOU 14 C00E UNK
                                 160 142
                                          -30
                                                34
                                                    -7
                                                          C
                       1
                            175
                             5.884 2.718 1.521 1.00 1.42
HETATM 15 COOF UNK
                                                            C
ANISOU 15 COOF UNK
                           179
                                150 211
                                           46
                                               -17
                                                    18
                                                          C
                             4.447 3.082 7.007
                                              1.00 1.41
                                                            C
HETATM 16 COOG UNK
                        1
                            184
                                180 173
                                                 3
ANISOU 16 COOG UNK
                                           -49
                                                   -40
HETATM 17 C00H UNK
                             4.768 1.872 1.512 1.00 1.44
                        1
                                                            C
                                                          C
ANISOU 17 C00H UNK
                        1
                            202
                                190
                                     153
                                           43
                                               -38
                                                            C
HETATM 18 C00I UNK
                            6.365 1.699 6.290 1.00 1.52
                                90
                                    275
                                          14
                                              -59
                                                         C
ANISOU 18 C00I UNK
                       1
                           214
                                                   -13
HETATM 19 C00J UNK
                        1
                            5.388 2.082 7.218 1.00 1.58
                                                            C
ANISOU 19 C00J UNK
                       1
                           275
                                170
                                    154 -30
                                              -53
                                                    74
                                                          C
HETATM 20 COOK UNK
                             3.518 7.004 2.511 1.00 2.16
                                                            \mathbf{C}
                        1
ANISOU 20 COOK UNK
                        1
                                 240 330
                                          -14
                                               -109
                                                           C
                             2.921 6.375 2.054 1.00 3.24
HETATM 21 H00A UNK
                        1
                                                            Η
HETATM 22 H00B UNK
                             3.952 7.582 1.850 1.00 3.24
                        1
                                                            Η
```

```
HETATM 23 H00C UNK
                       1
                           2.997 7.553 3.135 1.00 3.24
                                                        Η
                                                        C
HETATM 24 COOL UNK
                           3.397 3.428 8.025 1.00 2.35
                      1
ANISOU 24 COOL UNK
                          331 350 214
                                        47
                                             74
                                                      \mathbf{C}
                      1
                                                 18
HETATM 25 H00D UNK
                           2.832 4.151 7.680 1.00 3.55
                                                        Η
                       1
HETATM 26 H00E UNK
                       1
                           3.829 3.719 8.855 1.00 3.55
                                                        Η
                           2.844 2.639 8.205 1.00 3.55
HETATM 27 H00F UNK
                       1
                                                        Η
HETATM 28 COOM UNK
                           2.780 0.664 2.573 1.00 1.98
                                                         C
                       1
                                                       C
ANISOU 28 COOM UNK
                          240 150 360 -31 -17 -44
                      1
HETATM 29 H00G UNK
                       1
                           2.470 0.474 3.484 1.00 3.00
                                                        Η
HETATM 30 H00H UNK
                           3.082 -0.167 2.151 1.00 3.00
                                                         Η
HETATM 31 H00I UNK
                          2.045 1.049 2.051 1.00 3.00
                      1
                                                        Η
HETATM 32 COON UNK
                           8.013 6.857 4.885 1.00 2.03
                       1
                                                        C
ANISOU 32 COON UNK
                      1
                          242 220 310 -64 -33
                                                      \mathbf{C}
HETATM 33 H00J UNK
                      1
                          7.806 7.489 5.605 1.00 3.00
                                                        Η
                           8.392 7.343 4.123 1.00 3.00
HETATM 34 H00K UNK
                       1
                                                        Η
HETATM 35 H00L UNK
                           8.662 6.197 5.207 1.00 3.00
                       1
                                                        Η
HETATM 36 C000 UNK
                       1
                           6.743 2.949 0.303 1.00 2.13
                                                        C
ANISOU 36 C000 UNK
                      1
                          249
                              330 231 -16
                                             25 -18
                                                       \mathbf{C}
HETATM 37 H00M UNK
                       1
                           6.196 3.329 -0.416 1.00 3.24
                                                         Η
HETATM 38 HOON UNK
                       1
                           7.125 2.097 0.006 1.00 3.24
                                                         Η
HETATM 39 H000 UNK
                           7.467 3.571 0.526 1.00 3.24
                       1
                                                        Η
HETATM 40 COOP UNK
                      1
                           7.409 0.659 6.593 1.00 2.40
                                                        C
                          363 230 320
                                                       C
ANISOU 40 COOP UNK
                      1
                                        54 -100
HETATM 41 HOOP UNK
                      1
                           6.977 -0.210 6.725 1.00 3.63
                                                        Η
HETATM 42 H000 UNK
                           7.894 0.910 7.408 1.00 3.63
                       1
                                                        Η
                           8.039 0.600 5.844 1.00 3.63
HETATM 43 HOOR UNK
                                                        Η
                       1
CONECT 1 17
CONECT 2 11
CONECT 3 19
CONECT 4 5
              6 7 8
CONECT 4 9 10
CONECT 5 4 13
CONECT 6 4 14
CONECT
        7
           4 16
           4 12
CONECT 8
CONECT 9 4 18
CONECT 10
            4 15
CONECT 11
            2 12
                  14
CONECT 12 8 11
                  20
CONECT 13
            5 17
                  28
CONECT 14 6 11
                  32
CONECT 15 10 17 36
CONECT 16
            7 19 24
CONECT 17
            1 13 15
CONECT 18
            9 19 40
CONECT 19
            3 16 18
CONECT 20 12 21 22 23
CONECT 21 20
CONECT 22
            20
CONECT 23 20
CONECT 24 16 25 26 27
```

```
CONECT 25 24
CONECT 26 24
CONECT 27 24
CONECT 28 13
             29 30 31
CONECT 29 28
CONECT 30 28
CONECT 31 28
CONECT 32 14
             33 34 35
CONECT 33 32
CONECT 34 32
CONECT 35 32
CONECT 36 15 37 38 39
CONECT 37 36
CONECT 38 36
CONECT 39 36
CONECT 40 18 41 42 43
CONECT 41 40
CONECT 42 40
CONECT 43 40
MASTER
         0 0 0 0 0 0 0 3 43
END
```

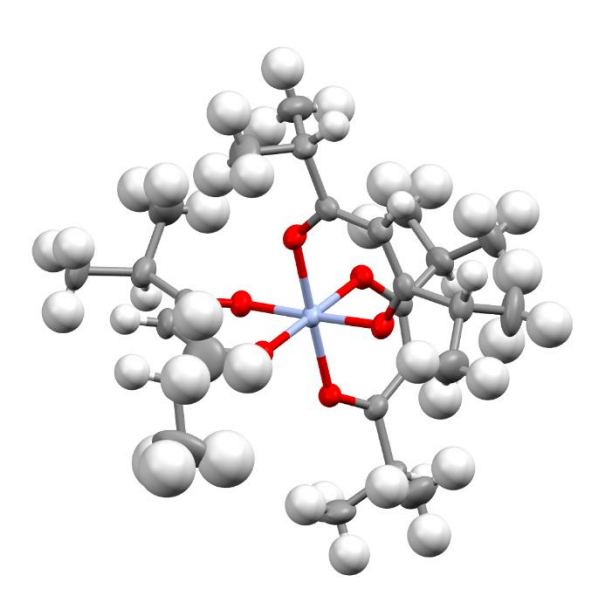


**Figure 2.A.1.** Crystal structure for Cr(DMHD)<sub>3</sub> that was collected by Sara Adelman and solved by Professor Richard Staples.

The Following is the PDB file for the crystal structure of Cr(DMHD)3.

```
HEADER CSD ENTRY sla_bcp_1142
CRYST1 18.7029 15.7164 20.7137 90.00 90.00 90.00 Pbca
SCALE1 0.053468 0.000000 0.000000 0.000000
SCALE2 0.000000 0.063628 0.000000 0.000000
SCALE3 0.000000 0.000000 0.048277 0.000000
HETATM 1 Cr01 UNK 1 4.895 4.757 6.752 1.00 2.20 Cr
```

```
ANISOU 1 Cr01 UNK
                          352 255 228 -32 -58
                      1
                                                   11
                                                        Cr
                            3.923 6.224 5.911 1.00 2.54
HETATM 2 0002 UNK
                       1
                                                           0
ANISOU 2 0002 UNK
                           404 287
                                    274
                                          10
                                              -38
                                                         O
                       1
                                                    4
                            6.158 5.949 7.665 1.00 2.52
HETATM 3 O003 UNK
                       1
                                                           0
ANISOU 3 0003 UNK
                       1
                           373
                               342 241
                                         -71
                                              -36
                                                         0
                            6.108 4.680 5.219 1.00 2.81
HETATM 4 O004 UNK
                       1
                                                           O
                                380
                                    288
                                              -33
ANISOU 4 O004 UNK
                                          31
                                                   -22
                                                         O
                       1
                           401
HETATM 5 0005 UNK
                            3.678 4.850 8.287 1.00 2.83
                                                           0
                       1
ANISOU 5 0005 UNK
                       1
                           382
                               428
                                    264
                                         -93
                                              -22
                                                    32
                                                         0
HETATM 6 0006 UNK
                            3.665 3.536 5.858 1.00 2.77
                                                           O
ANISOU 6 O006 UNK
                       1
                           423
                                289 341 -39 -122
                                                         0
                            5.830 3.257 7.592 1.00 3.00
HETATM 7 0007 UNK
                       1
                                                           O
ANISOU 7 0007 UNK
                           461
                                311
                                    368 -22 -139
                                                          O
                       1
HETATM 8 C008 UNK
                       1
                            3.591 2.274 6.012 1.00 2.51
                                                           C
ANISOU 8 C008 UNK
                      1
                          389
                               306
                                   259
                                         -45
                                               44
                                                         C
                                                           C
HETATM 9 C009 UNK
                            3.887 6.475 4.653 1.00 2.70
                       1
ANISOU 9 C009 UNK
                          443
                              270 311
                                         -61
                                              -86
                                                         C
                      1
                                                    15
HETATM 10 C00A UNK
                             6.219 6.124 8.928 1.00 2.63
                                                            \mathbf{C}
                        1
                                                          \mathbf{C}
ANISOU 10 C00A UNK
                       1
                            375
                                330 295
                                           17
                                               -52
                                                   -34
                             3.982 5.251 9.457 1.00 2.86
HETATM 11 C00B UNK
                                                            C
                                                         C
ANISOU 11 C00B UNK
                           422 364 300
                                          -11
                                                9
                                                    34
HETATM 12 COOC UNK
                        1
                             5.515 2.023 7.523 1.00 2.61
                                                            C
ANISOU 12 COOC UNK
                           406
                               313 273
                                           41
                                               48
                                                    20
                                                          C
                       1
HETATM 13 C00D UNK
                             4.450 1.508 6.802 1.00 2.71
                                                            C
                        1
                                                         \mathbf{C}
ANISOU 13 C00D UNK
                            410 269 351
                                           -1
                                                1
HETATM 14 H00D UNK
                             4.292 0.572 6.848 1.00 3.24
                        1
                                                            Η
HETATM 15 COOE UNK
                        1
                             5.894 5.192 4.069 1.00 2.94
                                                            C
ANISOU 15 COOE UNK
                       1
                           464
                               395 259
                                          -56
                                                5
                                                   -36
                                                         \mathbf{C}
HETATM 16 COOF UNK
                            7.525 6.686 9.440 1.00 3.35
                                                            C
ANISOU 16 COOF UNK
                           390
                               560 322 -52
                                               -65
                                                          C
HETATM 17 H00F UNK
                        1
                            7.418 6.928 10.404 1.00 4.03
                                                            Η
HETATM 18 COOG UNK
                             4.811 5.993 3.742 1.00 3.21
                                                            C
                        1
ANISOU 18 COOG UNK
                       1
                           535 442 244
                                            3
                                               -49
                                                    46
                                                         \mathbf{C}
HETATM 19 H00G UNK
                        1
                             4.694 6.228 2.829 1.00 3.87
                                                            Η
HETATM 20 C00H UNK
                        1
                             5.195 5.818 9.811 1.00 3.11
                                                            C
ANISOU 20 C00H UNK
                       1
                           432 499 251 -37
                                               -26
HETATM 21 H00H UNK
                        1
                             5.338 6.012 10.730 1.00 3.71
                                                            Η
HETATM 22 C00I UNK
                       1
                            6.412 1.089 8.322 1.00 3.33
                                                           \mathbf{C}
ANISOU 22 C00I UNK
                       1
                           540 332 393
                                          84
                                              -80
                                                         C
HETATM 23 H00I UNK
                            6.146 0.146 8.124 1.00 4.03
                                                           Η
                       1
HETATM 24 C00J UNK
                            2.906 5.039 10.513 1.00 3.66
                                                            C
                       1
ANISOU 24 C00J UNK
                           499
                                556
                                    337
                                         -90
                                               87
                       1
                                                    6
                                                         C
HETATM 25 H00J UNK
                            3.086 5.667 11.270 1.00 4.42
                        1
                                                            Η
HETATM 26 COOK UNK
                             2.729 7.362 4.242 1.00 3.46
                                                            C
ANISOU 26 COOK UNK
                                369 402
                                           56 -138
                       1
                            542
                                                          C
HETATM 27 HOOK UNK
                        1
                             2.805 8.215 4.758 1.00 4.18
                                                            H
HETATM 28 COOL UNK
                        1
                             2.470 1.616 5.236 1.00 3.37
                                                            C
ANISOU 28 COOL UNK
                                375
                                     396 -123
                                                          \mathbf{C}
                       1
                           508
                                               -91
HETATM 29 H00L UNK
                        1
                             2.435 0.648 5.481 1.00 4.03
                                                            Η
                             6.951 4.891 3.027 1.00 4.50
                                                            C
HETATM 30 C00M UNK
                         1
ANISOU 30 C00M UNK
                            626 720 363 126 103 -16
                                                           \mathbf{C}
                        1
```

```
HETATM 31 H00M UNK
                        1
                            6.632 5.237 2.146 1.00 5.37
                                                           Η
HETATM 32 COON UNK
                            7.938 7.929 8.662 1.00 4.63
                                                           C
                        1
ANISOU 32 COON UNK
                           494 573 691 -175 -127 -76
                                                          C
                       1
                            7.986 7.715 7.708 1.00 6.95
                                                           Η
HETATM 33 H00A UNK
                        1
HETATM 34 H00B UNK
                        1
                            8.817 8.232 8.973 1.00 6.95
                                                           Η
HETATM 35 H00C UNK
                        1
                            7.277 8.639 8.807 1.00 6.95
                                                           Η
                            8.593 5.602 9.318 1.00 5.25
                                                           C
HETATM 36 C000 UNK
                        1
                                                         C
ANISOU 36 C000 UNK
                           450 786 758
                                          92 -196 -62
                       1
HETATM 37 H00E UNK
                        1
                            8.325
                                 4.819 9.841 1.00 7.90
                                                          Η
HETATM 38 HOON UNK
                        1
                            9.447 5.944 9.657 1.00 7.90
                                                           H
HETATM 39 H000 UNK
                        1
                            8.693 5.347 8.377 1.00 7.90
                                                           Η
                            1.141 2.260 5.589 1.00 5.03
                                                          C
HETATM 40 COOP UNK
                       1
ANISOU 40 COOP UNK
                           448
                              593 870 -88 -172
                                                         C
                       1
HETATM 41 HOOP UNK
                       1
                            1.001 2.207 6.558 1.00 7.58
                                                          Η
HETATM 42 H000 UNK
                        1
                            0.417 1.789 5.127 1.00 7.58
                                                           Η
                            1.148 3.200 5.311 1.00 7.58
HETATM 43 HOOR UNK
                                                           Η
                        1
HETATM 44 C00Q UNK
                        1
                            7.868 1.276 7.917 1.00 5.21
                                                           C
ANISOU 44 C000 UNK
                           519 591 870 115 -150
                                                          C
                       1
HETATM 45 HOOS UNK
                       1
                            7.966 1.095 6.958 1.00 7.82
                                                          Η
HETATM 46 H00T UNK
                        1
                            8.431 0.655 8.424 1.00 7.82
                                                          Η
HETATM 47 H00U UNK
                            8.143 2.197 8.105 1.00 7.82
                        1
                                                           Η
HETATM 48 COOR UNK
                        1
                            1.522 5.328 9.984 1.00 5.61
                                                           C
                           500 790 840
                                                         C
ANISOU 48 COOR UNK
                                         68
                                             214
                       1
HETATM 49 H00V UNK
                            1.498 6.235 9.611 1.00 8.45
                                                           Η
                        1
HETATM 50 HOOW UNK
                             0.873 5.257 10.715 1.00 8.45
                                                            Η
HETATM 51 H00X UNK
                            1.298 4.680 9.284 1.00 8.45
                        1
                                                           Η
HETATM 52 COOS UNK
                            2.685 7.727 2.758 1.00 4.96
                                                          C
                       1
                                                          \mathbf{C}
ANISOU 52 COOS UNK
                           820
                               563 502 133 -244 126
                       1
HETATM 53 H00Y UNK
                            3.505 8.206 2.515 1.00 7.42
                                                           Η
HETATM 54 H UNK
                           1.908 8.300 2.585 1.00 7.42
                                                         Η
                           2.613 6.909 2.223 1.00 7.42
HETATM 55 HA UNK
                                                          Η
HETATM 56 C00T UNK
                            1.432 6.684 4.664 1.00 5.66
                                                          C
                       1
ANISOU 56 COOT UNK
                               850 840 119 -123 168
                                                          \mathbf{C}
                       1
                            1.348 5.823 4.205 1.00 8.45
HETATM 57 H00Z UNK
                                                          Η
                           0.673 7.256 4.424 1.00 8.45
HETATM 58 HB UNK
                                                          Η
HETATM 59 HC UNK
                           1.440 6.540 5.632 1.00 8.45
                                                          Η
                       1
HETATM 60 C00U UNK
                            2.758 1.735 3.744 1.00 5.50
                                                           C
                        1
ANISOU 60 COOU UNK
                       1
                           1060 633 395 -214 -188 -83
                                                          \mathbf{C}
HETATM 61 H00 UNK
                           2.837 2.681 3.501 1.00 8.21
                                                          Η
                       1
                                                          Η
HETATM 62 HD UNK
                           2.026 1.328 3.238 1.00 8.21
HETATM 63 HE UNK
                       1
                           3.597 1.273 3.536 1.00 8.21
                                                          Η
HETATM 64 C00V UNK
                            3.007 3.627 11.039 1.00 5.42
                        1
                                                           C
ANISOU 64 C00V UNK
                           710 696 655
                                                         \mathbf{C}
                       1
                                           2 167 301
                                                            Η
HETATM 65 HOAA UNK
                             2.850 2.994 10.307 1.00 8.13
HETATM 66 HF UNK
                           2.334 3.491 11.738 1.00 8.13
                      1
                                                          Η
HETATM 67 HG UNK
                           3.901 3.481 11.413 1.00 8.13
                                                          Η
HETATM 68 C00W UNK
                        1
                             6.204 1.349 9.803 1.00 5.97
                                                           C
ANISOU 68 COOW UNK
                                635 382 323 -136
                                                          \mathbf{C}
                       1
                           1250
HETATM 69 H1AA UNK
                             6.424 2.282 10.005 1.00 8.92
                                                            H
                           6.785 0.756 10.324 1.00 8.92
HETATM 70 HH UNK
                                                          Η
                      1
HETATM 71 HI UNK
                          5.269 1.177 10.036 1.00 8.92
                                                         Η
                      1
```

```
HETATM 72 C00X UNK 1
                         7.178 3.420 2.900 1.00 6.97
                                                    \mathbf{C}
                       1070 840 740 230 180 -323
                                                    C
ANISOU 72 C00X UNK 1
HETATM 73 H2AA UNK 1
                         7.485 3.060 3.760 1.00 10.42
                                                     Η
HETATM 74 HJ UNK 1
                       7.861 3.252 2.216 1.00 10.42
                                                   Η
                        6.342 2.980 2.643 1.00 10.42
HETATM 75 HK UNK 1
                                                   Η
HETATM 76 C00Y UNK 1
                         8.217 5.614 3.387 1.00 9.19
                                                    C
ANISOU 76 C00Y UNK 1
                        750 1110 1630 -250 690 -350
                                                    \mathbf{C}
                         8.055 6.580 3.374 1.00 13.74
HETATM 77 H3AA UNK 1
                                                    Η
HETATM 78 HL UNK 1
                        8.916 5.391 2.738 1.00 13.74
                                                   Н
HETATM 79 HM UNK 1
                        8.504 5.342 4.284 1.00 13.74
                                                    Η
CONECT 1 2 3 4 5
CONECT 1 6
            7
CONECT 2 1 9
CONECT 3 1 10
CONECT 4 1 15
CONECT 5 1 11
CONECT 6 1 8
CONECT 7 1 12
CONECT 8 6 13 28
CONECT 9 2 18 26
CONECT 10 3 16 20
CONECT 11 5 20 24
CONECT 12 7 13 22
CONECT 13 8 12 14
CONECT 14 13
CONECT 15 4 18 30
CONECT 16 10 17 32 36
CONECT 17 16
CONECT 18 9 15 19
CONECT 19 18
CONECT 20 10 11 21
CONECT 21 20
CONECT 22 12 23 44 68
CONECT 23 22
CONECT 24 11 25 48 64
CONECT 25 24
CONECT 26 9 27 52 56
CONECT 27 26
CONECT 28 8 29 40 60
CONECT 29 28
CONECT 30 15 31 72 76
CONECT 31 30
CONECT 32 16 33 34 35
CONECT 33 32
CONECT 34 32
CONECT 35 32
CONECT 36 16 37 38 39
CONECT 37 36
CONECT 38 36
CONECT 39 36
CONECT 40 28 41 42 43
```

```
CONECT 41 40
CONECT 42 40
CONECT 43 40
CONECT 44 22 45 46 47
CONECT 45 44
CONECT 46 44
CONECT 47 44
CONECT 48 24
             49 50 51
CONECT 49 48
CONECT 50 48
CONECT 51 48
CONECT 52 26 53 54 55
CONECT 53 52
CONECT 54 52
CONECT 55 52
CONECT 56 26 57 58 59
CONECT 57 56
CONECT 58 56
CONECT 59 56
CONECT 60 28
             61 62 63
CONECT 61 60
CONECT 62 60
CONECT 63 60
CONECT 64 24
             65 66 67
CONECT 65 64
CONECT 66 64
CONECT 67 64
CONECT 68 22 69 70 71
CONECT 69 68
CONECT 70 68
CONECT 71 68
CONECT 72 30 73 74 75
CONECT 73 72
CONECT 74 72
CONECT 75 72
CONECT 76 30 77 78 79
CONECT 77 76
CONECT 78 76
CONECT 79 76
MASTER
          0 0 0 0 0 0 0 3 79 0 80 0
END
```

The Following is a PDB file for the crystal structure of Cr(4-Cl-TMHD)<sub>3</sub>. The structure is quite disordered

but still shows that the compound was made.

```
HEADER CSD ENTRY jkm519a
CRYST1 18.4350 12.4657 18.8857 90.00 118.96 90.00 P21/n
SCALE1 0.054245 0.000000 0.030024 0.000000
SCALE2 0.000000 0.080220 0.000000 0.000000
SCALE3 0.000000 0.000000 0.060520 0.000000
```

```
HETATM 1 Cr1 UNK
                          2.600 4.347 12.216 1.00 4.13
                    1
                                                        Cr
                         518 401 650
                                       47
ANISOU 1 Cr1 UNK
                     1
                                             8 -15
                                                     Cr
HETATM 2 Cl1 UNK
                          2.177 9.356 12.105 1.00 10.24
                     1
                                                        Cl
ANISOU 2 Cl1 UNK
                        2495 437 960 278
                     1
                                             6
                                                 26
                                                      Cl
HETATM 3 O1 UNK
                          2.772 5.774 13.511 1.00 4.37
                                                         0
ANISOU 3 O1 UNK
                     1
                         662 462 536
                                        67
                                           -38
                                                 27
                                                      0
                          2.800 5.719 10.859 1.00 4.44
HETATM 4 O2 UNK
                     1
                                                         O
ANISOU 4 O2 UNK
                         626 524 537
                                        73
                                            6
                                               -14
                                                     0
                     1
HETATM 5 C1 UNK
                          2.508 7.009 13.397 1.00 4.42
                                                        C
ANISOU 5 C1 UNK
                         552 511
                                  617
                                        64
                                            22
                                                -29
                                                      C
                     1
HETATM 6 C2 UNK
                     1
                          2.404 7.617 12.143 1.00 4.70
                                                        C
ANISOU 6 C2 UNK
                        641
                             508 635
                                       64
                                           -26
                                                      C
                     1
                                                 16
HETATM 7 C3 UNK
                          2.567 6.960 10.914 1.00 4.60
                                                        C
                     1
ANISOU 7 C3 UNK
                         568
                             564 617
                                       51
                                            21
                                                58
                                                      C
HETATM 8 C4 UNK
                          2.265 7.696 14.749 1.00 5.01
                                                        C
ANISOU 8 C4 UNK
                     1
                         666 589 650
                                       84 -26
                                               -68
HETATM 9 C5 UNK
                     1
                          2.284 6.631 15.844 1.00 9.32
                                                        C
ANISOU 9 C5 UNK
                        1851 1110 580 376
                                             68 -40
                                                       \mathbf{C}
                     1
HETATM 10 H5A UNK
                       1
                           1.670 5.906 15.605 1.00 13.98
                                                          Η
                           2.004 7.030 16.694 1.00 13.98
HETATM 11 H5B UNK
                      1
                                                          Η
HETATM 12 H5C UNK
                           3.192 6.273 15.935 1.00 13.98
                       1
                                                          Η
HETATM 13 C6 UNK
                      1
                          3.329 8.730 15.053 1.00 8.29
                                                         C
                                                        \mathbf{C}
ANISOU 13 C6 UNK
                     1
                         811 1240 1100
                                         1 -152 -580
HETATM 14 H6A UNK
                           4.183 8.281 15.218 1.00 12.48
                                                          Η
                       1
HETATM 15 H6B UNK
                           3.069 9.241 15.849 1.00 12.48
                      1
                                                          Η
HETATM 16 H6C UNK
                           3.420 9.339 14.291 1.00 12.48
                       1
                                                          H
HETATM 17 C7 UNK
                          0.864 8.337 14.795 1.00 7.37
                                                         C
                      1
ANISOU 17 C7 UNK
                         711 1050 1040 90 156 -410
                                                        \mathbf{C}
                     1
HETATM 18 H7A UNK
                       1
                           0.804 9.040 14.115 1.00 11.05
                                                          Η
HETATM 19 H7B UNK
                      1
                           0.712 8.727 15.682 1.00 11.05
                                                          Η
HETATM 20 H7C UNK
                           0.186 7.652 14.619 1.00 11.05
                       1
                                                          Η
HETATM 21 C8 UNK
                          2.451 7.618 9.518 1.00 5.30
                      1
                                                        C
ANISOU 21 C8 UNK
                     1
                         702 650 660 46 -50 100
                                                       C
HETATM 22 C9 UNK
                                                        C
                     1
                          3.591 8.621 9.293 1.00 8.06
ANISOU 22 C9 UNK
                     1
                         1063 1180 820 -192 -42 450
                                                         C
HETATM 23 H9A UNK
                       1
                           3.473 9.388 9.892 1.00 12.08
                                                          Η
HETATM 24 H9B UNK
                       1
                           3.576 8.929 8.363 1.00 12.08
                                                          Η
HETATM 25 H9C UNK
                       1
                           4.449 8.188 9.481 1.00 12.08
                                                          Η
HETATM 26 C10 UNK
                      1
                           1.079 8.262 9.328 1.00 7.83
                                                         C
                         983 1040 950 210 -160 240
                                                         C
ANISOU 26 C10 UNK
                      1
HETATM 27 H10A UNK
                       1
                            0.382 7.640 9.625 1.00 11.76
                                                          Η
HETATM 28 H10B UNK
                       1
                            0.946 8.472 8.379 1.00 11.76
                                                          Η
HETATM 29 H10C UNK
                            1.029 9.086 9.854 1.00 11.76
                       1
                                                          Η
HETATM 30 C11 UNK
                           2.576 6.491 8.445 1.00 7.83
                                                         C
                      1
                         1244 1200 530 132
ANISOU 30 C11 UNK
                                               4 50
                                                        C
                      1
HETATM 31 H11A UNK
                       1
                            3.415 6.004 8.580 1.00 11.69
                                                          Η
                            2.568 6.890 7.550 1.00 11.69
HETATM 32 H11B UNK
                       1
                                                          H
HETATM 33 H11C UNK
                            1.821 5.872 8.533 1.00 11.69
                      1
                                                          Η
HETATM 34 Cl2 UNK
                      1
                          4.675 0.015 13.140 0.75 7.50
                                                        Cl
                         944 485 1419 199 483 132
                                                        Cl
ANISOU 34 C12 UNK
                     1
HETATM 35 Cl3 UNK 1
                         -1.407 2.057 10.093 0.75 7.95
                                                         Cl
```

```
ANISOU 35 Cl3 UNK
                     1
                         659 1014 1349 -108 18 -408
                                                        Cl
HETATM 36 O3 UNK
                          2.311 3.040 13.620 0.75 4.71
                      1
                                                         O
ANISOU 36 O3 UNK
                         490 440 860
                                        13
                     1
                                             4
                                                100
                                                      0
HETATM 37 O4 UNK
                          4.482 3.852 12.356 0.75 4.16
                      1
                                                         0
ANISOU 37 O4 UNK
                     1
                         508 434 640
                                        17
                                            -46
                                                      \mathbf{O}
                          0.673 4.556 12.254 0.75 4.36
HETATM 38 O5 UNK
                      1
                                                         O
ANISOU 38 O5 UNK
                         537 480 640
                                            34
                     1
                                        86
                                                 10
                                                      O
HETATM 39 O6 UNK
                          2.274 2.959 10.892 0.75 4.58
                                                         0
                      1
ANISOU 39 O6 UNK
                     1
                         479 480 780 -42
                                             71
                                               -130
                                                       0
                           2.940 1.968 13.863 0.75 4.46
HETATM 40 C12 UNK
                                                         C
                                                       C
ANISOU 40 C12 UNK
                      1
                         535 482 679
                                        28
                                            112
                                                  40
HETATM 41 C13 UNK
                           4.132 1.687 13.184 0.75 4.52
                      1
                                                         C
ANISOU 41 C13 UNK
                      1
                         541 489
                                   687
                                        53
                                            104
                                                  26
                                                       C
HETATM 42 C14 UNK
                      1
                           4.927 2.679 12.581 0.75 4.57
                                                         C
ANISOU 42 C14 UNK
                      1
                         522 533
                                   682
                                         35
                                            115
                                                       C
HETATM 43 C15 UNK
                      1
                           2.233 1.017 14.865 0.75 4.56
                                                         C
ANISOU 43 C15 UNK
                     1
                         548 495
                                  690
                                        13
                                            105
                                                  63
                                                       C
HETATM 44 C16 UNK
                           1.169 1.827 15.618 0.75 5.52
                                                         C
                      1
ANISOU 44 C16 UNK
                     1
                         758 640 700
                                        44
                                            184
                                                        C
HETATM 45 H16A UNK
                            1.602 2.545 16.124 0.75 8.29
                       1
                                                          Η
HETATM 46 H16B UNK
                            0.686 1.238 16.236 0.75 8.29
                       1
                                                          Η
HETATM 47 H16C UNK
                       1
                            0.537 2.215 14.977 0.75 8.29
                                                          Η
HETATM 48 C17 UNK
                      1
                           1.494 -0.026 14.014 0.75 6.26
                                                         C
ANISOU 48 C17 UNK
                     1
                         948 630 800 -211 220
                                                  30
                                                        C
HETATM 49 H17A UNK
                            0.770 0.411 13.517 0.75 9.32
                       1
                                                          Η
HETATM 50 H17B UNK
                       1
                            1.118 -0.718 14.598 0.75 9.32
                                                          Η
HETATM 51 H17C UNK
                       1
                            2.121 -0.437 13.383 0.75 9.32
                                                          Н
                           3.186 0.425 15.904 0.75 6.17
                                                         \mathbf{C}
HETATM 52 C18 UNK
                      1
ANISOU 52 C18 UNK
                     1
                         805 760 780 73
                                             48
                                                260
                                                       C
HETATM 53 H18A UNK
                       1
                            3.751 -0.253 15.479 0.75 9.24
                                                          Η
HETATM 54 H18B UNK
                       1
                            2.666 0.012 16.625 0.75 9.24
                                                          Η
HETATM 55 H18C UNK
                       1
                            3.749 1.137 16.272 0.75 9.24
                                                          Η
HETATM 56 C19 UNK
                      1
                           6.389 2.498 12.191 0.75 4.66
                                                         C
                                                       C
                         516 565 690 30 120
ANISOU 56 C19 UNK
                     1
                           7.094 1.720 13.310 0.75 7.75
                                                         C
HETATM 57 C20 UNK
                      1
ANISOU 57 C20 UNK
                     1
                         1264 810 870 178
                                                       \mathbf{C}
                                             -1
                                                  70
HETATM 58 H20A UNK
                            7.099 2.259 14.129 0.75 11.61
                                                           Η
                      1
HETATM 59 H20B UNK
                       1
                            8.017 1.526 13.042 0.75 11.61
                                                           Η
HETATM 60 H20C UNK
                       1
                            6.617 0.880 13.474 0.75 11.61
                                                           Η
HETATM 61 C21 UNK
                           6.458 1.631 10.904 0.75 6.15
                                                         C
                      1
ANISOU 61 C21 UNK 1
                         567 900 870 45 239 -60
HETATM 62 H21A UNK
                            6.360 0.685 11.141 0.75 9.24
                      1
                                                          Η
HETATM 63 H21B UNK
                            7.323 1.767 10.463 0.75 9.24
                       1
                                                          Η
                            5.737 1.891 10.295 0.75 9.24
HETATM 64 H21C UNK
                       1
                                                          Η
                           7.083 3.795 12.031 0.75 6.90
HETATM 65 C22 UNK
                                                         C
                      1
ANISOU 65 C22 UNK 1
                         560 820 1240 -56 -23
                                                  80
HETATM 66 H22A UNK
                      1
                            6.727 4.260 11.244 0.75 10.34
                                                           Η
HETATM 67 H22B UNK
                            8.043 3.640 11.912 0.75 10.34
                      1
                                                           Η
HETATM 68 H22C UNK
                       1
                            6.936 4.344 12.828 0.75 10.34
                                                           Η
                          -0.264 3.851 11.771 0.75 4.71
HETATM 69 C23 UNK
                                                         C
                      1
ANISOU 69 C23 UNK 1
                         530 572 687
                                        20
                                            82
                                                  7
                                                      C
```

```
HETATM 70 C24 UNK
                           -0.008 2.852 10.833 0.75 4.76
                                                            \mathbf{C}
ANISOU 70 C24 UNK
                           556 554 700 -20
                                               66
                                                         C
                       1
                                                    -4
HETATM 71 C25 UNK
                            1.266 2.487 10.390 0.75 4.76
                                                            \mathbf{C}
                       1
ANISOU 71 C25 UNK
                                    699 -10
                                                         \mathbf{C}
                       1
                           566 545
                                               73
                                                   -34
                           -1.657 4.149 12.393 0.75 4.88
HETATM 72 C26 UNK
                                                            C
ANISOU 72 C26 UNK
                       1
                           555 600 700
                                          38
                                               69
                                                   -5
HETATM 73 C27 UNK
                           -1.446 5.257 13.460 0.75 7.77
                                                            C
                       1
ANISOU 73 C27 UNK
                           652 1430 870 211
                                                79 -320
                                                           \mathbf{C}
                       1
HETATM 74 H27A UNK
                            -0.888 4.909 14.187 0.75 11.69
                                                              Η
                        1
HETATM 75 H27B UNK
                        1
                            -2.314 5.535 13.820 0.75 11.69
                                                             Η
HETATM 76 H27C UNK
                            -1.001 6.027 13.048 0.75 11.69
                        1
                                                             Η
                           -2.585 4.773 11.342 0.75 6.78
HETATM 77 C28 UNK
                       1
                                                            C
ANISOU 77 C28 UNK
                           677 980 920 216 -63
                                                          \mathbf{C}
                       1
                                                   -60
HETATM 78 H28A UNK
                        1
                            -2.133 5.530 10.914 0.75 10.19
                                                             Η
HETATM 79 H28B UNK
                        1
                            -3.407 5.086 11.775 0.75 10.19
                                                             Η
HETATM 80 H28C UNK
                            -2.809 4.101 10.664 0.75 10.19
                        1
                                                             Η
HETATM 81 C29 UNK
                           -2.285 2.947 13.022 0.75 7.77
                                                            C
                       1
                                                           \mathbf{C}
ANISOU 81 C29 UNK
                           732 1240 980
                                          48
                                               201
                       1
HETATM 82 H29A UNK
                        1
                            -2.935 2.555 12.401 0.75 11.69
                                                              Η
HETATM 83 H29B UNK
                        1
                            -2.741 3.210 13.848 0.75 11.69
                                                             Η
HETATM 84 H29C UNK
                            -1.591 2.286 13.228 0.75 11.69
                        1
                                                             Η
HETATM 85 C30 UNK
                       1
                            1.558 1.466 9.266 0.75 5.01
                                                           C
                                                         \mathbf{C}
ANISOU 85 C30 UNK
                           614
                               569 720
                                          10
                                               48
                                                  -61
                       1
                                                           C
HETATM 86 C31 UNK
                            0.904 1.948 7.900 0.75 7.02
                       1
                          1236 850 580 -161
                                                          \mathbf{C}
ANISOU 86 C31 UNK
                                                45 -40
HETATM 87 H31A UNK
                            -0.062 2.066 8.024 0.75 10.58
                        1
                                                             H
HETATM 88 H31B UNK
                        1
                             1.063 1.275 7.205 0.75 10.58
                                                             Η
                             1.304 2.800 7.628 0.75 10.58
HETATM 89 H31C UNK
                        1
                                                             H
HETATM 90 C32 UNK
                       1
                            1.059 0.067 9.648 0.75 6.34
                                                           C
ANISOU 90 C32 UNK
                           918 620 870 142 -173 -70
                                                          \mathbf{C}
                             1.425 -0.183 10.522 0.75 9.47
HETATM 91 H32A UNK
                        1
                                                             Η
HETATM 92 H32B UNK
                        1
                             1.354 -0.580 8.973 0.75 9.47
                                                            H
HETATM 93 H32C UNK
                        1
                             0.080 0.070 9.692 0.75 9.47
                                                            Η
                            3.056 1.421 9.014 0.75 7.78
HETATM 94 C33 UNK
                       1
                                                           C
                           805 1100 1050 -21 139 -520
                                                           \mathbf{C}
ANISOU 94 C33 UNK
HETATM 95 H33A UNK
                        1
                             3.398 2.334 8.920 0.75 11.69
                                                             Η
HETATM 96 H33B UNK
                        1
                             3.233 0.919 8.191 0.75 11.69
                                                             H
HETATM 97 H33C UNK
                        1
                             3.501 0.981 9.768 0.75 11.69
                                                             Η
HETATM 98 Cl2B UNK
                            4.564 0.014 11.072 0.25 7.50
                                                            Cl
ANISOU 98 C12B UNK
                           944 485 1419 199 483
                                                           Cl
                       1
                                                    132
HETATM 99 Cl3B UNK
                            -1.213 2.132 14.366 0.25 7.95
                                                            Cl
                        1
ANISOU 99 Cl3B UNK
                           659 1014 1349 -108
                                                 18 -408
                                                           Cl
                       1
HETATM 100 O3B UNK
                             2.539 3.091 13.698 0.25 4.71
                        1
                                                             0
ANISOU 100 O3B UNK
                            490 440 860
                                           30
                                                4
                                                    90
                                                         0
HETATM 101 O4B UNK
                             0.707 4.774 12.112 0.25 4.36
                                                             0
ANISOU 101 O4B UNK
                        1
                            537 480 640
                                           86
                                                34
                                                    10
                                                          O
HETATM 102 O5B UNK
                        1
                             4.462 3.827 11.918 0.25 4.28
                                                             O
ANISOU 102 O5B UNK
                            536 440 650
                       1
                                           17
                                               -63
                                                     10
                                                          0
HETATM 103 O6B UNK
                        1
                             2.454 3.191 10.654 0.25 4.54
                                                             O
ANISOU 103 O6B UNK
                        1
                            466 480 780 -37
                                                83 -140
                                                           O
HETATM 104 C12B UNK 1
                             1.446 2.474 13.855 0.25 4.63
                                                             C
```

```
ANISOU 104 C12B UNK
                            560 507 690
                                            20
                                                 94
                                                     47
                             0.152 2.916 13.577 0.25 4.83
                                                              C
HETATM 105 C13B UNK
                         1
ANISOU 105 C13B UNK
                                                           C
                        1
                            584 550
                                      700
                                            18
                                                 70
                                                     30
                             -0.152 3.985 12.614 0.25
                                                              \mathbf{C}
HETATM 106 C14B UNK
                         1
                                                    4.84
ANISOU 106 C14B UNK
                            557 580
                                      700
                                            27
                                                 70
                                                      9
                                                          C
HETATM 107 C15B UNK
                         1
                              1.761 1.295 14.830 0.25 4.61
                                                              C
ANISOU 107 C15B UNK
                            563
                                 498
                                      690
                                            18
                                                103
                                                      55
                        1
                                                           C
HETATM 108 C16B UNK
                              1.288 -0.087 14.359 0.25 5.75
                                                              C
                         1
ANISOU 108 C16B UNK
                            956
                                560 670 -107
                                                 155
                                                      70
                                                            C
HETATM 109 H16D UNK
                              0.471 -0.328 14.852 0.25 8.69
                                                              Η
HETATM 110 H16E UNK
                         1
                              1.985 -0.746 14.547 0.25 8.69
                                                              Η
HETATM 111 H16F UNK
                         1
                             1.100 -0.058 13.405 0.25 8.69
                                                              Η
HETATM 112 C17B UNK
                             3.286 1.195 14.980 0.25 6.90
                                                              C
                         1
ANISOU 112 C17B UNK
                        1
                            1062
                                  690 870
                                            -8 -162
                                                      180
                                                            C
HETATM 113 H17D UNK
                              3.715 1.475 14.145 0.25 10.34
                                                              Η
HETATM 114 H17E UNK
                         1
                              3.534 0.268 15.181 0.25 10.34
                                                              Η
HETATM 115 H17F UNK
                         1
                             3.581 1.777 15.711 0.25 10.34
                                                              Η
HETATM 116 C18B UNK
                              1.190 1.558 16.215 0.25 6.16
                                                              C
                         1
ANISOU 116 C18B UNK
                            939 680 720 179
                                                -33
                                                     110
                                                            C
HETATM 117 H18D UNK
                              1.913 1.530 16.876 0.25 9.24
                                                              Η
                             0.519 0.884 16.428 0.25 9.24
HETATM 118 H18E UNK
                         1
                                                              Η
HETATM 119 H18F UNK
                         1
                             0.775 2.451 16.229 0.25 9.24
                                                              Η
HETATM 120 C19B UNK
                         1
                             -1.558 4.510 12.247 0.25 4.85
                                                              C
                                                          \mathbf{C}
ANISOU 120 C19B UNK
                                 590
                                      700
                                            27
                                                 75
                                                      5
                        1
                             -1.428 5.683 11.324 0.25 6.99
                                                              C
HETATM 121 C20B UNK
ANISOU 121 C20B UNK
                                 880 910 144 -184
                        1
                            865
                                                      70
HETATM 122 H20D UNK
                             -1.007 6.430 11.800 0.25 10.50
                                                               Η
                         1
HETATM 123 H20E UNK
                         1
                             -2.316 5.953 11.011 0.25 10.50
                                                              H
HETATM 124 H20F UNK
                         1
                             -0.873 5.433 10.554 0.25 10.50
                                                              Η
HETATM 125 C21B UNK
                             -2.443 4.862 13.430 0.25 7.05
                                                              C
ANISOU 125 C21B UNK
                            720 1080 880
                                            22
                                                     -20
                        1
                                                 62
HETATM 126 H21D UNK
                             -2.213 4.283 14.191 0.25 10.58
                         1
                                                               Η
HETATM 127 H21E UNK
                         1
                             -3.383 4.715 13.188 0.25 10.58
                                                              H
HETATM 128 H21F UNK
                         1
                             -2.308 5.795 13.677 0.25 10.58
                                                              Η
HETATM 129 C22B UNK
                             -2.285 3.386 11.466 0.25 7.64
                                                              C
ANISOU 129 C22B UNK
                            1024 920 960
                                            22 -211
                        1
                                                      -40
HETATM 130 H22D UNK
                             -1.815 3.215 10.623 0.25 11.45
                                                               Η
                         1
HETATM 131 H22E UNK
                             -3.206 3.663 11.276 0.25 11.45
                                                              Η
HETATM 132 H22F UNK
                         1
                             -2.295 2.567 12.005 0.25 11.45
                                                              Η
HETATM 133 C23B UNK
                         1
                             4.975 2.699 11.611 0.25 4.66
                                                              C
ANISOU 133 C23B UNK
                            530 552
                                      690
                                            29
                                                      3
                        1
                                                111
HETATM 134 C24B UNK
                             4.113 1.729 11.044 0.25 4.77
                         1
                                                              C
ANISOU 134 C24B UNK
                                 547
                                      700
                                            22
                                                           \mathbf{C}
                        1
                            565
                                                 87
                                                     -13
                                                              C
HETATM 135 C25B UNK
                             2.917 2.090 10.398 0.25 4.89
                                                           C
ANISOU 135 C25B UNK
                            590
                                 557
                                      710
                                             4
                                                61
                                                    -39
                        1
HETATM 136 C26B UNK
                         1
                              6.466 2.418 11.963 0.25 4.65
                                                              C
ANISOU 136 C26B UNK
                            518
                                558
                                      690
                                            33
                                                120
                                                      5
                                                           C
                        1
HETATM 137 C27B UNK
                             6.818 3.913 11.590 0.25 4.84
                         1
                                                              C
ANISOU 137 C27B UNK
                            291
                                 710 840
                                            94
                                                 95
                                                     120
                                                           C
                              6.202 4.231 10.897 0.25 7.26
HETATM 138 H27D UNK
                                                              Η
HETATM 139 H27E UNK
                         1
                             7.738 3.959 11.253 0.25 7.26
                                                              Η
```

```
HETATM 140 H27F UNK
                       1
                            6.734 4.478 12.386 0.25 7.26
                                                          Η
HETATM 141 C28B UNK
                            7.337 2.169 13.244 0.25 4.87
                                                          C
                       1
                           350 690 810
ANISOU 141 C28B UNK
                                         36
                                             203 100
                                                        C
HETATM 142 H28D UNK
                            7.083 2.816 13.939 0.25 7.34
                                                          Η
HETATM 143 H28E UNK
                            8.284 2.289 13.023 0.25 7.34
                                                          Η
HETATM 144 H28F UNK
                       1
                            7.186 1.262 13.571 0.25 7.34
                                                          Η
HETATM 145 C29B UNK
                            7.232 1.645 10.854 0.25 6.62
                                                          C
                       1
ANISOU 145 C29B UNK
                           743 980 790
                                         74
                                              66
                                                  10
                                                       \mathbf{C}
                       1
HETATM 146 H29D UNK
                            6.618 1.043 10.393 0.25 9.95
                                                          Η
HETATM 147 H29E UNK
                            7.961 1.134 11.258 0.25 9.95
                                                          Η
HETATM 148 H29F UNK
                            7.605 2.290 10.210 0.25 9.95
                       1
                                                          Η
HETATM 149 C30B UNK
                            2.210 1.190 9.387 0.25 4.92
                                                          C
                       1
ANISOU 149 C30B UNK
                           599 560 710
                                          8
                                             53
                                                 -50
                                                       \mathbf{C}
                       1
                                                          C
HETATM 150 C31B UNK
                       1
                            3.121 0.598 8.293 0.25 7.71
ANISOU 150 C31B UNK
                           941 1060 930 136 -69 -390
                                                         C
HETATM 151 H31D UNK
                            3.648 1.323 7.887 0.25 11.61
                                                          Η
HETATM 152 H31E UNK
                       1
                            2.570 0.174 7.606 0.25 11.61
                                                          Η
HETATM 153 H31F UNK
                            3.723 -0.059 8.691 0.25 11.61
                                                          Η
                       1
HETATM 154 C32B UNK
                            1.484 0.025 10.048 0.25 6.31
                                                          C
ANISOU 154 C32B UNK
                           968 570 860 -34 -133
                                                        C
                            2.092 -0.433 10.666 0.25 9.47
HETATM 155 H32D UNK
                                                          Η
HETATM 156 H32E UNK
                       1
                            1.185 -0.606 9.359 0.25 9.47
                                                          Η
                            0.707  0.360  10.542  0.25  9.47
HETATM 157 H32F UNK
                       1
                                                          Η
HETATM 158 C33B UNK
                            1.153 2.006 8.619 0.25 5.78
                                                          C
ANISOU 158 C33B UNK
                           916 630 650 -86 -28
                                                        C
HETATM 159 H33D UNK
                            0.572 2.471 9.255 0.25 8.69
                       1
                                                          Η
HETATM 160 H33E UNK
                       1
                            0.614 1.402 8.065 0.25 8.69
                                                          Η
HETATM 161 H33F UNK
                            1.600 2.662 8.044 0.25 8.69
                       1
                                                         Н
              4 36 37
CONECT
        1 3
CONECT 1 38 39
CONECT 2
           6
        3
CONECT
           1
              5
CONECT 4 1
CONECT 5
            3
                 8
               6
           2
               5
CONECT 6
                 7
CONECT 7
            4
               6 21
            5
CONECT 8
              9 13 17
CONECT 9 8 10 11 12
CONECT 10 9
CONECT 11
            9
CONECT 12
            9
CONECT 13
            8 14 15 16
CONECT 14 13
CONECT 15 13
CONECT 16 13
CONECT 17 8 18 19 20
CONECT 18 17
CONECT 19 17
CONECT 20 17
CONECT 21
            7 22 26 30
CONECT 22 21 23 24 25
```

```
CONECT 74 73
CONECT 75 73
CONECT 76 73
CONECT 77 72 78 79 80
CONECT 78 77
CONECT 79 77
CONECT 80 77
CONECT 81 72
               82 83 84
CONECT 82 81
CONECT 83 81
CONECT 84 81
CONECT 85 71
               86 90 94
CONECT 86 85
               87 88 89
CONECT 87 86
CONECT 88 86
CONECT 89 86
               91 92 93
CONECT 90 85
CONECT 91 90
CONECT 92 90
CONECT 93 90
CONECT 94 85 95 96 97
CONECT 95 94
CONECT 96 94
CONECT 97 94
           0 \quad 3 \quad 161 \quad 0 \quad 98 \quad 0
MASTER
END
```

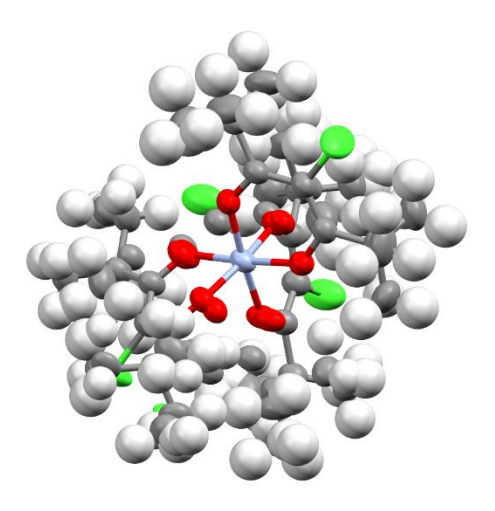


**Figure 2.A.2.** Crystal structure for Cr(4-Cl-TMHD)<sub>3</sub> that was collected by Sara Adelman and solved by Professor Richard Staples. The structure is highly disordered but still shows the desired compound.

# **Appendix 2.B. Dephasing Times of Common Solvent Modes**

**Table 2.B.1.** Frequencies and dephasing times of common solvent vibrational modes as determined from transient absorption spectroscopy.

Solvent	Coherent Mode and Dephasing Time					
THF	913 (6) cm <sup>-1</sup>					
1111		950 (140) fs				
MeCN	377 (11) cm <sup>-1</sup>	922 (11) cm <sup>-1</sup>				
MECIN	600 (250) fs	1300 (900) fs				
Dioxane	425 (5) cm <sup>-1</sup>	836 (4)				
Dioxaile	440 (200) fs	2100 (1100) fs				
Benzene*		995 cm <sup>-1</sup>				
Denzene		~3000 fs				

<sup>\*</sup>Only from a single measurement

## Appendix 2.C. Fit of Cr(acac)<sub>3</sub> Raman Spectrum

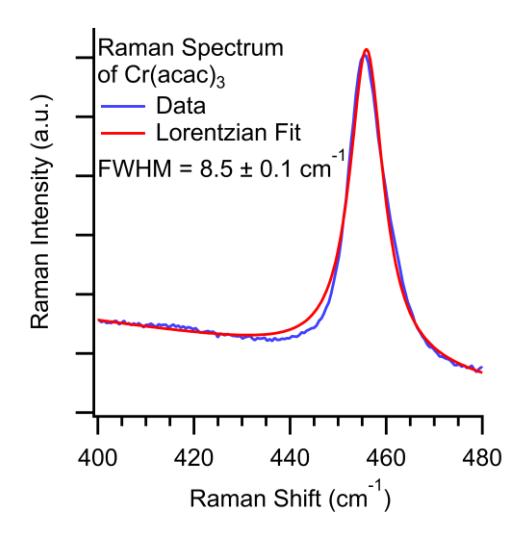


**Figure 2.C.1.** Resonance Raman spectrum of  $Cr(acac)_3$  in THF solution (blue) in the vicinity of the 455 cm<sup>-1</sup> solute mode. The 488 nm excitation source is resonant with the blue edge of the  ${}^4A_2 \rightarrow {}^4T_2$  transition. A fit of the 455 cm<sup>-1</sup> band to a Lorentzian function with a polynomial background (red) shows a FWHM of 8.5  $\pm$  0.1 cm<sup>-1</sup> corresponding to a dephasing time of 1.25  $\pm$  0.02 ps.

REFERENCES

#### REFERENCES

- (1) Bolletta, F.; Maestri, M.; Moggi, L.; Balzani, V. Bimolecular Electron Transfer Reactions of Electronically Excited States of Co-Ordination Compounds. *J. Chem. Soc.*, *Chem. Commun.* **1975**, 901–902.
- (2) Kirk, A. D. Photochemistry and Photophysics of Chromium(III) Complexes. *Chem. Rev.* **1999**, *99*, 1607–1640.
- (3) Maiman, T. H. Stimulated Optical Radiation in Ruby. *Nature* **1960**, *187*, 493–494.
- (4) Becquerel, E. La Lumiere, Ses Causes et Ses Effects. Gauthier-Villars: Paris. 1867.
- (5) Chromium https://www.rsc.org/periodic-table/element/24/chromium.
- (6) Shriver, D. F.; Atkins, P. W.; Langford, C. H.; Overton, T. L.; Rourke, J. P.; Weller, M. T.; Armstrong, F. A. Inorganic Chemistry, 5th ed.; W. H. Freeman and Company: New York, 2010.
- (7) Juban, E. A.; McCusker, J. K. Ultrafast Dynamics of <sup>2</sup>E State Formation in Cr(acac)<sub>3</sub>. *J. Am. Chem. Soc.* **2005**, *127*, 6857–6865.
- (8) Ando, H.; Iuchi, S.; Sato, H. Theoretical Study on Ultrafast Intersystem Crossing of Chromium(III) Acetylacetonate. *Chem. Phys. Lett.* **2012**, *535*, 177–181.
- (9) Bendix, J.; Borson, M.; Schäffer, C. E. Accurate Empirical Spin-Orbit Coupling Parameters. ζ<sub>nd</sub> for Gaseous nd<sup>q</sup> Transition Metal Ions. The Parametrical Multiplet Term Model. *Inorg. Chem.* 1993, 32, 2838–2849.
- (10) Schrauben, J. N.; Dillman, K. L.; Beck, W. F.; McCusker, J. K. Vibrational Coherence in the Excited State Dynamics of Cr(acac)<sub>3</sub>: Probing the Reaction Coordinate for Ultrafast Intersystem Crossing. *Chem. Sci.* **2010**, *1*, 405–410.
- (11) McCusker, J. K. Femtosecond Absorption Spectroscopy of Transition Metal Charge-Transfer Complexes. *Acc. Chem. Res.* **2003**, *36*, 879–887.
- (12) Foszcz, E. D. Understanding the Interplay Between Geometry and Ultrafast Dynamics in Ligand Field Excited States of Inorganic Chromophores, Michigan State University, 2015.
- (13) Maçôas, E. M. S.; Kananavicius, R.; Myllyperkiö, P.; Pettersson, M.; Kunttu, H. Relaxation Dynamics of Cr(acac)<sub>3</sub> Probed by Ultrafast Infrared Spectroscopy. *J. Am. Chem. Soc.* **2007**, *129*, 8934–8935.
- (14) Maçôas, E. M. S.; Mustalahti, S.; Myllyperkiö, P.; Kunttu, H.; Pettersson, M. Role of Vibrational Dynamics in Electronic Relaxation of Cr(acac)<sub>3</sub>. *J. Phys. Chem. A* **2015**, *119*, 2727–2734.
- (15) Schrauben, J. N. Electronic Structure and Excited State Dynamics of Chromium(III) Complexes, Michigan State University, 2010.
- (16) Collman, J. P.; Moss, R. A.; Maltz, H.; Heindel, C. C. The Reaction of Metal Chelates. I. Halogenation of Metal Chelates of 1,3-Diketones. *J. Am. Chem. Soc.* **1961**, *83*, 531–534.

- (17) Frisch, M. J.; Trucks, G. W.; Schlegel, H. B.; Scuseria, G. E.; Robb, M. A.; Cheeseman, J. R.; Scalmani, G.; Barone, V.; Petersson, G. A.; Nakatsuji, H.; *et al.* Gaussian, Inc.: Wallingford CT 2009.
- (18) Humphrey, W.; Dalke, A.; Schulten, K. VMD: Visual Molecular Dynamics. *J. Mol. Graph. Model.* **1996**, *14*, 33–38.
- (19) Brown, A. M.; McCusker, C. E.; Carey, M. C.; Blanco-Rodríguez, A. M.; Towrie, M.; Clark, I. P.; Vlček, A. .; McCusker, J. K. Vibrational Relaxation and Redistribution Dynamics in Ruthenium(II) Polypyridyl-Based Charge-Transfer Excited State: A Combined Ultrafast Electronic and Infrared Absorption Study. J. Chem. Phys. A 2018, 122, 7941–7953.
- (20) Albrecht, H.; Heist, P.; Kleinschmidt, J.; Lap, D. V. Single-Shot Measurement of Ultraviolet and Visible Femtosecond Pulses Using the Optical Kerr Effect. *Appl. Opt.* **1993**, *32*, 6659–6663.
- (21) Righini, R. Ultrafast Optical Kerr Effect in Liquids and Solids. *Science* **1993**, 262, 1386-1390.
- (22) Slavov, C.; Hartmann, C.; Wachtveitl, J. Implementation and Evaluation of Data Analysis Stratefies for Time-Resolved Optical Spectroscopy. *Ann. Chem.* **2018**, 87, 2328–2336.
- (23) Rosca, F.; Kumar, A. T. N.; Ye, X.; Sjodin, T.; Demidov, A. A.; Champion, P. M. Investigations of Coherent Vibrational Oscillations in Myoglobin. *J. Phys. Chem. A* **2000**, *104*, 4280–4290.
- (24) Hamm, P.; Zanni, M. Concepts and Methods of 2D Infrared Spectroscopy; Cambridge University Press: Cambridge, 2011.
- (25) Kim, J.; Kim, D. O.; Joo, T. Excited-State Dynamics of Thioflavin T: Planar Stable Intermediate Revealed by Nuclear Wave Packet Spectroscopies. *J. Phys. Chem. A* **2018**, *122*, 1283–1290.
- (26) De Silvestri, S.; Cerullo, G.; Lanzani, G. Coherent Vibrational Dynamics; CRC Press: Boca Raton, FL, 2008.
- (27) Reid, P. J.; Silva, C.; Barbara, P. F. Electronic Coherence, Vibrational Coherence, and Solvent Degrees of Freedom in the Femtosecond Spectroscopy of Mixed-Valence Metal Dimers in H2O and D2O. *J. Phys. Chem.* **1995**, *99*, 2609–2616.
- (28) Monni, R.; Auböck, G.; Kinschel, D.; Aziz-lange, K. M.; Gray, H. B.; Vlc´ek, A.; Chergui, M. Conservation of Vibrational Coherence in Ultrafast Electronic Relaxation: The Case of Diplatinum Complexes in Solution. *Chem. Phys. Lett.* **2017**, *683*, 112–120.
- Wang, Q.; Schoenlein, R. W.; Peteanu, L. A.; Mathies, R. A.; Shank, C. V. Vibrationally Coherent Photochemistry in the Femtosecond Primary Event of Vision. *Science* **1994**, *266*, 422–424.
- (30) Rafiq, S.; Scholes, G. D. Slow Intramolecular Vibrational Relaxation Leads to Long-Lived Excited-State Wavepackets. *J. Chem. Phys. A* **2016**, *120*, 6792–6799.
- (31) Rafiq, S.; Scholes, G. D. From Fundamental Theories to Quantum Coherences in Electron Transfer. *J. Am. Chem. Soc.* **2019**, *141*, 708–722.
- (32) Cho, H.; Strader, M. L.; Hong, K.; Jamula, L.; Gullikson, E. M.; Kim, T. K.; de Groot, F. M. F.; McCusker, J. K. Ligand-Field Symmetry Effects in Fe(II) Polypyridyl Compounds Probed by Transient X-Ray Absorption Spectroscopy. *Faraday Discuss.* **2012**, *157*, 463–474.

- (33) Gershgoren, E.; Wang, Z.; Ruhman, S.; Vala, J.; Kosloff, R. Investigating Pure Vibrational Dephasing of I<sub>3</sub><sup>-</sup> in Solution: Temperature Dependence of T<sub>2</sub>\* for the Fundamental and First Harmonic of v<sub>1</sub>. *J. Chem. Phys.* **2003**, *118*, 3660–3667.
- (34) Furukawa, T.; Fox, K. E.; White, W. B. Raman Spectroscopic Investigation of the Structure of Silicate Glasses III. Raman Intensities and Structural Units in Sodium Silicate Glasses. *Chem. Phys.* **1981**, 75, 3226–3237.
- (35) Liebel, M.; Schnedermann, C.; Wende, T.; Kukura, P. Principles and Applications of Broadband Impulsive Vibrational Spectroscopy. *J. Chem. Phys. A* **2015**, *119*, 9506–9517.
- (36) Myers, A. B. MOLECULAR ELECTRONIC SPECTRAL BROADENING IN LIQUIDS AND GLASSES. *Annu. Rev. Phys. Chem.* **1998**, 49, 267–295.
- (37) Kubo, R. Fluctuation, Relaxation and Resonance in Magnetic Systems; ter Haar, D.; Plenum Press: New York, 1962; pp 23–69.
- (37) Perkovic, M. W.; Endicott, J. F. Stereochemical Tuning of Chromium(III) Photophysics With N,N',N"-tris(alkylamine)-1,4,7-triazacyclononane complexes. *J. Phys. Chem.* **1990**, *94*, 1217–1219.
- (39) Perkovic, M. W.; Heeg, M. J.; Endicott, J. F. Stereochemical Perturbations of the Relaxation Behavior of (2E)Chromium(III). Ground-State x-Ray Crystal Structure, Photophysics, and Molecular Mechanics Simulations of the Quasi-Cage Complex [4,4',4''-Ethylidynetris(3-Azabutan-1-Amine)]Chromium Tribromid. *Inorg. Chem.* **1991**, *30*, 3140–3147.
- (40) Purcell, K. F. Pseudorotational Intersystem Crossing in d<sup>6</sup> Complexes. *J. Am. Chem. Soc.* **1979**, *101*, 5147–5152.
- (41) Vanquickenborne, L. G.; Pierloot, K. Role of Spin Change in the Stereomobile Reactions of Strong-Field d<sup>6</sup> Transition-Metal Complexes. *Inorg. Chem.* **1981**, *20*, 3673–3677.
- (42) McCusker, J. K.; Rheingold, A. L.; Hendrickson, D. N. Variable-Temperature Studies of Laser-Initiated  ${}^5T_2 \rightarrow {}^1A_1$  Intersystem Crossing in Spin-Crossover Complexes: Empirical Correlations between Activation Parameters and Ligand Structure in a Series of Polypyridyl Ferrous Complexes. *Inorg. Chem.* **1996**, *35*, 2100–2112.
- (43) Stock, P.; Deck, E.; Hohnstein, S.; Korzekwa, J.; Meyer, K.; Heinemann, F. W.; Breher, F.; Hörner, G. Molecular Spin Crossover in Slow Motion: Light-Induced Spin-State Transitions in Trigonal Prismatic Iron(II) Complexes. *Inorg. Chem.* **2016**, *55*, 5254–5265.
- (44) Lewis, G. N.; Calvin, M. The Color of Organic Substances. *Chem. Rev.* **1939**, 25, 273–328.

## Chapter 3: Excited State Dynamics of a Series of Co(acac')<sub>3</sub> Derivatives

### 3.1. Introduction

The previous chapter established a kinetic model to describe the excited state dynamics in a series of Cr(acac')<sub>3</sub> derivatives. Furthermore, the relationship between dephasing times of the coherent vibrational modes active in the excited electronic states of Cr(acac')<sub>3</sub> complexes and their dynamical role in the photophysics was discussed. It also illustrated the similarity in nuclear motion across each of the Cr(acac')<sub>3</sub> compounds studied following excitation into the lowest energy spin allowed ligand field band. We next assess how these results transfer to other transition metal systems.

Aside from  $d^3$  chromium compounds, the next most studied electronic configuration for transition metal chromophores is the  $d^6$  configuration. Much of this work has been focused on ruthenium(II) complexes due to their applicability towards photoinduced electron transfer based applications arising from their long lived (ns-us)<sup>1</sup> metal to ligand charge transfer (MLCT) excited state lifetimes. Some important applications, such as dye sensitized solar cells (DSSCs), however, rely on light harvesting, an inherently material intensive process due to the relatively low solar flux on Earth. This makes the use of ruthenium, one of the rarest substances on the planet,<sup>2</sup> a poor choice when scaling up these applications. This has prompted the search for alternative transition metals with charge separated excited states that are long lasting enough to be coupled to electron transfer processes. While several such systems exist, such as the class of  $d^{10}$  copper(I) polypyridyl compounds, perhaps the easiest conceptual alternative to  $d^6$  ruthenium(II) compounds are the complexes of their vastly more earth abundant  $d^6$  iron(II) congener. A crucial consequence of switching from a 4d to a 3d metal, however, is the reduced ligand field splitting (an effect that will be discussed in more detail in chapter 5). Whereas the lowest energy excited states of many ruthenium(II) polypyridyl compounds are MLCT in nature, the lowest energy excited states of the iron(II) analogues are typically ligand field states. These low-lying metal-centered excited states provide for extremely rapid deactivation pathways from the initially generated charge transfer states. 1,3 Significant effort from many research groups has been put forth to understand why these deactivation pathways are so efficient and how to control the rate of MLCT state decay. Two such methods will be investigated in detail

in chapter 4 and 5 of this dissertation. Given that much of the excited state dynamics in these compounds occurs within ligand field excited states, it would be desirable to investigate the dynamics upon direct excitation into specific ligand field states. Unfortunately, the vastly higher oscillator strengths of the MLCT transitions of the ground state often swamp out the Laporte forbidden ligand field transitions. The higher oxidation potential of the isoelectronic cobalt(III) analogues, however, result in a significant blue shift of these charge transfer features and allow for the clean observation of several ligand field bands in the ground state absorption spectrum. Furthermore, due to the considerably lower extinction coefficients of the ground state electronic transitions, any excited state absorption features in the visible region may be more distinguishable since they won't be superimposed on an intense ground state bleach, as is the case for many iron(II) polypyridyls. Thus, cobalt(III) compounds may offer a more direct way to probe the excited state dynamics within the ligand field manifold for  $d^6$  electronic configurations.

The work in this chapter will focus on understanding the excited state dynamics of a series cobalt(III) compounds in hopes of establishing the underpinnings of a roadmap to six-coordinate cobalt(III) photophysics. To achieve this, transient absorption experiments will be performed on a series of cobalt(III) trisbetadiketonate compounds (Figure 3.1) which have a number of desirable properties. First, the synthesis of these compounds is quite simple, with a preparation for the control Co(acac)<sub>3</sub> molecule found in the Journal of Chemical Education,<sup>4</sup> and various substitution reactions available for adaptation from the work on chromium in the previous chapter. Additionally, the presence of high oscillator strength charge transfer transitions in the excited states of Co(acac')<sub>3</sub> systems (similar to their chromium(III)

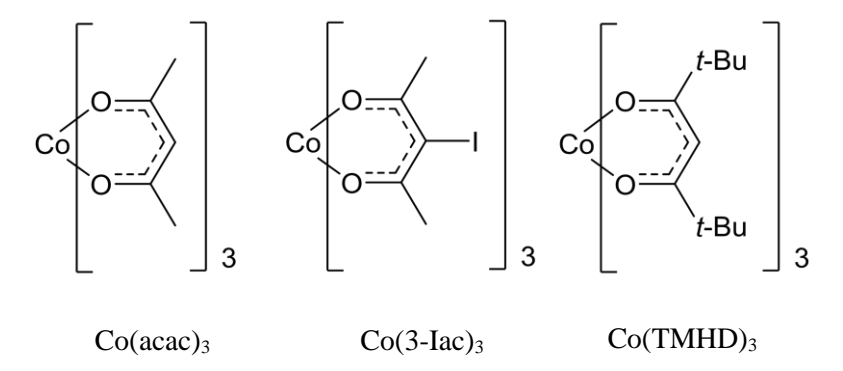


**Figure 3.1.** Series of cobalt complexes to be studied in this chapter.

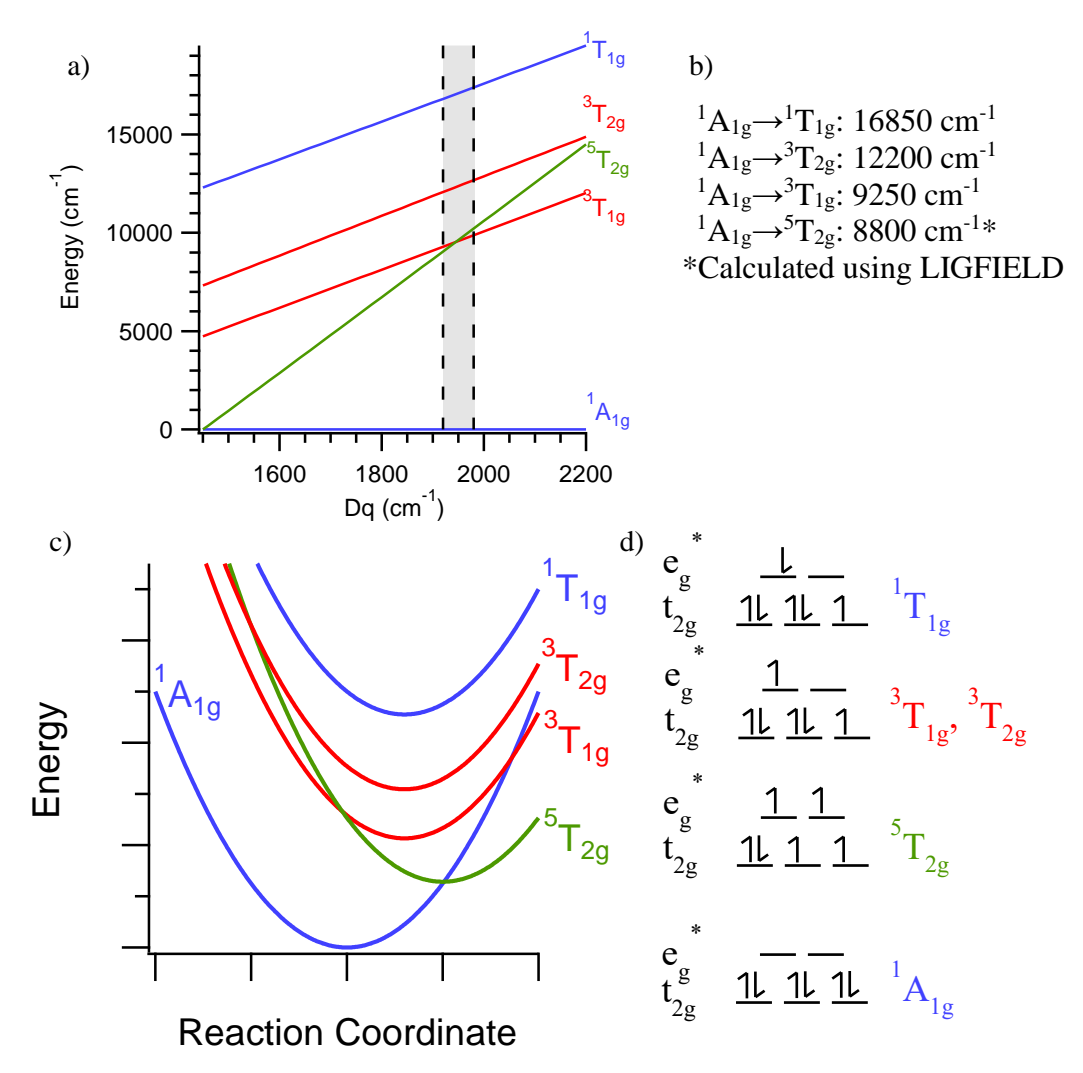


**Figure 3.2.** (a) Tanabe-Sugano diagram for Co(acac)<sub>3</sub> calculated by McCusker group Member Jonathan Yarranton using the dtansug program written by Professor Joshua Telser of Roosevelt University and using the Racah B and C interelectronic repulsion parameters from reference 5. The rightmost dashed line corresponds to the value of Dq presented in that paper and the left most dashed line corresponds better to the vertical transition energies presented therein. (b) Vertical transition energies acquired from reference 5. The <sup>5</sup>T<sub>2g</sub> band was not observed experimentally but calculated using the LIGFIELD program of reference 6. (c) Qualitative potential energy surface diagram based on the Tanabe-Sugano diagram in part a. (d) One-electron pictures of relevant electronic states.

analogues) provides for ample signal when performing transient absorption experiments. Furthermore, the redshifted absorption spectrum of  $Co(acac')_3$  compounds relative to other six-coordinate Co(III) alternatives such as  $[Co(bpy)_3]^{3+}$  make this system both instrumentally easier to study due to the ease with which laser pulses in this spectral region can be generated and compressed on the McCusker group laser system and allow for compensation of the increase in ligand field strength relative to  $[Fe(bpy)_3]^{2+}$  upon

increasing the oxidation state of the metal center. Finally, the structural similarity to the Cr(acac')<sub>3</sub> compounds discussed in chapter 2 may allow for some interesting comparisons regarding the nuclear motion and the vibrational dephasing times. The two derivatives shown in Figure 3.1 were chosen to observe the effects of both a change in vibrational frequency of the symmetric breathing mode and change in steric encumbrance, which in the chromium systems resulted in significant changes to the vibrational dephasing times and the observed spectral evolution respectively.

The electronic structure of Co(acac)<sub>3</sub> can be summarized in Figure 3.2. The Tanabe-Sugano diagram shown in Figure 3.2a was calculated by McCusker group member Jonathan Yarranton using the dtansug program written by professor Joshua Telser of Roosevelt university and using the Racah B (425 cm<sup>-1</sup>) and C (3650 cm<sup>-1</sup>) interelectronic repulsion parameters from the work of Tsiamis et al.<sup>5</sup> Additionally, a full  $d^6$  analysis was performed on Co(acac)<sub>3</sub> using the LIGFIELD program<sup>6</sup> and the energies of the  $^1A_{1g} \rightarrow \,^1T_{1g},\,^3T_{2g},\,^3T_{1g}$  transitions from the work of Tsiamis  $\it{et~al.}^5$  to redetermine the ligand field strength (19243 cm<sup>-1</sup>) as well as the Racah B (455 cm<sup>-1</sup>) and C (3678 cm<sup>-1</sup>) parameters. These values were subsequently used to rediagonalize the energy matrices to provide the predicted  $^1A_{1g} \rightarrow \,^5T_{2g}$  vertical excitation energy listed in Figure 3.2b. In addition to illustrating the relative energies of each excited state at the Frank Condon position, the slopes of each line on the Tanabe-Sugano diagram are also very informative about the nature of each excited state. Lines with approximately zero slope (no such lines are observed for the strong-field portion of the Tanabe-Sugano diagram shown in Figure 3.2a) are rather insensitive to the ligand field strength of the molecule and hence typically correspond to intraconfigurational or spin-flip transitions. Lines with nonzero slopes, however, do exhibit a dependence on the ligand field strength of the molecule and thus are typically interconfigurational transitions in which electrons are moving between the  $t_{2g}$  and  $e_g^*$  sets of orbitals on the metal center. Because of the population of  $e_g^*$  antibonding orbitals, electronic states resulting from interconfigurational transitions exhibit geometric distortions and, by extension, displaced potential energy surfaces relative to the ground state. Lines with steeper slopes correspond to transitions that place more electrons in the  $e_g^*$  set of orbitals and are hence more distorted. Thus, the  ${}^5T_{2g}$  state, which has the steepest slope on the Tanabe-Sugano diagram has the

most displaced potential energy surface. Each of these deductions is consistent with the potential energy surface diagram and electronic configurations (in the 1-electron picture) shown in Figure 3.2c and d. We see that the lowest energy excited state in this system is the  ${}^5T_{2g}$  state, similar to what is observed in many iron(II) polypyridyl complexes.<sup>1,7</sup>

### 3.2. Summary of Previous Results

**Table 3.1.** Summary of the observed kinetics in reference 8.

	$[Co(en)_3]^{3+}$	$[Co(tpen)]^{3+}$	$[Co(tppn)]^{3+}$
$\tau_I$ , ps	$2 \pm 1$	$4\pm2$	$3 \pm 1$
$\tau_2$ , ps	$450 \pm 100$	$44 \pm 5$	$51 \pm 3$

In contrast to the photophysical literature on six-coordinate ruthenium(II) or iron(II) compounds, the literature concerning the photophysics of six-coordinate cobalt(III) compounds is quite sparse, with only a small handful of publications showing transient absorption data.<sup>4,8–10</sup> There have been numerous investigations into the photochemistry of cobalt(III) compounds that do help paint a photophysical picture of these chromophores, however these studies will not be described in significant detail in this dissertation and the relevant results will only be brought up when needed. This short review of previous results will focus on a transient absorption investigation on several CoN<sub>6</sub> compounds performed by McCusker *et al.*<sup>8</sup> and another study on Co(acac)<sub>3</sub> published by Ferrari *et al.*<sup>4</sup> at the time of writing this dissertation.

We may first discuss the study of McCusker *et al.*<sup>8</sup> on a series of CoN<sub>6</sub> coordination compounds:  $[Co(en)_3](ClO_4)_3$ ,  $[Co(tpen)](ClO_4)_3$ , and  $[Co(tppn)](ClO_4)_3$ . Transient absorption experiments were performed by using a 314 nm ~500 fs excitation laser pulse, corresponding to  ${}^1A_{1g} \rightarrow {}^1LMCT$  excitation for both  $[Co(tpen)]^{3+}$  and  $[Co(tppn)]^{3+}$  or  ${}^1A_{1g} \rightarrow {}^1T_{2g}$  excitation for  $[Co(en)_3]^{3+}$ . Each compound showed biphasic kinetics (Table 3.1). A representative dataset on  $[Co(tppn)]^{3+}$  is shown in Figure 3.3. On the basis of lack of emission in these complexes ( $[Co(CN)_6]^{3-}$ , a compound of sufficiently higher ligand field strength than the compounds discussed here to produce a triplet metal-centered lowest energy excited state, exhibits emission from the  ${}^3T_{1g}$  state) ${}^{11,12}$  and a single crystal absorption spectrum and vibrational fine structure

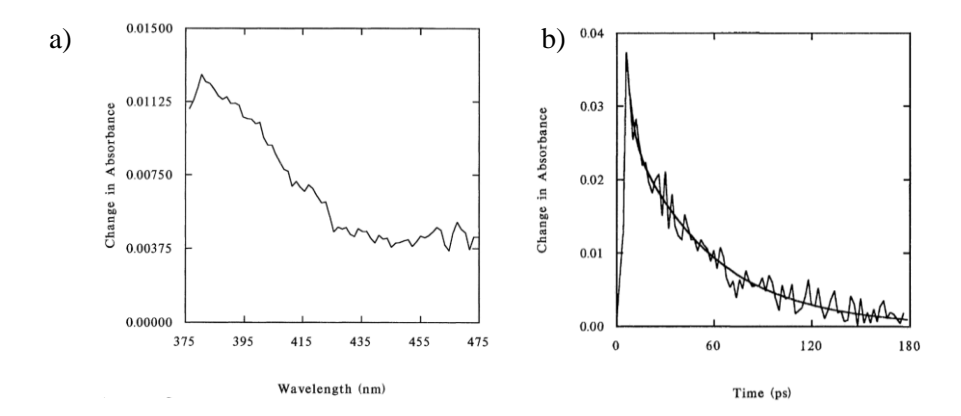


**Figure 3.3.** (a) Transient absorption spectrum for an aqueous solution of [Co(tppn)](ClO<sub>4</sub>)<sub>3</sub> following ~500 fs excitation at 314 nm. (b) Transient absorption data measured at 390 nm with a biexponential fit. Reprinted with permission from reference 8. © (1993) American Chemical Society.

analysis showing a  ${}^5T_{2g}$  lowest energy excited state for a similar ligand field strength CoN<sub>6</sub> compound (Figure 3.4),  ${}^{13}$  they assigned the slower  $\tau_2$  component to ground state recovery from the  ${}^5T_{2g}$  state. Additionally, studies on quenching of photosubstitution reactions of a series of  $[Co(NH_3)_5X]^{n+}$  compounds

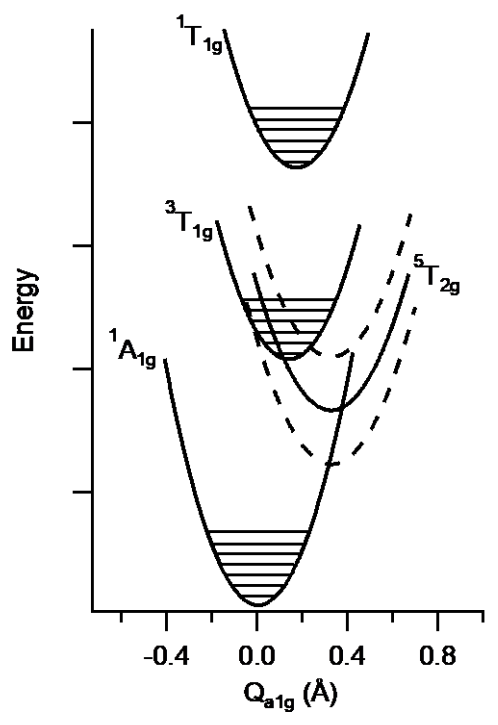


**Figure 3.4.** Potential energy surface diagram for the  ${}^{1}T_{1g}$ ,  ${}^{3}T_{1g}$ ,  ${}^{5}T_{2g}$  and  ${}^{1}A_{1g}$  states of  $[Co(NH_3)_6]^{3+}$  along the  $\nu(a_{1g})$  vibrational coordinate. The  ${}^{5}T_{2g}$  surface is depicted as several dashed lines to represent a range of possible positions and a solid line to represent the position with largest overlap with the relaxed  ${}^{3}T_{1g}$  state. Digitized from data in reference 13.

was also ascribed to conversion to the  ${}^5T_{2g}$  state which was of sufficiently low energy such that ligand substitution could not be achieved. 14,15 This is consistent with the assessment by McCusker et al. 8 that the <sup>5</sup>T<sub>2g</sub> state is formed in each of the three compounds shown in Table 3.1. Next, in trying to assign the origin of the fast kinetic component it was noted that the peak in the transient spectrum for [Co(en)<sub>3</sub>]<sup>3+</sup> (not shown here) corresponded almost exactly to the difference in vertical excitation energies between the  ${}^{1}A_{1g} \rightarrow$  $^{1}LMCT$  and  $^{1}A_{1g} \rightarrow ^{1}T_{1g}$  transitions suggesting that the origin of the observed excited state absorption band may be the  ${}^{1}T_{1g} \rightarrow {}^{1}LMCT$  transition from the Frack Condon position of the  ${}^{1}T_{1g}$  state. The fast component for  $[Co(en)_3]^{3+}$  was then tentatively assigned to depopulation of the  ${}^1T_{1g}$  state. It should be noted that a singular valued decomposition (SVD) of the full spectrum dataset had shown that the entirety of the transient spectrum could be described by a single basis spectrum at all time delays, thus somewhat weakening the above argument that the excited state absorption band corresponds to the  $^1T_{1g} \rightarrow ^1LMCT$ transition. Finally, the biphasic nature of the excited state deactivation in each compound, regardless of the fact that different excited states were produced initially between [Co(en)<sub>3</sub>]<sup>3+</sup> (<sup>1</sup>T<sub>2g</sub>) and both [Co(tpen)]<sup>3+</sup> and [Co(tppn)]<sup>3+</sup> (<sup>1</sup>LMCT), suggested a similar kinetic origin for the time constants in each compound and, by extension, that no dynamics within the LMCT manifold were observed for the latter two compounds. In summary, the study by McCusker et al. 8 had established that LMCT excited state lifetimes in a few CoN<sub>6</sub> cobalt complexes are less than a picosecond and that, in each of the compounds studied, the <sup>5</sup>T<sub>2g</sub> state was formed and subsequently depopulated with lifetimes of several tens of picoseconds to several hundred picoseconds. An additional faster kinetic component was tentatively assigned to the loss of the lowest energy singlet excited state.

The next work to be summarized comes from Ferrari *et al.*<sup>4</sup> concerning the first ultrafast transient absorption study of Co(acac)<sub>3</sub> that was published at the time of writing this dissertation. Figure 3.5 shows the relevant transient absorption data acquired from the study. The dynamics following both charge transfer and ligand field excitation showed relatively similar biphasic kinetics with the charge transfer excitation showing a 70  $\pm$  40 fs rise time followed by a 1.5  $\pm$  0.3 ps decay to baseline and the ligand field excitation showing a 70  $\pm$  40 fs rise time followed by a 1.8  $\pm$  0.3 ps decay to baseline. The absorption spectra of the

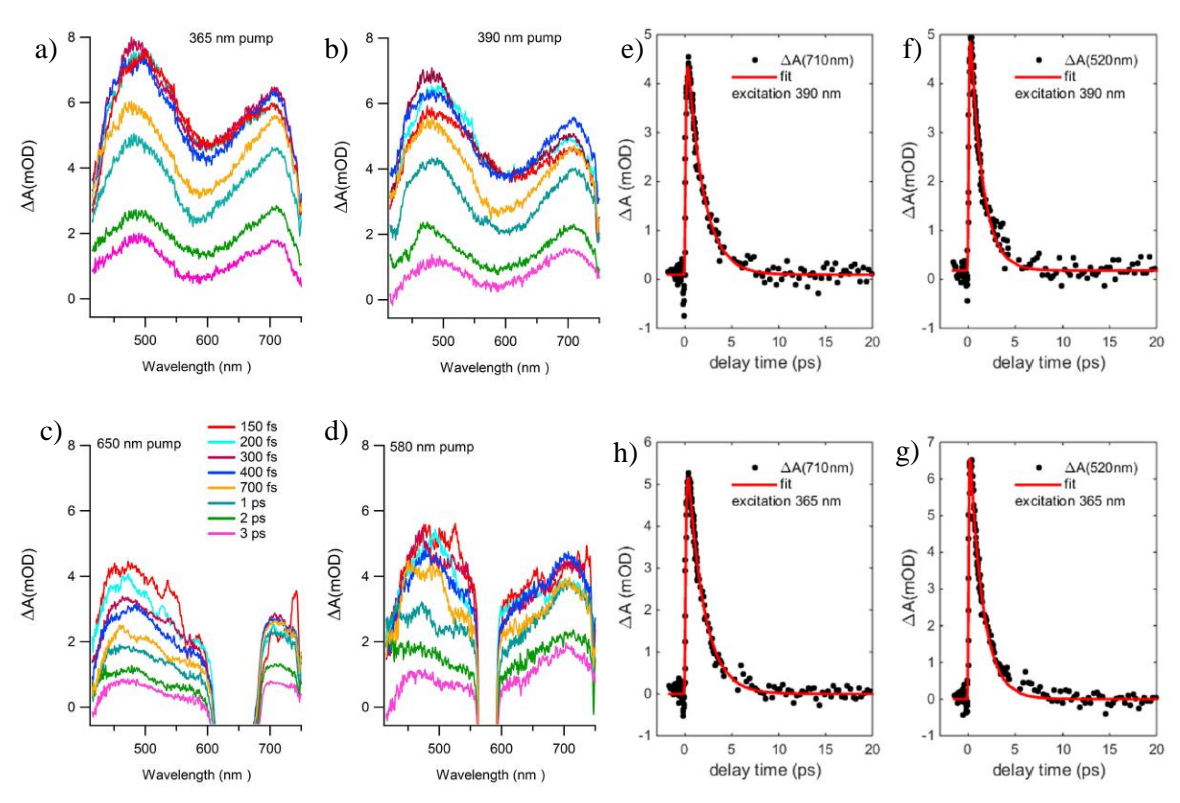


**Figure 3.5.** Full spectrum transient absorption data on Co(acac)<sub>3</sub> in acetonitrile solution following excitation at (a) 365 nm, (b) 390 nm, (c) 650 nm, and (d) 580 nm. Transient absorption data averaged ± 5 nm from center wavelengths of (e) 710 nm and (f) 520 nm following 390 nm excitation. (h) and (g) represent analogous datasets following 365 nm excitation. Reprinted with permission from reference 4. © 2019 Ferrari, Satta, Palma, Di Mario, Catone, O'Keeffe, Xema, Prosperi and Turchini.

lowest energy triplet and quintet excited states were calculated using time-dependent density functional theory calculations (not shown) to help identify which excited states were contributing to the observed spectral features. It was found that the absorption spectrum of the lowest energy triplet excited state ( ${}^{3}T_{1g}$ ) qualitatively matched the dual peaks seen in the transient data, although the energetic matching could be better. In contrast, the spectrum of the  ${}^{5}T_{2g}$  state showed only a single band centered approximately at the energy of the high energy band shown in Figure 3.5, although with an order of magnitude reduction in the oscillator strength relative to the same band in the triplet absorption spectrum. Based on this, the ~1.8 ps feature was assigned as depopulation of the  ${}^{3}T_{1g}$  state to reform the ground  ${}^{1}A_{1g}$  state. The fast rise time was assigned as a convolution of several processes including vibrational cooling and intersystem crossing resulting in the formation of the triplet metal-centered excited state.

## 3.3. Experimental Methods

# 3.3.1. Synthesis of Co(acac')<sub>3</sub> Compounds

- i. tris(2,4-pentanediono)cobalt(III),  $Co(acac)_3$ . This compound was made according to literature procedures without modification. <sup>16</sup> <sup>1</sup>H NMR (CDCl<sub>3</sub>)  $\delta 5.54$  (s, 3 H), 2.20 (s, 18 H).
- ii. tris(3-iodo-2,4-pentanediono)cobalt(III), Co(3-Iac)<sub>3</sub>. This compound was synthesized from Co(acac)<sub>3</sub> according to literature procedures.<sup>17</sup> H NMR (toluene-d<sub>8</sub>)  $\delta$ 2.41 (s, 18 H).
- iii. tris(2,2,6,6-tetramethyl-3-5-heptanediono)cobalt(III),  $Co(TMHD)_3$ . This compound was synthesized according to literature procedures. <sup>16</sup> <sup>1</sup>H NMR (CDCl<sub>3</sub>)  $\delta$  5.64 (s, 3 H), 1.10 (s, 48 H).

# 3.3.2. Computational Methods

All calculations were performed on Gaussian 16 software<sup>18</sup> on the Michigan State University High Performance Computing Center servers. Optimizations were performed using the unrestricted B3LYP functional, 6-311G (d,p) basis set, tight convergence criteria, and a polarizable continuum model for the acetonitrile solvent for the Co(acac)<sub>3</sub> and Co(TMHD)<sub>3</sub> compounds. The basis set and solvent were switched to LANL2DZ and toluene respectively for Co(3-Iac)<sub>3</sub>. Optimizations and frequency calculations were performed on the lowest energy singlet ( ${}^{1}A_{1g}$ ), triplet ( ${}^{3}T_{1g}$ ), and quintet ( ${}^{5}T_{2g}$ ) electronic states. Mass weighted vector displacement diagrams of each pertinent vibrational mode were created in the Visual Molecular Dynamics program.<sup>19</sup>

## 3.3.3. Duschinsky Displacement Vector Calculations

A Duschinsky displacement vector is a vector that describes the distortions in each of the molecular normal modes that are necessary to distort a molecule from one geometry to another. Or, in simpler terms, it is a normal mode representation for a molecular distortion. This vector was calculated according to the equation described in the work of Ando *et al.*<sup>20</sup> and shown in equation 3.1.

$$K = \left\lceil ML^r \right\rceil^{\dagger} \Delta R \tag{3.1}$$

Here, the Duschinsky displacement vector, K, is determined from M, a diagonal matrix containing the atomic masses of each of the atoms in the molecule,  $L^r$ , the matrix that diagonalizes the mass weighted

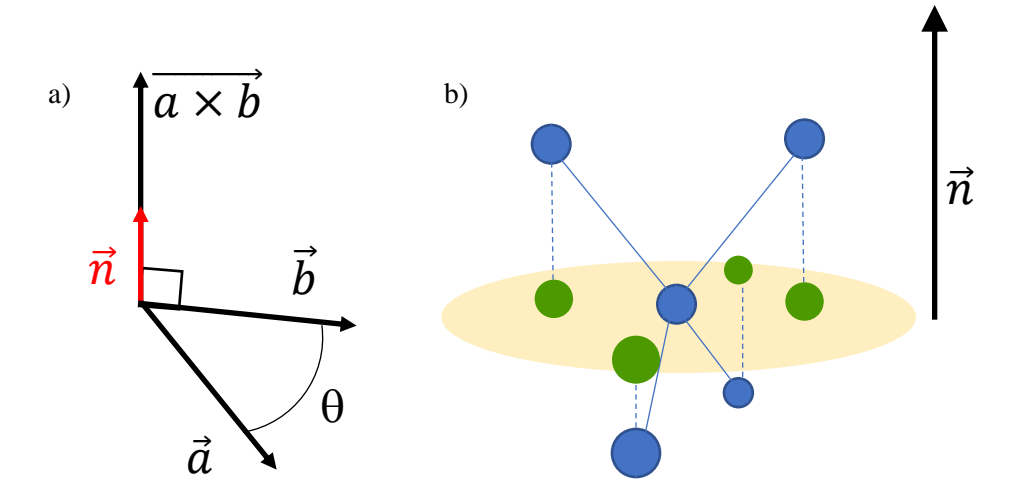


Figure 3.6. (a) A pictorial representation of a cross product between two vectors,  $\mathbf{a}$  and  $\mathbf{b}$  separated by angle  $\theta$ . The cross product,  $\mathbf{a} \times \mathbf{b}$ , is perpendicular to the plane that contains  $\mathbf{a}$  and  $\mathbf{b}$ . The vector,  $\mathbf{n}$ , is a unit vector in the same direction as  $\mathbf{a} \times \mathbf{b}$ . (b) A pictorial representation of the process by which each atom is projected onto the plane perpendicular to the unit vector determined by the sum of the mass weighted cross products of the position vectors and that contains the center of mass of the molecule. This is to eliminate extra contributions to the moment of inertia to ensure an accurate angle,  $\theta$ , is calculated which is needed to rotate the structure to nullify the angular momentum between two geometries.

Cartesian Hessian of the reactant geometry, and  $\Delta R$ , the Cartesian displacement vector between the reactant and product geometry.

An important requirement of the above calculation is that the reactant and product coordinates must have the proper orientation such that there is no linear or angular momentum between the two geometries. A procedure for performing this reorientation is described in the work of Miller *et al.*<sup>21</sup> It is relatively simple to ensure that there is no linear momentum between the reactant and product geometries by setting the origin of each axis system at the center of mass of each. If this is not satisfied initially, then the position vector describing the center of mass for a given geometry must be subtracted from the position vector of each atom in the molecule of interest. Ensuring that there is no angular momentum between the reactant and product geometries is far less trivial. The work of Miller *et al.*<sup>21</sup> describes several equations that must hold for this condition to be satisfied and they also describe how to actually achieve this with a 2-dimensional molecule. Unfortunately, adding a third dimension to a molecule makes this methodology cease to work. Because no literature procedure could be found that works on a three dimensional molecule

and because all of the relevant molecules in this dissertation are three dimensional, a new more general procedure for ensuring that there is no angular momentum between two geometries was developed here and will be described below.

To ensure that there is no angular momentum between the reactant and product geometries, we must first perform the procedure to eliminate linear momentum outlined above. Next, we must try to achieve the conditions in equation  $3.2^{21}$ 

$$0 = \sum_{i} m_i \left( \vec{R}_i^r \times \vec{R}_i^p \right) \propto \vec{L}$$
 3.2

Where  $\vec{L}$ , is the angular momentum, a function of  $m_i$ , the mass of the ith atom, and  $\overrightarrow{R_l^p}$  and  $\overrightarrow{R_l^p}$  the cartesian coordinates for the ith atom of the reactant and product geometries respectively. Typically, the right-hand side of equation 3.2 is initially nonzero, i.e. it is a nonzero vector. If we multiply this vector by the reciprocal of its norm, it becomes a unit vector pointing in the same direction as the angular momentum vector. This is shown in equation 3.3.

$$\vec{n} = \frac{\sum_{i} m_{i} \left( \vec{R}_{i}^{r} \times \vec{R}_{i}^{p} \right)}{\left\| \sum_{i} m_{i} \left( \vec{R}_{i}^{r} \times \vec{R}_{i}^{p} \right) \right\|}$$
3.3

Next, it is helpful to remember that the cross product between two vectors is another vector perpendicular to the plane that contains the two original vectors. A pictorial representation of this is shown in Figure 3.6a. If the two vectors being crossed are parallel, i.e. the angle between them is zero, then the cross product will be the zero vector and equation 3.2 will be satisfied. Thus, to eliminate the angular momentum, we need to rotate each  $\vec{R}_i^p$  by  $\theta$  about the unit vector  $\vec{n}$  so that the sum of the mass weighted cross products is the zero vector. We know from any introductory physics course that the angular momentum is proportional to the moment of inertia, I, and the angular speed,  $\omega$ , via  $L=I\omega$ . The angular speed can also be related to the ratio of the cartesian displacement and the distance from the axis of rotation. For small displacements, the angular speed can be replaced with  $\tan(\theta)$ . It follows that  $\theta$  can be found by equation 3.4.

$$\theta = \tan^{-1} \left( \frac{L}{I} \right)$$
 3.4a

$$\theta = \tan^{-1} \left( \frac{\left\| \sum_{i} m_{i} \left( \vec{R}_{i}^{r} \times \vec{R}_{i}^{p} \right) \right\|}{\sum_{i} m_{i} \left( \vec{R}_{i,proj}^{r} \cdot \vec{R}_{i,proj}^{p} \right)} \right)$$
3.4b

$$\vec{R}_{i,proj}^o = \vec{R}_i^o - (\vec{R}_i^o \cdot \vec{n})\vec{n}$$
 3.4c

In order to find  $\theta$ , we must find the moment of inertia. Since the molecule is rotated about the axis determined by the unit vector  $\vec{n}$ , then the position of each atom along the  $\vec{n}$  coordinate does not contribute to the moment of inertia. Thus, in order to not overcount the moment of inertia in the denominator of equation 3.4a and b, we must first project the position vectors of each atom in the reactant and product geometries onto the plane perpendicular to  $\vec{n}$  (and by extension the residual angular momentum that we seek to eliminate) and that contains the center of mass. This is performed in equation 3.4c and depicted pictorially in Figure 3.6b.

Now that we have determined the angle of rotation required to nullify the angular momentum between the reactant and product geometries, we need to perform the actual rotation. In principle, either the reactant or the product position vectors could be rotated, however, since we will later use the Hessian of the reactant geometry to determine the Duschinsky displacement vector, it is simpler to rotate the position vectors of the product geometry about the unit vector  $\vec{n}$ . This is performed in equation 3.5a with the general rotation matrix, T, defined in equations 3.5b-f.

$$\vec{R}_{i rot}^{p} = T \vec{R}_{i}^{p} \tag{3.5a}$$

$$T = \begin{bmatrix} tu_x^2 + c & tu_x u_y - su_z & tu_x u_z + su_y \\ tu_x u_y + su_z & tu_y^2 + c & tu_y u_z - su_x \\ tu_x u_z - su_y & tu_y u_z + su_x & tu_z^2 + c \end{bmatrix}$$
3.5b

$$\vec{n} = (u_x, u_y, u_z)$$
 3.5c

$$c = \cos(\theta) \tag{3.5d}$$

$$s = \sin(\theta) \tag{3.5e}$$

$$t = 1 - \cos(\theta) \tag{3.5f}$$

Following this matrix manipulation, the reactant and product geometries will have zero relative linear or angular momentum and they will be ready to be used in the Duschinsky displacement vector calculation described in equation 3.1. These calculations were performed in a MATLAB script that will be added to the appendix of this chapter. Instructions for its use are provided in annotations throughout the document.

# 3.3.4. Time Resolved Spectroscopic Methods

All spectroscopic measurements were performed on the same laser system and with the same procedures as outlined in chapter 2 of this dissertation. Each sample will be excited at 600 nm, in resonance with the  ${}^{1}A_{1g} \rightarrow {}^{1}T_{1g}$  lowest energy spin allowed ligand field transition. All full spectrum experiments used a white light continuum probe generated in a sapphire window. A single TA experiment performed on  $Co(acac)_3$  utilized nondegenerate pump and probe beams. In this experiment the probe beam with center wavelength of 520 nm was generated in a second OPA and a small slice of this spectrum centered at 520 nm was measured for the TA experiment. The IRF for this experiment was ~110 fs. All other single wavelength measurements performed in this chapter were degenerate pump probe experiments with ~45 fs IRFs where the probe pulse was a replica of the pump pulse. Small slices of this transmitted probe spectrum were measured at specified wavelengths.

# 3.4. Results and Discussion

### 3.4.1. $Co(acac)_3$

The ground state absorption spectrum of Co(acac)<sub>3</sub> can be seen in Figure 3.7. The band centered at 594 nm (127 M<sup>-1</sup>cm<sup>-1</sup>) can be assigned to the lowest energy spin allowed ligand field transition. More

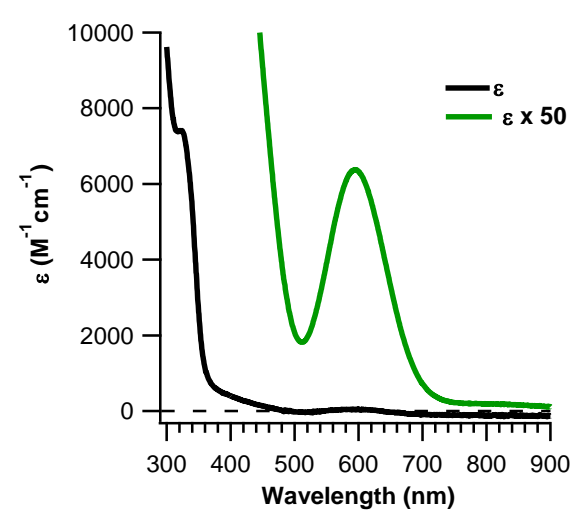


**Figure 3.7.** Ground state absorption spectrum of Co(acac)<sub>3</sub> in acetonitrile.

specifically, this corresponds to the  ${}^{1}A_{1g} \rightarrow {}^{1}T_{1g}$  transition. The shoulder featured at 324 nm (~7400 M-1cm-1) has been assigned to a MLCT transition by Hadjikostas and coworkers and Barnum<sup>22</sup>. Additionally, the lower energy hump at ~375 nm has been assigned to an LMCT type transition by Ferrari *et al.* using density functional theory calculations. The work in this dissertation will focus solely on the excited state dynamics following  ${}^{1}A_{1g} \rightarrow {}^{1}T_{1g}$  ligand field excitation.

Although only a single ligand field transition was highlighted in Figure 3.7, we already have a rather detailed picture of the energetic ordering of many of the electronic states pertinent to this system. We know from the sharp lines in the NMR spectrum (Figure 3.A.1) that Co(acac)<sub>3</sub> has a diamagnetic,  ${}^{1}A_{1g}$  ground state. Next, as discussed earlier, the series of absorption bands presented in the work of Hadjikostas and coworkers<sup>5</sup> and summarized in Figure 3.2 directly provides the energies of two additional spin forbidden transitions to the  ${}^{3}T_{2g}$  and  ${}^{3}T_{1g}$  states. The similar  $(t_{2g})^{5}(e^{*}_{g})$  strong-field electronic configurations of each of the  ${}^{1}T_{1g}$ ,  ${}^{3}T_{2g}$ , and  ${}^{3}T_{1g}$  states suggests their equilibrium geometries are quite similar and by extension that the ordering of the vertical transition energies to these states translates to the ordering of their zero-point energies as well. Finally, the vertical transition energy for the  ${}^{1}A_{1g} \rightarrow {}^{5}T_{2g}$  transition as calculated by McCusker group member Jon Yarranton using the LIGFIELD program<sup>6</sup> yet falls slightly lower in energy despite the larger distortions and hence more displaced potential energy surface inherent to the  $(t_{2g})^{4}(e^{*}_{g})^{2}$ 

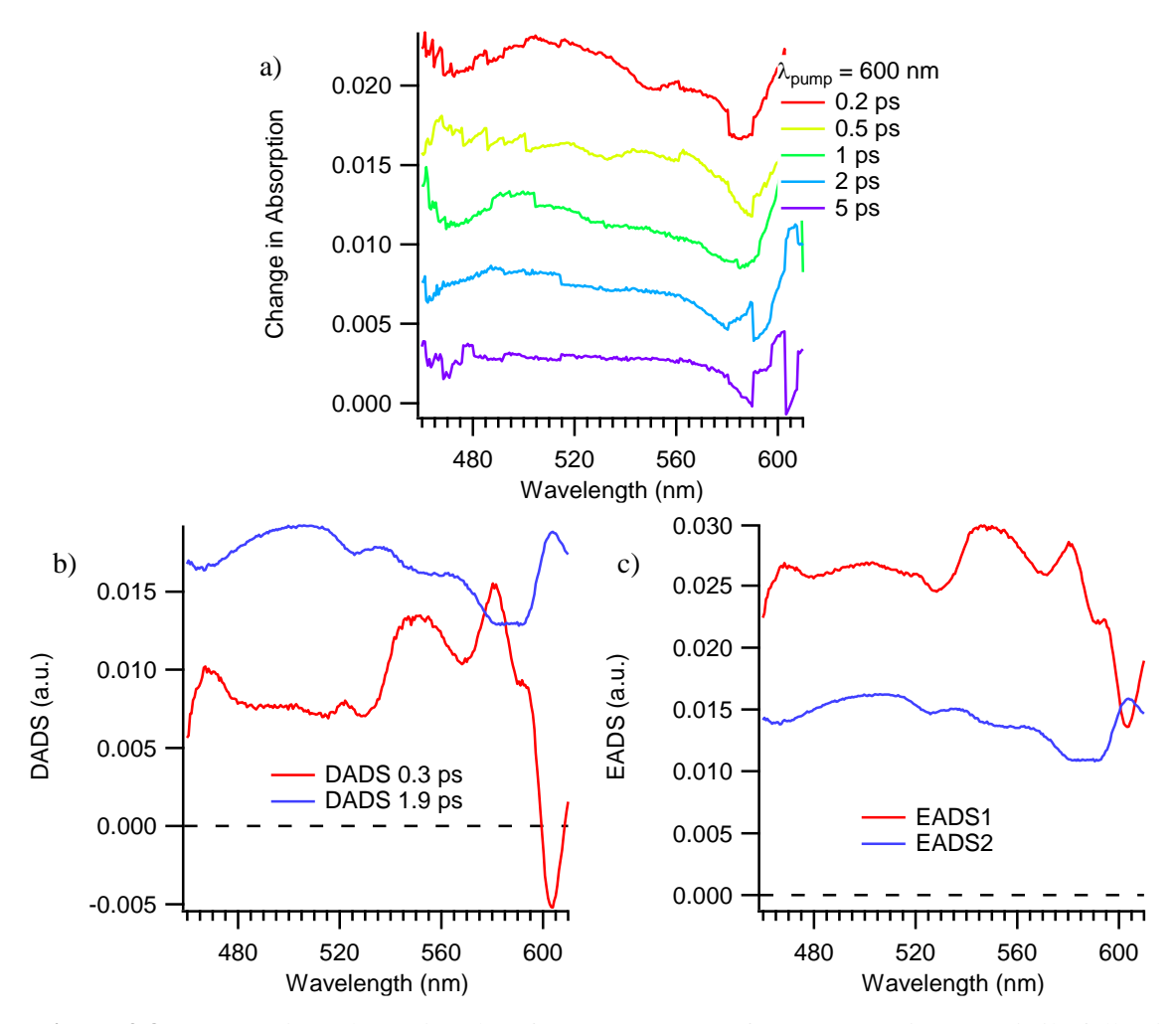


**Figure 3.8.** (a) Transient absorption data from 460-610 nm for  $Co(acac)_3$  in acetonitrile following 600 nm excitation into the  ${}^{1}T_{1g}$  state. (b) Decay associated difference spectrum associated with a global fit to two sequentially decaying exponential kinetic components. (c) Evolution associated difference spectra for the two kinetic components extracted from a global fit of the dataset.

electron configuration. This establishes the  ${}^5T_{2g}$  state as the lowest energy excited state of the system and an energetic ordering for the pertinent electronic excited states of  $E({}^5T_{2g}) < E({}^3T_{1g}) < E({}^3T_{2g}) < E({}^1T_{1g})$ .

With an idea of the excited state ordering in hand, we can now turn to investigating the photophysical properties of  $Co(acac)_3$ . Figure 3.8 shows the transient absorption spectrum from 460-610 nm for  $Co(acac)_3$  following 600 nm excitation into the  ${}^{1}T_{1g}$  state. The best global fit of this dataset requires two exponentially decaying kinetic components with time constants of 0.3 and 1.9 ps. The resulting DADS and EADS can be seen in Figure 3.8b and c respectively. The corresponding experiment recently performed by Ferrari *et al.*<sup>4</sup> exhibited a 70  $\pm$  40 fs rise time and a 1.8  $\pm$  0.3 ps decay. While the 70 fs rise

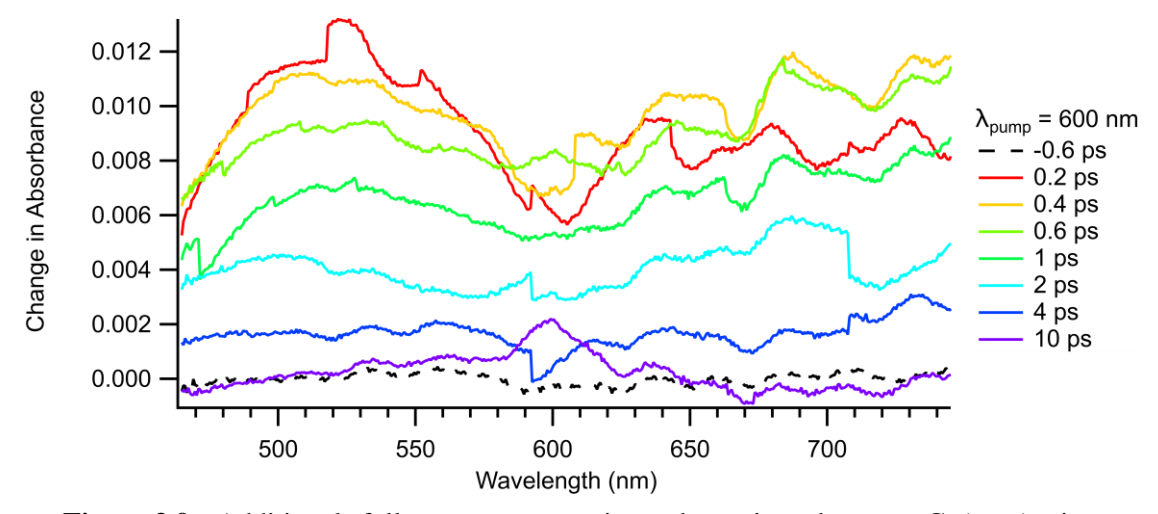


**Figure 3.9.** Additional full spectrum transient absorption data on Co(acac)<sub>3</sub> in acetonitrile following 600 nm excitation.

time was too close to the instrument response function to be observed here, the  $1.8 \pm 0.3$  ps time constant is in excellent agreement with the 1.9 ps decay observed in Figure 3.8. Interestingly, we also observe an additional 0.3 ps kinetic component. By inspection of the DADS and EADS we see that this faster process results in a decrease of the magnitude of the transient signal while not significantly perturbing the shape of the spectrum and the slower process returns the spectrum back to baseline. Additional transient absorption data over a broader wavelength range can be seen in Figure 3.9 which shows good qualitative agreement to the literature data shown in Figure 3.5.4

To get a more precise idea of the kinetics of this system, single wavelength measurements were performed. Several representative datasets using a degenerate pump and probe are shown in Figure 3.10

**Table 3.2.** Summary of kinetic components from single wavelength transient absorption experiments on  $Co(acac)_3$  in acetonitrile following 600 nm excitation into the  ${}^1T_{1g}$  state.

Probe, nm	$\tau_1$ , fs	$\tau_2$ , fs
620	780	2200
$620^{a}$	385ª	1930 <sup>a</sup>
600	620	2200
600	540	2080
580	370	1700
580	440	1700
520	430	2100
Average (σ)	510 (150)	2000 (200)

<sup>&</sup>lt;sup>a</sup> Time constants acquired from LPSVD fit.

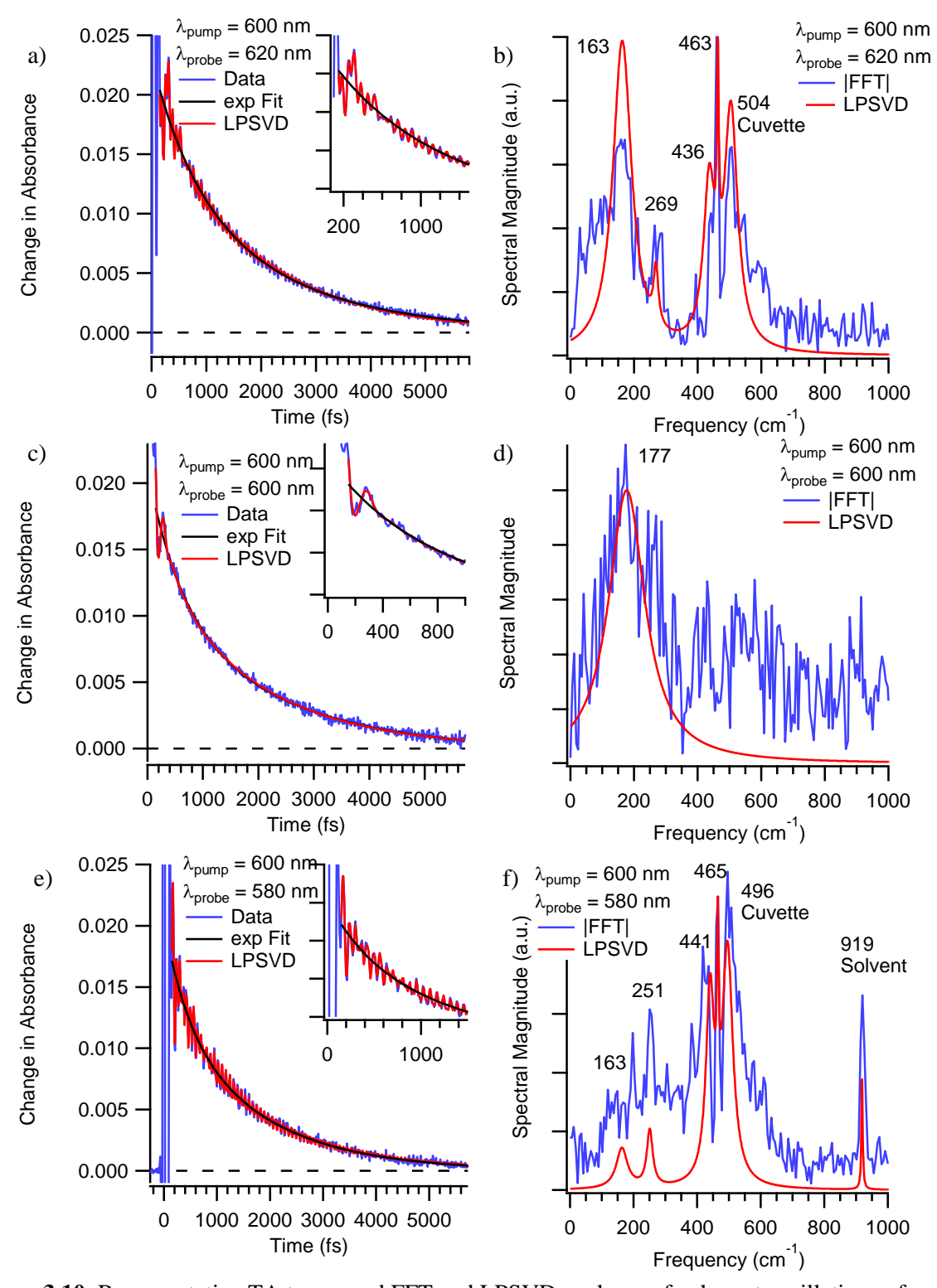


**Figure 3.10.** Representative TA traces and FFT and LPSVD analyses of coherent oscillations of  $Co(acac)_3$  in acetonitrile following 600 nm excitation into the  ${}^1T_{1g}$  state. Kinetics were monitored at (a) 620 nm, (c) 600 nm, and (e) 580 nm using a probe beam with a spectrum centered at 600 nm. Insets show coherent oscillations at early times. Corresponding FFT and LPSVD vibrational spectra are shown in (b), (d), and (f).

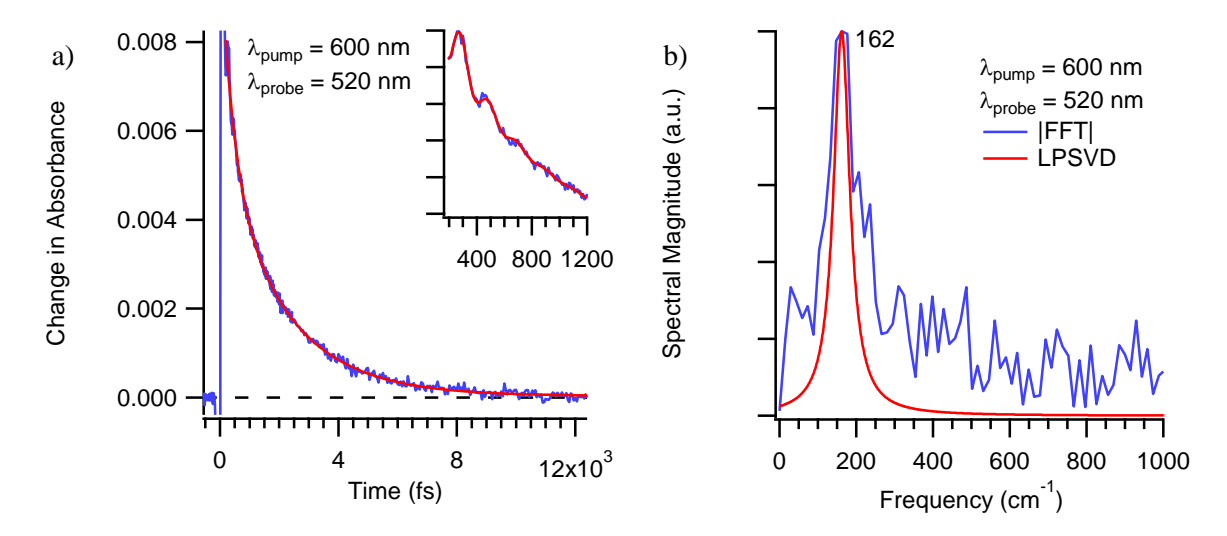


**Figure 3.11.** (a) Transient absorption data on  $Co(acac)_3$  measured at the peak of the high energy band of the transient spectrum at 520 nm following 600 nm excitation into the  ${}^{1}T_{1g}$  state. The inset shows the coherent oscillations at early time and an LPSVD fit. (b) Corresponding LPSVD and FFT vibrational spectrum.

and a summary of the observed kinetics is shown in Table 3.2. An additional non-degenerate pump probe experiment was performed in which the probe beam spectrum was centered at 520 nm (Figure 3.11), the maximum of the high energy peak in the transient spectrum, and the transient signal was collected with sufficient pump-probe delay such that the signal returned to baseline. These single wavelength datasets again reveal biphasic kinetics with  $510 \pm 150$  fs and  $2000 \pm 200$  fs time constants in good agreement with the global fits of the full spectrum data. Additionally, coherent oscillations can be observed at early times in each dataset in Figures 3.10 and 3.11. A summary of these coherences as well as their dephasing times can be seen in Table 3.3. The above results contain observations that were absent in the recently published investigation into the photophysics of Co(acac)<sub>3</sub> by Ferrari *et al.*<sup>4</sup> and will be discussed in detail below. We will begin with a discussion of the coherent oscillations and end with an analysis of the population dynamics for this system.

When analyzing the coherent oscillations observed for Co(acac)<sub>3</sub>, we can benefit from the groundwork already laid out for the related Cr(acac)<sub>3</sub> system in Chapter 2 of this dissertation. First, based on the magnitude of the dephasing times, we can readily conclude that these coherences survive too long to be purely electronic coherences. The two remaining possible origins for the coherent oscillations are then

**Table 3.3.** Summary of the coherent vibrational modes observed for  $Co(acac)_3$  in acetonitrile. Pump and probe pulse energies,  $E_{pu}$  and  $E_{pr}$ , are provided for each experiment. The IRF was 40 fs for each experiment except the 520nm probe dataset which had a 110 fs IRF.

Probe, nm	$E_{pu}(E_{pr}), \mu J$	F	Frequency, cm <sup>-1</sup> (	Damping Time,	fs)
620	3 (0.3)	163 (148)	269 (591)	436 (250)	463 (1489)
620	2.9 (0.4)	154 (115)			462 (5738)
600	3 (0.3)	159 (129)	272 (275)		473 (730)
600	2.9 (0.4)	177 (76)			
580	3 (0.3)	153 (102)	259 (456)	444 (405)	465 (1945)
580	2.9 (0.4)	163 (248)	251 (475)	441 (346)	465 (1642)
520	3 (0.3)	162 (205)			
Average	Frequency	$162 \pm 8$	$263 \pm 10$	$440 \pm 4$	$466 \pm 4$
Average Damping Time		$150 \pm 60$	$450 \pm 130$	$330 \pm 80$	$1450 \pm 520$

vibrational coherences on an excited electronic state or vibrational coherences on the ground electronic state generated via impulsively stimulated Raman scattering. Because the oscillator strength for the Laporte-forbidden ground state absorption is so small relative to the excited state absorption features resulting from a much more allowed charge transfer transition, we can unequivocally conclude that all vibrational coherences of the solute must be on an excited electronic state. A similar argument was made for Cr(acac)<sub>3</sub> in the previous chapter.

Before we make assignments of vibrational coherences to specific excited states, it may be fruitful to predict which types of vibrational modes might be expected on each electronic state. One way to achieve this is to use the Duschinsky displacement vector described in section 3.3.3. This displacement vector is a normal mode representation for a change in molecular geometry. In, other words, the Duschinsky displacement vector describes the difference between two geometries in terms of displacement along the 3N-6 vibrational modes of a molecule. Because wave packets, at least initially, move in the direction of steepest descent along a potential energy surface, <sup>23</sup> then by identifying which vibrational modes show the highest reorganization energy for a given electronic transition, we may be able to identify which vibrational modes are likely to be coherently active in a particular electronic state.

We can first group the electronic excited states into two groups: those with the  $(t_{2g})^5(e_g^*)^1$  electronic configuration ( ${}^1T_{1g}$ ,  ${}^3T_{2g}$ , and  ${}^3T_{1g}$  states) and those with the  $(t_{2g})^4(e_g^*)^2$  electronic configuration ( ${}^5T_{2g}$  state). We assume that electronic states within the same group will make similar nuclear distortions so that only a

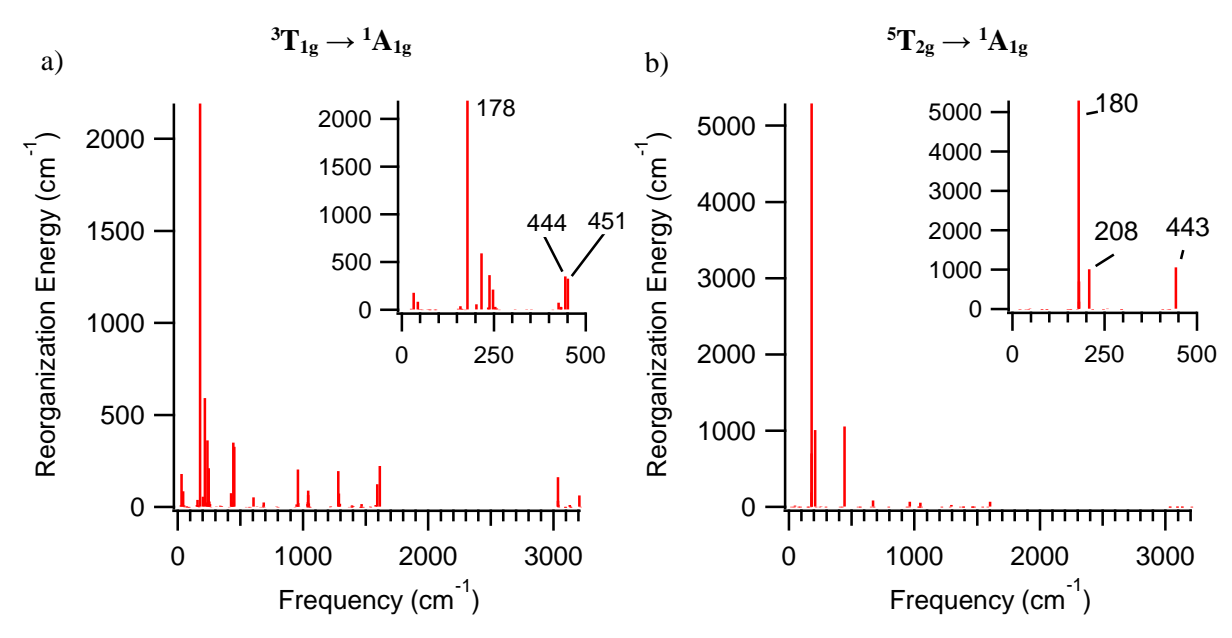


**Figure 3.12.** Plots of the calculated inner-sphere reorganization energy as a function of normal mode frequency for pertinent electronic transitions of  $Co(acac)_3$ . (a) Plot of the reorganization energy for the  ${}^3T_{1g} \rightarrow {}^1A_{1g}$  transition as a function of the frequencies of the vibrational modes of the  ${}^3T_{1g}$  electronic excited state. (b) Plot of the reorganization energy for the  ${}^5T_{2g} \rightarrow {}^1A_{1g}$  transition as a function of the frequencies of the vibrational modes of the  ${}^5T_{2g}$  electronic excited state. Reorganization energies were calculated from the nuclear displacements of the Duschinsky displacement vectors for the corresponding electronic transitions.

single displacement vector for each group need be calculated. Plots of the Duschinsky displacement vectors in terms of inner-sphere reorganization energy for the  ${}^3T_{1g} \rightarrow {}^1A_{1g}$  and  ${}^5T_{2g} \rightarrow {}^1A_{1g}$  transitions are shown in Figure 3.12. These vectors were calculated as a function of the normal modes on the  ${}^3T_{1g}$  and  ${}^5T_{2g}$  excited states for Figure 3.12 a and b respectively so that we may better portray the vibrational modes to be expected on excited states of  $(t_{2g})^5(e_g^*)^1$  and  $(t_{2g})^4(e_g^*)^2$  electronic configurations. An initial inspection of both reorganization energy plots in Figure 3.12 shows that most of the distortions characterizing the  ${}^1A_{1g} \leftrightarrow {}^3T_{1g}$  and  ${}^1A_{1g} \leftrightarrow {}^5T_{2g}$  transitions are low frequency modes which can be attributed to deformations of the primary coordination sphere. Additionally, the overall reorganization energy (i.e. the sum of the reorganization energy contributions along each normal mode) is larger for the  ${}^5T_{2g} \to {}^1A_{1g}$  transition than it is for the  ${}^3T_{1g} \to {}^1A_{1g}$  transition. This is consistent with the greater number of electrons occupying  $\sigma$ -antibonding orbitals in the  ${}^5T_{2g}$  state. Finally, we observe that there are simply fewer distorted modes for the  ${}^5T_{2g} \to {}^1A_{1g}$  transition. This reflects the relative symmetry between the final and initial states for each transition. The

 ${}^5T_{2g}$  state results from a symmetric expansion of the ground state geometry, whereas the Jahn-Teller active  ${}^3T_{1g}$  state exhibits an axial compression and equatorial expansion and hence additional vibrational modes to achieve the necessary geometry.

We can now begin to compare the collection of experimentally observed coherent nuclear vibrations listed in Table 3.3 to the nuclear distortions depicted by the Duschinsky displacement vectors in Figure 3.12. Both the experimentally observed modes at 162 and 440 cm<sup>-1</sup> match well with the peaks around 180 and 440 cm<sup>-1</sup> in each plot of the Duschinsky displacement vector for the  ${}^3T_{1g} \rightarrow {}^1A_{1g}$  and  ${}^5T_{2g} \rightarrow {}^1A_{1g}$  transitions. However, only the  ${}^3T_{1g} \rightarrow {}^1A_{1g}$  transition exhibits distortions in vibrational modes around 450 and 250 cm<sup>-1</sup>, which are necessary to explain the experimentally observed 263 and 466 cm<sup>-1</sup> oscillatory components. We thus see that the observed coherent nuclear motion most resembles the distortions expected on an electronic state of  $(t_{2g})^5(e_g^*)^1$  character, i.e. the observed modes are likely active on the  ${}^1T_{1g}$ ,  ${}^3T_{2g}$ , or  ${}^3T_{1g}$  excited states and not on the  ${}^5T_{2g}$  state. This observation marks a significant departure from the dynamics seen in the related  $d^6$  compound, [Fe(bpy)<sub>3</sub>]<sup>2+</sup>, in which coherent nuclear motion occurs on the  ${}^5T_{2g}$  lowest energy excited state after rapidly depopulating (< 200 fs) the initially formed MLCT excited state.  ${}^{24,25}$ 

Now that we have narrowed down the possible electronic states that the experimentally observed vibrational coherences could be active on, we can begin to assign them to specific vibrational modes calculated on the  ${}^{3}T_{1g}$  excited state. We may first start with the  $162 \pm 8 \text{ cm}^{-1}$  mode which appears most robustly in the TA data. This mode is in relatively good agreement with the calculated  $178 \text{ cm}^{-1}$  mode with the largest inner-sphere reorganization energy shown in Figure 3.12a. We can thus assign this  $162 \text{ cm}^{-1}$  experimental frequency to the calculated  $178 \text{ cm}^{-1}$  symmetric breathing mode shown in Figure 3.13a. Although there is a large uncertainty in the experimental frequency of this mode due to the rapid dephasing time and the relatively long vibrational period, the decent frequency matching between experimental and calculated modes, the large calculated inner-sphere reorganization energy for the assigned mode and the similarity of the observed motion to that observed for the analogous  $Cr(acac)_3$  and each of its derivatives discussed in Chapter 2 of this dissertation all support this assignment. Next, we can readily assign the

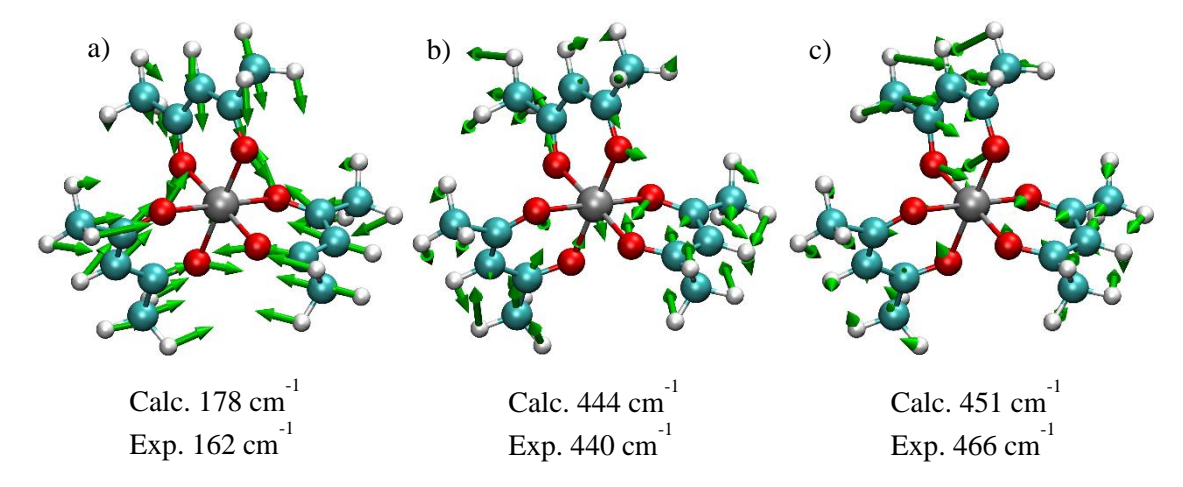


**Figure 3.13.** Nuclear deformations associated with the (a) 162 cm<sup>-1</sup>, (b) 440 cm<sup>-1</sup>, and (c) 466 cm<sup>-1</sup> experimentally observed vibrational modes of Co(acac)<sub>3</sub>.

experimentally observed 466 cm<sup>-1</sup> mode to the 451 cm<sup>-1</sup> calculated mode (Figure 3.13c) corresponding to a Co-O stretching mode with noticeable reorganization energy depicted in Figure 3.12a. Not only is the general motion of this vibrational mode similar to what was observed for Cr(acac)<sub>3</sub> but the magnitudes of the observed and calculated frequencies are almost identical as well (453 cm<sup>-1</sup> calculated and 461 cm<sup>-1</sup> experimentally. The experimentally observed 440 cm<sup>-1</sup> mode can next be assigned to the 444 cm<sup>-1</sup> calculated mode (Figure 3.13b) which also shows noteworthy reorganization energy in Figure 3.12a. Interestingly, this Co-O stretching mode is antisymmetric, showing a compression of the Cr-O bonds of the bottom two acac ligands seen in Figure 3.13b while the top acac ligand shows increasing M-L bond lengths.

The final,  $263 \pm 10$  cm<sup>-1</sup> mode is more challenging to assign. There is not only a relatively high density of states in this frequency region but also a large uncertainty in the frequency of the vibrational mode. Several plausible assignments can be seen in Figure 3.14 along with the calculated inner-sphere reorganization energy along each coordinate according to the Duschinsky displacement vector shown in Figure 3.12a. We see that the frequency matching between the observed 263 cm<sup>-1</sup> oscillation and the  $265 \text{ cm}^{-1}$  calculated mode in Figure 3.14 is quite good, however the predicted reorganization energy along this coordinate is zero. While this is not definitive proof that this assignment is incorrect, it does suggest that substantial migration along this coordinate immediately after photoexcitation is rather unlikely. In this light, both the  $259 \text{ cm}^{-1}$  and  $254 \text{ cm}^{-1}$  modes in Figure 3.14 also show minute reorganization energies. In

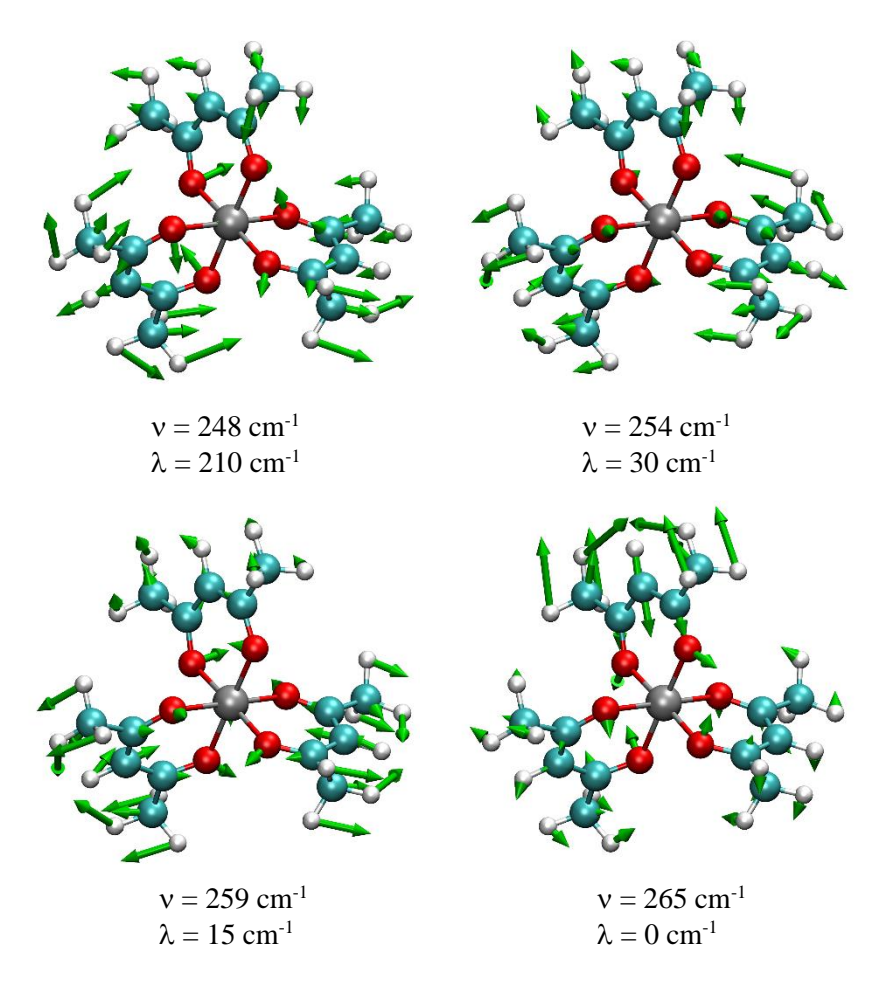


**Figure 3.14.** Possible assignments for the 263 cm<sup>-1</sup> experimentally observed coherent vibrational mode of  $Co(acac)_3$  along with the corresponding inner-sphere reorganization energies for each mode along the  ${}^3T_{1g} \rightarrow {}^1A_{1g}$  reaction coordinate determined from the Duschinsky displacement vector.

contrast, the remaining 248 cm<sup>-1</sup> mode shown in Figure 3.14 has a substantially larger reorganization energy and is still relatively close to the experimentally observed 263 cm<sup>-1</sup> frequency. We thus, tentatively assign the 248 cm<sup>-1</sup> vibrational mode as the observed nuclear motion.

With an assignment of the nuclear motion associated with each of the coherently active vibrational modes in Table 3.3, we can begin a preliminary discussion of their dephasing times. With the exception of the  $466 \text{ cm}^{-1}$  mode with  $1450 \pm 520$  fs dephasing time, each normal mode has a dephasing time well under a picosecond. It seems that the dephasing time of the  $466 \text{ cm}^{-1}$  mode for  $Co(acac)_3$  is also on par with the 1.1 ps dephasing time of the analogous mode for  $Cr(acac)_3$  shown in Chapter 2. The  $162 \text{ cm}^{-1}$  breathing

mode of  $Co(acac)_3$  however has a very short  $150 \pm 60$  fs dephasing time that is even faster than the analogous mode for  $Cr(acac)_3$ . While the origin of the dephasing of this mode was assigned to rapid IVR in  $Cr(acac)_3$  it is difficult to discern if this is true for the cobalt system without further information. This point will be revisited following a comparison of the vibrational coherences in other  $Co(acac')_3$  derivatives later in this chapter.

The above discussion has both identified the initial nuclear motion of Co(acac)<sub>3</sub> upon photoexcitation and narrowed down the populated excited states at very early times to those with  $(t_{2g})^5(e_g^*)$ electronic configurations, thus providing a nice starting point to analyze the population dynamics. We know from Figures 3.8 and 3.9 that there are no significant changes to the initial qualitative shape of the transient spectrum over the course of the excited state dynamics. While we may expect that an intraconfigurational electronic transition may only lead to subtle changes in a transient absorption spectrum, we would expect much more dramatic changes for an interconfigurational transition. Thus, since no such dramatic change in the transient spectrum is observed and because we know that, at least during the initial few hundred femtoseconds, an excited state of  $(t_{2g})^5(e_g^*)$  electronic configuration is populated ( ${}^1T_{1g}$ ,  ${}^3T_{2g}$ , or  ${}^3T_{1g}$ ), then we know that the observed transient spectrum must not be representative of the  $^5T_{2g}$  state. This is further supported by the qualitative agreement between the <sup>3</sup>T<sub>1g</sub> absorption spectrum calculated by Ferrari et al.<sup>4</sup> and the observed TA data as well as the poor matching of the calculated <sup>5</sup>T<sub>2g</sub> spectrum in the same paper. Additionally, we note that the energy difference between the charge transfer band in the ground state absorption spectrum<sup>5</sup> of Co(acac)<sub>3</sub> at 30,100 cm<sup>-1</sup> and the excited state absorption band at ~480 nm  $(20,830 \text{ cm}^{-1})$  in Figure 3.5 is 9,270 cm<sup>-1</sup>, remarkably close to the vertical transition energy of the  ${}^{3}T_{1g}$  state listed in Figure 3.2. This may suggest that the observed transient species is the  ${}^3T_{1g}$  state, however, the broad maximum in Figure 3.5 and the shift to slightly longer wavelengths in the dataset provided in Figure 3.9 make this assignment tenuous at best.

Inspection of the TA data in Figures 3.8 and 3.9 show that the 2.0 ps kinetic component results in a complete return to baseline and thus must represent either ground state recovery or formation of a lower energy dark state. We can further disprove that the 2.0 ps process is representative of loss of the lowest

energy  ${}^5T_{2g}$  excited state by considering the timescale for this supposed  ${}^5T_{2g} \rightarrow {}^1A_{1g}$  process. In the work of McCusker *et al.*<sup>8</sup> that was summarized earlier in this chapter, several six-coordinate cobalt(III) compounds were observed to have  ${}^5T_{2g} \rightarrow {}^1A_{1g}$  lifetimes of  $\sim 40$ -450 ps, much slower than the observed 2.0 ps time constant in this study. Likewise, recent variable temperature experiments on several octahedral  $d^6$  Fe(II) compounds had shown the extracted barrierless  ${}^5T_{2g} \rightarrow {}^1A_{1g}$  lifetimes on the order of multi-hundred picoseconds.  ${}^{26}$  The 1-2 orders of magnitude shorter time constant observed in this study suggest it is likely from a fundamentally different process. Coincidentally, an additional faster single digit picosecond kinetic component observed in the cobalt work of McCusker, was assigned to depopulation of an excited state with  $(t_{2g})^5(e_g^*)$  electronic configuration (specifically the  ${}^1T_{1g}$  state). This benchmark value for depopulation of the manifold of states with  $(t_{2g})^5(e_g^*)$  electron configuration is much closer to the 2.0 ps ground state recovery observed here suggesting that it too may be a result of depopulation of an excited state with  $(t_{2g})^5(e_g^*)$  electron configuration. Additionally, this occurs on a comparable timescale as the 1.1 ps  ${}^4T_{2g} \rightarrow {}^4A_{2g}$  internal conversion observed for Cr(acac)<sub>3</sub> in which a similar process of removing a single electron from the  $e_g^*$  orbital set and placing it in the  $t_{2g}$  orbitals occurs.

We now know from consideration of the time constant for return of the transient signal to baseline, a comparison of the calculated and experimental transient spectra, and lack of significant change of the spectral shape after initially persisting on an excited state of  $(t_{2g})^5(e_g^*)$  electronic configuration that the 2.0 ps kinetic component of  $Co(acac)_3$  either represents ground state recovery from one of the  ${}^1T_{1g}$ ,  ${}^3T_{2g}$ , or  ${}^3T_{1g}$  excited states, or formation of the  ${}^5T_{2g}$  excited state which must be effectively dark to avoid showing any transient signal. In what follows, we will assess the viability of a "dark"  ${}^5T_{2g}$  state. Certainly, the intensity of charge transfer transitions from the  ${}^5T_{2g}$  excited state are likely to be reduced relative to similar transitions in excited states of shorter M-L bond lengths due to reduced orbital overlap. This phenomenon has been shown quite clearly in the absorption spectra of the  $d^6$  low-spin  $[Fe(tren(py)_3)]^{2+}$  and high-spin  $[Fe(tren(6-Me-py)_3)]^{2+}$  compounds which show approximately an order of magnitude reduction in the extinction coefficient of the MLCT absorption band.  ${}^{27}$  Despite this reduction in signal magnitude, however, spectral changes in TA experiments in the visible region resulting from vibrational relaxation within the

 ${}^5T_{2g}$  state have been observed in [Fe(tren(py)<sub>3</sub>)]<sup>2+</sup> implying that this state is not always completely dark in TA experiments.<sup>27</sup> Furthermore, a noticeable baseline offset in the visible region was observed in the spectrum of the  ${}^5T_{2g}$  state for [Co(tppn)]<sup>3+</sup> in Figure 3.3, again showing that the  ${}^5T_{2g}$  state of a cobalt(III) compound is not necessarily devoid of signal in a TA experiment.<sup>8</sup> Density functional theory calculations of the excited state absorption spectra performed by Ferrari *et al.*<sup>4</sup> show that the spectrum of the  ${}^3T_{1g}$  state qualitatively matches the double peaked transient spectrum that decays with a 2 ps time constant whereas the calculated  ${}^5T_{2g}$  spectrum only has a single peak in the visible spectrum centered at approximately the energy of the high energy band in the TA spectrum. Although the calculated oscillator strength for the band in the  ${}^5T_{2g}$  state spectrum was approximately an order of magnitude lower than that for the  ${}^3T_{1g}$  state, the lack of any baseline offset while probing at 520 nm (Figure 3.11), the maximum of the calculated  ${}^5T_{2g}$  band, strongly suggests that the  ${}^5T_{2g}$  state is not being populated by the 2 ps process, and by extension that the 2.0 ps process is representative of ground state recovery from one of the  ${}^1T_{1g}$ ,  ${}^3T_{2g}$ , or  ${}^3T_{1g}$  states.

We next turn to the 510 fs kinetic component listed in Table 3.2 to characterize the excited state dynamics of Co(acac)<sub>3</sub>. This kinetic component was not observed by Ferrari *et al.*<sup>4</sup> however, they do note a change in the relative peak heights during the first picosecond which could be due to a kinetic process which they did not fit for. In the data presented here, it also seems as though no significant changes to the spectral shape are occurring during this 510 fs process, but rather a decrease in the magnitude of the signal. This spectral change is likely either attributed to nuclear motion (vibrational cooling or a Jahn-Teller distortion) or an electronic state change. We will address the likelihood of each of these possibilities.

We may first deliberate the merits of attributing the 510 fs kinetic component to nuclear motion, starting with the prospect of vibrational cooling and ending with the notion of a Jahn-Teller distortion. Considering that vibrational cooling on the structurally similar  $Cr(acac)_3$  occurs on the 7-10 ps timescale, <sup>28</sup> a 510 fs time constant for vibrational cooling in  $Co(acac)_3$  seems rather fast. Although the electronic state on which this process occurs is quite different for each compound (in  $Cr(acac)_3$  all d electrons reside within  $t_{2g}$  orbitals, whereas in the excited state of  $Co(acac)_3$  an electron is populating the antibonding  $e_g^*$  orbital), it seems unlikely that vibrational cooling would occur with such disparate rates between the two structurally

similar compounds. A Jahn-Teller distortion, however, may occur as fast as the frequency of the normal modes driving it allow. According to density functional theory calculations, the <sup>3</sup>T<sub>1g</sub> excited state (and presumably the  $^1T_{1g}$  and  $^3T_{2g}$  excited states with similar electronic configurations) shows an equatorial elongation relative to the ground state with average bond lengths of  $d_{axial} = 1.89$  Å and  $d_{eq} = 1.99$  Å. This is in contrast to the uniform bond lengths calculated for the  $^1A_{1g}$  ground state (1.90 Å) or  $^5T_{2g}$  excited state (1.99 Å). One might expect that the reduced net overlap upon settling into the equilibrium geometry of the <sup>3</sup>T<sub>1g</sub> (or <sup>1</sup>T<sub>1g</sub> or <sup>3</sup>T<sub>2g</sub>) state should result in diminished oscillator strength for a CT transition, consistent with the observations in the TA spectra. Additionally, inspection of the dephasing times shown in Table 3.3, show that several of the dephasing times are qualitatively similar to this 510 fs time constant. It seems plausible that these modes are dephased as the molecule settles into its equilibrium geometry similar to how the flattening distortion of Cu(I) polypyridyls is dephased as the flattening is completed.<sup>29</sup> A closer look at the Duschinsky displacement vector diagram in Figure 3.12a shows that the primary vibrational mode responsible for this distortion is the 162 cm<sup>-1</sup> symmetric breathing mode depicted in Figure 3.13a. In theory, we may be able to gain insight into the relevance of nuclear motion to the 510 fs spectral changes by comparing the magnitude of the coherent oscillations to the magnitude of the preexponential factor for the 510 fs kinetic component. As, the excited state wavepacket travels from one turning point to the other, the molecule experiences it's most distorted geometries which result in the positive and negative extrema of the oscillations in the TA data. If this oscillation amplitude is significantly less than the preexponential factor for the 510 fs kinetic component, then it is unlikely that it results from nuclear motion since the extrema of the nuclear motion are not enough to produce the necessary  $\Delta\Delta A$ . A summary of this comparison is shown in Table 3.4. Unfortunately, it is rather inconclusive. When comparing oscillation and exponential decay amplitudes acquired directly from the LPSVD fit of each dataset, we see that the 162 cm<sup>-1</sup> oscillation can describe 100 % of the exponential decay, albeit with a large standard deviation. In contrast, the same values acquired through direct exponential fitting of each dataset show that only ~50 % of the exponential decay could be described from nuclear motion. Thus, at this point it is rather inconclusive if the 510 fs kinetic component of Co(acac)<sub>3</sub> is due solely to distortions of the molecule.

**Table 3.4.** Comparison of the oscillation amplitude and the preexponential factor for the 510 fs kinetic component of Co(acac)<sub>3</sub> observed during TA experiments. Oscillation amplitudes and preexponential factors were either both directly acquired from LPSVD fits or separately acquired from an exponential fit to the data and the oscillation magnitude of the residual of the exponential fit.

Probe Wavelength, nm	LPSVD: $A_v/A_{exp}$	Residuals: $A_{\nu}/A_{exp}$
620	97 %	59 %
620	165 %	*
600	55 %	21%
600	280 %	44%
580	11%	117%
580	68%	54%
520	27%	26%
Average (σ)	100 (90) %	50 (30) %

<sup>\*</sup> Could not acquire value for this dataset

An alternative assignment for the 510 fs kinetic component of  $Co(acac)_3$  besides distortion of the molecule would be an electronic state change. It was noted that the spectrum after the first picosecond qualitatively resembled a calculated spectrum of the  ${}^3T_{1g}$  state in the work of Ferrari *et al.*<sup>4</sup> and that the energy differences between the high energy band maximum in the TA spectrum and the charge transfer band in the ground state absorption spectrum<sup>5</sup> is fortuitously close to the vertical transition energy of the  ${}^3T_{1g}$  state, both suggesting that the  ${}^3T_{1g}$  state might be the sampled in the transient absorption experiment and necessitating an electronic state change from the initially populated  ${}^1T_{1g}$  state. Additionally, since each of the plausibly accessible excited states ( ${}^1T_{1g}$ ,  ${}^3T_{2g}$ , and  ${}^3T_{1g}$ ) have a similar electronic configuration, we may expect only subtle changes to the absorption spectrum if transitions between these states were to occur, fitting with the subtle changes arising from the 510 fs kinetic component. If a single change in electronic state is observed then it must either be  ${}^1T_{1g} \rightarrow {}^3T_{2g}$  intersystem crossing from the initially populated  ${}^1T_{1g}$  state (followed by a fast IC to form the  ${}^3T_{1g}$  state) or  ${}^3T_{2g} \rightarrow {}^3T_{1g}$  internal conversion (implying a prompt, unobservable ISC). It stands to reason that the slower process is the most observable. We can thus evaluate both options on the basis of expected rates.

We can deduce from the similarity in the 1-electron picture electronic configurations for each of the  ${}^{1}T_{1g}$ ,  ${}^{3}T_{2g}$ , and  ${}^{3}T_{1g}$  states, as well as the similar slopes on the Tanabe Sugano diagram in Figure 3.2 that each of these electronic states should show fairly similar distortions from the ground state equilibrium

geometry and thus their potential energy surfaces should be fairly nested relative to each other. With regards to the energy gap law as applied to weakly coupled systems<sup>30,31</sup> (i.e. nested potentials) a smaller energy gap between a pair of nested states should result in a larger rate constant for nonradiative decay. Since the potential energy surfaces of interest here are all nested and likely exhibit similar force constants, we may approximate the energy gaps based on the vertical transition energies listed in Figure 3.2. We see that the energy gap between the  ${}^{1}T_{1g}$  and  ${}^{3}T_{2g}$  states is larger than that for the  ${}^{3}T_{2g}$  and  ${}^{3}T_{1g}$  states alluding to slower ISC. Furthermore, we can infer from spin selection rules that the coupling between the  ${}^{1}T_{1g}$  and  ${}^{3}T_{2g}$  excited states is substantially weaker than that between the two triplet excited states. All of this suggests that  ${}^{1}T_{1g}$   $\rightarrow$   ${}^{3}T_{2g}$  ISC is slower than IC within the triplet manifold. Thus, we can say that the likely slowest observable transition is the  ${}^{1}T_{1g} \rightarrow {}^{3}T_{2g}$  transition. If the 510 fs kinetic component of Co(acac)<sub>3</sub> is indeed due to an electronic state change then it is most likely ISC from the initially populated singlet excited state.

We have at this point described several plausible scenarios to describe the observed kinetics of the  $Co(acac)_3$  system following  $^1A_{1g} \rightarrow {}^1T_{1g}$  excitation. It seems evident that the  ${}^5T_{2g}$  lowest energy excited state remains unpopulated throughout the course of the excited state dynamics, in stark contrast to many iron(II) polypyridyl systems. We further know that the initial nuclear motion following  ${}^1A_{1g} \rightarrow {}^1T_{1g}$  excitation resembles the distortions expected on an excited state of  $(t_{2g})^5(e_g^*)$  character and that ground state recovery occurs from one of these states  $({}^1T_{1g}, {}^3T_{2g}, {}^3T_{1g})$  with a 2.0 ps time constant. An additional 510 fs process is assigned either to settling into the equilibrium geometry of this manifold of states or to intersystem crossing from the initially populated  ${}^1T_{1g}$  state. Unfortunately, there is not enough evidence at present to definitively prove either of these scenarios so additional experiments are needed to help further refine the kinetic model of  $Co(acac)_3$ . Ideally, ultrafast X-ray fluorescence spectroscopy could be used to measure the transient  $K\beta$  emission spectrum, which is highly sensitive to the 3d spin moment and hence could be used to definitively identify the presence of a singlet or triplet excited state. Similar experiments were recently performed on  $[Fe(bpy)_3]^{2+}$  and  $[Fe(dccp)_2]^{2+}$  to quantify the influence of the  ${}^3T_{1g}$  state on the excited state dynamics. Such an experiment, however, is difficult to get access to. We will thus instead

attempt to glean more information about this chemical system by studying the small series of derivatives displayed in Figure 3.1.

### 3.4.2. $Co(3-Iac)_3$

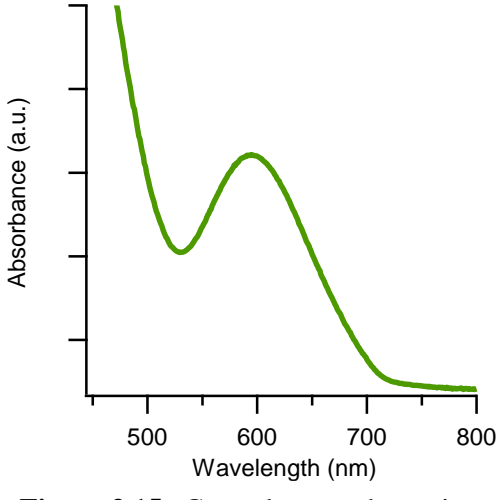


**Figure 3.15.** Ground state absorption spectrum of  $Co(3\text{-Iac})_3$  in toluene.

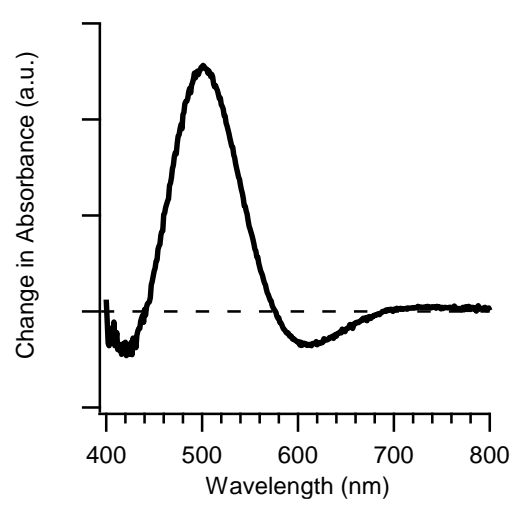


**Figure 3.16.** Difference spectrum of  $Co(3\text{-Iac})_3$  in toluene before and after significant light exposure.

The ground state absorption spectrum of  $Co(3\text{-Iac})_3$  can be seen in Figure 3.15. The band centered at 595 nm can be assigned to the  ${}^1A_{1g} \rightarrow {}^1T_{1g}$  lowest energy spin-allowed ligand field transition, similar to what was observed for the unsubstituted  $Co(acac)_3$  system. The identical peak position between these two compounds suggests that the effect of the iodine substitution on the ligand field strength is quite small, in good agreement with the observations in the  $Cr(acac')_3$  systems. The remainder of this section will discuss the dynamics following 600 nm  ${}^1A_{1g} \rightarrow {}^1T_{1g}$  excitation.

On an experimental note, the Co(3-Iac)<sub>3</sub> system was not as photostable as the unsubstituted Co(acac)<sub>3</sub> system and a significant change in the absorption spectrum could be seen if a solution of Co(3-Iac)<sub>3</sub> was exposed to light for too long. A representative difference spectrum highlighting the sample degradation can be seen in Figure 3.16, in which a significant increase in absorbance around 500 nm occurs resulting in an increasingly brownish color to the solution. This is likely attributable to the release of iodine from the ligand backbone. This is not expected to have significantly affected the results shown in this dissertation since the observed frequencies of the coherent oscillations discussed shortly are exceptionally

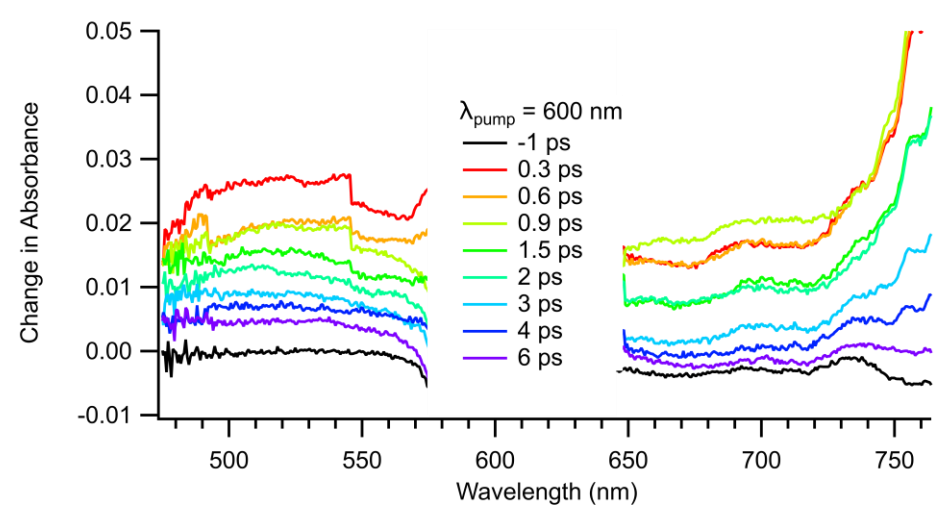


**Figure 3.17.** Full spectrum TA data on  $Co(3-Iac)_3$  in toluene following 600 nm excitation into the  ${}^1T_{1g}$  state. The region from ~570-640 nm was omitted due to contamination from pump scatter.

close to the calculated frequencies for the undegraded compound and are highly dependent on the presence of iodine on the ligand backbone.

Full spectrum transient absorption data on  $Co(3\text{-Iac})_3$  in toluene following 600 nm excitation into the  $^1T_{1g}$  state is shown in Figure 3.17. The data is qualitatively similar to the data for the unsubstituted  $Co(acac)_3$  and show that most of the transient signal is lost in the first six picoseconds. Single wavelength TA measurements were used to acquire a more precise view of the kinetics of this system. A summary of the kinetics can be seen in Table 3.5 with representative data sets shown in Figure 3.18. We again see biphasic kinetics in this system with  $180 \pm 150$  fs and  $2070 \pm 160$  fs time constants. Additionally, a  $94 \pm 1$  cm<sup>-1</sup> coherent oscillation with  $320 \pm 100$  fs dephasing time attributable to the excited state of the solute was observed in several datasets as summarized in Table 3.6.

**Table 3.5.** Summary of kinetic components from single wavelength transient absorption experiments on  $Co(3\text{-Iac})_3$  in toluene following 600 nm excitation into the  ${}^1T_{1g}$  state.

Probe, nm	$\tau_{1}$ , fs	$\tau_2$ , fs
620	110	2000
620	90	1900
600	400	2280
580	110	2100
Average (σ)	180 (150)	2070 (160)

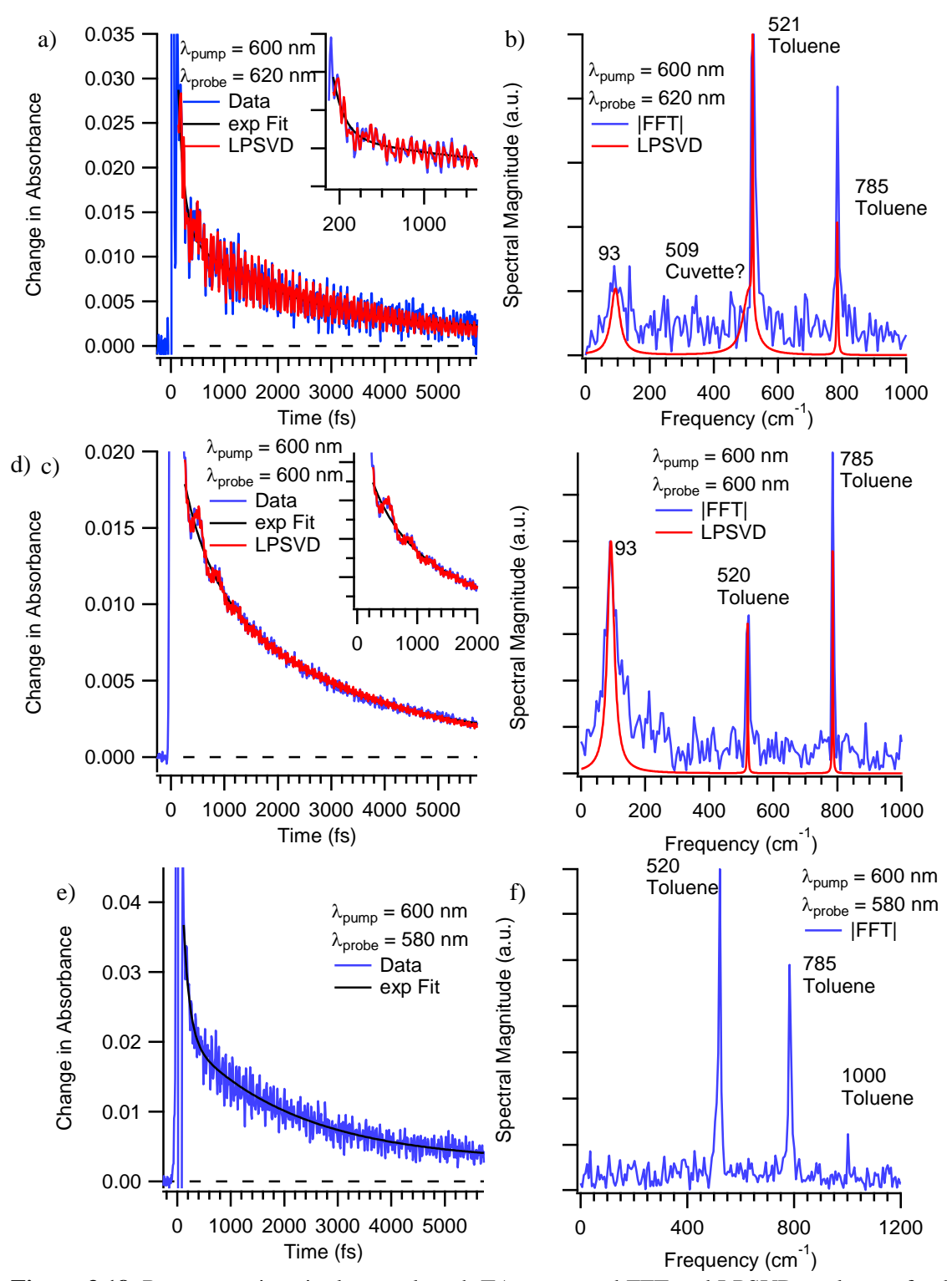


**Figure 3.18.** Representative single wavelength TA traces and FFT and LPSVD analyses of coherent oscillations of  $Co(3-Iac)_3$  in toluene following 600 nm excitation into the  ${}^1T_{1g}$  state. Kinetics were monitored at (a) 620 nm, (c) 600 nm, and (e) 580 nm using a probe beam with a spectrum centered at 600 nm. Insets show coherent oscillations at early times. Corresponding FFT and LPSVD vibrational spectra are shown in (b), (d), and (f). LPSVD contributions are omitted from the 580 nm probe data due to lack of solute oscillations.

**Table. 3.6.** Summary of the coherent vibrational modes observed for  $Co(3-Iac)_3$  in toluene following 600 nm excitation into the  ${}^1T_{1g}$  state. All measurements had a 40 fs IRF and employed 2.9 and 0.4  $\mu J$  pump and probe pulse energies respectively.

Probe, nm	Frequency, cm <sup>-1</sup> (Damping Time, fs)		
620	95 (216)		
620	93 (320)		
600	93 (411)		
Avg. Frequency	94 ± 1		
Avg. Damping	$320 \pm 100$		

The above results in Figure 3.17 and Table 3.5 show that both the spectral evolution and kinetics for ground state recovery of Co(3-Iac)<sub>3</sub> are essentially identical to the unsubstituted Co(acac)<sub>3</sub> control molecule. This further suggests a similar decay cascade between the two compounds. While the faster kinetic component seen here is significantly shorter than what was observed in Co(acac)<sub>3</sub>, it is possible that the large amplitude, low-frequency oscillatory component occurring concomitant with the exponential decay distorted the measured time constant. The insensitivity of the excited state dynamics to the iodo-substituent in the 3-position of the ligand backbone is also consistent with the lack of effect observed in the Cr(acac)<sub>3</sub> systems discussed in chapter 2 of this dissertation.

As summarized in Table 3.6, only a single coherent vibrational mode of  $Co(3-Iac)_3$  could be observed. Given the frequency region and the types of motion already observed in  $Co(acac)_3$  as well as each of the  $Cr(acac')_3$  compounds discussed in chapter 2, it is clear that the observed  $94 \pm 1$  cm<sup>-1</sup> vibration of  $Co(3-Iac)_3$  corresponds to a symmetric breathing mode. Figure 3.19 shows this symmetric breathing mode

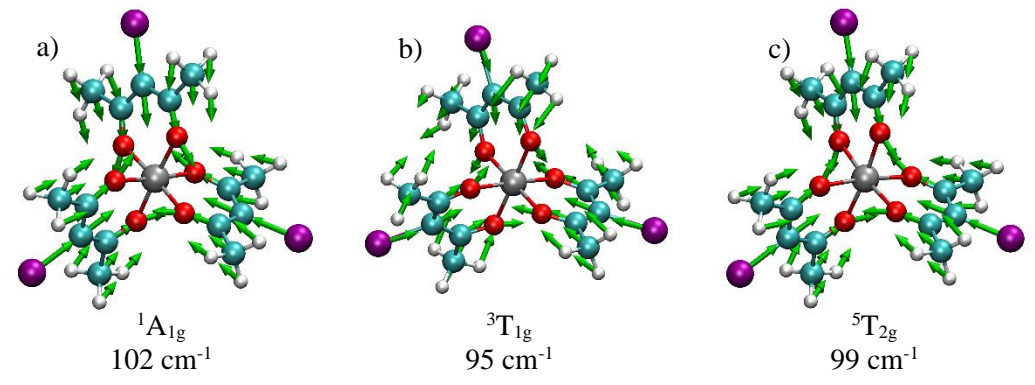


**Figure 3.19.** DFT calculated symmetric breathing mode of  $Co(3-Iac)_3$  on (a) the  ${}^1A_{1g}$  ground state, (b) the  ${}^3T_{1g}$  lowest energy triplet excited state, and (c) the  ${}^5T_{2g}$  lowest energy excited state of the system.

as calculated on the  ${}^{1}A_{1g}$  ground state, the  ${}^{3}T_{1g}$  lowest energy triplet excited state, and the  ${}^{5}T_{2g}$  lowest energy excited state of the system. We already know from consideration of the low extinction coefficient for the initial excitation that a vibrational coherence on the ground electronic state is not observed in this system. Furthermore, from consideration of the discussion of the unsubstituted  $Co(acac)_3$  compound, it is unlikely that the  ${}^{5}T_{2g}$  lowest energy excited state of this system is accessed. These findings are confirmed by the excellent agreement between the  $94 \pm 1$  cm<sup>-1</sup> observed and 95 cm<sup>-1</sup> calculated frequency of the  ${}^{3}T_{1g}$  excited state in Figure 3.19b. While this doesn't mean that this mode is observed on the  ${}^{3}T_{1g}$  state specifically, it does indicate that it is observed on an excited state of  $(t_{2g})^{5}(e_{g}^{*})$  electronic configuration ( ${}^{1}T_{1g}$ ,  ${}^{3}T_{2g}$ ,  ${}^{1}T_{1g}$ ), consistent with the dynamics in  $Co(acac)_3$ .

What is perhaps more interesting here is the dephasing time of this mode. In the chromium systems, iodo-substitution led to a dramatic order of magnitude increase in the vibrational dephasing time relative to Cr(acac)<sub>3</sub>, which was attributed to a decrease in efficiency of IVR. In contrast, iodo-substitution seems to have very little effect on the dephasing time in these cobalt systems. This could imply a fundamentally different dephasing mechanism between these two sets of compounds. A more complete discussion of this will be made after the results of the final Co(TMHD)<sub>3</sub> compound are revealed.

#### 3.4.3. Co(TMHD)<sub>3</sub>

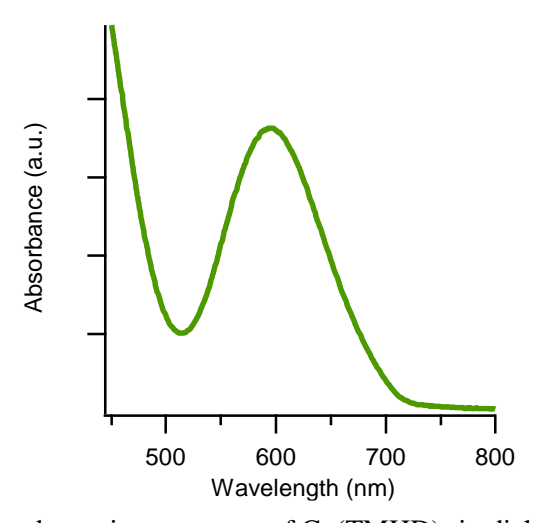
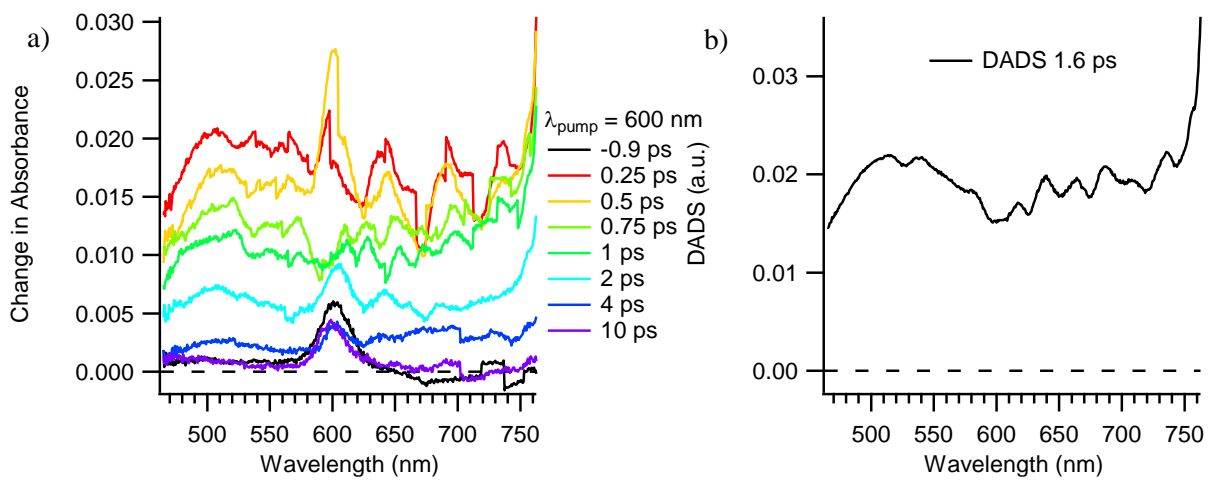


Figure 3.20. Ground state absorption spectrum of Co(TMHD)<sub>3</sub> in dichloromethane solution.



**Figure 3.21.** (a) Full spectrum TA data on Co(TMHD)<sub>3</sub> in DCM following 600 nm  $^{1}A_{1g} \rightarrow {}^{1}T_{1g}$  excitation. Anomalies around 600 nm are due to excess pump scatter. (b) DADS associated with a global fit of the data to a single exponential kinetic component.

The visible region of the ground state absorption spectrum of  $Co(TMHD)_3$  can be seen in Figure 3.20. A peak centered at 594 nm can be assigned to the  ${}^1A_{1g} \rightarrow {}^1T_{1g}$  lowest energy spin allowed ligand field transition, similar to what is observed for the previous two  $Co(acac')_3$  compounds. The spectral shape and position are unperturbed relative to the  $Co(acac)_3$  control molecule suggesting that this substitution has little effect on the ligand field strength or the initial geometry of the molecule. The following transient absorption experiments on  $Co(TMHD)_3$  will employ an excitation pulse that is in resonance with this  ${}^1A_{1g} \rightarrow {}^1T_{1g}$  transition.

Full spectrum transient absorption data on Co(TMHD)<sub>3</sub> is shown in Figure 3.21 along with the DADS associated with a global fit of the data to a single exponentially decaying kinetic component. The timescale and shape of the spectral evolution is qualitatively similar to that for Co(acac)<sub>3</sub> and Co(3-Iac)<sub>3</sub> suggesting a similar decay cascade. Single wavelength TA measurements were conducted to get a more precise idea of the kinetics of this system. These data are shown in Figure 3.22 along with the corresponding vibrational spectra from FFT and LPSVD analyses. A summary of the kinetics and coherent oscillations is shown in Table 3.7 and Table 3.8 respectively. We again see that the dynamics in this system are biphasic with time constants that are essentially identical to the Co(acac)<sub>3</sub> control molecule. An analysis of the coherent vibrational motion reveals a 163 cm<sup>-1</sup> frequency with large error bars due to the rapid dephasing

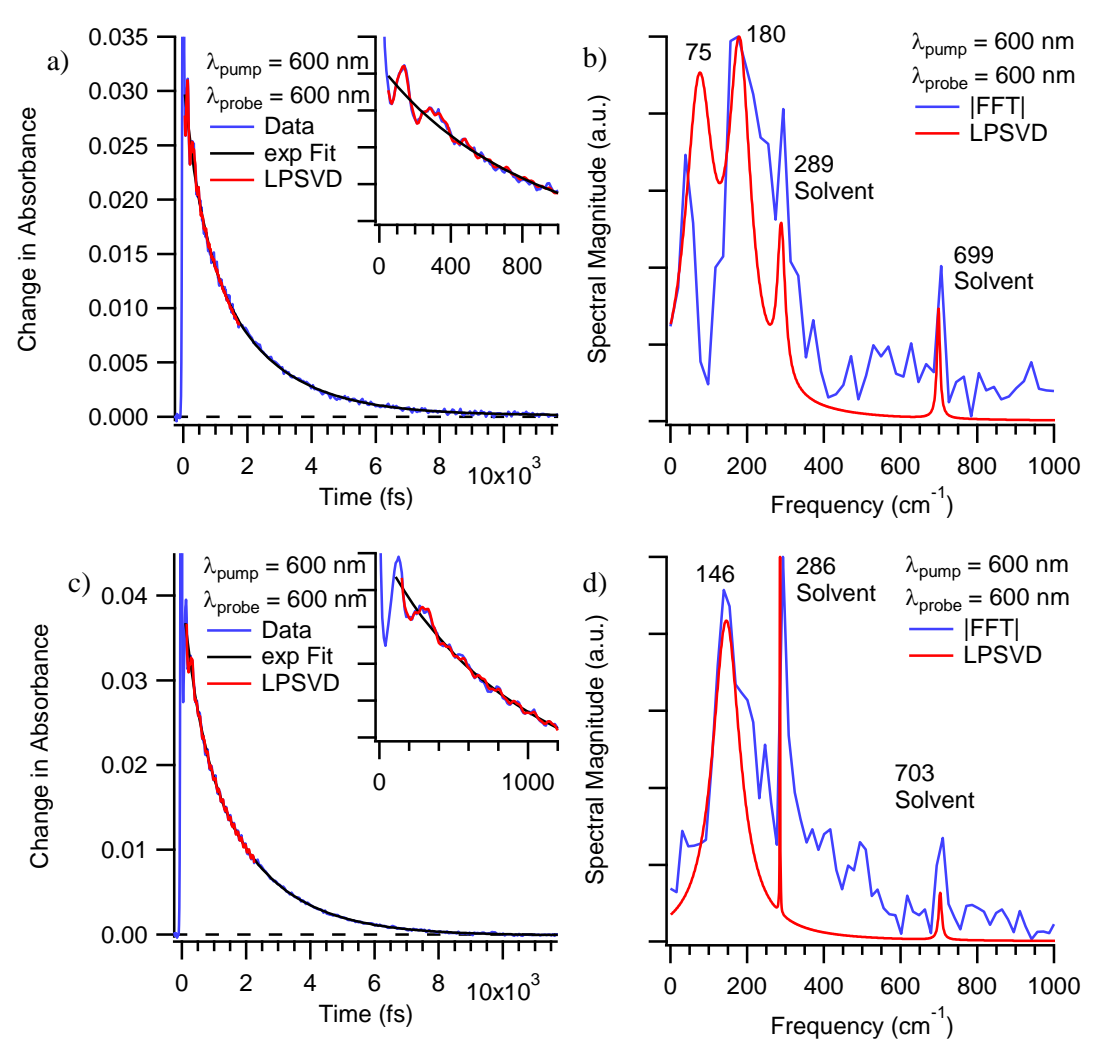


**Figure 3.22.** (a) and (c) Single wavelength TA data on  $Co(TMHD)_3$  in DCM following 600 nm  $^1A_{1g} \rightarrow ^1T_{1g}$  excitation. (b) and (d) corresponding vibrational spectra from FFT and LPSVD analysis.

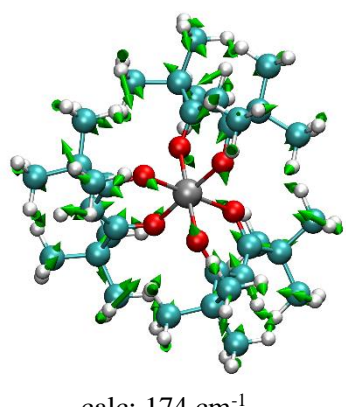
**Table 3.7.** Summary of kinetic components of Co(TMHD)<sub>3</sub> in DCM following 600 nm excitation.

Probe, nm	$\tau_1$ , fs	$\tau_2$ , fs
600	530	2000
600	500	1900
Avg (σ)	520 (20)	1950 (70)

**Table 3.8.** Summary of coherent oscillations of Co(TMHD)<sub>3</sub> monitored at 600 nm in DCM following 600 nm excitation.

IRF, fs	$E_{pu}(E_{pr}),\mu J$	(Damping Time, fs)		
45	3.6 (0.4)		146 (120)	
55	2 (0.3)	75 (118)	180 (148)	
Avg. Frequency		-	$163 \pm 24$	
Avg. Damping		_	130 + 20	

times and difficulty in fitting. This is likely the symmetric breathing mode calculated at 174 cm<sup>-1</sup> on the  ${}^{3}T_{1g}$  excited state and depicted in Figure 3.23. A second 75 cm<sup>-1</sup> oscillatory component was acquired in a single data set but is likely due to poor exponential fitting rather than coherent vibrational motion.



calc: 174 cm<sup>-1</sup> exp: 163 cm<sup>-1</sup>

Figure 3.23. Nuclear distortion associated with the coherent vibrational mode of Co(TMHD)<sub>3</sub>.

## 3.5. Concluding Thoughts on Co(acac')<sub>3</sub> Dynamics

**Table 3.9.** Summary of the kinetic components and coherent oscillations of each of the Co(acac')<sub>3</sub> compounds investigated in this chapter.

Compound	$\tau_1$ , fs	$\tau_2$ , fs	$v_{breath,obs}, cm^{-1}$	ν <sub>breath,calc</sub> , cm <sup>-1</sup>	$\tau_{\text{dephase}}$ , fs
Co(acac) <sub>3</sub>	510 (150)	2000 (200)	162 (8)	178	150 (60)
$Co(3-Iac)_3$	180 (150)	2070 (160)	94 (1)	95	320 (100)
$Co(TMHD)_3$	520 (20)	1950 (70)	163 (23)	174	130 (20)

The excited state dynamics of a series of cobalt(III) trisbetadiketonate complexes have been investigated in this chapter. A summary of the kinetics and coherent oscillations is shown in Table 3.9. We see that each of the compounds studied exhibit identical spectral evolution in the visible region following  ${}^{1}A_{1g} \rightarrow {}^{1}T_{1g}$  excitation. Furthermore, the measured kinetics for  $Co(acac)_3$ ,  $Co(3-Iac)_3$ , and  $Co(TMHD)_3$  are all within error, except for the fast component of  $Co(3-Iac)_3$  which may have been influenced by the large amplitude oscillatory component. Because of these findings, we can conclude that the iodo and t-butyl substitutions have little effect on the excited state dynamics (a finding that is consistent with the data on the related chromium compounds of the previous chapter) and that each compound has an identical decay

cascade. The discussions in sections 3.4.1 and 3.4.2 have shown that the  ${}^5\mathrm{T}_{2\mathrm{g}}$  lowest energy excited state remains unpopulated during the course of the excited state dynamics, in stark contrast to many  $d^6$  six-coordinate iron(II) polypyridyl systems.<sup>1</sup> Furthermore, following  ${}^1\mathrm{A}_{1\mathrm{g}} \to {}^1\mathrm{T}_{1\mathrm{g}}$  excitation, the system remains in excited states of  $(t_{2g})^5(e_g^*)$  electronic configuration ( ${}^1\mathrm{T}_{1\mathrm{g}}$ ,  ${}^3\mathrm{T}_{2\mathrm{g}}$ ,  ${}^3\mathrm{T}_{1\mathrm{g}}$ ) until the ground state is recovered with a  $\sim$ 2 ps time constant. The dynamics prior to ground state recovery are more ambiguous. The fast time constant was proposed to represent either a change in electronic state ( ${}^1\mathrm{T}_{1\mathrm{g}} \to {}^3\mathrm{T}_{1,2\mathrm{g}}$  ISC) or a change in geometry.

An additional important observation is that the dephasing time of the symmetric breathing mode of each cobalt compound was quite rapid. In contrast, both synthetic modifications to the acac ligand shown here resulted in significant, up to an order of magnitude, changes in the dephasing times of the symmetric breathing mode in the structurally similar Cr(acac')<sub>3</sub> compounds discussed in chapter 2. Whereas the changes to the dephasing times in the chromium systems were ascribed to changes in IVR rates resulting from changes to the vibrational density of states, the invariance of the dephasing times in the cobalt systems suggests a fundamentally different dephasing mechanism. While it is difficult to conclusively identify the exact origin for dephasing in these compounds, we may be able to rule out a notion that was suggested originally for the Cr(acac')<sub>3</sub> systems<sup>34</sup> (and later disproven for that particular system by the results of chapter 2 of this dissertation), i.e. that the rapid dephasing is indicative of such modes driving an electronic state change. To achieve this, we can perform wave packet simulations to model how state changes affect the dispersion or dephasing of the wavepacket. We will employ the split operator method, first developed by Feit, Fleck, and Steiger.<sup>35</sup> For the purposes of this dissertation a homebuilt MATLAB script for this procedure was written based on the work of Tanner, <sup>36</sup> and Reber et al. <sup>37</sup> A detailed description of the mechanics of this methodology is beyond the scope of this dissertation, and the interested reader is directed to the references just listed. However, in brief, the split operator method uses propagators to advance the wave function (or wave packet) in time. The principle idea of the split operator method is to split the Hamiltonian operator into propagators which are diagonal in the basis of position or momentum. By performing half-propagation steps in momentum and then position space and then another set of half-steps in the reverse order the wavepacket is advanced in time. The Fourier transform relationship between position and momentum space makes it easy to convert the wavepacket into the proper representation. In what follows, we will show how the relative displacement of excited state potential energy surfaces affects dephasing times.

Figure 3.24a shows a two-level system in which the potential energy surfaces are significantly displaced relative to each other. An initial gaussian wavepacket was placed at 0 Å on the upper surface and allowed to propagate as shown in Figure 3.24b. The wavepacket immediately splits to the upper and lower

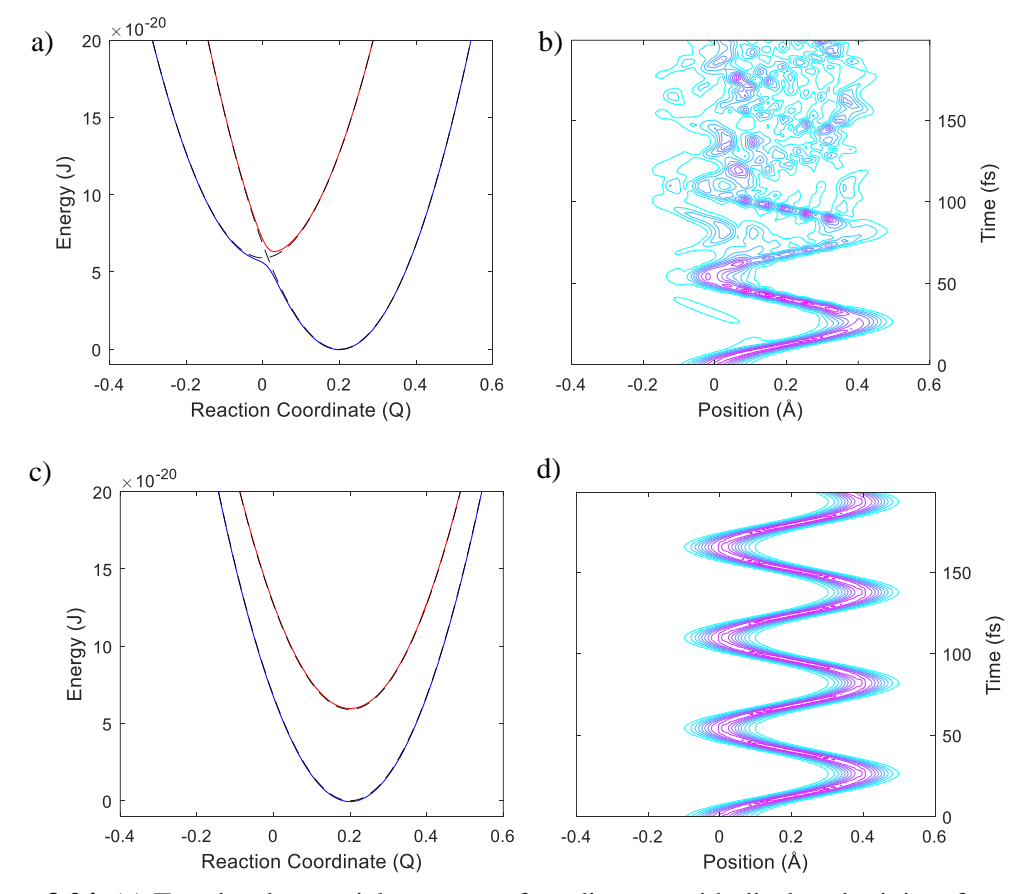


**Figure 3.24.** (a) Two-level potential energy surface diagram with displaced minima for use in wavepacket calculation. Diabatic and adiabatic representations are shown as dashed and solid lines respectively. The initial gaussian wavepacket is placed at 0 Å on the upper surface and allowed to propagate. (b) Contour plot showing the sum of the amplitude of the corresponding wavepackets on both excited states in position space as a function of time. (c) Two-level potential energy surface diagram with nested potentials for use in wavepacket simulations. The initial gaussian wavepacket is placed at 0 Å on the upper surface. (d) Contour plot showing the sum of the amplitude of the corresponding wavepackets on both excited states. Despite continuously cycling population from one surface to the other, the wavepacket retains a well-defined phase relationship.

surfaces with the bulk of the amplitude on the lower potential. As each wavelet reaches the initial crossing point more amplitude is transferred to the other surface thus distributing the phase of the overall wavepacket resulting in significant dephasing in only a few hundred femtoseconds. In contrast, nesting of the potential surfaces as seen in Figure 3.24c results in a dramatically different dephasing rate. Here, despite continuously cycling from the upper and lower states, the identical forces on each potential surface keep each wavelet propagating identically thus retaining their phase relationship. We thus see that when potential energy surfaces of identical curvature are nested along a particular nuclear coordinate, electronic state changes do not dephase a vibrational coherence. Thus, since each of the  ${}^{1}T_{1g}$ ,  ${}^{3}T_{2g}$ , and  ${}^{3}T_{1g}$  excited states of Co(acac')<sub>3</sub> are nested, then the rapid vibrational dephasing times must not be due to electronic state changes.

The results of this chapter have shed new insight into the ultrafast excited state dynamics of six-coordinate cobalt(III) compounds, however additional experiments are needed to conclusively characterize these ultrafast processes. Ideally measurement techniques that are sensitive to the spin-state of the metal center such as ultrafast X-ray emission spectroscopy could be used to clear up some of the ambiguities of spin-state assignment to build a more complete picture of the decay cascade. Furthermore, with a better understanding of why the lowest energy  ${}^5T_{2g}$  excited state of this system is not populated on ultrafast timescales, we may be able to engineer six-coordinate Fe(II) compounds that do not rapidly depopulate their MLCT states in favor of this lower energy ligand field state. Additional future efforts on cobalt(III) compounds may focus on extending the LMCT state lifetimes which have been shown to be exceedingly fast in both Co(acac)<sub>3</sub> by Ferrari *et al.*<sup>4</sup> and Several CoN<sub>6</sub> compounds by McCusker *et al.*<sup>8</sup> Long lasting LMCT excited states of earth abundant cobalt compounds could then potentially have wide-ranging applications for use in photo-induced electron transfer chemistry.

**APPENDICES** 

# Appendix 3.A. NMR Spectra

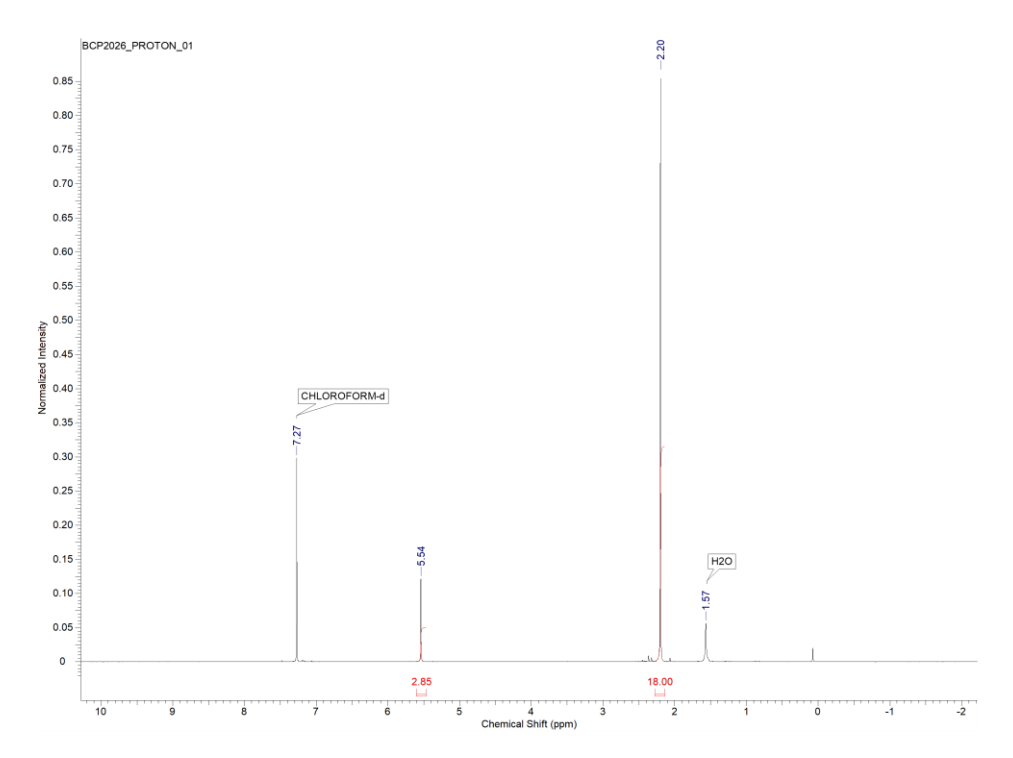
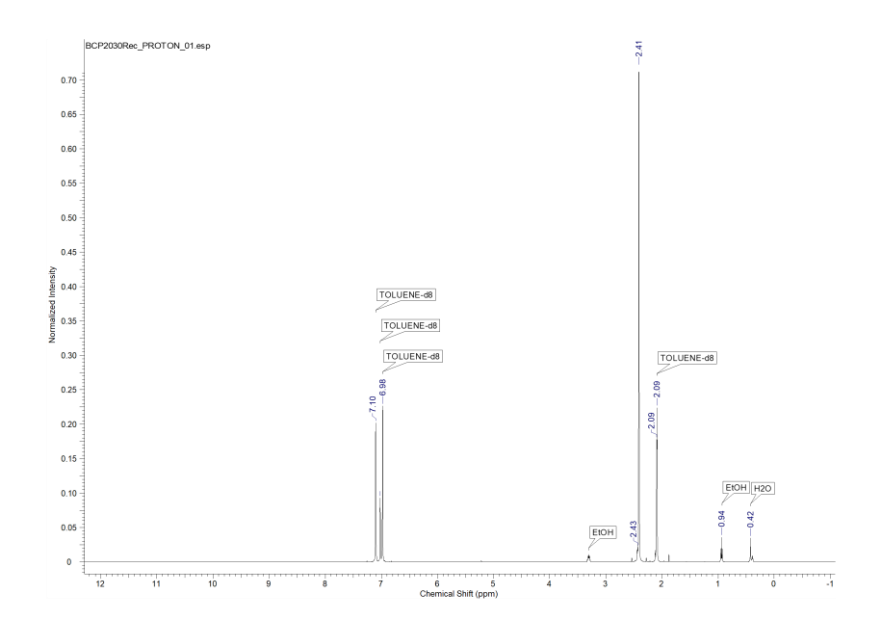


Figure 3.A.1. NMR spectrum of Co(acac)<sub>3</sub> in CDCl<sub>3</sub>.



**Figure 3.A.2.** NMR spectrum of Co(3-Iac)<sub>3</sub> in deuterated toluene.

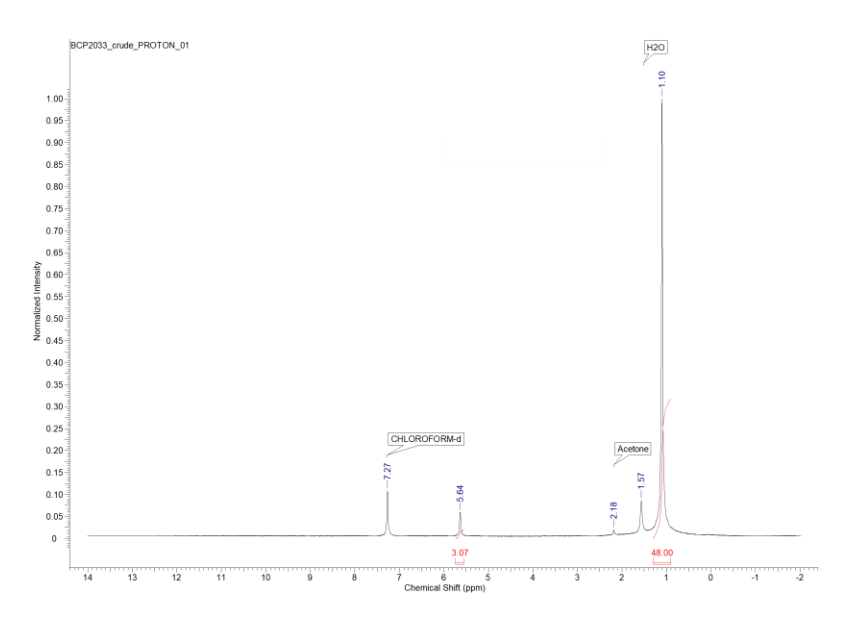


Figure 3.A.3. NMR spectrum of Co(TMHD)<sub>3</sub> in CDCl<sub>3</sub>.

## Appendix 3.B. Duschinsky Displacement Vector Calculation MATLAB Script

The following contains the code for the MATLAB script that performed the Duschinsky displacement vector calculations used for this dissertation work. It should be noted that, due to formatting restrictions, the code below was pasted directly from a working MATLAB script. Because of this, there may be several instances in which the written code runs beyond the margins used here and hence wraps around to the following line. As such, this code may not work properly until these disjointed portions of the code are brought back together on the same line.

#### clear all clc

% This is a script that uploads the coordinates from excel files that were % created from pbd files and reorients them both so that they have no % relative linear or angular momentum. The procedure of [Miller, w. H.; Ruf, %B. A.; Chang, Y.-T. J chem phys. 89 (10), 1988] was followed for this. % Then once there is no Linear or Angular momentum between these two % geometries, it uses the hessian calculated for one geometry to calculate % the Duschinsky displacement vector that describes the displacement of each % vibrational mode necessary to distort the reactant state to the product % state geometry. The procedure of [Ando, S.; Iuchi, S.; Sato, H. Chem. % Phys. Let. 2012, 535, 177-181.] was used for this. Finally, The reduced % masses for each vibrational mode as well as the force constant was % calculated so that the innersphere reorgonization energy for each normal % mode could be obtained using lamda\_i\_tot=sum(0.5\*f\_j\*(K\_j)^2).



%This script will ask for three files before doing any calculations. It % will ask for the coordinates of the reactant state followed by the % coordinates of the product state followed by the hessian for the reactant % state. These files must be in the correct format for this script to work. %To make the coordinate files, first create a pdb file that contains the % geometry of the molecule and then import the data into excell so that not % all of the data is in the first column. This will initially create 8 % columns of values. Delete the first, third and last (eigth) columns by %right clicking the top of the column in excel and selecting delete. Now, % delete the top row by selecting row 1 on the side of the excel doc and % selecting delete. Next, scroll down to the end of the coordinates and % delete all of the values that describe the connectivity of atoms. We now %have a file that has columns with atom index, atom type, x coordinate, y %coordinate, and z coordinate. We also need to add the masses of each of % these atoms in amu. Add this in by hand after the z coordinate column. %Save it as an excell file and its ready for use. To get the Hessian, we % first need to create a formatted checkpoint file for the frequency

```
% calculation of the reactant state. to do this, log onto the terminal in
%HPCC and go to the directory that contains the checkpoint file (.chk) for
%the relevant frequency calculation. next, type "formchk -3 filename.chk
%newfilename.fchk" without the quotes. This creates a formated checkpoint
% file. Now, open this document in excel and delete everything but the
% cartesian force constants and save the file. Now open up a new excel doc
% and import these cartesian force constants using fixed width cells to get
% five columns with all of the lower triangle of the symmetric hessian
% matrix. Delete everything but these hessian values (ie no text should be
% present, just the five columns of data). Save this as an excel file and it
% should be ready for use.
% First we will import an excel file with the reactant state geometry and
% save it as Reactant.
[filename, pathname]=uigetfile;
s=strcat(pathname, filename);
Reactant=xlsread(s);
% Next, we will do the same with an excel file with the product state
% geometry and save it as Product.
[filename, pathname]=uigetfile;
ss=strcat(pathname, filename);
Product=xlsread(ss);
% Note, These excel files are arranged in columns from left to right as atom
%index number, atom type (ie C, H, etc), x coord, y coord, z coord, and
%mass (in amu).
% The following makes column vectors of the x, y, z components of each atom
% first for the reactant state and then for the product state.
Rrinix=Reactant(:,3);
Rriniy=Reactant(:,4);
Rriniz=Reactant(:,5);
mir=Reactant(:,6); %masses of each reactant atom
Rpinix=Product(:,3);
Rpiniy=Product(:,4);
Rpiniz=Product(:,5);
mip=Product(:,6); % masses of each product atom
% we get rid of any linear momentum between reactant and product states by
% setting the origin of each of their axis systems at the center of mass of
% each. The result is colum vectors of the x, y, and z components
%(separately) of all the atoms
mRrinix=Rrinix.*mir;
mRriniy=Rriniy.*mir;
mRriniz=Rriniz.*mir;
mRpinix=Rpinix.*mip;
mRpiniy=Rpiniy.*mip;
mRpiniz=Rpiniz.*mip;
```

```
Rcomrx=sum(mRrinix)/sum(mir);
Rcomry=sum(mRriniy)/sum(mir);
Rcomrz=sum(mRriniz)/sum(mir);
Rcompx=sum(mRpinix)/sum(mip);
Rcompy=sum(mRpiniy)/sum(mip);
Rcompz=sum(mRpiniz)/sum(mip);
Rrfinalx=Rrinix-Rcomrx;
Rrfinaly=Rriniy-Rcomry;
Rrfinalz=Rriniz-Rcomrz;
Rpfinalx=Rpinix-Rcompx;
Rpfinaly=Rpiniy-Rcompy;
Rpfinalz=Rpiniz-Rcompz;
% Now we must insure that there is no angular momentum between the two
% structures. To do this, we must ensure that the sum of the cross products
% of each of the position vectors for each element multiplied by the scalar
% of their respective masses is zero.
% We use the procedure of [Miller, w. H.; Ruf, B. A.; Chang, Y.-T. J.
%chem. phys. 89 (10), 1988] for this.
Rri_z0=[0,0,0];
Rpi_z0=[0,0,0];
% First, we find the current angular momentum of the system by summing the
% mass weighted cross products of the position vectors.
for i = 1: length(Rrfinalx);
  Rri=[Rrfinalx(i),Rrfinaly(i),Rrfinalz(i)];
  Rpi=[Rpfinalx(i),Rpfinaly(i),Rpfinalz(i)];
  mcross_sub=mir(i)*cross(Rri,Rpi);
  cross_sub=cross(Rri,Rpi);
  if i==1
    mcrossA=mcross sub;
    crossA=cross sub;
    mcrossB=mcrossA;
    crossB=crossA;
  else
    mcrossA=mcrossB;
    crossA=crossB;
    mcrossB=mcrossA+mcross_sub;
    crossB=crossA+cross_sub;
  end
end
% Next, we create a unit vector, N, that points in the direction fo the sum
% of the mass weighted cross product of the position vectors
nx=mcrossB(1)/sqrt(mcrossB(1)^2+mcrossB(2)^2+mcrossB(3)^2);
ny=mcrossB(2)/sqrt(mcrossB(1)^2+mcrossB(2)^2+mcrossB(3)^2);
nz=mcrossB(3)/sqrt(mcrossB(1)^2+mcrossB(2)^2+mcrossB(3)^2);
```

```
N=[nx,ny,nz];
%Now, before we determine the angle that the position vectors of one system
% needs to be rotated by (along the N unit vector) we must first project all
% atoms onto the plane perpendicular to the N unit vector. This will ensure
%that there is no overcounting towards the sum of the mass weighted dot
% product of the position vectors which is used to determine the angle of
%rotation.
for i=1: length(Rrfinalx);
  Rri=[Rrfinalx(i),Rrfinaly(i),Rrfinalz(i)];
  Rpi=[Rpfinalx(i),Rpfinaly(i),Rpfinalz(i)];
  Rri projection=Rri-dot(Rri,N)*N;
  Rpi_projection=Rpi-dot(Rpi,N)*N;
  mdot(i)=mir(i)*(dot(Rri_projection,Rpi_projection));
%phi= angle that Rr is needed to be rotated about the vector sum of the mass
% weighted cross products of Rr and Rp
phi=-atan(sqrt(dot(mcrossB,mcrossB))/sum(mdot));
C=cos(phi);
S=sin(phi);
t=1-\cos(phi);
T = [t*(nx^2)+Ct*nx*ny-S*nzt*nx*nz+S*ny;t*nx*ny+S*nzt*(ny^2)+Ct*ny*nz-S*nx;t*nx*nz-S*ny]
t*nv*nz+S*nx t*(nz^2)+C];
%T is the rotation matrix that rotates Rp about mcrossB by angle phi
Rpi_rotx=zeros(size(Rrfinalx));
Rpi_roty=zeros(size(Rrfinaly));
Rpi rotz=zeros(size(Rrfinalz));
for i =1: length(Rrfinalx);
  Rpi=[Rpfinalx(i),Rpfinaly(i),Rpfinalz(i)];
  Rpi_rot=T*Rpi.';
  Rpi_rotx(i)=Rpi_rot(1);
  Rpi_roty(i)=Rpi_rot(2);
  Rpi rotz(i)=Rpi rot(3);
end
% Now we will check that the rotation is done correctly.
for i=1: length(Rrfinalx);
  Rri=[Rrfinalx(i),Rrfinaly(i),Rrfinalz(i)];
  Rpi=[Rpi_rotx(i),Rpi_roty(i),Rpi_rotz(i)];
  mcross_sub=mir(i)*cross(Rri,Rpi);
  if i==1
    mcrossA=mcross sub;
    mcrossB=mcrossA;
  else
    mcrossA=mcrossB;
    mcrossB=mcrossA+mcross_sub;
  mdot(i)=mir(i)*dot(Rri,Rpi);
end
```

```
% Next we import the data necessary to create the hessian matrix by
%importing an excel file with the lower triangular elements. This file
% should have all of the data from a formated checkpoint file where each
% matrix element is listed in five columns.
[filename, pathname]=uigetfile;
Hess=strcat(pathname, filename);
H_xl=xlsread(Hess);
hessLTcount=(((3*length(Rrfinalx)-1)*(3*length(Rrfinalx)))/2)+(3*length(Rrfinalx));
% First, we create one long column array with all of the hessian elements
for i=1:ceil(hessLTcount/5);
  if i == 1
    Hvect=[H_xl(i,1);H_xl(i,2);H_xl(i,3);H_xl(i,4);H_xl(i,5)];
  else
     Htempsub=[H_xl(i,1);H_xl(i,2);H_xl(i,3);H_xl(i,4);H_xl(i,5)];
     Hvect=vertcat(Hvect,Htempsub);
  end
end
% Because of how Hvect was just made, if hessLTcount is not a multiple of 5
%then there will be several NAN values in Hvect. We remove those using the
% following line.
Hvect(find(isnan(Hvect)))=[];
numb=0:
HessLD=zeros(3*length(Rrfinalx));
% Next, we create the lower diagonal Hessian matrix
for i=1:3*length(Rrfinalx)
  for j=1:i
    numb=numb+1;
     HessLD(i,j)=Hvect(numb);
  end
end
%now, we make the full hessian.
Hessfull=HessLD+tril(HessLD,-1).';
% Now we create the mass weighted cartesian hessian which we then will
% diagonallize to determine the appropriate eigen vectors (vibrational
%modes).
%Lets first create another array that carries all the masses of our system
for i=1:length(mir)
  if i == 1
    Mbig_sub=[mir(i);mir(i);mir(i)];
    Mbig=Mbig_sub;
  else
     Mbig sub=[mir(i);mir(i);mir(i)];
    Mbig=vertcat(Mbig,Mbig_sub);
  end
%Lets now generate the mass weighted cartesian coordinates
Hm=zeros(size(Hessfull));
for i=1:(3*length(Rrfinalx));
```

```
for j=1:(3*length(Rrfinalx));
    Hm(i,j)=Hessfull(i,j)/sqrt(Mbig(i)*Mbig(j));
  end
end
% Now we diagonalize the mass weighted cartesian coordinates, Hm, and
%extract out the eigen vectors ,L.
[V,D,L]=eig(Hm);
% now, we generate the displacement vector that discribes the displacement
% between the two equilibrium geometries.
for i=1:length(Rrfinalx)
  if i==1
  Rdiff sub=[Rpi rotx(i)-Rrfinalx(i);Rpi roty(i)-Rrfinaly(i);Rpi rotz(i)-Rrfinalz(i)];
  Rdiff=Rdiff_sub;
  else
  Rdiff_sub=[Rpi_rotx(i)-Rrfinalx(i);Rpi_roty(i)-Rrfinaly(i);Rpi_rotz(i)-Rrfinalz(i)];
  Rdiff=vertcat(Rdiff,Rdiff sub);
  end
end
freq=real(1.890152771.*(diag(D).*(4.35974e-
18)*(1e20)*(6.022e23)*1000/(4*(pi()^2)*(299792548^2)*(1e4))).(0.5));% array of frequencies in units
of cm-1
% Now, we calculate the reduced masses, mu, of each vibrational mode
lcart=zeros(length(Mbig),length(Mbig));
for i=1 :length(Mbig);
  for j=1:length(Mbig);
 lcart_small(j)=(L(j,i)^2)/Mbig(j);
  end
  lcartsum(i)=sum(lcart_small);
  mu(i)=(lcartsum(i)^(-1));% reduced masses
end
K=((diag(Mbig).^(0.5))*L)'*Rdiff; %Duschinsky displacement vector
kf=diag(D).*mu.';%Force constants
lamda=(219470)*0.5.*kf.*K.^2;%Reorganization energies in cm^-1 I think.
%The ~220000 number is to convert from hartrees to wavenumbers.
% Now, we remove the rotational and transaltional modes.
Kcut=K(7:length(K));
freqcut=freq(7:length(freq));
lamdacut=lamda(7:length(lamda));
figure(1)
bar(abs(Kcut))
xlabel('Normal Mode Number');
ylabel('Elements of the Duschinsky K vector in absolute value (Aamu^1^/^2)')
```

```
figure(2)
stem(freqcut,abs(Kcut))
xlabel('Frequency (cm^-^1)');
ylabel('Elements of the Duschinsky K vector in absolute value (Aamu^1^/^2)');
figure(3)
stem(freqcut,Kcut)
xlabel('Frequency (cm^-^1)');
ylabel('Elements of the Duschinsky K vector (Aamu^1^/^2)');
figure(4)
stem(freqcut,lamdacut)
xlabel('Frequency (cm^-^1)');
ylabel('Reorgonization Energy (cm^-^1)')
lamdatot=sum(lamdacut)%Total Reorganization energy in cm^-1
Kabs=abs(Kcut);
%Uses the absolute displacements to compute a weighted average frequency
ABSweightavg=sum(abs(Kcut).*freqcut)/sum(abs(Kcut))
rmsfreq a=(sum((Kabs.^2).*freqcut)/sum(Kabs.^2))
rmsfreq_b=(sum((Kabs.*freqcut).^2)/sum(Kabs.^2))^(0.5)
ReorgWieghtedFreq=sum(lamdacut.*freqcut)/sum(lamdacut)
```

REFERENCES

#### REFERENCES

- (1) Wenger, O. S. Is Iron the New Ruthenium? *Chem. Eur. J.* **2019**, 25, 6043–6052.
- (2) Hexel, G. B.; Hedrick, J. B.; Orris, G. J. Rare Earth Elements-Critical Resources for High Technology https://pubs.usgs.gov/fs/2002/fs087-02.
- (3) Auböck, Gerald; Chergui, M. Sub-50-Fs Photoinduced Spin Crossover in [Fe(bpy)<sub>3</sub>]<sup>2+</sup>. *Nat Chem.* **2015**, 7, 629–633.
- (4) Ferrari, L.; Satta, M.; Palma, A.; Di Mario, L.; Catone, D.; O'Keeffe, P.; Zema, N.; Prosperi, T.; Turchini, S. A Fast Transient Absorption Study of Co(acac)<sub>3</sub>. *Front. Chem.* **2019**, *7*, 1–12.
- (5) Tsiamis, C.; cambanis, S.; Hadjikostas, C. Spectral Study of Tris(β-dionato) Cobalt(III) Chelates. Structure-Redox Potential Relations. *Inorg. Chem.* **1987**, *26*, 26–32.
- (6) Bendix, J.; Borson, M.; Schäffer, C. E. Accurate Empirical Spin-Orbit Coupling Parameters  $\zeta_{nd}$  for Gaseous nd<sup>q</sup> Transition Metal Ions. The Parametrical Multiplet Term Model. *Inorg. Chem.* **1993**, 32, 2838–2849.
- (7) McCusker, J. K.; Walda, K. N.; Dunn, R. C.; Simon, J. D.; Magde, D.; Hendrickson, D. N. Subpicosecond ¹MLCT → ⁵T₂ Intersystem Crossing of Low-Spin Polypyridyl Ferrous Complexes. *J. Am. Chem. Soc.* **1993**, *115*, 298–307.
- (8) McCusker, J. K.; Walda, K. N.; Magde, D.; Hendrickson, D. N. Picosecond Excited-State Dynamics in Octahedral Cobalt(III) Complexes: Intersystem Crossing versus Internal Conversion. *Inorg. Chem.* **1993**, *32*, 394–399.
- (9) Langford, C. H.; Malkhasian, A. Y. S.; Sharma, D. K. Subnanosecond Transients in the Spectra of Cobalt(III) Amine Complexes. *J. Am. Chem. Soc.* **1984**, *106*, 2727–2728.
- (10) Kirk, A. D.; Langford, C. H.; Sharma, D. K. Comparison of Subnanosecond Transients from Cobalt(III) Linkage Isomers: Ligand Field Triplets versus the Radical Pair. *Inorg. Chem.* **1989**, 28, 974–975.
- (11) Hipps, K. W.; Crosby, G. A. Geometrical Distortion and Spin-Orbit Splitting in Excited Transition Metal Complexes. *Inorg. Chem.* **1974**, *13*, 1543–1544.
- (12) Miskowski, V. M.; Gray, H. B.; Wilson, R. B.; Solomon, E. I. Position of the <sup>3</sup>T<sub>1g</sub> ← <sup>1</sup>A<sub>1g</sub> Transition in Hexacyanocobaltate(III). Analysis of Absorption and Emission Results. *Inorg. Chem.* **1979**, *18*, 1410–1412.
- Wilson, R. B.; Solomon, E. I. Spectroscopic Studies of Photochemically Important Transition Metal Excited States. 2. The <sup>1</sup>T<sub>1g</sub>, <sup>3</sup>T<sub>1g</sub>, and <sup>5</sup>T<sub>2g</sub> Excited States of Hexaamminecobalt(III). *J. Am. Chem. Soc.* **1980**, *102*, 4085–4095.
- (14) Langford, C. H. Quantum Yield Variation over Narrow Spectral Regions in Coordination Photochemistry. *Acc. Chem. Res.* **1984**, *17*, 96–103.

- (15) Langford, C. H.; Malkhasiah, A. Y. S. Wavelength Dependence over the Envelope of a Single Electronic Band in the Photochemistry of the Penta-Amminechlorocobalt(III) Ion. *J. Chem. Soc.*, *Chem. Commun.* **1982**, 1210–1211.
- (16) Shalhoub, G. M. Co(acac)<sub>3</sub>: Synthesis, Reactions, and Spectra An Experiment for General Chemistry. *J. Chem. Ed.* **1980**, *57*, 525–526.
- (17) Collman, J. P.; Moss, R. A.; Maltz, H.; Heindel, C. C. The Reaction of Metal Chelates. I. Halogenation of Metal Chelates of 1,3-Diketones. *J. Am. Chem. Soc.* **1961**, *83*, 531–534.
- (18) Frisch, M. J.; Trucks, G. W.; Schlegel, H. B.; Scuseria, G. E.; Robb, M. A.; Cheeseman, J. R.; Scalmani, G.; Barone, V.; Petersson, G. A.; Nakatsuji, H.; Li, X.; Caricato, M.; Marenich, A. V.; Bloino, J.; Janesko, B. G.; Gomperts, R.; Mennucci, B.; Hratch, D. J. Gaussian 16, Revision C.01. 2016.
- (19) Humphrey, W.; Dalke, A.; Schulten, K. VMD: Visual Molecular Dynamics. *J. Mol. Graph. Model.* **1996**, *14*, 33–38.
- (20) Ando, H.; Iuchi, S.; Sato, H. Theoretical Study on Ultrafast Intersystem Crossing of Chromium(III) Acetylacetonate. *Chem. Phys. Lett.* **2012**, *535*, 177–181.
- (21) Miller, W. H.; Ruf, B. A.; Chang, Y.-T. A Diabatic Reaction Path Hamiltonian. *J. Chem. Phys.* **1988**, 89, 6298–6304.
- (22) Barnum, D. W. Electronic Absorption Spectra of Acetyl-Acetonato Complexes. 1. Complexes With Trivalent Transition Metal Ions. *J. Inorg. Nucl. Chem.* **1961**, *21*, 221–237.
- (23) Heller, E. J. The Semiclassical Way to Molecular Spectroscopy. *Acc. Chem. Res.* **1981**, *14*, 368–375.
- (24) Lemke, H. T.; Kjaer, K. S.; Hartsock, R.; van Driel, T. B.; Chollet, M.; Glownia, J. M.; Song, S.; Zhu, D.; Pace, E.; Matar, S. F.; Nielsen, M. M.; Benfatto, M.; Gaffney, K. J.; Collet, E.; Cammarata, M. Coherent Structural Trapping through Wave Packet Dispersion during Photoinduced Spin State Switching. *Nat. Commun.* **2017**, *8*, 15342.
- (25) Auböck, G.; Chergui, M. Sub-50-Fs Photoinduced Spin Crossover in [Fe(bpy)<sub>3</sub>]<sup>2+</sup>. *Nat. Chem.* **2015**, 7, 629–633.
- (26) Carey, M. C.; Adelman, S. L.; McCusker, J. K. Insights into the Excited State Dynamics of Fe(II) Polypyridyl Complexes from Variable-Temperature Ultrafast Spectroscopy. *Chem. Sci.* **2019**, *10*, 134–144.
- (27) Monat, J. E.; McCusker, J. K. Femtosecond Excited-State Dynamics of an Iron(II) Polypyridyl Solar Cell Sensitizer Model. *J. Am. Chem. Soc.* **2000**, *122*, 4092–4097.
- (28) Maçôas, E. M. S.; Mustalahti, S.; Myllyperkiö, P.; Kunttu, H.; Pettersson, M. Role of Vibrational Dynamics in Electronic Relaxation of Cr(acac)<sub>3</sub>. *J. Phys. Chem. A* **2015**, *119*, 2727–2734.
- (29) Iwamura, M.; Takeuchi, S.; Tahara, T. Ultrafast Excited-State Dynamics of Copper(I) Complexes. *Acc. Chem. Res.* **2015**, *48*, 782–791.
- (30) Bixon, M.; Jortner, J. Intramolecular Radiationless Transitions. J. Chem. Phys. 1968, 78, 715–726.

- (31) Englman, R.; Jortner, J. The Energy Gap Law for Radiationless Transitions in Large Molecules. *Mol. Phys.* **1970**, *18*, 145–164.
- (32) Zhang, W.; Alonso-Mori, R.; Bergmann, U.; Bressler, C.; Chollet, M.; Galler, A.; Gawelda, W.; Hadt, R. G.; Hartsock, R. W.; Kroll, T.; *et al.* Tracking Excited-State Charge and Spin-Dynamics in Iron Coordination Complexes. *Nature* **2014**, *509*, 345–348.
- (33) Britz, A.; Gawelda, W.; Assefa, T. A.; Jamula, L. L.; Yarranton, J. T.; Galler, A.; Khakhulin, D.; Diez, M.; Harder, M.; Doumy, G.; *et al.* Using Ultrafast X-Ray Spectroscopy to Address Questions in Ligand-Field Theory: The Excited State Spin and Structure of [Fe(dcpp)<sub>2</sub>]<sup>2+</sup>. *Inorg. Chem.* **2019**, 58, 9341–9350.1
- (34) Schrauben, J. N.; Dillman, K. L.; Beck, W. F.; McCusker, J. K. Vibrational Coherence in the Excited State Dynamics of Cr(acac)<sub>3</sub>: Probing the Reaction Coordinate for Ultrafast Intersystem Crossing. *Chem. Sci.* **2010**, *1*, 405–410.
- (35) Feit, M. D.; Fleck, J. A.; Steiger, A. Solution of the Schrodinger Equation by a Spectral Method. *J. Comput. Phys.* **1982**, *47*, 412–433.
- (36) Tanner, J. J. A Computer-Based Approach to Teaching Quantum Dynamics. *J. Chem. Ed.* **1990**, 67, 917-921.
- (37) Reber, C.; Zink, J. I. Interference Dips in Molecular Absorption Spectra Calculated for Coupled Electronic State Potential Surfaces. *J. Chem. Phys.* **1992**, *96*, 2681-2690.

# Chapter 4: Geometric Control of Ultrafast Charge-Transfer Relaxation Dynamics in Fe(II)-Based Chromophores: Using Coherence to Inform Synthetic Design

The work presented in this chapter was a collaborative effort between this author and Sara Adelman and was submitted for publication in *Nature* under the following citation: [Paulus, B. C.; Adelman; Jamula, L. L.; McCusker, J. K. *Nature* **2020**, xx, xx-xx]. BCP collected and analyzed all ultrafast TA data, performed DFT optimizations and frequency calculations, and made vibrational mode figures. SLA synthesized all complexes and carried out ground-state and nanosecond time-resolved characterizations. LLJ developed the initial synthetic route to produce the main ligand and compound **2**.

## 4.1. Introduction

Quantum mechanical coherences have received significant attention for their potential role in coupling to and/or directing photophysical processes.¹ Coherences have been observed and analyzed in a variety of chemical systems ranging from small molecules to proteins in the context of characterizing ultrafast dynamics.²-8 These studies represent pioneering efforts that are providing new, fundamental insights into the quantum mechanical nature of photo-induced processes. As suggested recently,¹ observation of coherences during an electronic transition also has the potential to inspire synthetic design to access historically difficult transformations due to the fact that in many chemical systems there exists an intricate relationship between electronic and nuclear degrees of freedom. This leads to significant mixing of their wavefunctions and an interdependence of these molecular properties that can map onto the photophysical and photochemical dynamics. In systems such as these, vibronic (as opposed to purely electronic and purely vibrational) coherences can in principle provide unique insight into the nature of this coupling, potentially affording subtle clues for how one could exert some degree of control through informed structural, compositional, and environmental modifications. 9-12

Molecules for which a design approach targeting the interplay between electronic and vibrational degrees of freedom might be particularly advantageous are those involving first-row transition metal ions. Compounds of this class are actively being pursued as earth-abundant replacements for applications that leverage photo-induced electron transfer reactivity, <sup>13,14</sup> but such systems have been challenging to develop.

Ruthenium-based compounds, for example, have proven to be extremely effective for light-actuated redox chemistry, but their isoelectronic iron(II) analogs typically undergo ultrafast (< 200 fs) conversion from the initially formed metal-to-ligand charge transfer (MLCT) excited state to low-lying ligand field (LF) excited states. <sup>15–17</sup> These latter states are localized on the metal center and are therefore not characterized by charge separation, a fact that significantly limits their ability to engage in electron transfer reactions. The underlying reasons for this dramatic difference in photo-induced excited-state reactivity between first-row and second- and third-row-based chromophores have recently been discussed in detail; <sup>18</sup> the fact that the origin of these effects stems from fundamental properties of atomic orbital wavefunctions that lie at the very core of quantum mechanics underscores the difficulty associated with circumventing this problem.

Despite the challenging nature of this problem, the desirability of translating the photo-induced reactivity endemic to complexes employing some of the rarest elements on Earth to their more abundant congeners in the first transition series has catalyzed research geared toward altering this paradigm. Due in part to its isoelectronic relationship with ruthenium, complexes of iron have attracted considerable attention. The most successful efforts in this area have focused on energetically reordering the LF and charge-transfer excited states – primarily through the use of strongly σ-donating ligands – leading to the preparation of molecules exhibiting charge-transfer excited-state lifetimes on the order of a nanosecond. <sup>19–22</sup> With this report, we introduce an alternate approach, one that exploits the ultrafast nature of MLCT-state deactivation as well as the large amplitude geometric distortions that accompanies it. Specifically, we demonstrate that the observation and identification of excited-state coherence can provide critical insight into the geometric nature of the reaction coordinate associated with MLCT-to-LF conversion in such a way as to inform synthetic design, in effect creating new strategies for imparting synthetic control over ultrafast dynamics.

# 4.2. Experimental Methods

## 4.2.1. Synthesis

All synthesis and ground state characterization was performed by Sara Adelman of the McCusker group.

# 4.2.2. Density Functional Theory Calculations

Vibrational frequencies were calculated on the high spin (HS) and low spin (LS) states of [Fe(L)]<sup>2+</sup> (1) as well as the LS ground state of [FeCu<sub>2</sub>(L)]<sup>4+</sup> (2) using the B3LYP functional and 6-31G basis set. Frequency calculations of the LS 1 were also conducted with polarizability functions and showed little change in the calculated frequencies. All calculations were conducted using Gaussian16 code<sup>23</sup> on the High Performance Computing Center (HPCC) at Michigan State University. Mass weighted vector displacement diagrams of each pertinent vibrational mode were created in the Visual Molecular Dynamics (VMD) program.<sup>24</sup>

# 4.2.3. Ultrafast Transient Absorption Spectroscopy

The ultrafast transient absorption spectroscopy setup was described in Chapter 2 of this dissertation.

Samples were dissolved in spectrophotometric grade acetonitrile in an argon-filled glovebox such that they had an absorbance between 0.3 and 0.8 at the center of the pump wavelength in a 1 mm air-free cuvette. Samples were checked for degradation by comparing UV-Vis spectra taken before and after the experiment. The instrument response function (IRF) for single wavelength kinetics traces was determined from the optical Kerr effect in methanol by fitting the early half of the signal to a Gaussian and extracting the full width at half maximum (FWHM).<sup>25</sup> During full spectrum measurements, the IRF and dispersion are measured by collecting TA data on the neat solvent and then used to chirp correct the sample with solute. During single wavelength measurements, the probe beam was directed into a monochromator placed after the sample. The monochromator selected a 3.8 nm FWHM slice of the probe beam spectrum to be measured. The center wavelength of this slice of the probe spectrum is specified for each single wavelength TA trace. Each experiment was repeated at least three times and each value listed is the average of all values obtained by fit, while the error is listed as one standard deviation.

Population dynamics were modeled by use of equation 4.1, in which the total signal, S, is described by the summation of several exponentially decaying components convolved with a Gaussian IRF (G).

$$S(t) = \left[\sum_{i=1}^{n} A_i \exp\left(\frac{-(t - t_0)}{\tau_i}\right)\right] \otimes G(t)$$
4.1

As mentioned above, for single wavelength measurements, the IRF was determined by use of the optical Kerr effect in methanol. Next, each dataset was fit to as few exponential components as necessary to adequately reproduce the data. For 1, this involved two components: one to describe the ultrafast MLCT  $\rightarrow$  LF conversion and one to describe the slow  $^5T_{2g} \rightarrow {}^1A_{1g}$  ground state recovery which effectively describes the y-offset present following MLCT decay. This long time component was locked in at 25 ns as determined by Sara Adelman of the McCusker group using nanosecond transient absorption spectroscopy; however its exact value does not have a significant impact on the fit as the measured window in time is much slower than the rate of this process. For 2, we use three exponential components with the third and slowest component describing  $^5T_{2g} \rightarrow {}^1A_{1g}$  ground state recovery locked in at 7 ns (determined separately on the ns TA system by Sara Adelman of the McCusker group).

For fitting oscillatory components, we employ a linear predictive singular value decomposition (LPSVD) program written in MATLAB originally by Dr. Andrey Demidov and Paul Champion and edited by Dan Roscioli of the Beck group at MSU. This program fits the data to a series of exponentially damped cosinusoids as shown in equation 4.2.

$$S(t) = \sum_{i=1}^{n} A_i \exp\left(\frac{-t}{\tau_i}\right) \cos\left(2\pi \nu_i t + \phi_i\right)$$
 4.2

This program allows the user to fit population dynamics using zero frequency components as well as extract exponentially damped oscillations. Due to the drastically different time scales between some of the population dynamics and the damping times of the vibrational coherences, we use LPSVD to fit the oscillations on the first ~2 ps of data and use the exponential fitting described above for extracting population dynamics. The program makes use of the Fourier relationship between damping time and width in the frequency domain to produce a vibrational spectrum which is then compared to as fast Fouier transform (FFT) of the residuals of a fit to the population dynamics. To identify coherent oscillations due to the solvent and cuvette, TA experiments were performed on neat solvent and an empty cuvette.

#### 4.3. Results and Discussion

The excited state ultimately formed subsequent to MLCT-LF state conversion in Fe(II) polypyridyl complexes is characterized by a significant (~0.2 Å) lengthening of Fe-N bonds, <sup>26</sup> which in turn has fueled a long-standing assumption that the Fe-N breathing mode dominates the excited state reaction coordinate. <sup>15,16</sup> While structural changes along the Fe-N coordinate unquestionably occur, the available data do not allow one to differentiate between causation, in which the specific mode(s) is kinetically competent for determining the dynamics, versus correlation in which the structural change is a consequence of a process that is driven by other degrees of freedom. There is a significant body of work going back to Purcell's use of the angular overlap model to rationalize the rapid racemization of [Fe(phen)<sub>3</sub>]<sup>2+</sup>, suggesting that torsional modes may play a role in both the ground-state recovery (GSR) process as well as MLCT-state deactivation. <sup>27–29</sup> When viewed through this lens, the possibility that other degrees of freedom could be involved in defining the reaction coordinate for the overall photophysical transformation of these chromophores must be considered.

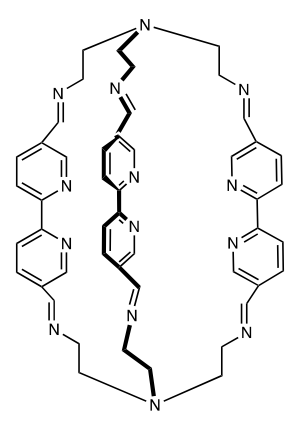


**Figure 4.1.** Drawing of cage ligand (**L**) used in this study.

With these ideas in mind, we designed a new iron(II) complex based on a polypyridyl ligand (L) that could impose stricter steric rigidity about both Fe-N breathing and torsional degrees of freedom that tris-bpy while still maintaining some level of structural tunability. This structural motif employs a macrocyclic cage ligand first described by Lehn<sup>30</sup> and is composed of three bipyridine (bpy) units tethered together by tertiary amine-capped triimines (Figure 4.1). The bpy-based cored of the assembly is well suited

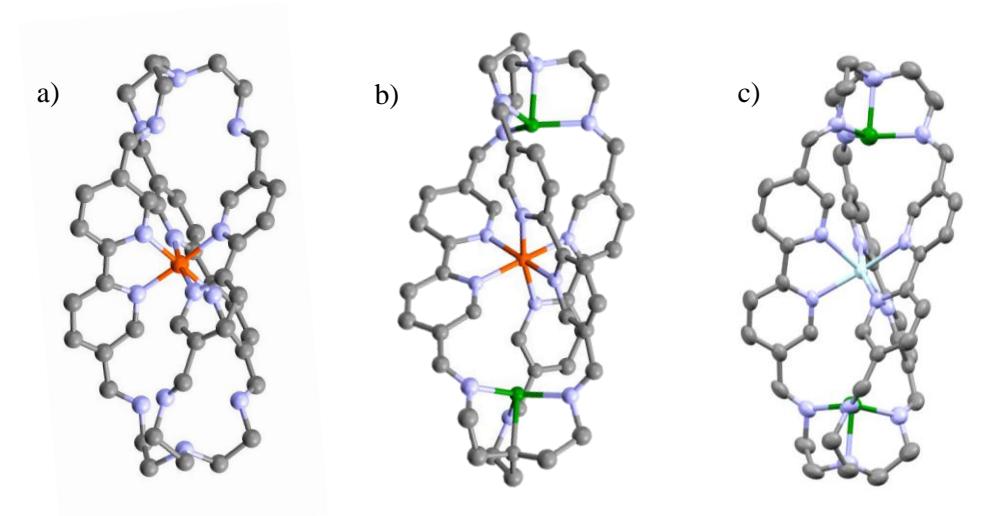


**Figure 4.2.** Single-crystal x-ray structures of the cations of (a)  $[Fe(L)](PF_6)_2$  (1), (b)  $[FeCu_2(L)](PF_6)_4$  (2), and (c)  $[ZnCu_2(L)](PF_6)_4$  (3). The hydrogen atoms have been removed for clarity. For metal ions: red = Fe, green = Cu, light blue = Zn.

to bind Fe(II), whereas the four nitrogen atoms that comprise the imine caps provide for the introduction of additional ions that can impart added rigidity to the overall framework.

The synthesis and characterization of the three compounds prepared for this study was performed by Sara Adelman of the McCusker group and will not be shown here. Single-crystal x-ray structures for  $[Fe(L)]^{2+}$  (1),  $[FeCu_2(L)]^{4+}$  (2), and  $[ZnCu_2(L)]^{4+}$  (3) are shown in Figures 4.2 a-c respectively. Focusing initially on compound 1, we find that the primary coordination sphere about the Fe(II) center is unremarkable and indeed typical for low-spin Fe(II) polypyridyl complexes with the exception that the ligand framework imparts a local symmetry about the iron center closer to  $D_{3h}$  than the  $D_3$  symmetry that characterizes most tris-bidentate coordination compounds. The optical properties of compound 1 are dominated in the visible by an intense, broad feature centered at 580 nm (Figure 4.3) assigned to an MLCT absorption envelope. Although we do note an attenuation in the intensity of the absorption envelope relative to  $[Fe(bpy)_3]^{2+}$  - a consequence, we believe, of the aforementioned change in symmetry – the overall band shape is essentially the same for the two compounds. The absorption spectrum for compound 3 reveals features toward the blue region associated with the  $Cu^+$  chromophores, but these absorptions do not significantly overlap with the red portion of the Fe(II)-based MLCT transition that will be the focus of the experiments described below.

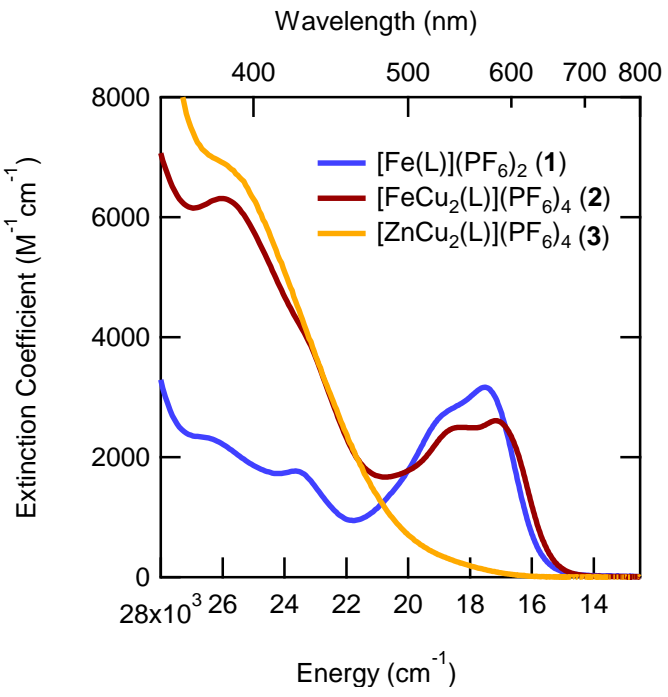


**Figure 4.3.** Ground state electronic absorption spectra of  $[Fe(L)](PF_6)_2$  (1),  $[FeCu_2(L)](PF_6)_4$  (2), and  $[ZnCu_2(L)](PF_6)_4$  (3). The spectra were acquired at room temperature in  $CH_3CN$  solutions.

Time-resolved electronic absorption data acquired on [Fe(L)](PF<sub>6</sub>)<sub>2</sub> (1) in CH<sub>3</sub>CN solution following  ${}^{1}A_{1g} \rightarrow {}^{1}MLCT$  excitation at 600 nm are illustrated in Figure 4.4. As suggested by previous work on low-spin iron(II) polypyridyls<sup>31</sup> as well as spectroelectrochemical measurements on compound 1 specifically (Figure 4.5), the ligand-based radical anion – which serves as an optical marker for the presence of the MLCT state in this class of compounds – will manifest as a broad absorption in the far red region of the visible spectrum. The absence of such a feature at  $\lambda > 600$  nm in Figure 4.4a indicates that the initially formed charge-transfer excited state for this compound is depopulated in less than 200 fs following excitation. This is confirmed by single-wavelength kinetic data (Figures 4.4 b and d) that allow us to ascribe a time constant for MLCT deactivation of  $110 \pm 30$  fs under these conditions. This time scale is fairly typical for MLCT relaxation in Fe(II) polypyridyl complexes; 15,16,32 in a similar vein, we believe that the MLCT state is rapidly converting to the ligand-field manifold of the transition metal ion, ultimately forming the high-spin  ${}^{5}T_{2g}$  state as the lowest energy excited state of the system. Nanosecond time-resolved electronic absorption measurements performed by Sara Adelman of the McCusker group reveal single exponential kinetics leading to ground-state recovery with a time constant of  $24 \pm 2$  ns.

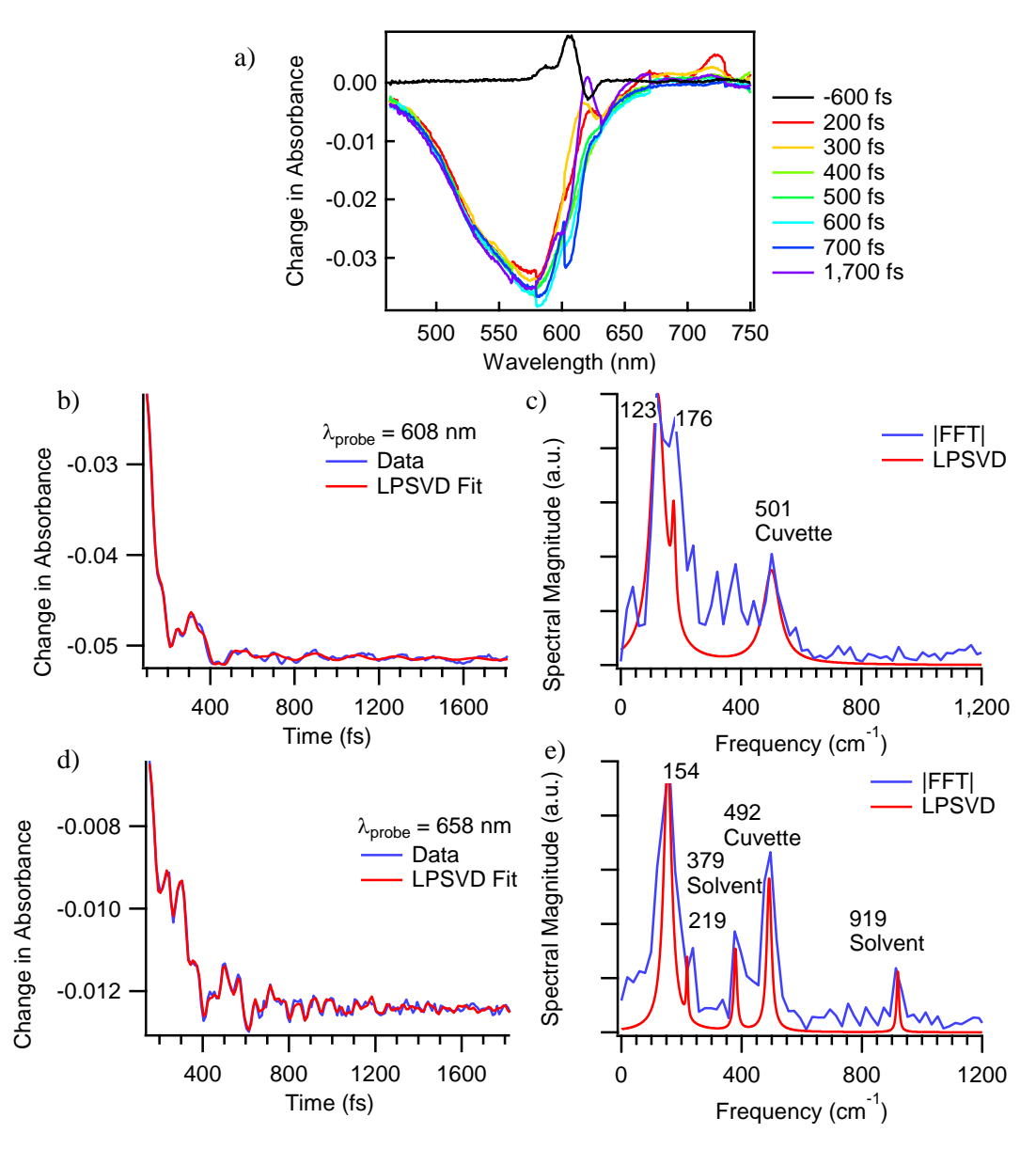


**Figure 4.4.** Femtosecond time-resolved absorption data of [Fe(L)](PF<sub>6</sub>)<sub>2</sub> (1) acquired in CH<sub>3</sub>CN solution. (a) Full spectrum data collected over the first few ps following MLCT excitation at 600 nm. The anomalous features near 600 nm are due to scattered light from the excitation source. (b) Single wavelength kinetics trace monitored at 608 nm with LPSVD fit. (c) Resulting vibrational spectrum corresponding to the FFT of the residuals of an exponential fit (blue) and the oscillations extracted through LPSVD fitting (red). (d) Single wavelength kinetics trace monitored at 658 nm with LPSVD fit. (e) Vibrational spectrum of the kinetic data collected at 658 nm.

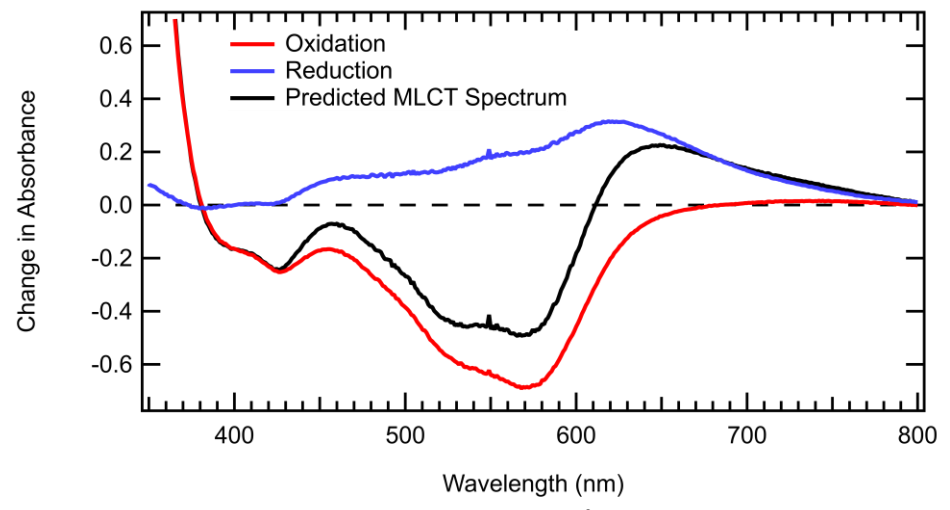


**Figure 4.5.** Spectroelectrochemical data on  $[Fe(L)]^{2+}$  (1) collected by Sara Adelman.

Time-resolved absorption data acquired on compound 1 revealed coherent oscillations superimposed on the single-wavelength kinetics. The frequencies giving rise to these oscillations were extracted via both fast Fourier transform (FFT) and linear predictive singular value decomposition (LPSVD) analyses (Figure 4.4c and e); the latter also afforded the dephasing times associated with these oscillations (vida infra). The strongly allowed nature of the MLCT absorption in compound 1 requires that we consider both ground- and excited-state origins for these features. In this regard, we argue that the observed dephasing times are too rapid to be attributable to purely vibrational coherences on the ground electronic state from impulsively stimulated Raman scattering where picosecond dephasing times are more typical.<sup>9,33–35</sup> The notion that instead these coherences are generated directly on the MLCT excited-state surface and survive the transfer to the ligand-field manifold is supported by the fact that our observations are similar to those reported by Chergui (127 and 157 cm<sup>-1</sup>,  $\tau_{OSC} = 400 \pm 100$  fs)<sup>16</sup> and Gaffney (126 cm<sup>-1</sup>,  $\tau_{\rm OSC} = 310 \pm 10 \, \text{fs}$ ), 15 both of whom associated these features to the excited state(s) of  $[\text{Fe}(\text{bpy})_3]^{2+}$ . Accordingly, we assign the oscillations to vibronic coherences in the excited state(s) of compound 1. We note the similarities in the MLCT decay rates, frequencies, and dephasing times of the coherently activated vibrational modes between compound 1 and [Fe(bpv)<sub>3</sub>]<sup>2+</sup>, suggesting that compound 1's similarity to [Fe(bpy)<sub>3</sub>]<sup>2+</sup> extends not only to the ground-state absorption spectrum and MLCT decay kinetics, but likely to the nature of the reaction coordinate for MLCT-to-LF conversion as well.

Coherent oscillations can be observed for degrees of freedom that are linked or orthogonal to a reaction coordinate of interest and are therefore not necessarily diagnostic in and of themselves. We hypothesized that one marker for identifying coherences that are vibronic in nature – and therefore potentially coupled to an excited-state evolution trajectory defined by significant geometric changes – could be their dephasing times. Coherence that is purely electronic in origin is expected to dephase on a sub-100 fs time scale in most chemical systems. <sup>36</sup> In contrast, pure vibrational coherences can last for several picoseconds under certain conditions. <sup>9,33–35,37,38</sup> Since a vibronic feature implies a mixing of electronic and vibrational degrees of freedom, we posited that coherent oscillations that were vibronic in origin would exhibit dephasing times intermediate between the two extremes just mentioned, e.g., on a time scale of hundreds of fs. We therefore proposed to use this hypothesis as a basis for selecting which subset of the 3N-6 vibrational degrees of freedom of the chromophore to target for chemical modification. The ultimate test of whether these modes are indeed part of the reaction coordinate would come from experiment, i.e., if the modes we identify in this manner are helping to define the reaction coordinate for ultrafast MLCT-state relaxation, we should observe a concomitant effect on the MLCT-state lifetime upon synthetic tailoring of these specific degrees of freedom.

**Table 4.1.** Summary of the coherent vibrational modes of  $[Fe(L)](PF_6)_2$  (1) observed during TA experiments following 600 nm excitation in acetonitrile solution.

#### Coherent Vibrational Modes of 1

Frequency, cm <sup>-1</sup>	127 (5)	156 (2)	173 (3)	215 (12)
Dephasing Time, fs	230 (90)	300 (30)	360 (230)	730 (600)

The data presented in Figure 4.4 reveal features at 127 (5) cm<sup>-1</sup>, 156 (2) cm<sup>-1</sup>, 173 (3) cm<sup>-1</sup>, and 215 (12) cm<sup>-1</sup>, all of which exhibit dephasing times that we would consider intermediate in nature (Table 4.1). DFT frequency calculations carried out on the high-spin (i.e. <sup>5</sup>T<sub>2g</sub>) excited state of compound **1** shows reasonable agreement with these experimental values, lending further support to our assertion that the observed oscillations are associated with the excited-state manifold of compound **1**. We can immediately assign the experimentally observed 173 (3) cm<sup>-1</sup> mode to the pair of energetically isolated doubly

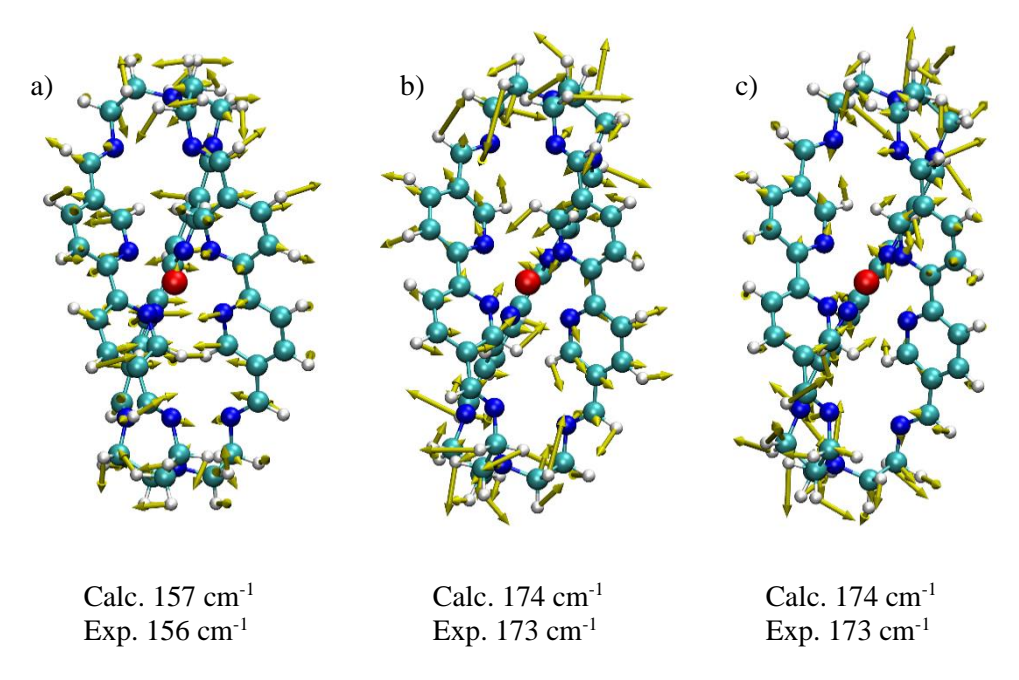


**Figure 4.6.** DFT calculated vector displacement diagrams of several of the coherently excited vibrational modes of  $[Fe(L)](PF_6)_2(1)$ .

degenerate modes (calculated at 174 cm<sup>-1</sup>) illustrated in Figure 4.6 b and c, corresponding to a wagging motion of the imine nitrogen atoms of the capping fragment concomitant with in-plane rocking of the bpy moieties. Possible candidates for the 156 (2) cm<sup>-1</sup> mode are three features calculated at 151 cm<sup>-1</sup>, 152 cm<sup>-1</sup>, and 157 cm<sup>-1</sup>. All three of these calculated vibrations are characterized by symmetric torsional motion about the tren cap coupled with a distortion of the primary coordination sphere of the metal center in which the ligated nitrogen atoms tilt (Figure 4.6a). The overall distortion is reminiscent of a modified Bailar twist recently described by the Jakubikova group.<sup>29</sup> The assignment of the 127 (5) cm<sup>-1</sup> feature is more challenging due to the high density of calculated modes in this region and the fact that the vibrational period for this frequency range is longer than the observed dephasing time (thereby resulting in larger uncertainty in the measured frequency). A similar challenge arises with the 215 (12) cm<sup>-1</sup> mode due to its relatively small amplitude.

The ambiguity associated with assigning these latter two modes notwithstanding, the coherence data on compound 1 is clearly revealing large amplitude motion of both the primary coordination sphere around the iron center that is propagating across the supramolecular structure to the polyimine capping

groups. This information immediately suggested an approach whereby we introduce an ion that can be sequestered by the  $N_4$  coordination environments on the periphery of the ligand framework. The new metalligand interactions in this region should attenuate the degrees of freedom identified from the coherence data and illustrated in Figure 4.6: if these modes are important with regard to the reaction coordinate for MLCT-to-LF state conversion, we should see an increase in the observed lifetime of the MLCT excited state of the chromophore.

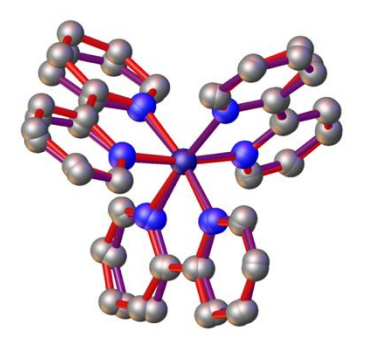


**Figure 4.7.** Overlay of the Fe-N<sub>6</sub> region of  $[Fe(L)](PF_6)_2$  (1) and  $[FeCu_2(L)](PF_6)_4$  (2) crystal structures. The complex drawn with red bonds is complex 1 and the complex with purple bonds is complex 2.

Figure 4.2b shows the single crystal x-ray structure of the cation of [FeCu<sub>2</sub>(L)](PF<sub>6</sub>)<sub>4</sub> (**2**) in which Cu(I) ions have been introduced into the two capping N<sub>4</sub> cavities of the ligand. A comparison of the Fe(bpy)<sub>3</sub> cores of compounds **1** and **2** (Figure 4.7) confirms that the presence of the Cu(I) ions is not significantly perturbing the primary coordination sphere of the Fe(II) chromophore in the ground state, implying that the MLCT excited state of the Fe(II) species in compound **2** should be essentially identical to that of compound **1**. To further establish the electronically benign nature of the Cu(I) ions in compound **2**, we also prepared [ZnCu<sub>2</sub>(L)]<sup>4+</sup> (**3**, Figure 4.2c) where the replacement of Fe(II) by Zn(II) allows us to look selectively at the spectral features associated with the Cu(I) ions due to the spectroscopically silent nature of Zn(II). It can be seen that absorbances from the Cu(I) ions are at much higher energy than those of the Fe(II) site, consistent with the yellow color of this compound (Figure 4.3). These near-UV features are most likely MLCT in nature involving the imine groups of the capping ligand. Excitation of compound **2** at 600 nm – the same wavelength used to acquire the data on compound **1** – is therefore cleanly selective for the Fe(II) chromophore. Both the structural and ground-state spectroscopic data on compounds **1** and **2** 

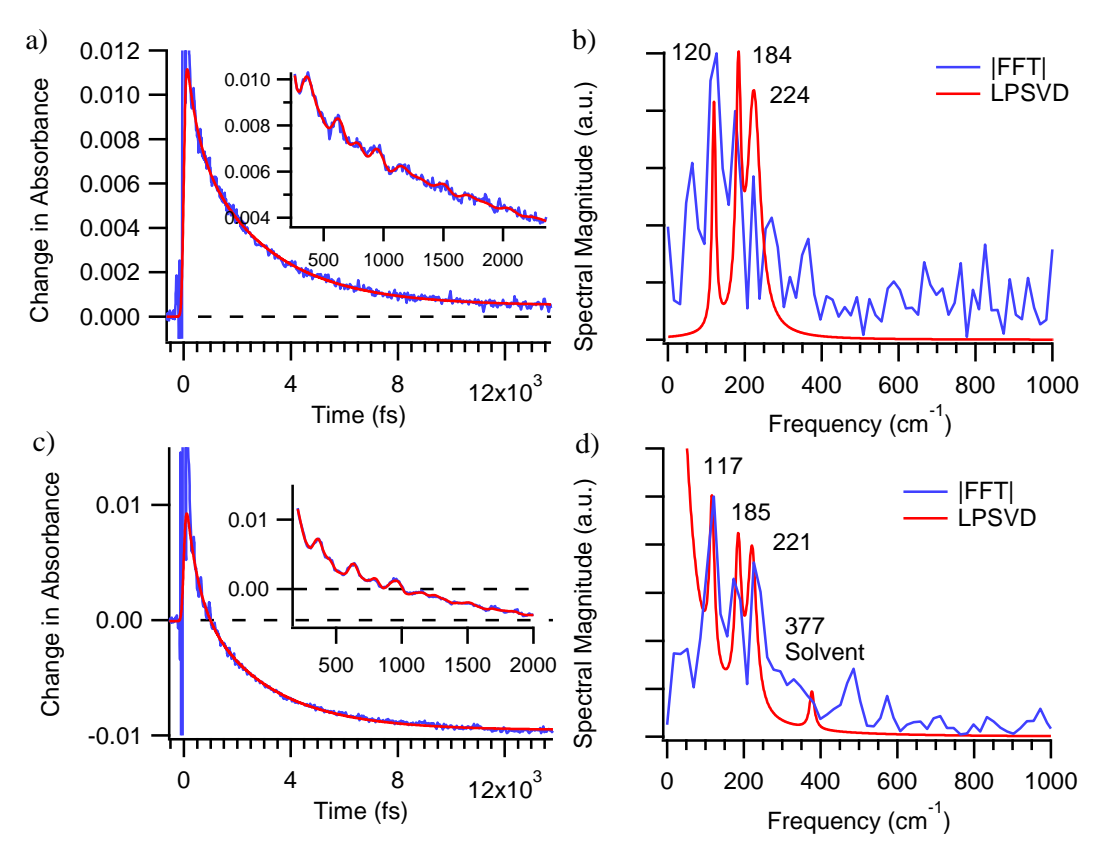


**Figure 4.8.** Representative TA data on  $[FeCu_2(L)](PF_6)_2$  (2) in acetonitrile following 600 nm excitation while monitoring at (a) 700 nm and (c) 650 nm (blue) with fit to equation 4.1 (red) and inset showing LPSVD fit to equation 4.2. Corresponding vibrational spectra (b) and (d) resulting from LPSVD fit (red) and FFT of the residuals of the exponential fit (blue). The appearance of an additional peak in the low frequency region in the LPSVD spectrum in part d can be attributed to error in exponential fitting in the LPSVD program, likely arising from fitting a small portion of the overall data set.

therefore establishes that excitation at 600 nm creates the same type of excited state in both chromophores, i.e. a <sup>1</sup>MLCT state associated with the Fe(II)-bpy fragment.

Ultrafast time-resolved absorption data were collected on compound 2 and are shown in Figure 4.8. As with compound 1, compound 2 exhibits coherent oscillations superimposed on the kinetics that define its population dynamics (Figure 4.8a, 4.8c, 4.A1a). An analysis of these features yields frequencies that are quite similar to those observed for compound 1 (Figures 4.8b, 4.8d, 4.A1b). We observe a slight lengthening of the dephasing times of these coherent oscillations relative to compound 1, which may indicate a partial decoupling of these degrees of freedom from the ultrafast electronic-state evolution of compound 2. Similar dephasing times are observed following MLCT excitation of compound 2 in several different solvents

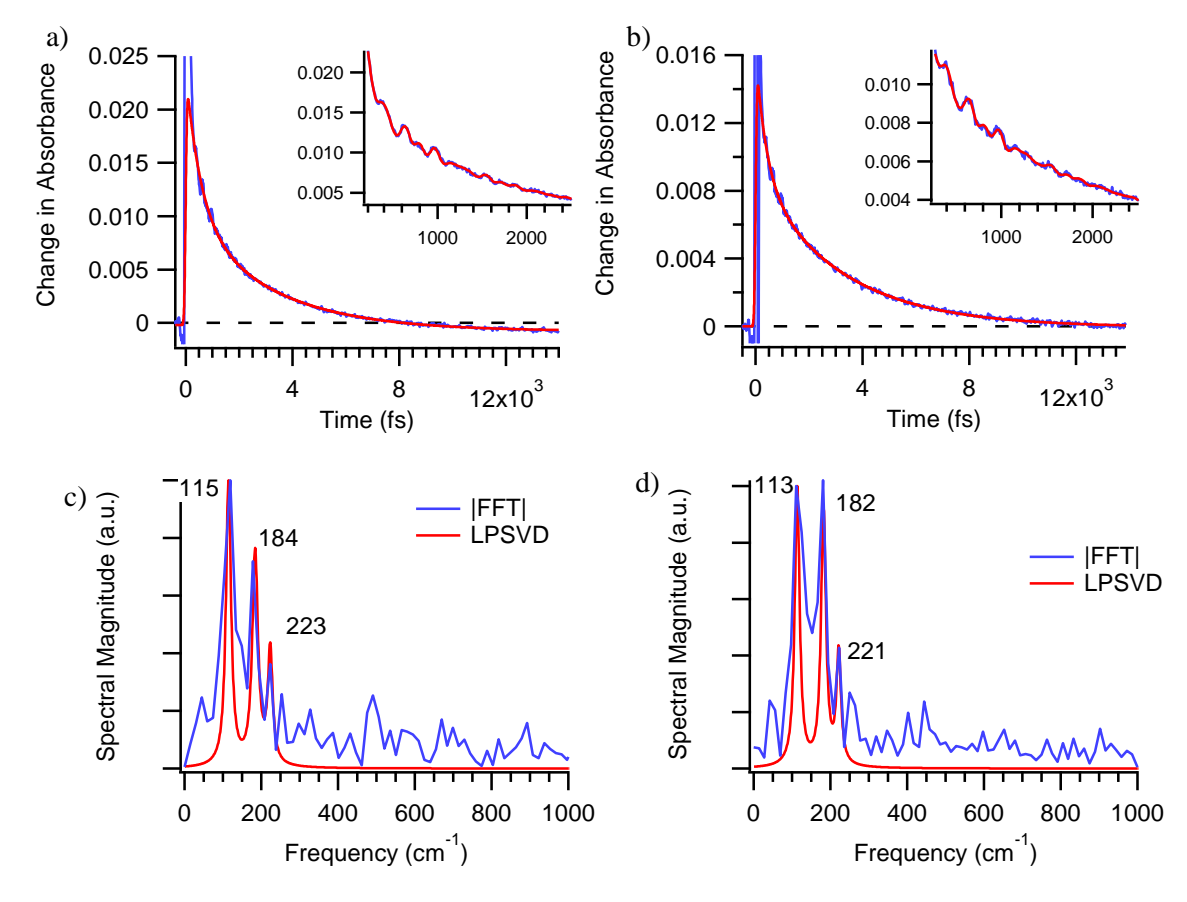


**Figure 4.9.** Representative TA data on  $[FeCu_2(L)](PF_6)_4$  (2) in (a) butyronitrile and (b) acetone following 600 nm excitation and monitoring at 700 nm with insets showing raw data (blue) and LPSVD fits (red) over the first few picoseconds. (c) and (d) show the vibrational spectra resulting from the FFT and LPSVD analyses of the data in butyronitrile and acetone respectively.

(Figure 4.9), which strongly supports an intramolecular origin for the dephasing mechanism. A summary of the coherent oscillations of compound **2** observed across each solvent can be seen in Table 4.2. Analyzing these data in a manner analogous to compound **1**, DFT calculations allow us to ascribe the 219 cm<sup>-1</sup> mode of compound **2** as one of three modes calculated between 225 and 227 cm<sup>-1</sup>, each of which exhibit a rocking

**Table 4.2.** Summary of the coherent vibrational modes of  $[FeCu_2(L)(PF_6)_4$  (2) in different solvents. All errors are expressed as the standard deviation of multiple trials.

Solvent	Coherent Vibrational Modes of 2			
MeCN	Frequency, cm <sup>-1</sup>	116 (3)	183 (3)	219 (5)
	Dephasing Time, fs	600 (210)	810 (270)	570 (190)
BuCN	Frequency, cm <sup>-1</sup>	114 (1)	182 (2)	219 (4)
	Dephasing Time, fs	800 (140)	580 (140)	450 (170)
Acetone	Frequency, cm <sup>-1</sup>	117 (1)	183 (2)	222 (2)
	Dephasing Time, fs	660 (200)	870 (400)	540 (140)

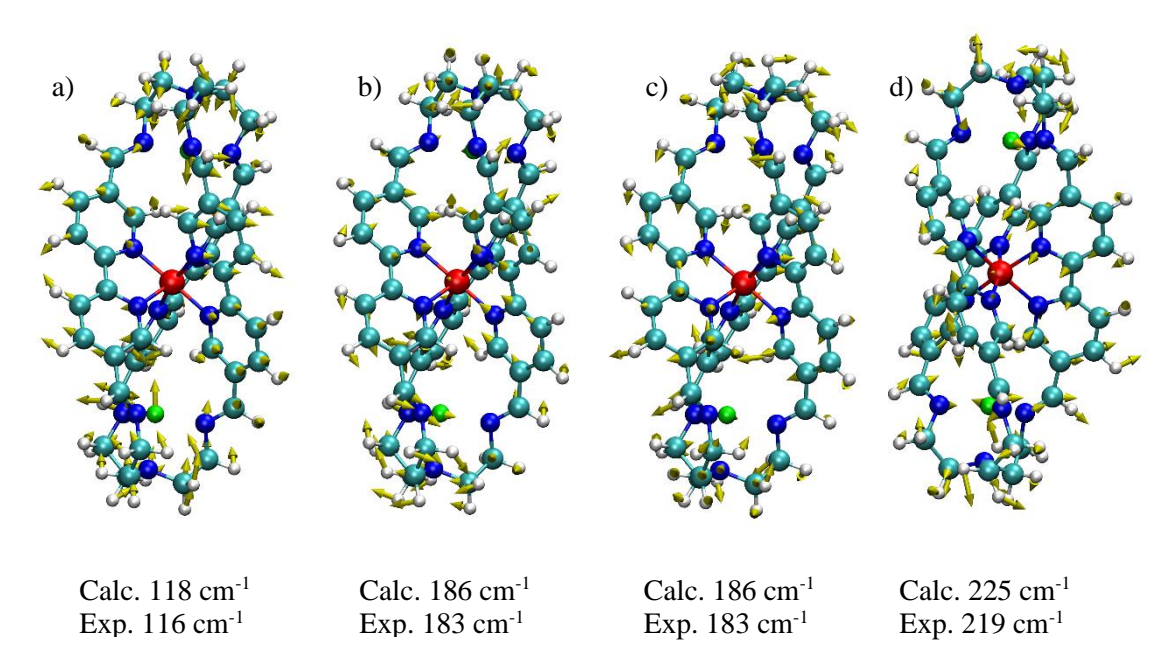


**Figure 4.10.** DFT calculated vector displacement diagrams of the coherent modes of **2** observed in this study.

motion of the bpy moieties along with an antisymmetric Cu-N stretch in the imine cap (Figure 4.10). A mode calculated at 186 cm<sup>-1</sup>, which is characterized by motions similar to those seen for the 174 cm<sup>-1</sup> mode of compound **1**, is likely the mode detected at 183 cm<sup>-1</sup>. Finally, the energetic match between the mode detected at 116 cm<sup>-1</sup> with a metal ligand breathing mode identified by Gaffney and co-workers<sup>15</sup> and a set of three near-degenerate modes calculated between 118 and 119 cm<sup>-1</sup> suggests a similar assignment to that of Gaffney.

Full spectrum time-resolved data on compound 2 are illustrated in Figure 4.11. Whereas spectral features associated with the radical anion of the ligand red of 600 nm are absent for  $\Delta t > 200$  fs in compound 1, the spectra in Figure 4.11 clearly show the presence of a strong absorption in this region that persists for several picoseconds following MLCT excitation of compound 2. Fitting of the single-wavelength data in this region reveals biphasic kinetics with time constants of  $\tau_1 = 430 \pm 50$  fs and  $\tau_2 = 2.6 \pm 0.1$  ps. Importantly, the longer component defines the eventual loss of absorption in the region of the bpy chromophore: we therefore assign the decay of the MLCT state of compound 2 to its ligand-field manifold to  $\tau_2$ . This represents a > 20-fold increase in the lifetime of the MLCT state of this system and is to our

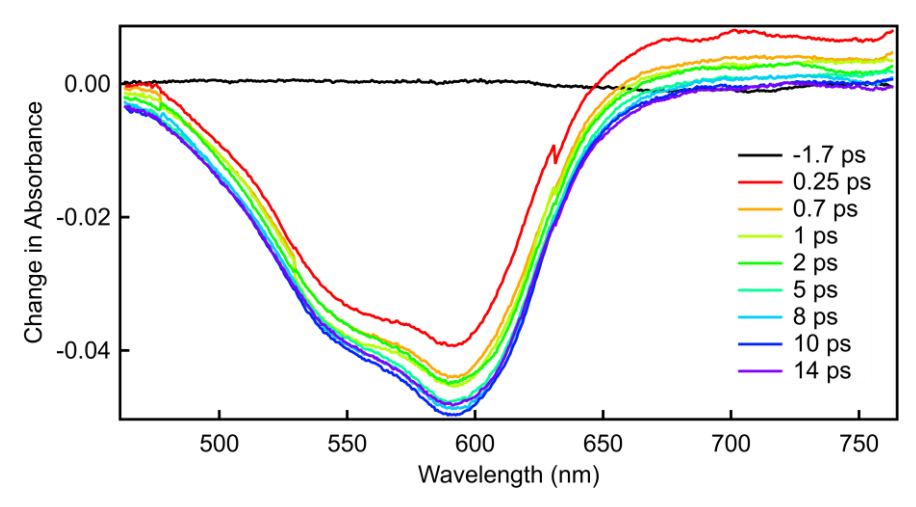


**Figure 4.11.** Femtosecond time-resolved absorption spectra of  $[FeCu_2(L)](PF_6)_4$  (2) following 600 nm excitation in acetonitrile solution.

knowledge the longest-lived charge-transfer excited state for a low-spin Fe(II) tris-polypyridyl complex in fluid solution. We believe this is the first example in which coherence data has been used to inform the synthetic redesign of a molecule to affect a significant, measurable change in the ultrafast excited-state dynamics of a charge-transfer chromophore. Specifically, we suggest that the increase in lifetime of the MLCT excited state of compound 2 relative to compound 1 is a direct consequence of the chemical modifications made to the ligand framework of the system, modifications that were informed by the analysis of the coherence featues observed in the excited-state dynamics of compound 1.

The origin of the faster component detected in the decay kinetics is unclear at the present time. We suspect that it is associated with solvent librational motion induced by the large redistribution of charge upon formation of the MLCT excited state. These sorts of perturbations have been observed in the ultrafast time-resolved measurements of compounds like  $[Ru(bpy)_3]^{2+}$ ,  $^{39,40}$  but are typically not seen in Fe(II)-based analogs most likely because the time scale for decay of the MLCT state in these systems is usually faster than the inertial response times of most polar solvents. Finally, nanosecond TA data collected by Sara Adelman of the McCusker group shows that compound 2 eventually returns to the ground-state with a time constant of  $7 \pm 3$  ns (not shown).

To better characterize the origin of the large change in the photophysical properties of compound **2** relative to compound **1**, additional TA measurements were conducted. First, we performed TA

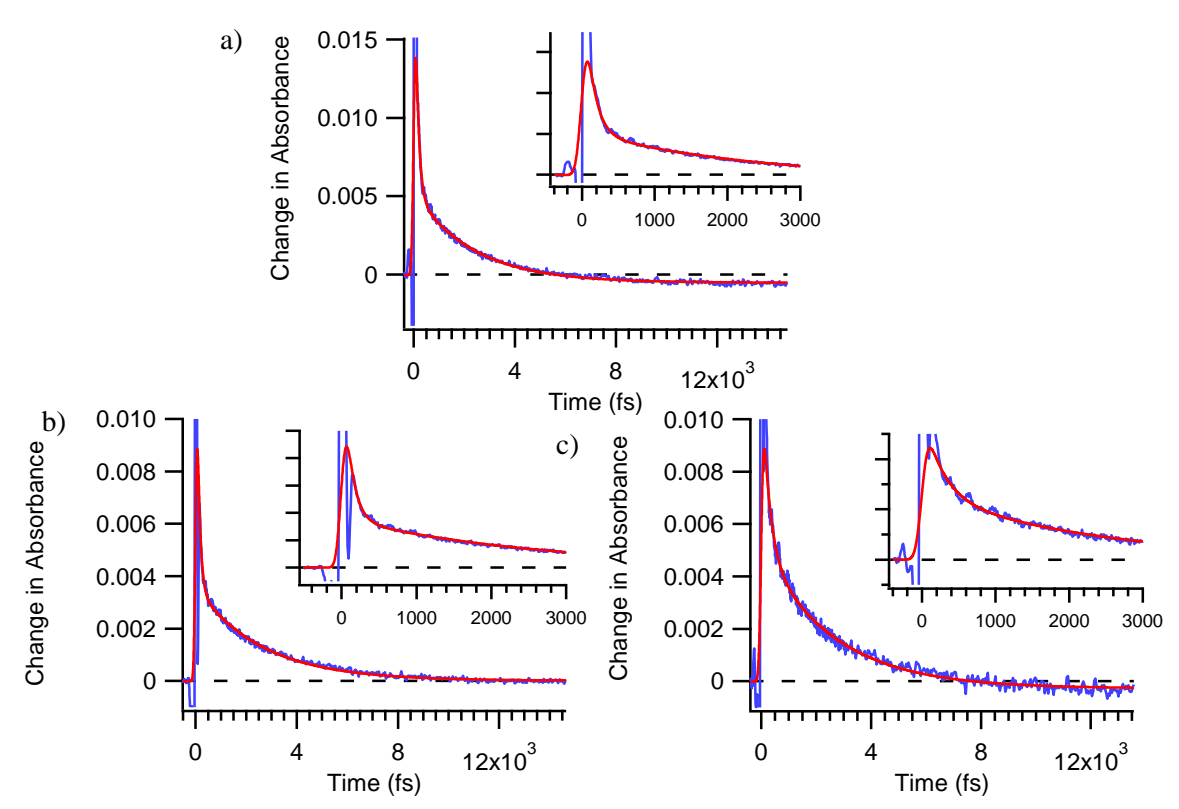


**Figure 4.12.** Representative datasets of  $[FeCu_2(L)](Bar^F)_4$  in (a) acetonitrile, (b) acetone, and (c) butyronitrile following 600 nm excitation while monitored at 700 nm.

measurements on 2 (Figure 4.A.1) while probing in the region of copper based MLCT absorption gleaned from the absorption spectra featured in Figure 4.3. We observed a bleach signal with small amplitude 2.6 ps decay to more negative  $\Delta A$  with large amplitude 116 cm<sup>-1</sup> oscillations, similar to those observed at longer wavelengths. The lack of a large amplitude decay to further negative  $\Delta A$  suggests that the copper atoms are not involved in reductive quenching of the iron based MLCT state as this process would lead to a loss of copper based MLCT absorption in this region. Additionally, TA experiments were performed on 2 in several different solvents (Figures 4.8, 4.9) as well as with a different counteranion (BAr<sup>F-</sup>) (Figure 4.12), in an effort to characterize the influence of interaction with the solute from the solvent bath and counteranion. The different solvents were chosen to observe the effect of a change in solvent dielectric (~21 for acetone and butyronitrile and ~38 for acetonitrile) as well as a change in inertial response of the solvent. These data clearly show the loss of the transient MLCT state absorption over the course of several picoseconds. A summary of the kinetics across each solvent and counter anion can be seen in Table 4.3.

**Table 4.3.** Summary kinetic components of  $[FeCu_2(L)]^{2+}$  in various solvents and with  $PF_6^-$  and  $Bar^{F-}$  counteranions. Errors are expressed as standard deviations from multiple trials.

Solvent	Counter Ion	Solvent Librational Motion, fs	MLCT→LF, ps
Acetonitrile	PF <sub>6</sub> -	430 (50)	2.6 (0.1)
Butyronitrile	$PF_6$	350 (150)	2.8 (0.4)
Acetone	$PF_{6}^{-}$	320 (80)	2.7 (0.4)
Acetonitrile	$\mathrm{BAr}^{\mathrm{F} ext{-}}$	260 (200)	2.6 (0.4)
Butyronitrile	$\mathrm{BAr}^{\mathrm{F} ext{-}}$	270 (50)	2.6 (0.1)
Acetone	$\mathrm{BAr}^{\mathrm{F} ext{-}}$	210 (90)	2.9 (0.2)

The fast, multi-hundred femtosecond component that we tentatively assigned to solvent librational motion above are all within error in Table 4.3, although the error bars are quite large relative to the magnitude of the time constant making it difficult to derive definitive conclusions about this fast process. Further work to conclusively identify this process is currently being pursued. The MLCT lifetimes across each solvent and counter anion are all within error. The insensitivity of the MLCT decay kinetics to counter anion suggest that ion pairing is not inducing the longer MLCT lifetime in compound 2, despite the 4+ charge on the cation. This is further supported by the identical MLCT lifetimes in different solvents despite the large variation in solvent dielectric.

The above results rule out factors such as reductive quenching of the MLCT state of compound 2 as well as solute-solvent or ion-pairing interactions as a major reason for the significant extension of the MLCT lifetime of 2 relative to 1. These findings thus bolster the assertion that the reason for the change in photophysical properties of 2 are from the hinderance of the vibrational modes that drive MLCT decay in 1. We can further prove this claim by performing Duschinsky displacement vector calculations to quantify the displacement of the lowest energy  ${}^5T_{2g}$  excited state. Figure 4.13 shows the calculated reorganization energies for the  ${}^5T_{2g} \rightarrow {}^1A_{1g}$  transitions of  $[Fe(L)]^{2+}$  (Figure 4.13a) and  $[FeCu_2(L)]^{4+}$  (Figure 4.13b). We see that the reorganization energy of compound 2 (9,320 cm<sup>-1</sup>) is significantly smaller than for compound 1 (12,100 cm<sup>-1</sup>) which is on par with the reorganization energy calculated in the same manner for the prototypical  $[Fe(bpy)_3]^{2+}$  (13,050 cm<sup>-1</sup>) (Figure 4.B.1). It should be noted that while the calculated reorganization energies for the reverse  ${}^1A_{1g} \rightarrow {}^5T_{2g}$  reaction are significantly different (19,870 cm<sup>-1</sup> for

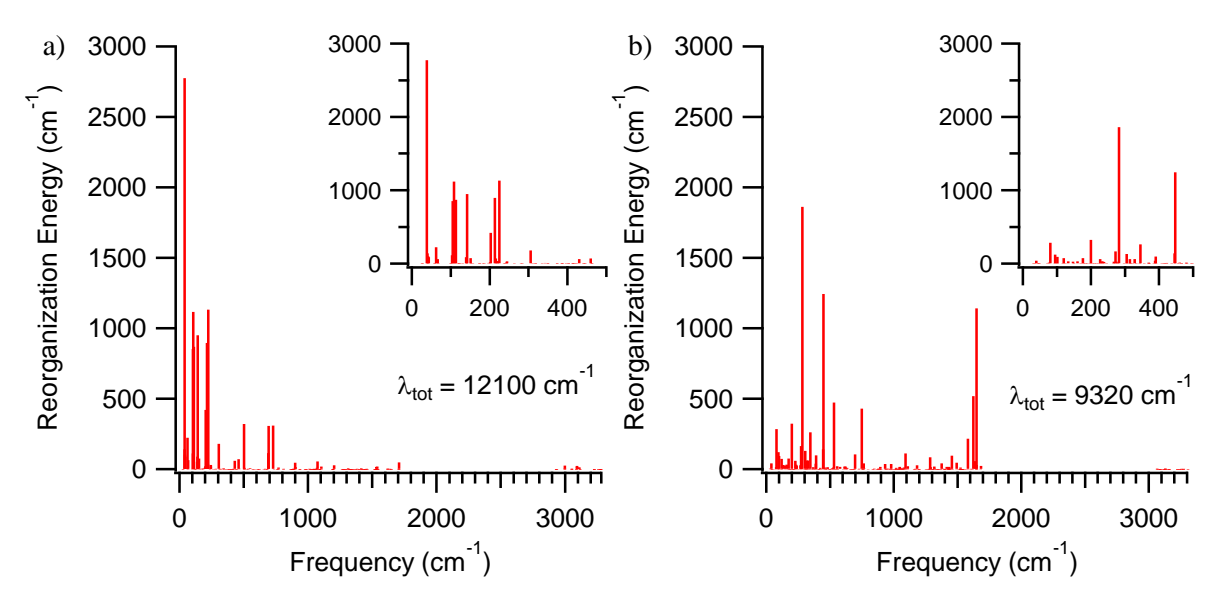


**Figure 4.13.** Plots of the calculated inner-sphere reorganization energy as a function of normal mode frequency for the  ${}^5T_{2g} \rightarrow {}^1A_{1g}$  transitions of (a)  $[Fe(L)]^{2+}$  and (b)  $[FeCu_2(L)]^{4+}$ . The normal modes used are inherent to the  ${}^5T_{2g}$  excited state. Reorganization energies were calculated from the nuclear displacements of the Duschinsky displacement vectors for the corresponding electronic transition.

compound **1**, 6,820 cm<sup>-1</sup> for compound **2**, and 18,820 cm<sup>-1</sup> for  $[Fe(bpy)_3]^{2+}$ , a testament to the different motions and force constants inherent to each electronic state, the overarching trend remains the same. We thus find that the  ${}^5T_{2g}$  excited state of compound **2** is less displaced than that of the compound **1** control molecule or the prototypical  $[Fe(bpy)_3]^{2+}$ , confirming that the synthetic modification did in fact hinder the vibrational modes of necessary for ultrafast MLCT decay in this class of compounds.

In summary, with this report we have demonstrated that it is possible to leverage the information afforded from excited-state coherence observations toward the synthetic redesign of a molecular chromophore. Large-amplitude distortions associated with MLCT-state excitation of an Fe(II)-based tris-bipyridine assembly that exhibited dephasing times intermediate between what is expected for pure electronic and pure vibrational coherences provided the impetus to target these degrees of freedom for altering the ultrafast excited-state dynamics of the compound. Ultimately, the fact that synthetic modification of these modes resulted in a 20-fold change in the observed kinetics confirmed that these specific degrees of freedom and the MLCT relaxation dynamics of the chromophore are indeed linked. We believe that these results suggest the viability of a fundamentally different approach to the manipulation of

excited-state dynamics wherein phenomena observed through ultrafast spectroscopic techniques can be exploited for the creation of chromophores with design-specific properties.

# **APPENDICES**

# Appendix 4.A. Additional Transient Absorption Data on Compound 2

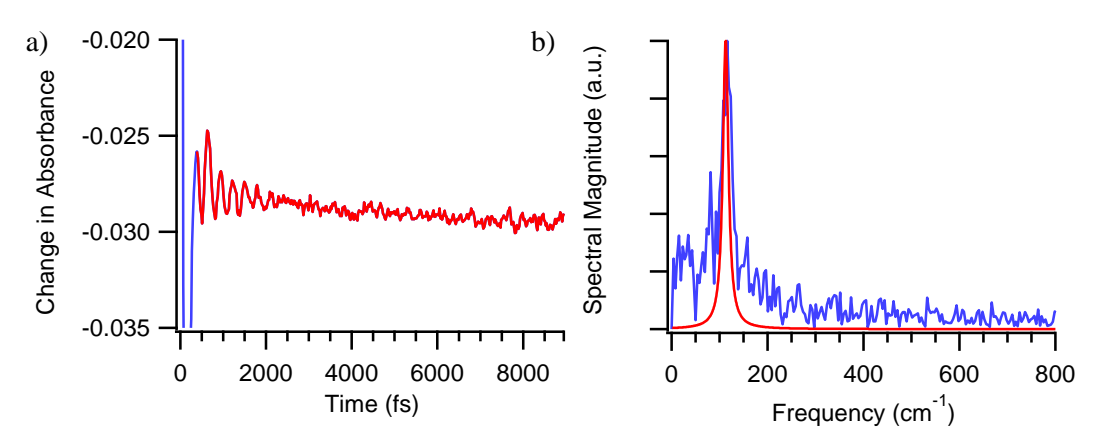
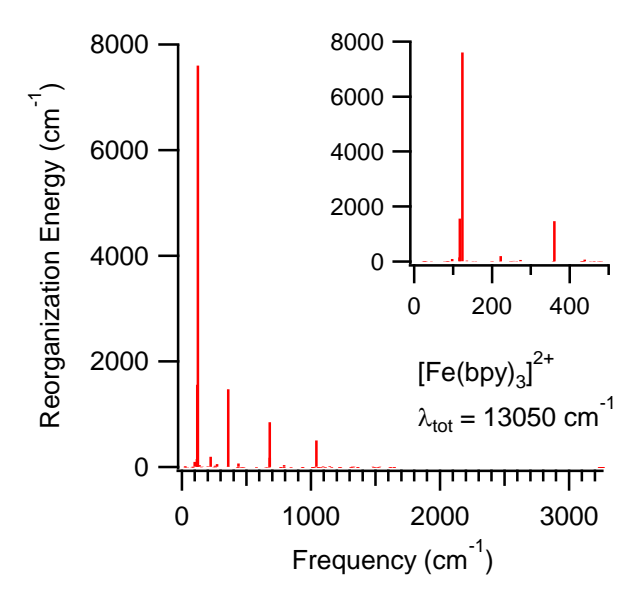


**Figure 4.A.1.** (a) TA data of  $[FeCu_2(L)](PF_6)_4$  (2) in acetonitrile while exciting at 600 nm and monitoring at 396 nm (blue) with LPSVD fit to equation 4.2 (red). (b) LPSVD vibrational spectrum (red) with corresponding FFT of the residuals to an exponential fit (blue).

# Appendix 4.B. Reorganization Energy Calculation for [Fe(bpy)<sub>3</sub>]<sup>2+</sup>



 $\begin{array}{lll} \textbf{Figure 4.B.1.} & Calculated & reorganization \\ energy & for & the \end{array} \ ^5T_{2g} \ \to \ ^1A_{1g} & transition & of \\ [Fe(bpy)_3]^{2^+}. \end{array}$ 

# Appendix 4.C. Additional Normal Mode Assignment for Compound 1

Since there was a large uncertainty in the experimentally observed frequency of the 127 (5) cm<sup>-1</sup> mode of compound **1** and a high density of vibrational states in that frequency region, an assignment during the initial characterization was forgone. Now that the vibrational modes of **2** have been assigned, however, we can turn back and assign the 123 cm<sup>-1</sup> mode of **1**. In compound **2** the low frequency mode corresponded to an Fe-N breathing mode in which the tren-caps compressed inwards towards the iron-center and elongated the Fe-N bond distance. In compound **1** we find an analogous motion at 113 cm<sup>-1</sup> on the high spin  ${}^5T_{2g}$  excited state, in reasonable agreement with the observed 127 cm<sup>-1</sup> frequency.

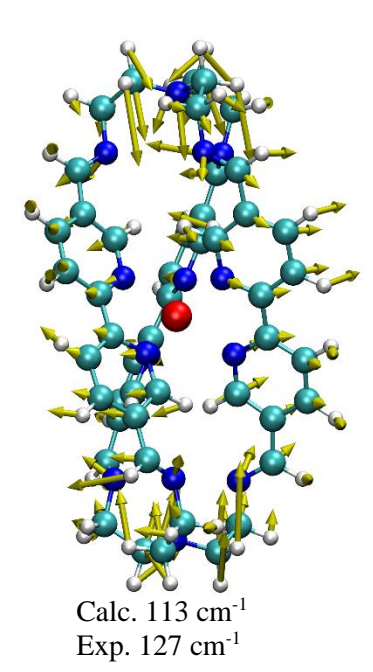


**Figure 4.C.1.** DFT calculated vector displacement diagram of the 127 cm<sup>-1</sup> vibrational mode of  $[Fe(L)]^{2+}$ .

# Appendix 4.D. Results of Kinetic and Oscillatory Analyses on Each Individual Dataset

**Table 4.D.1.** Coherent oscillatory components observed for individual TA datasets on  $[Fe(L)](PF_6)_2$  in acetonitrile solvent following 600 nm excitation.

Probe, nm	IRF, fs	Frequency, cm <sup>-1</sup> (Damping Time, fs)				
650	85			169 (241)	227 (1130)	
700	65				204 (588)	
650	60			173 (197)		
603	45	122 (155)			204 (263)	
594	45	131 (388)		173 (341)	248 (1133)	
600	50	132 (198)			229 (279)	
592	50	127 (250)			207 (349)	
608	50	123 (180)		176 (705)		
650	85		157 (276)			
642	85			173 (293)		
658	85		154 (320)		219 (1754)	
Average Freq	uency, cm <sup>-1</sup>	127	156	173	215	
Standard Deviation, cm <sup>-1</sup>		5	2	3	12	
Average Damp	Average Damping Time, fs		300	360	730	
Standard De	eviation, fs	90	30	230	600	

**Table 4.D.2.** Kinetic components and fit parameters for individual TA datasets on  $[FeCu_2(L)](PF_6)_4$  in various solvents following 600 nm excitation. A 7 ns kinetic component was locked in to describe the slow ground state recovery process and account for any baseline offset.

Probe, nm	Solvent	IRF, fs	$\tau_1$ , fs	$\tau_2$ , fs	$A_1 \times 10^3$	$A_2 \times 10^3$	$A_3 \times 10^3$
650	MeCN	85	450	2530	14.0	24.6	-12.0
650	MeCN	60	500	2680	12.5	21.3	-17.7
650	MeCN	90	340	2610	6.9	12.8	-9.1
650	MeCN	115	425	2610	6.9	11.8	-9.5
650	MeCN	70	330	2370	8.4	18.7	-14.2
700	MeCN	65	454	2660	4.5	14.9	-1.6
700	MeCN	100	450	2710	4.8	10.9	0.9
700	MeCN	100	470	2640	4.4	10.5	0.4
700	MeCN	110	424	2755	3.3	7.5	0.5
700	MeCN	90	410	2460	6.2	11.6	4
700	MeCN	90	475	2850	7.4	12.7	-0.5
400	MeCN	280	-	2515	-	-	-
396	MeCN	280	-	2645	-	-	-
650	Acetone	115	250	2460	11.2	14.1	-11.6
650	Acetone	70	250	2340	11.9	15.1	-13.4
700	Acetone	90	380	2780	7.0	12.0	5
700	Acetone	90	400	3140	5.7	8.7	0.0
650	BuCN	115	280	2460	11.9	12.4	-12.4
650	BuCN	70	360	3100	14.9	13.5	-13.1
700	BuCN	90	210	2390	10.3	10.7	2.2
700	BuCN	90	560	3070	11.2	10.7	-0.6
MeC	N Average (σ)	), fs	430	2600			
MeCN S	Standard Devia	tion, fs	50	100			
Ace	etone Average,	fs	320	2700			
Acetone	Standard Devi	ation, fs	80	400			
Bu	iCN Average,	fs	350	2800			
BuCN S	Standard Devia	tion, fs	150	400			

**Table 4.D.3.** Coherent oscillatory components observed in individual TA datasets on [FeCu<sub>2</sub>(L)](PF<sub>6</sub>)<sub>4</sub> in various solvents following 600 nm excitation. The observed sub-100 cm<sup>-1</sup> components are not expected to be physically meaningful.

Probe, nm	$E_{pu}$ ( $E_{pr}$ ), $\mu J$	IRF, fs	Solvent	Fre	equency, cm <sup>-1</sup> (I	Damping Time,	fs)
700	4 (0.2)	65	MeCN		117 (744)	177 (731)	
700	4 (0.4)	100	MeCN		117 (613)	180 (818)	220 (639)
700	4 (0.4)	100	MeCN	54 (840)	118 (902)	182 (645)	225 (465)
700	4 (0.4)	110	MeCN		120 (934)	184 (671)	224 (257)
700	4 (0.4)	90	MeCN		123 (357)		
700	3.6 (0.4)	90	MeCN		112 (419)	186 (651)	238 <sup>a</sup> (403)
650	4 (0.4)	85	MeCN	38 (1040)	115 (581)	181 (421)	217 (528)
650	4 (0.4)	60	MeCN	49 (562)	115 (720)	185 (767)	223 (743)
650	4 (0.4)	90	MeCN	62 (456)	114 (610)	184 (963)	220 (683)
650	4 (0.4)	115	MeCN		117 (676)	185 (529)	221 (369)
650	4 (0.4)	70	MeCN		119 (748)	184 (1225)	
610	4 (0.4)	45	MeCN		117 (1122)	183 (1358)	220 (850)
603	4 (0.4)	45	MeCN		115 (625)	183 (1058)	210 (429)
594	4 (0.4)	45	MeCN		112 (419)	181 (640)	212 (732)
400	3.4 (0.2)	280	MeCN		114 (696)		
396	3.3 (0.2)	280	MeCN		113 (757)		
700	4 (0.4)	110	Acetone		117 (433)	181 (454)	223 (508)
700	4 (0.4)	90	Acetone		116 (466)	185 (1183)	224 (626)
700	3.6 (0.4)	90	Acetone		115 (664)	184 (592)	223 (699)
650	4 (0.4)	90	Acetone		117 (667)	183 (751)	220 (518)
650	4 (0.4)	115	Acetone		118 (757)	185 (688)	224 (331)
650	4 (0.4)	70	Acetone		118 (992)	180 (1523)	219 (1794) <sup>b</sup>
700	4 (0.4)	110	BuCN		113 (584)	184 (385)	218 (360)
700	4 (0.4)	90	BuCN		112 (815)	180 (686)	226 (315)
700	3.6 (0.4)	90	BuCN		113 (701)	182 (690)	221 (752)
650	4 (0.4)	90	BuCN		114 (821)	181 (584)	217 (509)
650	4 (0.4)	115	BuCN		114 (926)	181 (445)	218 (376)
650	4 (0.4)	70	BuCN		115 (986)	182 (707)	216 (362)

a. 238 cm<sup>-1</sup> frequency was an outlier and not used in averaging

b. 1794 fs dephasing time was an outlier and not used in averaging.

**Table 4.D.4.** Kinetic components and fit parameters for individual TA datasets on  $[FeCu_2(L)](BAr^F)_4$  in various solvents following 600 nm excitation and while monitoring at 700 nm. A 7 ns kinetic component was locked in and used to describe the slow ground state recovery process and account for any baseline offset.

Solvent	IRF, fs	$\tau_1$ , fs	$\tau_2$ , fs	$A_1 \times 10^3$	$A_2 \times 10^3$	$A_3 \times 10^3$
MeCN	103	120	2300	9.4	5.4	-0.5
MeCN	84	400	2870	1.9	3.1	-0.2
MeCN	110	230	2580	3.5	6.3	-1.0
MeCN	110	300	2650	3.4	6.7	-0.3
Acetone	84	105	2580	5.8	3.4	-0.01
Acetone	110	280	3040	4.0	5.6	-0.2
Acetone	110	250	2960	4.7	6.6	-0.1
BuCN	110	270	2590	4.3	5.1	-0.3
BuCN	110	270	2580	1.2	1.5	-0.1
DCM	103	170	1360	12.8	4.9	-0.1
DCM	84	210	1390	4.6	2.3	-0.2

**Table 4.D.5.** Results of individual kinetic fits of  $[Fe(L)](PF_6)_2$  TA data following 600 nm excitation in acetonitrile solvent.

Probe, nm	IRF, fs	$\tau_1$ , fs	$\tau_2$ , fs
650	85	120	1400
650	60	133	1798
650	90	98	1285
603	45	123	
594	48	99	
592	48	110	
608	48	50	
650	85	134	
642	85	140	
658	85	115	

REFERENCES

#### REFERENCES

- (1) Scholes, G. D.; Fleming, G. R.; Chen, L. X.; Aspuru-Guzik, A.; Buchleitner, A.; Coker, D. F.; Engel, G. S.; van Grondelle, R.; Ishizaki, A.; Jonas, D. M.; *et al.* Using Coherence to Enhance Function in Chemical and Biophysical Systems. *Nature* **2017**, *543*, 647–656.
- (2) Zewail, A. H. Femtochemistry: Atomic-Scale Dynamics of the Chemical Bond. *J. Phys. Chem. A* **2000**, *104*, 5660–5694.
- (3) Bishop, M. M.; Roscioli, J. D.; Ghosh, S.; Mueller, J. J.; Shepherd, N. C.; Beck, W. F. Vibrationally Coherent Preparation of the Transition State for Photoisomerization of the Cyanine Dye Cy5 in Water. *J. Phys. Chem. B* **2015**, *119* (23), 6905–6915.
- (4) Schoenlein, R. W.; Peteanu, L. A.; Mathies, R. A.; Schank, C. V. The First Step in Vision: Femtosecond Isomerization of Rhodopsin. *Science* **1991**, *254*, 412–415.
- (5) Zhu, L.; Sage, J. T.; Champion, P. M. Observation of Coherent Reaction Dynamics in Heme Proteins. *Science* **1994**, *266*, 629–632.
- (6) Chenu, A.; Scholes, G. D. Coherence in Energy Transfer and Photosynthesis. *Annu. Rev. Phys. Chem.* **2015**, *66*, 69–96.
- (7) Delor, M.; Archer, S. A.; Keane, T.; Meijer, A. J. H. M.; Sazanovich, I. V.; Greetham, G. M.; Towrie, M.; Weinstein, J. A. Directing the Path of Light-Induced Electron Transfer at a Molecular Fork Using Vibrational Excitation. *Nat. Chem.* **2017**, *9*, 1099–1104.
- (8) Zerdane, S.; Wilbraham, L.; Cammarata, M.; Iasco, O.; Riviere, E.; Boillot, M.-L.; Ciofini, I.; Collet, E. Comparison of Structural Dynamics and Coherence of d-d and MLCT Light-Induced Spin State Trapping. *Chem. Sci.* **2017**, *8*, 4978–4986.
- (9) Monni, R.; Auböck, G.; Kinschel, D.; Aziz-lange, K. M.; Gray, H. B.; Vlc ek, A.; Chergui, M. Conservation of Vibrational Coherence in Ultrafast Electronic Relaxation: The Case of Diplatinum Complexes in Solution. *Chem. Phys. Lett.* **2017**, *683*, 112–120.
- (10) Kim, P.; Kelley, M. S.; Chakraborty, A.; Wong, N. L.; Van Duyne, R. P.; Schatz, G. C.; Castellano, F. N.; Chen, L. X. Coherent Vibrational Wavepacket Dynamics in Platinum(II) Dimers and Their Implications. *J. Phys. Chem. C* 2018, *122*, 14195–14204.
- (11) Gueye, M.; Manathunga, M.; Agathangelou, D.; Orozco, Y.; Paolino, M.; Fusi, S.; Haacke, S.; Olivucci, M.; Léonard, J. Engineering the Vibrational Coherence of Vision into a Synthetic Molecular Device. *Nat. Commun.* **2018**, *9*, 313.
- (12) Iwamura, M.; Takeuchi, S.; Tahara, T. Ultrafast Excited-State Dynamics of Copper(I) Complexes. *Acc. Chem. Res.* **2015**, *48*, 782–791.
- (13) Wenger, O. S. Is Iron the New Ruthenium? *Chem. Eur. J.* **2019**, *25*, 6043–6052.
- Wenger, O. S. Photoactive Complexes With Earth-Abundant Metals. *J. Am. Chem. Soc.* **2018**, *140*, 13522–13533.

- (15) Lemke, H. T.; Kjaer, K. S.; Hartsock, R.; van Driel, T. B.; Chollet, M.; Glownia, J. M.; Song, S.; Zhu, D.; Pace, E.; Matar, S. F.; Nielsen, M. M.; Benfatto, M.; Gaffney, K. J.; Collet, E.; Cammarata, M. Coherent Structural Trapping through Wave Packet Dispersion during Photoinduced Spin State Switching. *Nat. Commun.* **2017**, *8*, 15342.
- (16) Auböck, Gerald; Chergui, M. Sub-50-Fs Photoinduced Spin Crossover in [Fe(Bpy)3]2+. *Nat. Chem.* **2015**, 7, 629–633.
- (17) Monat, J. E.; McCusker, J. K. Femtosecond Excited-State Dynamics of an Iron(II) Polypyridyl Solar Cell Sensitizer Model. *J. Am. Chem. Soc.* **2000**, *122*, 4092–4097.
- (18) McCusker, J. K. Electronic Structure in the Transition Metal Block and Its Implications for Light Harvesting. *Science* **2019**, *363*, 484–488.
- (19) Liu, L.; Duchanois, T.; Etienne, T.; Monari, A.; Beley, M.; Assfeld, X.; Haacke, S.; Gros, P. C. A New Record Excited State 3MLCT Lifetime for Metalorganic Iron(II) Complexes. *Phys. Chem. Phys.* **2016**, *18*, 12550–12556.
- (20) Chabera, P.; Kjaer, K. S.; Prakash, O.; Honarfar, A.; Liu, Y.; Fredin, L. A.; Harlang, T. C. B.; Lidin, S.; Uhlig, J.; Sundstro, V.; *et al.* FeII Hexa N Heterocyclic Carbene Complex with a 528 ps Metalto- Ligand Charge-Transfer Excited-State Lifetime. *Phys. Chem. Lett.* **2018**, *9*, 459-463.
- (21) Steube, J.; Burkhardt, L.; Päpcke, A.; Moll, J.; Zimmer, P.; Schoch, R.; Wölper, C.; Heinze, K.; Lockbrunner, S.; Bauer, M. Excited-State Kinetics of an Air-Stable Cyclometalated Iron(II) Complex. *Chem. Eur. J.* **2019**, *25*, 11826–11830.
- (22) Kjær, K. S.; Kaul, N.; Prakash, O.; Chábera, P.; Rosemann, N. W.; Honarfar, A.; Gordivska, O.; Fredin, L. A.; Bergquist, K.-E.; Häggström, L.; Ericsson, T.; *et al.* Luminescence and Reactivity of a Charge-Transfer Excited Iron Complex with Nanosecond Lifetime. *Science* **2019**, *363*, 249–253.
- (23) Frisch, M. J.; Trucks, G. W.; Schlegel, H. B.; Scuseria, G. E.; Robb, M. A.; Cheeseman, J. R.; Scalmani, G.; Barone, V.; Petersson, G. A.; Nakatsuji, H.; Li, X.; Caricato, M.; Marenich, A. V.; Bloino, J.; Janesko, B. G.; Gomperts, R.; Mennucci, B.; Hratch, D. J. Gaussian 16, Revision C.01. **2016**.
- (24) Humphrey, W.; Dalke, A.; Schulten, K. VMD: Visual Molecular Dynamics. *J. Mol. Graph. Model.* **1996**, *14*, 33–38.
- (25) Albrecht, H.; Heist, P.; Kleinschmidt, J.; Lap, D. V. Single-Shot Measurement of Ultraviolet and Visible Femtosecond Pulses Using the Optical Kerr Effect. *Appl. Opt.* **1993**, *32*, 6659–6663.
- (26) Gütlich, P.; Goodwin, H. A. Spin Crossover in Transition Metals III; Springer-Verlag: Berlin, Heidelberg, **2004**.
- (27) Purcell, K. F. Pseudorotational Intersystem Crossing in d<sup>6</sup> Complexes. *J. Am. Chem. Soc.* **1979**, 101, 5147–5152.
- (28) McCusker, J. K.; Rheingold, A. L.; Hendrickson, D. N. Variable-Temperature Studies of Laser-Initiated 5 T 2 f 1 A 1 Intersystem Crossing in Spin-Crossover Complexes: Empirical Correlations between Activation Parameters and Ligand Structure in a Series of Polypyridyl Ferrous Complexes. *Inorg. Chem.* **1996**, *35*, 2100–2112.

- (29) Ashley, D. C.; Jakubikova, E. Ray-Dutt and Bailar Twists in Fe(II)-Tris(2,2'-bipyridine): Spin States, Sterics, and Fe-N Bond Strengths. *Inorg. Chem.* **2018**, *57*, 5585–5596.
- (30) De Mendoza, J.; Mesa, E.; Rodriguez-Ubis, J.-C.; Vázquez, P.; Vögtle, F.; Windscheif, P.-M.; Rissanen, K.; Lehn, J.-M.; Lilienbaum, D.; Ziessel, R. A New Macrobicyclic Tris-Bipyridine Ligand and Its Cu(I)<sub>2</sub> and Ag(I)<sub>3</sub> Complexes. *Angew. Chem. Int. Ed. Engl.* **1991**, *30*, 1331–1333.
- (31) Brown, A. M.; McCusker, C. E.; McCusker, J. K. Spectroelectrochemical Identification of Charge-Transfer Excited States in Transition Metal-Based Polypyridyl Complexes. *Dalt. Trans.* **2014**, 17635–17646.
- (32) Smeigh, A. L.; Creelman, M.; Mathies, R. A.; McCusker, J. K. Femtosecond Time-Resolved Optical and Raman Spectroscopy of Photoinduced Spin Crossover: Temporal Resolution of Low-to-High Spin Optical Switching. *J. Am. Chem. Soc.* **2008**, *130*, 14105–14107.
- Wang, Q.; Schoenlein, R. W.; Peteanu, L. A.; Mathies, R. A.; Shank, C. V. Vibrationally Coherent Photochemistry in the Femtosecond Primary Event of Vision *Science* **1994**, *266*, 422–424.
- (34) Hamm, P.; Zanni, M. Concepts and Methods of 2D Infrared Spectroscopy; Cambridge University Press: Cambridge, **2011**.
- (35) Rafiq, S.; Scholes, G. D. Slow Intramolecular Vibrational Relaxation Leads to Long-Lived. *J. Chem. Phys. A* **2016**, *120*, 6792–6799.
- (36) De Silvestri, S.; Cerullo, G.; Lanzani, G. Coherent Vibrational Dynamics; CRC Press: Boca Raton, FL, **2008**.
- (37) Reid, P. J.; Silva, C.; Barbara, P. F. Electronic Coherence, Vibrational Coherence, and Solvent Degrees of Freedom in the Femtosecond Spectroscopy of Mixed-Valence Metal Dimers in H<sub>2</sub>O and D<sub>2</sub>O. *J. Phys. Chem.* **1995**, *99*, 2609–2616.
- (38) Rafiq, S.; Scholes, G. D. From Fundamental Theories to Quantum Coherences in Electron Transfer. *J. Am. Chem. Soc.* **2019**, *141*, 708–722.
- (39) Damrauer, N. H.; Cerullo, G.; Yeh, A.; Boussie, T. R.; Shank, C. V.; McCusker, J. K. Femtosecond Dynamics of Excited-State Evolution in [Ru(bpy)<sub>3</sub>]<sup>2+</sup>. *Science* **1997**, *275*, 54–57.
- (40) Yeh, A. T.; Shank, C. V.; McCusker, J. K. Ultrafast Electron Localization Dynamics Following Photo-Induced Charge Transfer. *Science* **2000**, *289*, 935–938.

### Chapter 5: A Modular Approach to Controlling Excited State Properties of Iron(II) Polypyridyls

The work presented in this chapter was a collaborative effort between this author, and McCusker group members Karl C. Nielsen, Dr. Christopher R. Tichnell, and Dr. Monica C. Carey. The initial synthesis and impetus for the work was driven by CRT, with KCN performing all remaining synthesis and ground state characterizations. MCC performed an initial preliminary transient absorption experiment to show a compound had promising photophysical properties. All transient absorption data shown herein was collected and analyzed by the author of this dissertation.

#### 5.1. Introduction

Photoinduced electron transfer reactions are of interest for a wide range of applications. A significant portion of the work in this regard has focused on ruthenium(II) polypyridyl complexes which often have long-lived (ns-µs)¹ charge separated excited states, which survive long enough to be coupled to other processes. Some important applications of charge separated states, such as solar energy conversion, rely on light harvesting, an inherently material intensive process due to the relatively low solar flux on Earth. This makes the use of ruthenium, one of the rarest substances on the planet,² a poor choice when scaling up these applications. This has prompted the search for alternative first row transition metal chromophores with charge separated excited states that are long lasting enough to be coupled to electron

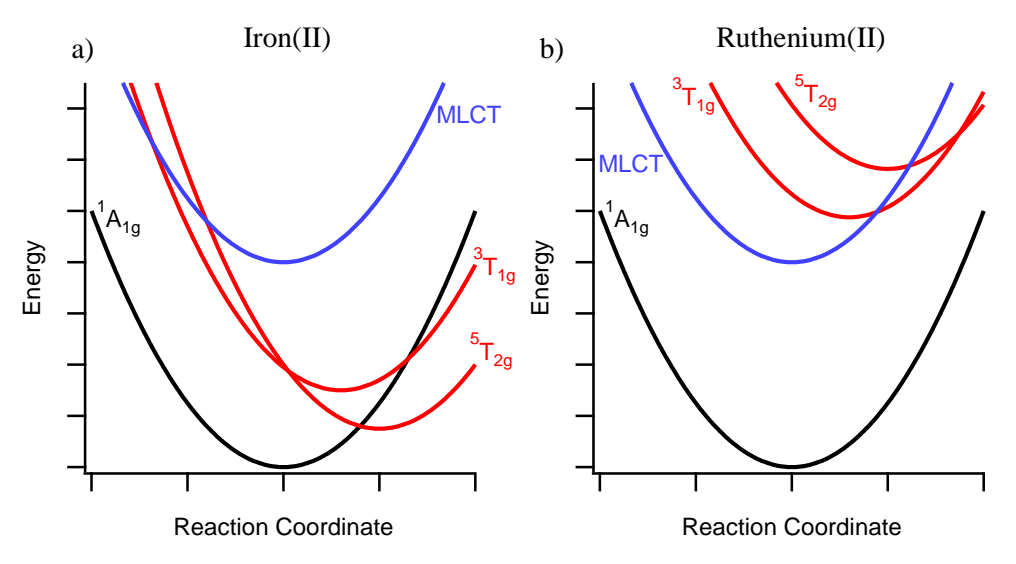


**Figure 5.1.** Qualitative potential energy surfaces for six-coordinate (a) iron(II) and (b) ruthenium(II) compounds.

transfer processes. While several such systems exist, such as the class of  $d^{10}$  copper(I) polypyridyl compounds, perhaps the easiest conceptual alternative to  $d^6$  ruthenium(II) compounds are the complexes of their vastly more earth abundant  $d^6$  iron(II) congener. Unfortunately, the exceedingly rapid MLCT deactivation of iron(II) polypyridyl compounds, (often sub-200 fs)<sup>3</sup> precludes their use in photo-actuated electron transfer reactions.

The origin for these short MLCT excited state lifetimes in iron-based compounds can be traced back to the presence of lower energy metal centered excited states that are less energetically accessible in their ruthenium counterparts (Figure 5.1). Framed differently, the smaller ligand field splitting inherent to 3d metals (a consequence of the shorter radial extension of the 3d orbitals relative to the 4d orbitals) is responsible for their lackluster performance. The lack of a radial node in the 3d orbitals of iron results in a contraction of this orbital relative to its 4d counterpart in ruthenium (Figure 5.2). The larger radial extension of the 4d orbitals of ruthenium then allow for increased overlap with ligand-based orbitals before electrostatic repulsion from the p and s electrons dominates. This in turn results in smaller ligand field splitting in 3d transition metal systems than their 4 and 5d congeners. Several research groups have thus sought to remedy this problem by utilizing strongly  $\sigma$ -donating ligands to raise the lower lying ligand field excited states of iron above the MLCT manifold. This approach has been rather successful in producing iron(II) compounds with significantly longer lasting MLCT excited states.<sup>4-7</sup>

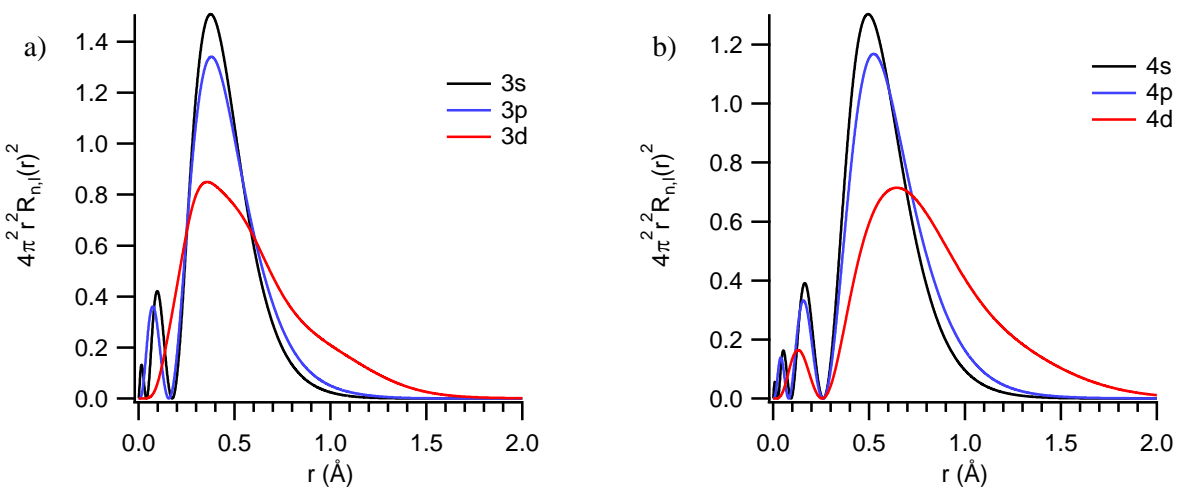


**Figure 5.2.** Radial distribution function for (a) the n = 3 orbitals of iron(II) and (b) the n = 4 orbitals of ruthenium(II).

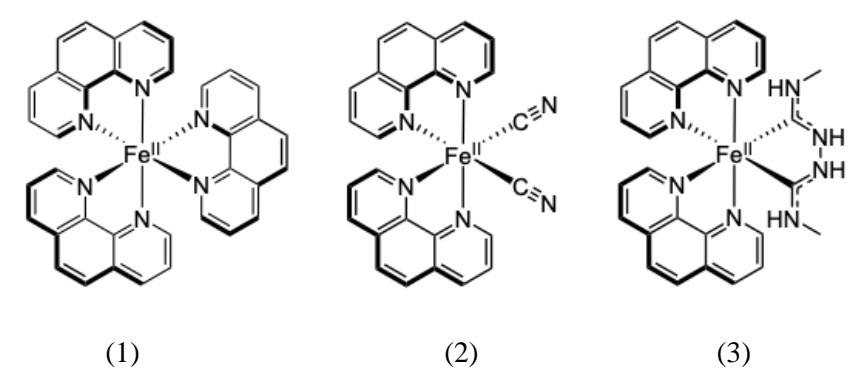


Figure 5.3. Drawing of the three compounds investigated in this study.

This work seeks to illustrate the benefits of a more modular approach to ligand design whereby the ligand field strength and, by extension, the photophysical properties can be systematically tuned by swapping a single phenanthroline ligand with stronger-field cyanide or dicarbene ligands, allowing for semi-orthogonal modulation of the ligand field. Figure 5.3 shows the series investigated in this work, which terminates with an acyclic carbene complex that was first synthesized 40 years ago. The metal-templated synthesis avoids the instability inherent to other carbene ligands which require *in situ* activation and coordination. This opens the door to further tuning of the spectral properties of these complexes by synthetic modification of the two remaining polypyridyl ligands which are intimately involved in the MLCT-based features in the ground state absorption spectrum for each compound.

### **5.2. Experimental Methods**

### 5.2.1. Synthesis and Characterization

All synthesis and ground state characterization on compounds 1, 2, and 3 were performed by McCusker group members Karl Nielsen and Dr. Christopher Tichnell according to literature procedures.<sup>8,9</sup>

All electrochemical and spectroelectrochemical experiments were conducted under an argon atmosphere in a drybox by Karl Nielsen. Cyclic voltammetry (CV) and differential pulse voltammetry (DPV) experiments were performed using an Electrochemical Workstation (CH-Instruments) potentiostat. The three-electrode setup included a platinum disk working electrode, a silver wire pseudo-reference electrode, and a platinum wire counter electrode. A saturated solution of tetrabutylammonium perchlorate (TBAClO<sub>4</sub> from Sigma Aldrich) was used in methanol. Ferrocene was used as an internal standard and all

potentials are reported against this reference herein. All spectroelectrochemical measurements were also conducted under an argon atmosphere in a drybox and performed in a manner similar to those described for electrochemical experiments. A Honeycomb spectroelectrochemical cell (Pine Research) was used. Gold honeycomb electrodes (which includes working and reference electrodes) were utilized. A silver wire pseudo-reference electrode in a glass fritted jacket was filled with the methanolic TBAClO<sub>4</sub> electrolyte. Bulk electrolysis was performed by holding potentials ~100 mV positive or negative of the anodic and cathodic current maxima for oxidation and reduction respectively. A 5.8 Spectrograph (Spectral Instruments Incorporated) was used to monitor changes in absorbance. Reductive and oxidative spectra from early electrolysis times were added together to simulate MLCT spectral features. <sup>10</sup>

#### **5.2.2.** Ultrafast Transient Absorption Spectroscopy

Details of the transient absorption set-up and methodology are provided in Chapter 2 of this dissertation. Samples were dissolved in HPLC grade methanol such that the absorbance at the center wavelength of the pump spectrum was between 0.3 and 0.8. A ground state UV-Vis spectrum was acquired before and after use to check for any degradation of the sample. Additionally, the signal for each compound was checked for linearity before data collection. All errors presented for single wavelength measurements are from the standard deviation of multiple datasets except where explicitly stated.

Full spectrum data was chirp corrected and fit using global analysis in OPTIMUS, a free, downloadable program for analysis of time resolved spectroscopic data. Decay associated difference spectra (DADS) and evolution associated difference spectra (EADS) were also calculated from OPTIMUS fits assuming sequential decay dynamics. Additionally, the chirp corrected data was subjected to singular value decomposition in MATLAB and the right eigenvectors, describing the time-dependent nature of the data, were subsequently fit with exponential functions to discern the kinetics of the underlying photophysical processes. The time constants acquired from fitting the right eigenvectors were implemented into the solution to a set of differential equations describing the kinetic model for a particular molecule to produce a concentration matrix, *C*, in which each column contains the concentration of a particular excited state as a function of time. Assuming the experimental data can be described in terms of a linear

combination of basis spectra for each chemical component, the data matrix, A, can be written in terms of a basis spectrum matrix, F, and the concentration matrix as in equation 5.1.

$$A = FC^{T}$$
 5.1

If the product C<sup>T</sup>C is invertible, then F can be calculated according to equation 5.2, <sup>12</sup>

$$F = AC(C^TC)^{-1}$$
 5.2

thus affording the EADS for each transient species as columns of the basis spectrum matrix, F. For this investigation we employ both the SVD analysis and the global fitting from the OPTIMUS software to provide a complimentary view of the kinetics and spectroscopic changes as a function of time. The MATLAB script used to perform SVD analysis is included in appendix A.

The full spectrum measurements in this study serve as a convenient way to qualitatively understand the spectral changes as a function of time, and the fitting techniques outlined above serve to estimate the timescale of the dynamics. These measurements, however, can sometimes suffer from a low signal to noise ratio, in part due to the limited intensity of the white light continuum probe, and in part due to the lack of lock-in amplification for this measurement on our laser system. For more precise kinetic measurements, we employ a second optical parametric amplifier (OPA) to generate a probe pulse, often of higher intensity than can be generated in a continuum and employ lock-in amplification to increase the signal to noise ratio. Coherent oscillations were observed in some datasets at short pump-probe delays. The oscillatory features in these data sets were analyzed the manner outlined in chapter 2 of this dissertation.

#### 5.3. Results and Discussion

## 5.3.1. Ground-State Properties of Compounds 1, 2, and 3

The ground state absorption spectrum of compounds 1, 2, and 3 can be seen in Figure 5.4, in which a broad, intense metal-to-ligand charge transfer (MLCT) based absorption band for each compound is observed. Replacement of a single phen ligand with the increasingly strong field cyanide and carbene ligands in compounds 2 and 3 results in consecutive redshifts of the MLCT band, in good agreement with the MLCT energies calculated from electrochemistry (Table 5.1). The redshift of the MLCT absorption

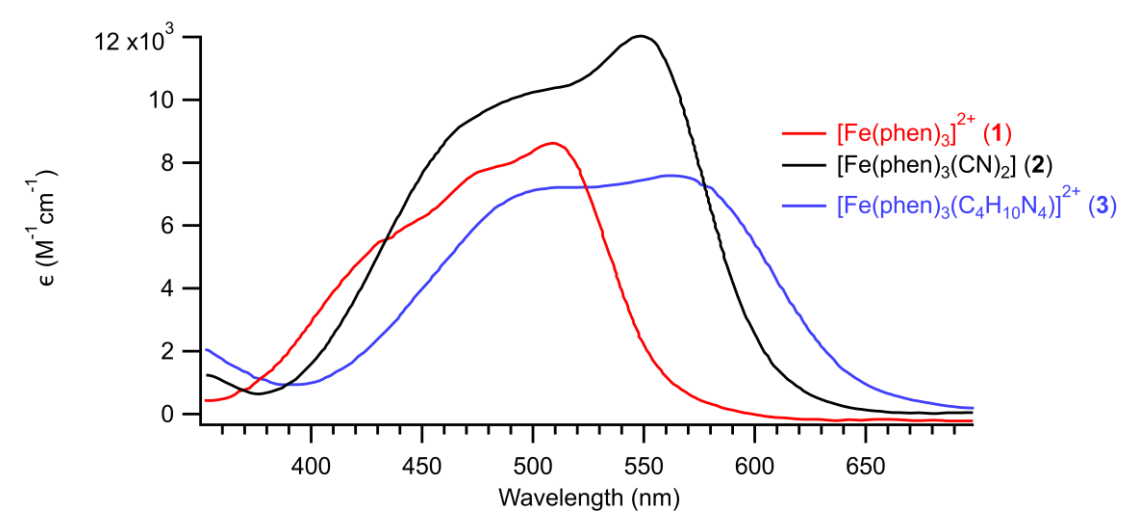


**Figure 5.4.** Ground state absorption spectra of  $[Fe(phen)_3](BF_4)_2$  (1),  $[Fe(phen)_2(CN)_2]$  (2), and  $[Fe(phen)_2(C_4H_{10}N_4)](PF_6)_2$  (3), collected by Karl Nielsen of the McCusker group.

feature in conjunction with the increasing ligand field strengths of compounds 2 and 3 suggest a decreasing energy gap between the MLCT and lowest energy ligand field excited state across the series. In what follows, we will investigate the resulting effect of these changes to the ligand field strength and MLCT energies on the excited state properties.

**Table 5.1.** Electrochemical and spectroscopic parameters of  $[Fe(phen)_3]^{2+}$  (1),  $[Fe(phen)_2(CN)_2]$  (2), and  $[Fe(phen)_2(C_4H_{10}N_4)]$  (3) collected by Karl Nielsen of the McCusker group.

Compound	$\lambda_{\text{max},\text{MLCT}}, nm$	Fe <sup>2+/3+</sup> , V vs. FC <sup>0/+</sup>	Phen <sup>-/0</sup> , V vs. FC <sup>0/+</sup>	Calculated MLCT, nm <sup>a</sup>
1	508	0.648	-1.78 <sup>b</sup>	510
2	550	0.082	$-2.16^{b}$	553
3	567	0.200	-1.92 <sup>b</sup>	584

<sup>&</sup>lt;sup>a</sup> Calculated from the difference in oxidation and reduction potential obtained electrochemically.

### 5.3.2. Exited State Dynamics of 1

Transient absorption data on compound 1 are illustrated in Figure 5.5. By ~500 fs following the initial photoexcitation, we observe that the TA data on 1 do not resemble the predicted MLCT spectrum as calculated using spectroelectrochemical measurements on similar compounds<sup>10</sup> as well as this compound specifically (Figure B1a). Furthermore, the congruence between the TA data and the inverted ground state absorption spectrum suggest that compound 1 is in the  ${}^5T_{2g}$  excited state by 500 fs as is typical for many iron(II) polypyridyl compounds.  ${}^{13-16}$  SVD analysis was performed on compound 1 (Figure 5.5 b and c)

<sup>&</sup>lt;sup>b</sup> Transition was irreversible.

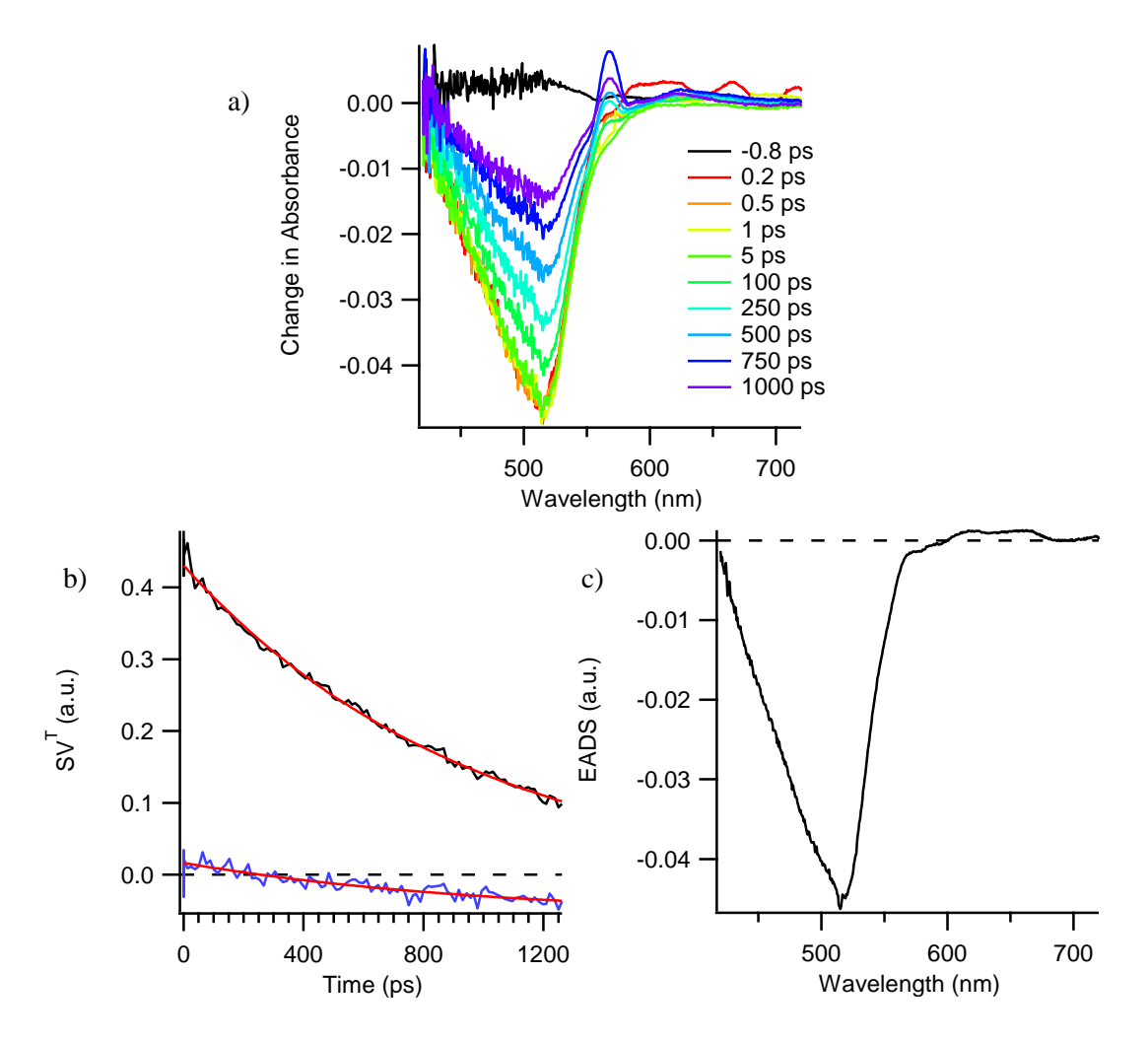


**Figure 5.5.** (a) Full spectrum TA data on [Fe(phen)<sub>3</sub>](BF<sub>4</sub>)<sub>2</sub> (1) in methanol following 570 nm excitation. Irregularities at 570 nm can be attributed to uncorrected pump scatter. (b) First (black) and second (blue) right eigenvectors from SVD of full spectrum dataset with 970 ps single exponential fits (red). (c) EADS for the single kinetic component obtained from SVD analysis.

alongside a global fit of the data (Figure 5.C1) in an effort to assess the spectral changes that occur and their timescales. A 970 ps single exponential fit of the first and second right eigenvectors in the SVD analysis (Figure 5.5b) agree well with the 940 ps single exponential fit from global analysis (Figure 5.C1a). Both procedures also produce similar EADS that resemble the inverse of the ground state absorption spectrum, as would be expected for a  ${}^5T_{2g}$  excited state population, which often have MLCT bands in the visible region of significantly lower oscillator strength than the MLCT transitions from the low-spin state. This kinetic process which results in a return to baseline across the entire spectrum can thus readily be

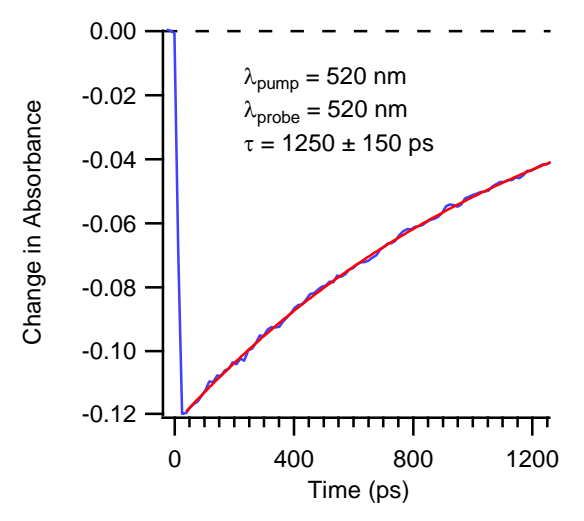


**Figure 5.6.** Single wavelength kinetics traces collected on  $[Fe(phen)_3](BF_4)_2$  (1) in methanol at 520 nm following 520 nm excitation. This particular dataset was fit to a  $1250 \pm 150$  ps time constant with the error bar representative of this single dataset.

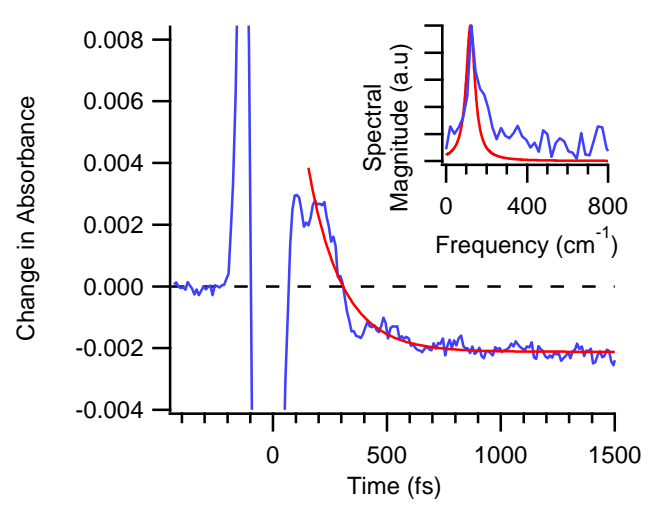


**Figure 5.7.** Single wavelength kinetics trace collected on [Fe(phen)<sub>3</sub>](BF<sub>4</sub>)<sub>2</sub> (1) in methanol at 610 nm following 520 nm excitation. Inset includes a fast Fourier transform of the residuals of an exponential fit to the population dynamics (blue) overlaid with a vibrational spectrum produced via LPSVD of the TA data (red).

assigned to  ${}^5T_{2g} \rightarrow {}^1A_{1g}$  ground state recovery. A more precise single wavelength measurement of this process (Figure 5.6) resulted in a 1,250  $\pm$  150 ps time constant, in good agreement with the full spectrum dataset.

To better quantify the rate of MLCT deactivation in this system, the kinetics were monitored in a region that was predicted by spectroelectrochemical measurements (Figure B1a) and confirmed in the earliest time trace of the full spectrum dataset to show a significant amount of excited state absorption (ESA) of the phenanthroline radical anion of the MLCT state (Figure 5.7). We observe a  $180 \pm 30$  fs decay that can be assigned to the loss of the MLCT excited state population. Interestingly, there appear to be  $115 \pm 5$  cm<sup>-1</sup> coherent oscillations superimposed upon the population dynamics which exhibit probe wavelength dependent dephasing times ranging from  $250 \pm 50$  fs when monitored in the red portion of the spectrum (Figure 5.7) to  $670 \pm 20$  fs when monitored in the center of the bleach feature (Figure D1). Given that similar observations were made on the closely related  $[Fe(bpy)_3]^{2+}$  compound by Chergui<sup>14</sup> and Gaffney<sup>13</sup> we also assign these coherent oscillations as vibrational coherences on the excited electronic state. A more complete discussion of the coherent oscillations can be seen in appendix D.

The results shown here are in good agreement with the work of Tribollet  $et~al.^{16}$  on  $[Fe(phen)_3]^{2+}$  in a different solvent (acetonitrile). The findings therein show an ultrafast deactivation of the MLCT state to the  ${}^5T_{2g}$  lowest energy excited state with a  $220 \pm 40$  fs time constant and subsequent ground state recovery with a  $1.1 \pm 0.1$  ns time constant. These findings indicate that compound 1 behaves as a typical iron(II) polypyridyl complex with an ultrafast MLCT lifetime and a ground state recovery lifetime on the order of a nanosecond.

## 5.3.3. Excited State Dynamics of Compound 2

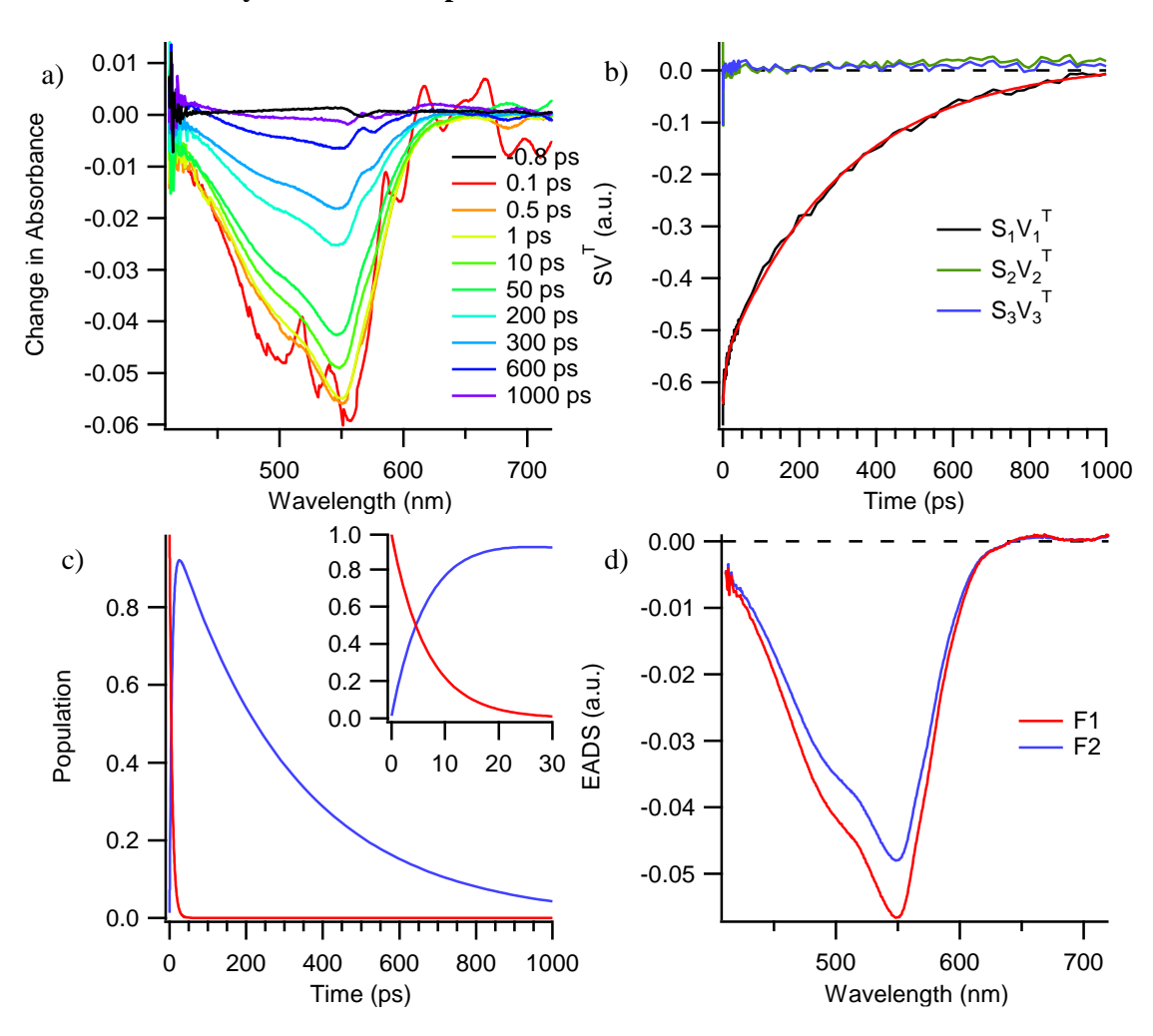


**Figure 5.8.** (a) Full spectrum TA data on [Fe(phen)<sub>2</sub>(CN)<sub>2</sub>] (2) in methanol following 570 nm excitation. (b) First (black), second (green), and third (blue) right eigen vectors from SVD of 2 and a biexponential fit (red) of the first right eigenvector to 6.6 and 315 ps kinetic components. (c) Simulated excited state populations using the time constants acquired from the right eigenvector fits and assuming sequential decay dynamics as shown in equation 5.3. (d) EADS calculated for the two kinetic components using equation 5.2. The red (F1) and blue (F2) spectra correspond to the fast and slowly decaying species respectively.

Full spectrum TA data on compound 2 can be seen in Figure 5.8, in which we observe a slight decrease in the magnitude of the ground state bleach over the first few picoseconds followed by multi-hundred picosecond ground state recovery. SVD analysis shows that the first right eigenvector is by far the most significant in describing the spectral evolution of the system (Figure 5.8b), suggesting that the spectral evolution can largely be described with a single basis spectrum. A fit of this eigenvector to a biexponential decay produces 6.6 ps and 310 ps time constants in good agreement with a global fit of the data to two 5.5 ps and 290 ps kinetic components using OPTIMUS fitting software (Figure 5.C2). Given that the TA data does not match the calculated MLCT spectrum (Figure 5.B.1b) by 500 fs, we can again say that the MLCT state is short lived and decays by this time.

We can next benefit from the increased signal to noise ratio and time resolution of single wavelength measurements to refine the above time constants and determine the lifetime of the short lived MLCT excited state. Single wavelength measurements while monitoring in the bleach region again reveal biphasic kinetics with ground state recovery occurring with a  $355 \pm 7$  ps time constant. The faster kinetic component exhibits a probe wavelength dependent time constant ranging from  $2.6 \pm 0.8$  ps when monitored at the maximum of the bleach (Figure 5.9a) to  $11 \pm 2$  ps when monitored towards the red edge of the bleach at 590 nm (Figure 5.9b). While not an exact match, these time constants are in good agreement with the full

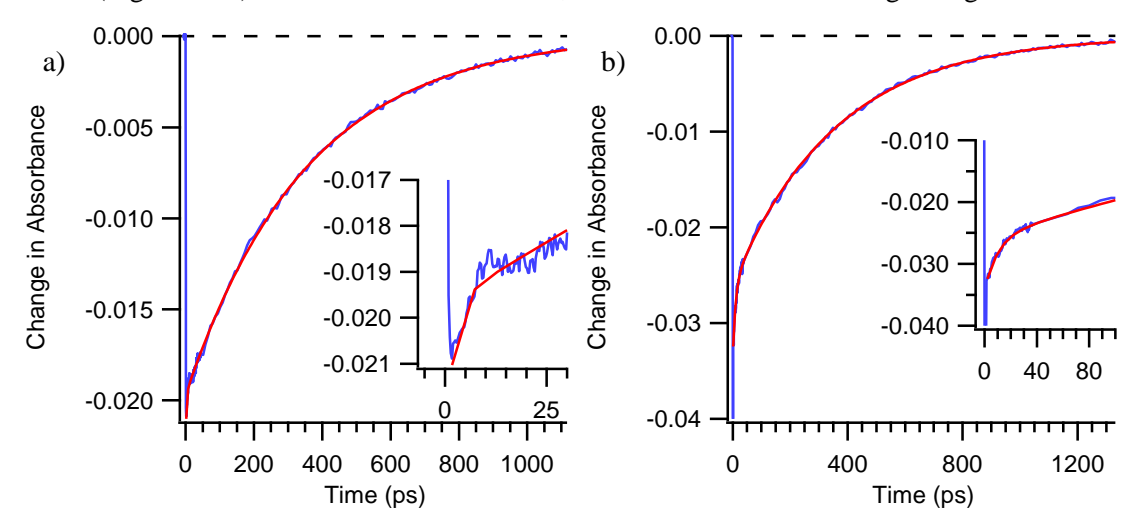


**Figure 5.9.** (a) Representative TA data of [Fe(phen)<sub>2</sub>(CN)<sub>2</sub>] (2) in methanol following 590 nm excitation and monitored at 550 nm in the center of the ground state bleach. (b) Representative TA data on 2 following 600 nm excitation and monitored at 590 nm, the red edge of the ground state bleach. The two data sets show different kinetics at early times.

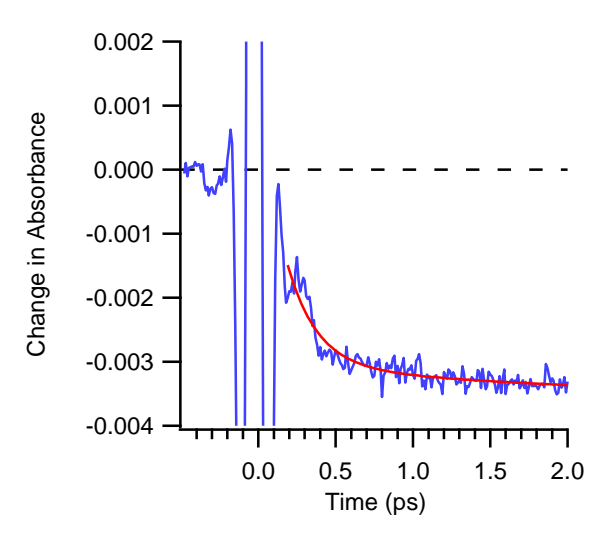


**Figure 5.10.** Single wavelength kinetics trace of [Fe(phen)<sub>2</sub>(CN)<sub>2</sub>] (**2**) monitored at 620 nm following 550 nm excitation. Oscillatory features near the coherent artifact can be attributed to vibrational coherences.

spectrum measurements discussed above. An additional  $250 \pm 90$  fs decay component can be observed at very early times when monitoring at 620 nm (Figure 5.10). By inspection of the simulated MLCT spectrum produced via spectroelectrochemical measurements (Figure 5.B.1b) we see that the absorption feature above 600 nm from the reduced phenanthroline ligand can serve as a convenient optical marker for the MLCT state population, similar to compound 1. We thus assign this rapid  $250 \pm 90$  fs component to decay of the MLCT state.

We next turn to the slowest  $355 \pm 6$  ps kinetic component which must result in the formation of the ground electronic state. We know that the vast majority of low-spin Fe(II) polypyridyl compounds undergo rapid initial decay from the initially populated MLCT state to the  ${}^5T_{2g}$  metal centered excited state and subsequently undergo  ${}^5T_{2g} \rightarrow {}^1A_{1g}$  ISC to recover the ground electronic state with time constants on the order of nanoseconds. According to the energy gap law for strongly coupled systems (i.e. displaced potential surfaces), we would predict that the rate of the nonradiative transition between the strongly displaced  ${}^5T_{2g}$  excited state and the  ${}^1A_{1g}$  ground state will increase as the energy gap between these two states and, by extension, the ligand field strength of the molecule increases. Thus, considering the increased ligand field strength of the cyanide ligands of compound 2 relative to the phenanthroline ligand of compound 1, a faster rate for ground state recovery from the  ${}^5T_{2g}$  state would be entirely consistent with

our observations. Furthermore, recent variable temperature ultrafast TA measurements have shown that the barrierless rate for  ${}^5T_{2g} \rightarrow {}^1A_{1g}$  ISC in several tris bidentate iron(II) polypyridyl compounds is ~230 ps.  ${}^{20}$  Given that the rate for ground state recovery of compound 2 is between the 1250 ps time constant of 1 and the ~230 ps barrierless time constants determined for several other tris-bidentate iron(II) polypyridyl analogues as predicted by Jortner and Marcus theory, we assign the 355 ps process of compound 2 as the  $\Delta S = 2$ ,  ${}^5T_{2g} \rightarrow {}^1A_{1g}$ . We can further eliminate the alternative  $\Delta S = 1$ ,  ${}^3T_{1,2g} \rightarrow {}^1A_{1g}$  assignment as the change in  $\Delta S$  would be expected to lead to an even more dramatic rate increase for ground state recovery relative to compound 1. Thus far, iron(II) compounds that have been identified to decay via a triplet metal centered (MC) state, do so with time constants on the order of ~10 ps,  ${}^{6,21}$  much faster than is observed for compound 2 in this study.

Finally, we consider the remaining 2.6 ps kinetic component. Given our previously discussed assignments of  $250 \pm 90$  fs MLCT  $\rightarrow$  MC as well as 355 ps  ${}^{5}T_{2g} \rightarrow {}^{1}A_{1g}$  ISC, we can narrow the possible kinetic assignments to a change in electronic state (i.e.  ${}^{3}T_{1.2g} \rightarrow {}^{5}T_{2g}$ ) or vibrational relaxation within the  ${}^{5}T_{2g}$  excited state. We first address the possibility of a change in electronic state by consulting the full spectrum TA data and DADS in Figure 5.C2b. Considering the  $(t_{2g})^{5}(e_{g}*)$  and  $(t_{2g})^{4}(e_{g}*)^{2}$  electron configurations of the  ${}^{3}T_{1.2g}$  and  ${}^{5}T_{2g}$  states respectively, we would expect a significant increase in the metal ligand bond length during a  ${}^{3}T_{1.2g} \rightarrow {}^{5}T_{2g}$  electronic transition. This increase in the metal ligand bond length should lead to a significant decrease in the mixing between the  $t_{2g}$  and ligand  $\pi$  symmetry orbitals and hence a reduction of the oscillator strength for a high intensity charge transfer type transition. The rising feature observed for compound 2 does not match this prediction and suggests that the 2.6 ps is not due to a change in electronic state. Alternatively, vibrational relaxation commonly occurs at this timescale and a vibrationally relaxed  ${}^{5}T_{2g}$  state population may be expected to exhibit increased oscillator strength for a MLCT type transition for similar reasons as stated above. We thus assign the 2.6 ps process to vibrational relaxation on the  ${}^{5}T_{2g}$  state. Each of these assignments also agree well with what has been observed for the closely related [Fe(byp)<sub>2</sub>(CN)<sub>2</sub>] complex by Gaffney and coworkers.<sup>22</sup>

With a kinetic model in hand, we can now further analyze the full spectrum TA data presented in Figure 5.8. By application of the kinetic model described above, we can create a population matrix describing the excited state populations as a function of time, which, when applied to the full spectrum TA data, will allow us to extract out the basis spectra or EADS for each chemical species. We note, however, that since the ultrafast MLCT deactivation was too fast to be observed in the full spectrum dataset we must omit that kinetic component from the analysis. The kinetics can thus be described according to the set of differential equations in equation 5.3 which describe the sequential decay of the hot and cool  ${}^5T_{2g}$  state populations.

$$\frac{d\left[{}^{5}T_{2g}^{hot}\right]}{dt} = -k_{VR}\left[{}^{5}T_{2g}^{hot}\right]$$
 5.3a

$$\frac{d\left[{}^{5}T_{2g}^{cool}\right]}{dt} = k_{VR}\left[{}^{5}T_{2g}^{hot}\right] - k_{GSR}\left[{}^{5}T_{2g}^{cool}\right]$$
5.3b

It should be noted that due to the disparate timescales of vibrational relaxation and ground state recovery in this system that a parallel decay pathway would yield similar results. The solutions to these differential equations are plotted in Figure 5.8c where the rapidly decaying red trace represents the population of the vibrationally excited  ${}^5T_{2g}$  state and the blue trace represents the vibrationally cool  ${}^5T_{2g}$  population that eventually converts to the ground state. Using these concentrations and the TA data, the basis spectra were calculated as outlined in equation 5.2. The resulting basis spectra for the hot and cold  ${}^5T_{2g}$  populations are shown as the F1 (red) and F2 (blue) spectra in Figure 5.8d.

## **5.3.4.** Excited State Dynamics of Compound 3

Full spectrum TA data on compound 3 are illustrated in Figure 5.11. Initial inspection of Figure 5.11a shows markedly different features from compounds 1 and 2, most notably, significant excited state absorption above 620 nm as well as decay of most of the transient signal by 20 ps. Fits of the first two right eigenvectors from SVD analysis (Figure 5.11b) show three kinetic components at 0.15 ps, 1.2 ps, and 5.3 ps, in qualitative agreement to the global fit shown in Figure 5.C3. The TA data clearly show a decay to less positive  $\Delta A$  in the red-most portion of the spectrum with a concomitant rise in the bleach region and

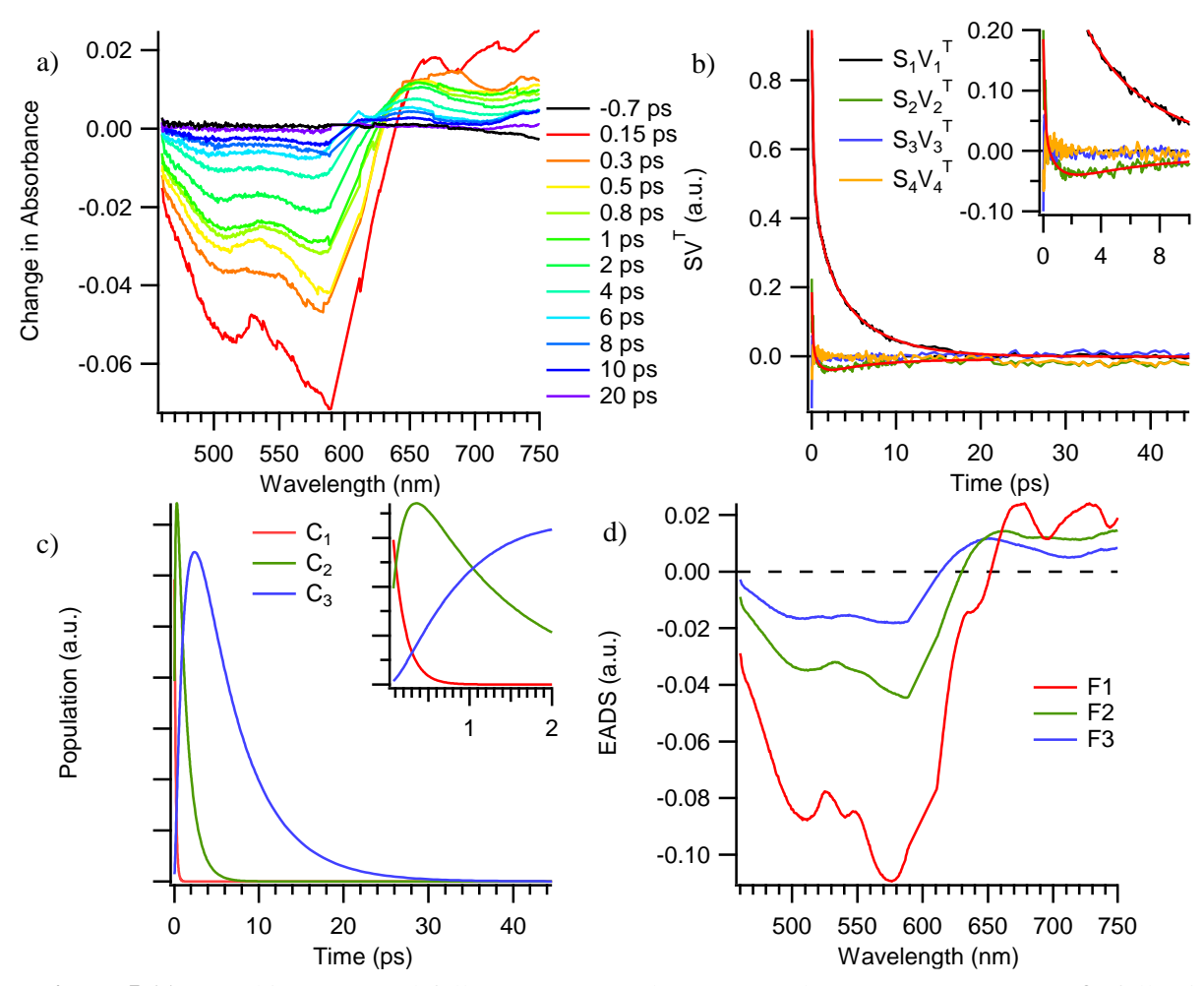


**Figure 5.11.** (a) Chirp corrected full spectrum TA data on  $[Fe(phen)_2(C_4H_{10}N_4)](PF_6)_2$  (3) following 600 nm excitation in methanol. The region between 590 and 610 nm has been removed and interpolated to remove the contribution from excess pump scatter. (b) First four right eigenvectors from SVD of TA data of compound 3 with triexponential fits (red) to 0.15, 1.2, and 5.3 ps time constants. An inset is included to highlight the dynamics over the first 10 ps. (c) Simulated excited state populations using the time constants acquired from the right eigenvector fits and assuming sequential decay dynamics as shown in equation 5.4. (d) EADS calculated from the time constants measured from SVD analysis assuming sequential decay dynamics.

a blueshifting of the intercept with the x-axis around 650 nm during the initial rapid process. The intermediate process then results in similar features but with lower amplitude changes. Finally, the slowest kinetic component results in a return of the signal to baseline and ground state recovery of 3. These observations are also reflected in the EADS resulting from the global fit shown in Figure 5.C3c (which assume sequential decay dynamics). It is interesting to note that the transient spectrum resembles the calculated MLCT spectrum from spectroelectrochemical measurements (Figure 5.B.1c) at all delay times.

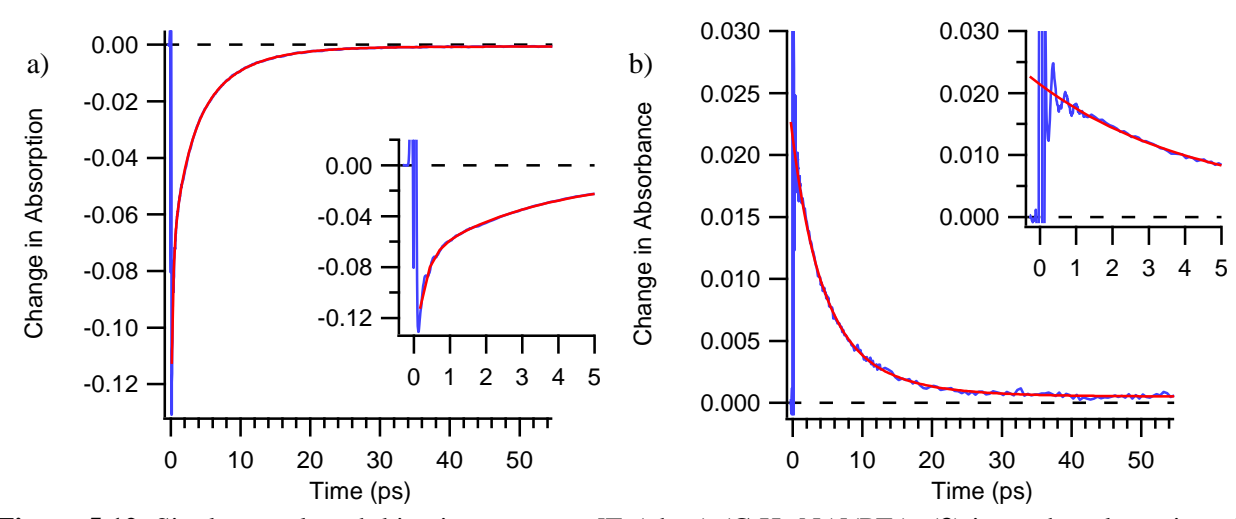


**Figure 5.12.** Single wavelength kinetics traces on  $[Fe(phen)_2(C_4H_{10}N_4)](PF_6)_2$  (3) in methanol monitored at (a) 650 nm abd (b) 550 nm following 600 nm excitation. Insets show first 5 ps and highlight observed coherent oscillations.

To obtain more accurate time constants, single wavelength measurements were also conducted (Figure 5.12) while monitoring the ESA feature at 650 nm and ground state bleach at 550 nm. These data reveal triexponential decay with  $260 \pm 40$  fs,  $3.4 \pm 1.2$  ps, and  $7.4 \pm 0.9$  ps kinetic components in relatively good agreement with the SVD results.

As mentioned above, the changes to the TA spectrum during the initial ultrafast process can be described as a decay in the magnitude of the signal with a slight blue shifting of the ESA feature above 600 nm. Interestingly, several photophysical studies on low-spin six-coordinate iron(II) carbene compounds exhibit kinetic components with time constants on the same order of magnitude. These have been assigned to several different processes from ¹MLCT → ³MLCT ISC,²¹¹ to localization of the MLCT excited state.²³ It is tempting to add solvent reorganization to the list of plausible possibilities as well. Given the presence of substantial ESA above 600 nm following this initial fast process and the agreement between the intermediate and late time transient spectra (or EADS1 and 2 from Figure 5.C3c) with the spectroelectrochemically approximated MLCT spectrum (Figure 5.B.1c), we can say that this initial rapid process does not represent MLCT deactivation, thus marking a substantial change in the excited state dynamics relative to compounds 1 and 2 which behave largely as typical low-spin iron(II) polypyridyl complexes. It is more difficult to discern between the other possible assignments for this process.

Considering that  ${}^{1}\text{MLCT} \rightarrow {}^{3}\text{MLCT}$  ISC often occurs on the order of ~30 fs in divalent transition metal polypyridyl compounds  ${}^{24,25}$  and that the ISC processes that have been assigned for carbene complexes have also been sub-100 fs, we cautiously rule out ISC as a possible origin for the  $260 \pm 40$  fs kinetic component. The remaining excited state localization and solvent librational motion options both seem viable. The large redistribution of charge upon formation of the MLCT excited state would be expected to induce significant reorganization of the solvent which occurs at similar rates.  ${}^{26,27}$  However, without further evidence, we are presently unable to definitively assign either of these two possible assignments and suggest both as plausible possibilities.

The intermediate 3.4 ps kinetic component is a bit more straightforward to assign. Inspection of the TA data in Figures 5.11a and 5.12 as well as the DADS in Figure 5.C3b show that this kinetic component is responsible for a slight rise to less negative ΔA in the region of the ground state bleach, with smaller amplitude decay in the ESA region above 600 nm. Considering that the transient spectrum resembles the predicted MLCT spectrum even at large pump-probe delay times, we find it unlikely that this process involves loss of an MLCT excited state. Alternatively, vibrational relaxation, which often occurs at similar timescales in analogous iron-carbene complexes, 5.23 seems more reasonable. In fact, many of the iron carbene compounds for which similar timescale vibrational relaxation occur in the MLCT excited state show similar spectral distortions. We thus also assign this 3.4 ps kinetic component to vibrational relaxation on an MLCT excited state.

Finally, the third,  $7.4 \pm 0.9$  ps kinetic component is responsible for the return of the transient signal to baseline and, by extension, the deactivation of the MLCT excited state and recovery of the ground electronic state. This represents a >25-fold increase in the MLCT lifetime relative to compounds 1 and 2, simply by swapping out a single phenanthroline ligand with an acyclic dicarbene. It is interesting to note the lack of a long lived ground state bleach as is typical of many iron(II) polypyridyl compounds including 1 and 2 which decay to the ground state via the  ${}^5T_{2g}$  excited state on timescales on the order of several hundreds of picoseconds to nanoseconds. We consider it unlikely that compound 3 undergoes 7.4 ps  ${}^5T_{2g}$  ISC followed by subsequent  ${}^5T_{2g} \rightarrow {}^1A_{1g}$  ISC on a significantly shorter timescale.

Furthermore, it seems improbable that a direct MLCT  $\rightarrow$   $^{1}A_{1g}$  ISC occurs on such a short timescale as well, considering many isoelectronic ruthenium(II) polypyridyl compounds require many nanoseconds to microseconds to depopulate their MLCT excited states and often proceed via an intermediate triplet metal centered (MC) excited state. It seems more likely that the ground state in this system is also recovered via an intermediate MC excited state. This leaves a  $^{3}MC$  excited state as the only remaining alternative. Thus, since the excited state absorption and bleach decay with the same time constant, we propose a 7.4 ps MLCT  $\rightarrow$   $^{3}MC$  conversion followed by a faster, undetected  $^{3}MC \rightarrow$   $^{1}A_{1g}$  ISC to recover the ground electronic state.

We next apply our kinetic model to the full spectrum TA data in a manner similar to what was done for compound 2. According to the above discussion, we have that compound 3 has an initial rapid localization of the excited state or solvent inertial response followed by loss of a vibrationally excited MLCT population largely due to vibrational relaxation, and finally loss of the vibrationally cool MLCT state. The excited state populations can thus be described by the set of differential equations shown in equation 5.4.

$$\frac{d\left[MLCT_{a}\right]}{dt} = -k_{1}\left[MLCT_{a}\right]$$
5.4a

$$\frac{d\left[MLCT_{b}^{hot}\right]}{dt} = k_{1}\left[MLCT_{a}\right] - k_{2}\left[MLCT_{b}^{hot}\right]$$
5.4b

$$\frac{d\left[MLCT_{b}^{cool}\right]}{dt} = k_{2}\left[MLCT_{b}^{hot}\right] - k_{3}\left[MLCT_{b}^{cool}\right]$$
5.4c

We note two important points. First, since the <sup>3</sup>MC intermediate decayed faster than it was populated and because it was not observed in the full spectrum data, then we do not need to include it in the model presented in equation 5.4. Second, we model the dynamics as sequential here, i.e. that every molecule must undergo each decay process and cannot bypass them. For example, a molecule must vibrationally relax prior to conversion to a <sup>3</sup>MC state in the above model. An alternative parallel decay kinetic model can be made with minor changes, however due to the significantly different timescales for each process, the results are largely identical. The solution set to equation 5.4 is plotted in Figure 5.11c with the basis spectrum for

each chemical species presented in Figure 5.11d. The resulting basis spectra clearly show the excited state evolution and unequivocally show that the last observed transient species is an MLCT excited state.

## **5.4.** Concluding Thoughts

**Table 5.2.** Summary of the kinetic components of  $[Fe(phen)_3](BF_4)_2$  (1),  $[Fe(phen)_2(CN)_2]$  (2), and  $[Fe(phen)_2(C_4H_{10}N_4)](PF_6)_2$  (3) in methanol solution.

Compound	$\tau_{Undefined}$ , fs	$\tau_{vib}$ , ps	$\tau_{MLCT}$ , fs	$\tau_{5T2g}$ , ps
1			$180 \pm 30$	1250 <sup>a</sup>
2		$2.6 \pm 0.8$	$250 \pm 90$	$355 \pm 7$
3	$260 \pm 40$	$3.4 \pm 1.2$	$7400 \pm 900$	

<sup>&</sup>lt;sup>a</sup> Value was the result of a single measurement and does not have an error bar

The photophysical properties of a series of low-spin six-coordinate iron(II) polypyridyl complexes have been investigated. By swapping out a single phenanthroline ligand with the stronger field cyanide or dicarbene ligands the photophysical properties have been dramatically altered as summarized in Table 5.2. For the intermediate ligand field strength of compound 2, it was shown that the overall decay pathway was similar to the control molecule, compound 1, however the rate of ground state recovery has been increased by more than a factor of two. The even greater ligand field strength of compound 3 was illustrated to not only exhibit a > 25-fold increase in the MLCT lifetime relative to compounds 1 and 2, but also to undergo a fundamentally different excited state decay pathway. This work illustrates a modular approach to tunning the photophysical properties of iron(II) polypyridyl complexes that not only is capable of demonstrating long enough MLCT lifetimes to be viable for electron transfer reactions, but also to allow for additional synthetic modifications of the polypyridyl ligand to tune, MLCT energetics, electron localization, and ability to bind to a semiconductor for interfacial electron transfer.

## **APPENDICES**

### Appendix 5.A. Singular Value Decomposition MATLAB Script for Full Spectrum TA Analysis

```
%This matlab script was written by Bryan Paulus of the McCusker group at
% Michigan State University.
clear all clc
[filename, pathname]=uigetfile;
s=strcat(pathname, filename);
FullSpecData=xlsread(s);
cut=50;% number of time points to cut********
r=3;%number of singular vectors to keep for reconstruction of Data Matrix
% Grabs Full spectrum data as an excell file where the first column is the
% wavelength wave (with a zero place holder in the 1,1 position), the top row is
% the time trace (again, with a zero place holder in the 1,1 position)
% and TA data everywhere else (ie starting at cell 2,2).
t=FullSpecData(1,:);
t=t(2:length(t));%time array
%Grabs the first row from the uploaded excel file and makes into an
% array called "t" then removed the first element of the array so that only
%time poins are present
w=FullSpecData(:,1);
w=w(2:length(w));
wt=w';%transpose of wavelength vector
% Grabs the first column of the uploaded excel file and makes it into a
% wavelength array similar to how the time array was made above
A=FullSpecData;
A(1,:)=[];
A(:,1)=[]; %Creates a matrix of the delta A data points
A(A==\inf) = 0; % turns any infinite values to 0
A(isnan(A)) = 0; % turns any NAN values to 0
% Next we remove any data corresponding to time points we don't wish to
if cut==0
  tcut=t;
  Acut=A;
else
  tcut=t(cut:length(t));
Acut=A(:,cut:end);
end
[U S V] = svd(Acut); \%perfoms SVD
A svd = U*S*V'; %recombines the decomposed vectors
figure(1)
surf(tcut,w,Acut,'EdgeColor','none');
title('Data')
xlabel('Time (ps)')
ylabel('Wavelength (nm)')
zlabel('Change in Absorbance')
```

```
figure(2)
plot(tcut,-V(:,1),tcut,V(:,2),tcut,-V(:,3),tcut,V(:,4),tcut,-V(:,5))
title('Vectors of Data Weight Matrix')
xlabel('Time (ps)')
ylabel('Data Weight')
legend('v1','v2','v3','v4','v5')
refline(0,0)% Adds zero line
figure(3)
plot(w,-U(:,1),w,U(:,2),w,U(:,3),w,U(:,4),w,-U(:,5))
title('Basis Spectra')
xlabel('Wavelength (nm)')
ylabel('Change in Absorbance (a.u.)')
legend('u1','u2','u3','u4','u5')
refline(0,0)% Adds a zero line
N=[1:1:length(tcut)];
figure(4)
scatter(N,diag(S))
title('Scree Plot')
xlabel('Component Number')
ylabel('Significance')
xlim([0 10])
hold
plot(N,diag(S))
hold off
figure(5)
scatter(N,log(diag(S)))
title('Scree Plot')
xlabel('Component Number')
ylabel('log(Significance)')
xlim([0 10])
hold
plot(N,log(diag(S)))
hold off
% If you want to reconstruct the data from a certain number of the most
% significant components then use the following where "r" represents the
% number of significant components. Replace "r" with a number. "r" can be
% found at the begining of this script.
Arec = U(:,1:r)*S(1:r,1:r)*V(:,1:r)'; %reconstruction of data set from significant vectors
Usmall=U(:,1:r);
Ssmall=S(1:r,1:r);
Vsmall=V(:,1:r);
figure(6)
surf(tcut,w,Arec,'EdgeColor','none');
title('Reconstructed Data')
xlabel('Time (ps)')
ylabel('Wavelength (nm)')
```

```
zlabel('Change in Absorbance')
Ares=zeros(size(Acut));
Ares=Acut-Arec;%Residual of Data matrix and reconstructed data matrix
figure(7)
surf(tcut,w,Ares,'Edgecolor','none');
title('Residual')
xlabel('Time (ps)')
ylabel('Wavelength (nm)')
zlabel('Change in Absorbance')
figure(8)
plot(tcut,Ares(150,:))
title('Residual At Single Wavelength')
xlabel('Time (ps)')
ylabel('Residual')
%Change the number in the above parentheses to plot the data at a different
% wavelength pixel.
figure(9)
plot(w,Ares(:,10))
xlabel('Wavelength (nm)')
ylabel('Residual')
title('Residual At a Single Time')
% Change the number in the above parentheses to plot the data at a different
%time step.
SVT=S*transpose(V); %Right singular vectors weighted by singular values.
%The rows of SVT correspond to
figure(10)
plot(tcut,SVT(1,:),tcut,SVT(2,:))
xlabel('Time (ps)')
ylabel('SV^T')
```

# Appendix 5.B. Simulated MLCT Spectra

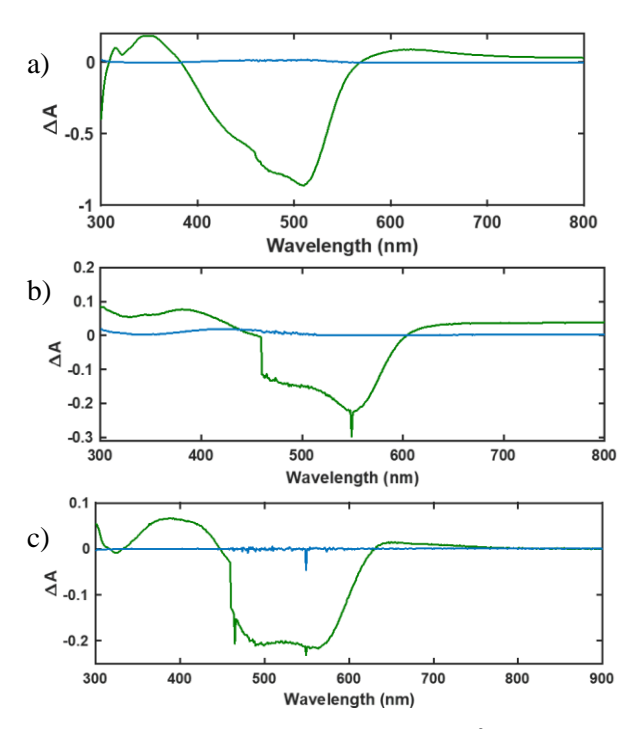


**Figure 5.B.1.** Simulated MLCT spectrum of (a)  $[Fe(phen)_3]^{2+}$  (1), (b)  $[Fe(phen)_2(CN)_2]$  (2), and (c)  $[Fe(phen)_2(C_4H_{10}N_4)]^{2+}$  (3) in methanol, predicted by summing the oxidative and reductive spectra.

## Appendix 5.C. Global Fits of Full Spectrum TA Data

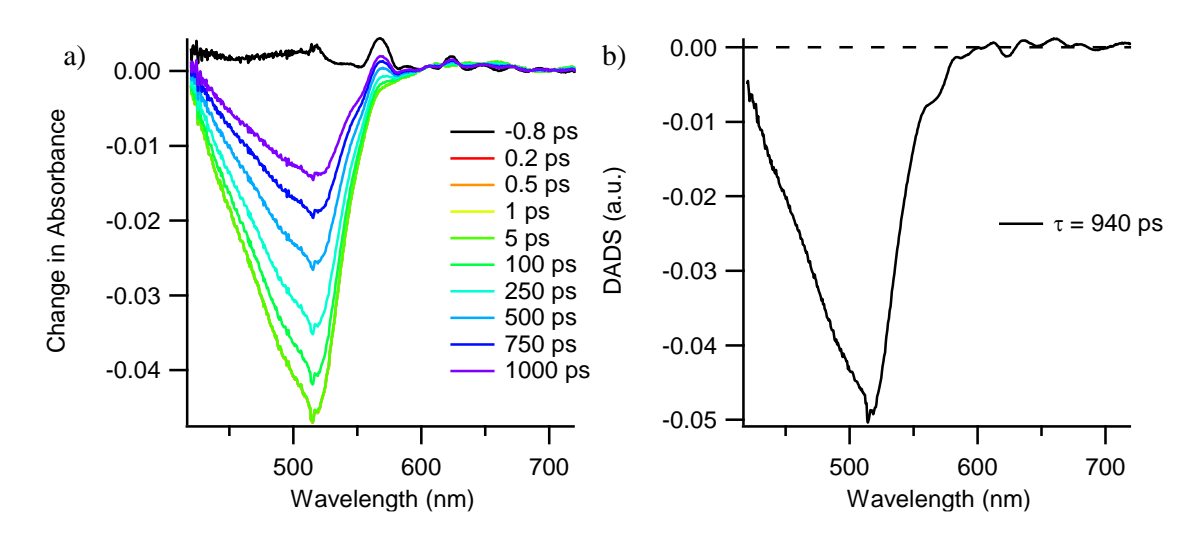


**Figure 5.C.1.** (a) Chirp corrected global fit using OPTIMUS fitting software on full spectrum data of  $[Fe(phen)_3]^{2+}$  (1) to a single 940 ps exponential kinetic component. (b) DADS from global fit of 1 full spectrum data. Since there was only a single kinetic component, the DADS is equivalent to the EADS.

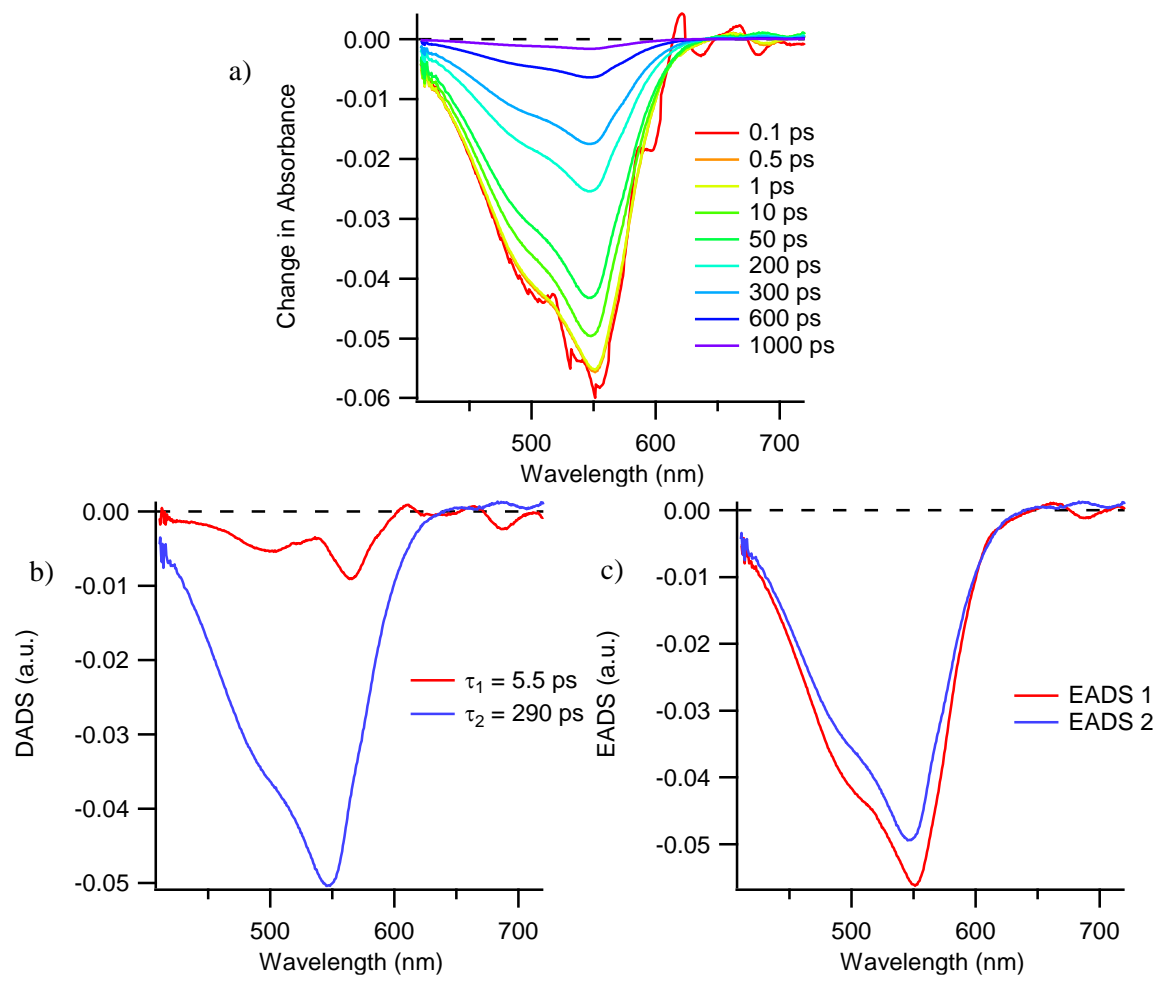


**Figure 5.C.2.** (a) Chirp corrected global fit using OPTIMUS fitting software on full spectrum data of [Fe(phen)<sub>2</sub>(CN)<sub>2</sub>] (2) to two 5.5 ps and 290 ps exponential kinetic components. (b) DADS from the global fit. (c) EADS from the global fit assuming sequential decay dynamics.

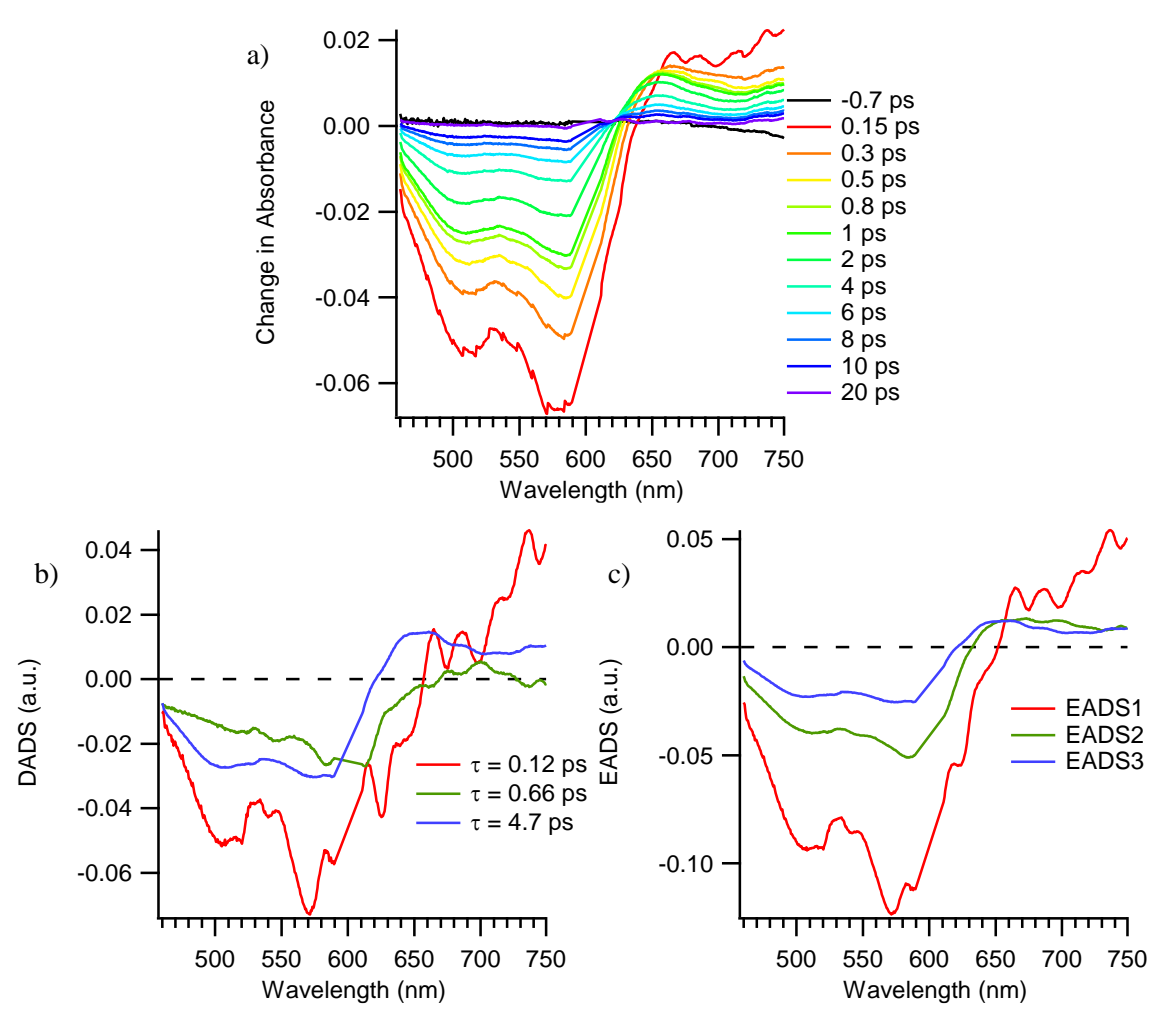


**Figure 5.C.3.** (a) Chirp corrected global fit using OPTIMUS fitting software on full spectrum data of  $[Fe(phen)_2(C_4H_{10}N_4)](PF_6)_2$  (3) to three 0.12, 0.66, and 4.7 ps exponential kinetic components. (b) DADS from the global fit. (c) EADS from the global fit assuming sequential decay dynamics.

## Appendix 5.D. Additional TA Data with Coherent Oscillations

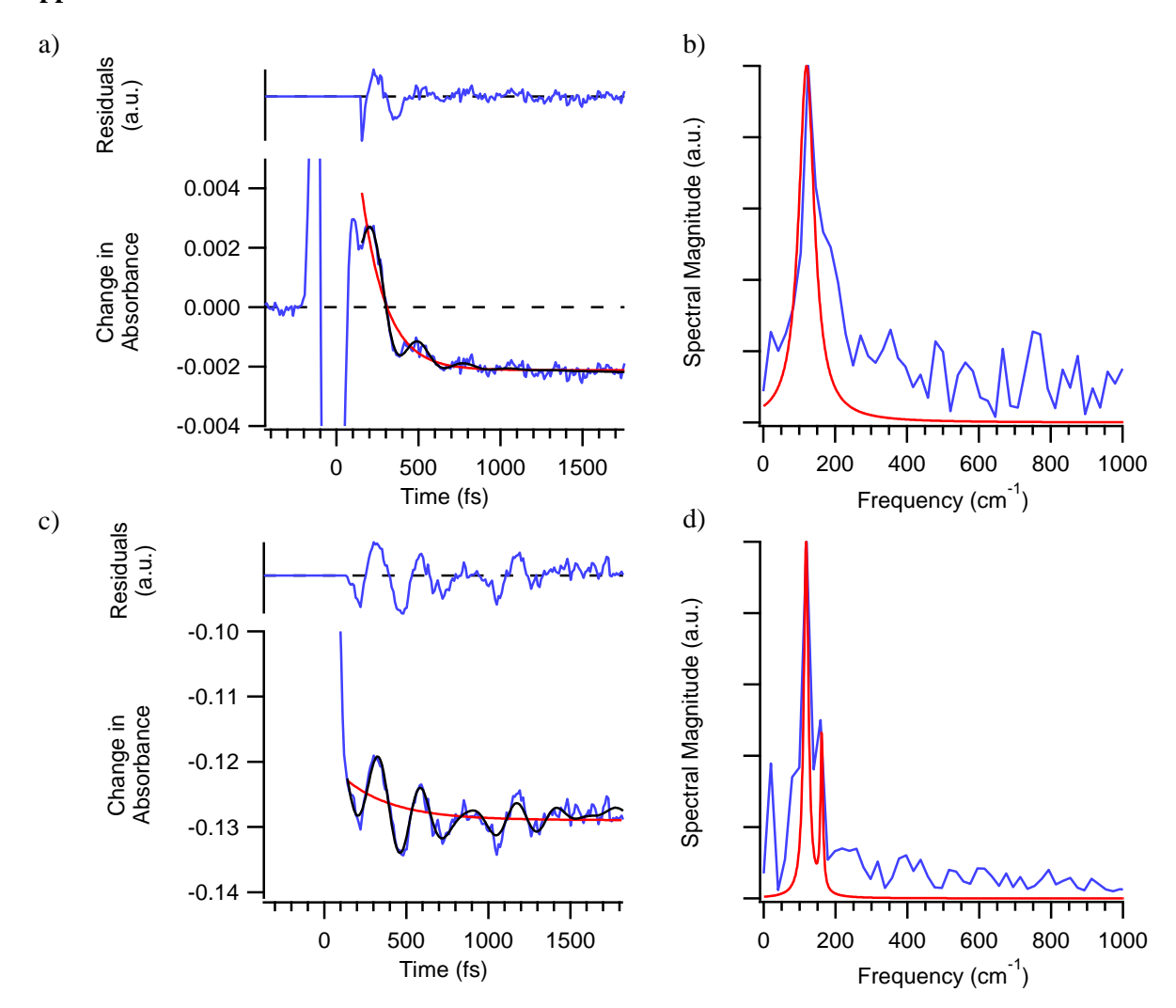


**Figure 5.D.1.** (a) Early time TA data (blue) on [Fe(phen)<sub>3</sub>](BF<sub>4</sub>)<sub>2</sub> (1) in methanol monitored at 610 nm following 520 nm excitation. An exponential fit (red) and a LPSVD fit (black) are superimposed on the data. (b) FFT of the residual of the exponential fit of the 610 nm TA data (blue) and LPSVD vibrational spectrum (red). (c) Early time TA data (blue) of compound (1) monitored in the bleach region at 520 nm with exponential (red) and LPSVD (black) fits. (d) Corresponding FFT (blue) and LPSVD vibrational spectra.

Several of the compounds investigated in this study exhibited coherent oscillations in the transient absorption data. Example datasets illustrating the coherent oscillations of compound 1 can be seen in Figure 5.D1 in which both FFT and LPSVD analyses are displayed side by side. A summary of the frequencies and dephasing times observed for 1 for two different probe wavelength regions can be seen in Table B1. Interestingly, a probe wavelength dependence was observed in the dephasing times of these

coherently active vibrational modes. Analogous results on a related compound,  $[Fe(bpy)_3]^{2+}$ , collected by Chergui and coworkers<sup>14</sup> had shown similar vibrational frequencies (127 cm<sup>-1</sup> and 157 cm<sup>-1</sup>) assigned as vibrational coherences in the  ${}^5T_{2g}$  excited state and also exhibited probe wavelength dependent dephasing times with the dephasing times observed in the red-most portion of the measured spectrum exhibiting the shortest dephasing times. These observations were rationalized in terms of a hot  ${}^5T_{2g}$  state population with an initially small  ${}^5T_{2g} \rightarrow {}^5MLCT$  energy gap rapidly falling out of resonance as the wave packet moved away from its initial position. Given the photophysical and structural similarities between compound 1 and  $[Fe(bpy)_3]^{2+}$  it is likely that the origins of the coherences and their dephasing times are similar in both complexes.

**Table 5.D.1.** Summary of coherent oscillations of  $[Fe(phen)_3](BF_4)_2$  (1) observed in TA experiments in methanol following 520 nm excitation. Experiments were conducted similarly in both wavelength regions, except that in the 610-630 nm region, several separate experiments were conducted individually at 610, 620, and 630 nm and the results of the LPSVD fits from each of these probe wavelengths were averaged together.

Probe Region	Frequency, cm <sup>-1</sup> (Damping Time, fs)		
520 nm	$117 \pm 1 \ (670 \pm 20)$	$156 \pm 7 \ (1300 \pm 100)$	
610 - 630  nm	$115 \pm 5 \ (250 \pm 50)$	_	

Coherent oscillations were also observed in the TA data of compound 3. Coherences were observed in both a spectral region dominated by excited state absorption at 650 nm and at 550 nm, a region exhibiting prominent ground state bleach. Additionally, analogous datasets were collected in methanol (Figure D2) and acetonitrile (Figure 5.D3) to ascertain the influence of the solvation shell on the observed vibrational modes and dephasing times. The results are summarized in Table 5.D2. We see that aside from the additional 225 cm<sup>-1</sup> oscillatory component observed in the methanolic sample, the frequencies and their dephasing times are similar in both solvents, suggesting that the origin for the dephasing process is largely intramolecular. Given that these signals are observed at 650 nm, a region that is dominated by excited state absorption, it is likely that these coherent vibrational modes are generated in the MLCT excited state, as opposed to the ground electronic state which can be produced via impulsively stimulated Raman scattering.

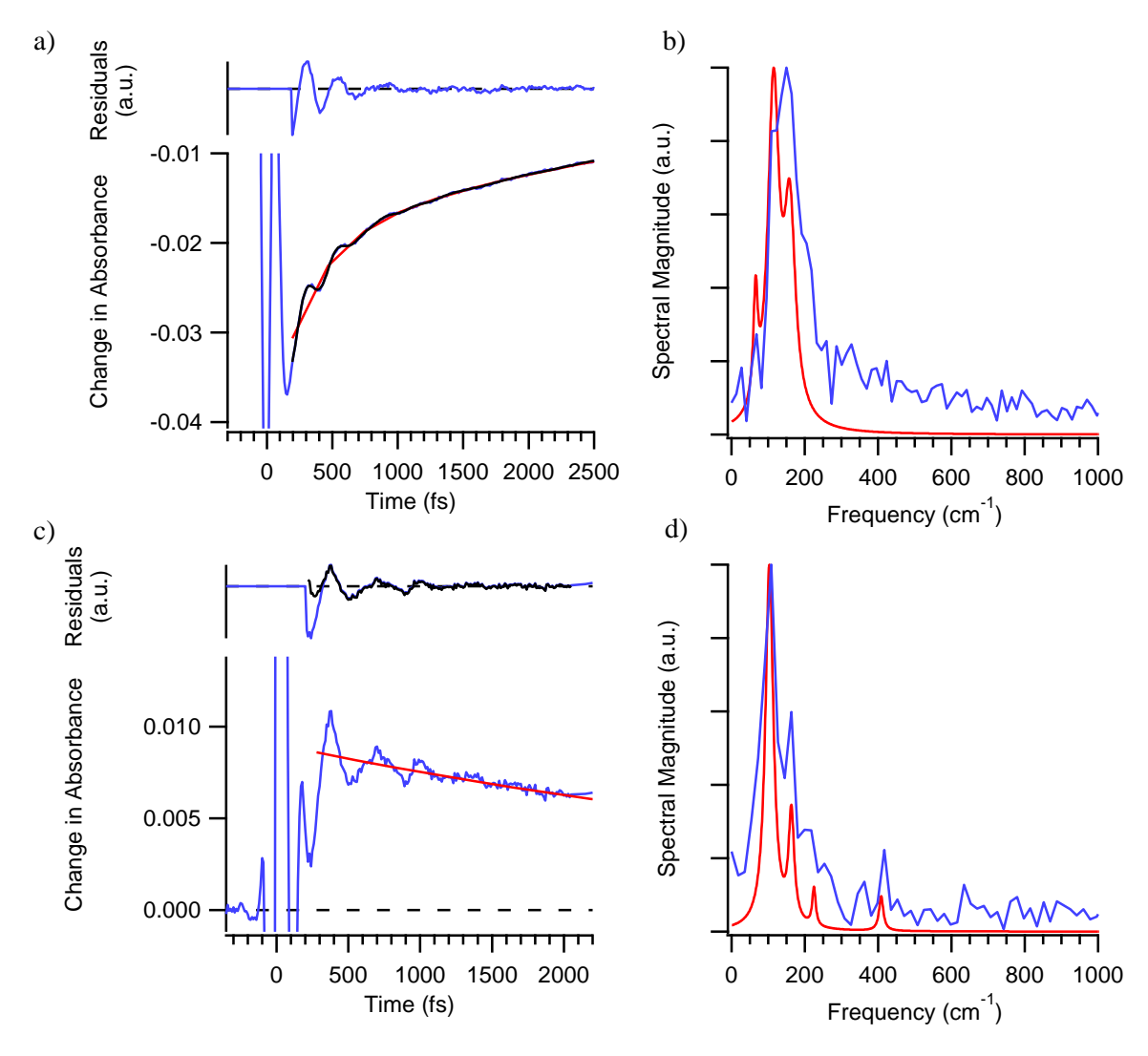


**Figure 5.D.2.** (a) Early time TA data (blue) on  $[Fe(phen)_2(C_4H_{10}N_4)](PF_6)_2$  (3) in methanol monitored at 550 nm following 600 nm excitation. Exponential fit (red) and LPSVD fit (black) are superimposed on the dataset. (b) Corresponding FFT of the residual of the exponential fit (blue) and LPSVD vibrational spectrum (red). (c) Analogous data monitoring at 650 nm and (d) corresponding FFT (blue) and LPSVD (red) vibrational spectra.

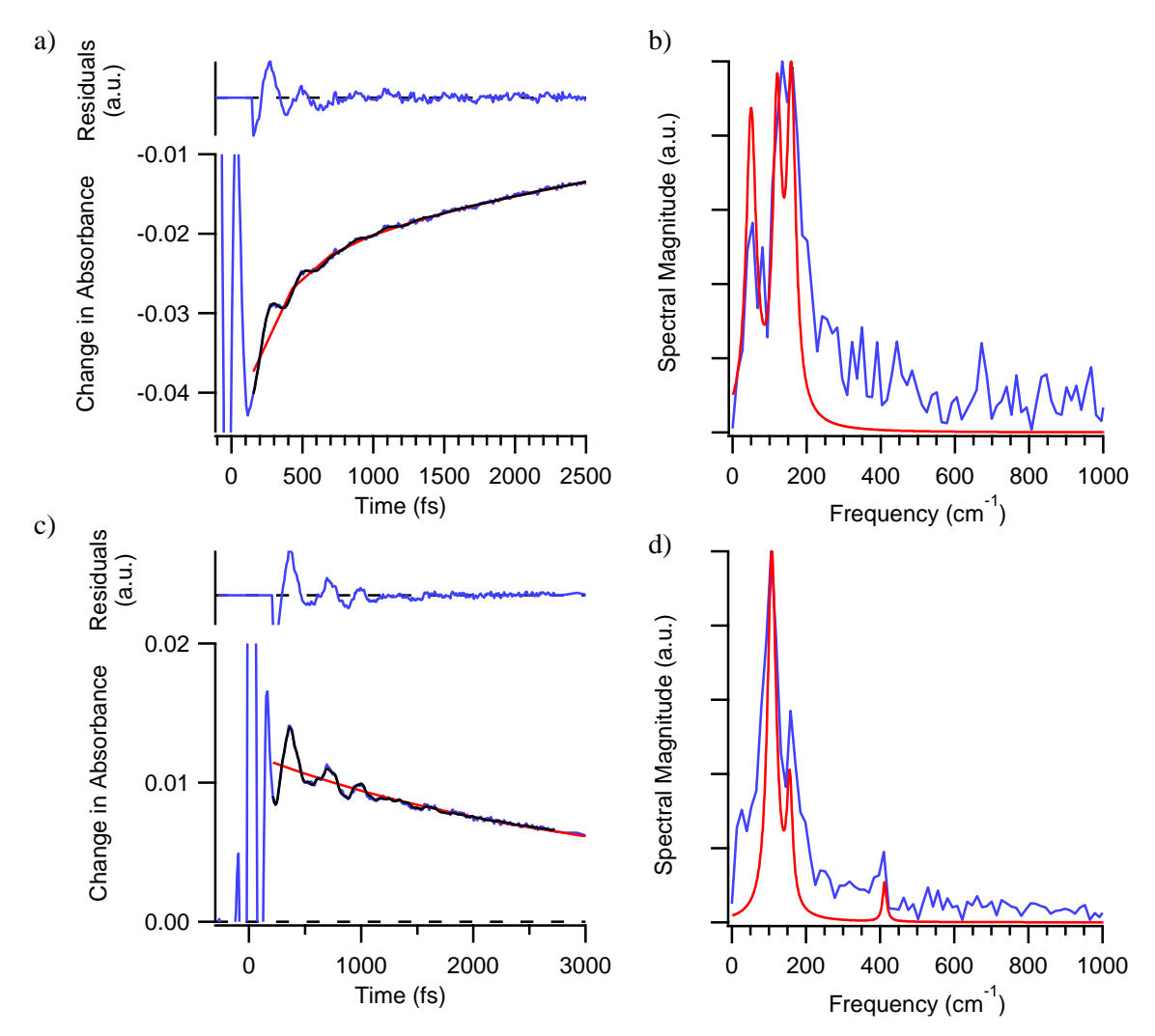


**Figure 5.D.3.** (a) Early time TA data (blue) on  $[Fe(phen)_2(C_4H_{10}N_4)](PF_6)_2$  (3) in acetonitrile monitored at 550 nm following 600 nm excitation. Exponential fit(red) and LPSVD fit (black) are superimposed on the dataset. (b) Corresponding FFT of the residual of the exponential fit (blue) and LPSVD vibrational spectrum (red). (c) Analogous TA data while monitoring at 650 nm and (d) corresponding FFT (blue) and LPSVD (red) vibrational spectra.

**Table 5.D.2.** Summary of the coherent oscillations of  $[Fe(phen)_2(C_4H_{10}N_4)](PF_6)_2$  (3) in methanol and acetonitrile following 600 nm excitation. The presented results are from a single dataset for each probe wavelength and solvent. As such, no error bars in the form of a standard deviation are presented for these values.

Probe λ	Solvent		Frequency	, cm <sup>-1</sup> (Dampin	g Time, fs)	
550 nm	MeOH	66 (730)	115 (280)	159 (290)		
	MeCN	50 (324)	120 (381)	159 (370)		
650 nm	MeOH		103 (400)	163 (570)	225 (940)	408 (760)
	MeCN		108 (370)	156 (560)		412 (850)

**Table 5.D.3.** Summary of the kinetic components of  $[Fe(phen)_2(C_4H_{10}N_4)](PF_6)_2$  (3) in methanol and acetonitrile following 600 nm excitation. Errors are reported as the standard deviation of multiple trials.

Solvent	$\tau_1$ , fs	$\tau_2$ , fs	$\tau_3$ , fs
MeCN	$210 \pm 30$	$2300 \pm 300$	$8900 \pm 600$
MeOH	$260 \pm 40$	$3400 \pm 1200$	$7400 \pm 900$

- (1) Juris, A.; Balzani, V.; Barigelletti, F.; Campagna, S.; Belser, P.; Von Zelewsky, A. Ru(II) Polypyridine Complexes: Photophysics, Photochemistry, Electrochemistry, and Chemiluminescence. *Coord. Chem. Rev.* **1988**, 84, 85–277.
- (2) Hexel, G. B.; Hedrick, J. B.; Orris, G. J. Rare Earth Elements-Critical Resources for High Technology https://pubs.usgs.gov/fs/2002/fs087-02.
- (3) Wenger, O. S. Is Iron the New Ruthenium? *Chem. Eur. J.* **2019**, 25, 6043–6052.
- (4) L., L.; Duchanois, T.; Etienne, T.; Monari, A.; Beley, M.; Assfeld, X.; Haacke, S.; Gros, P. C. A New Record Excited State 3MLCT Lifetime for Metalorganic Iron(II) Complexes. *Phys. Chem. Phys.* **2016**, *18*, 12550–12556.
- (5) Chabera, P.; Kjaer, K. S.; Prakash, O.; Honarfar, A.; Liu, Y.; Fredin, L. A.; Harlang, T. C. B.; Lidin, S.; Uhlig, J.; Sundstro, V.; *et al.* Fe<sup>II</sup> Hexa N Heterocyclic Carbene Complex with a 528 Ps Metalto- Ligand Charge-Transfer Excited-State Lifetime. *J. Phys. Chem. Lett.* **2018**, *9*, 459–463.
- (6) Steube, J.; Burkhardt, L.; Päpcke, A.; Moll, J.; Zimmer, P.; Schoch, R.; Wölper, C.; Heinze, K.; Lockbrunner, S.; Bauer, M. Excited-State Kinetics of an Air-Stable Cyclometalated Iron(II) Complex. *Chem. Eur. J.* **2019**, *25*, 11826–11830.
- (7) Kjær, K. S.; Kaul, N.; Prakash, O.; Chábera, P.; Rosemann, N. W.; Honarfar, A.; Gordivska, O.; Fredin, L. A.; Bergquist, K.-E.; Häggström, L.; *et al.* Luminescence and Reactivity of a Charge-Transfer Excited Iron Complex with Nanosecond Lifetime. *Science* **2019**, *363*, 249–253.
- (8) Doonan, D. J.; Balch, A. L. Carbene Complexes Resulting from the Addition of Various Amines to Isocyanide Complexes of Iron(II) and Ruthenium(II). *Inorg. Chem.* **1974**, *13*, 921–927.
- (9) Schilt, A, A. Mixed Ligand Complexes of Iron(II) and (III) with Cyanide and Aromatic Di-Immines. J. Am. Chem. Soc. **1960**, 82, 3000–3005.
- (10) Brown, A. M.; McCusker, C. E.; McCusker, J. K. Spectroelectrochemical Identification of Charge-Transfer Excited States in Transition Metal-Based Polypyridyl Complexes. *Dalt. Trans.* **2014**, 17635–17646.
- (11) Slavov, C.; Hartmann, C.; Wachtveitl, J. Implementation and Evaluation of Data Analysis Strategies for Time-Resolved Optical Spectroscopy. *Ann. Chem.* **2018**, 87, 2328–2336.
- (12) Henry, E. R.; Hofrichter, J. Singular Value Decomposition: Application to Analysis of Experimental Data. *Meothods Enzym.* **1992**, *210*, 129–192.
- (13) Lemke, H. T.; Kjaer, K. S.; Hartsock, R.; van Driel, T. B.; Chollet, M.; Glownia, J. M.; Song, S.; Zhu, D.; Pace, E.; Matar, S. F.; Nielsen, M. M.; Benfatto, M.; Gaffney, K. J.; Collet, E.; Cammarata, M. Coherent Structural Trapping through Wave Packet Dispersion during Photoinduced Spin State Switching. *Nat. Commun.* **2017**, *8*, 15342.
- (14) Auböck, Gerald; Chergui, M. Sub-50-Fs Photoinduced Spin Crossover in [Fe(bpy)<sub>3</sub>]<sup>2+</sup>. *Nat. Chem.* **2015**, 7, 629–633.

- (15) Monat, J. E.; McCusker, J. K. Femtosecond Excited-State Dynamics of an Iron(II) Polypyridyl Solar Cell Sensitizer Model. *J. Am. Chem. Soc.* **2000**, *122*, 4092–4097.
- (16) Tribollet, J.; Galle, G.; Jonusauskas, G.; Deldicque, D.; Tondusson, M.; Letard, J. F.; Freysz, E. Transient Absorption Spectroscopy of the Iron(II) [Fe(phen)<sub>3</sub>]<sup>2+</sup> Complex: Study of the Non-Radiative Relaxation of an Isolated Iron(II) Complex. *Chem. Phys.* **2011**, *513*, 42–47.
- (17) Gütlich, P.; Goodwin, H. A. Spin Crossover in Transition Metals III; Springer-Verlag: Berlin, Heidelberg, **2004**.
- (18) Bixon, M.; Jortner, J. Intramolecular Radiationless Transitions. J. Chem. Phys. 1968, 78, 715–726.
- (19) Englman, R.; Jortner, J. The Energy Gap Law for Radiationless Transitions in Large Molecules. *Mol. Phys.* **1970**, *18*, 145–164.
- (20) Carey, M. C.; Adelman, S. L.; McCusker, J. K. Insights into the Excited State Dynamics of Fe(II) Polypyridyl Complexes from Variable-Temperature Ultrafast Spectroscopy. *Chem. Sci.* **2019**, *10*, 134–144.
- (21) Liu, Y.; Harlang, T.; Canton, S. E.; Chabera, P.; Saurez-Alcantara, K.; Fleckhaus, A.; Vithanage, D. A.; Goransson, E.; Corani, A.; Lomoth, R.; *et al.* Towards Longer-Lived Metal-to-Ligand Charge Transfer States of Iron(II) Complexes: An N-Heterocyclic Carbene Approach. *Chem. Commun.* **2013**, *49*, 6412–6414.
- (22) Kjær, K. S.; Zhang, W.; Alonso-Mori, R.; Bergmann, U.; Chollet, M.; Hadt, R. G.; Hartsock, R. W.; Harlang, T.; Kroll, T.; Kubiček, K.; *et al.* Ligand Manipulation of Charge Transfer Excited State Relaxation and Spin Crossover in [Fe(2,2'-bipyridine)<sub>2</sub>(CN)<sub>2</sub>]. *Struct. Dyn.* **2017**, *4*, 44030.
- (23) Liu, Y.; Kjær, K. S.; Fredin, L. A.; Chabera, P.; Harlang, T.; Canton, S. E.; Lidin, S.; Zhang, J.; Lomoth, R.; Bergquist, K.; *et al.* A Heteroleptic Ferrous Complex with Mesoionic Bis(1,2,3-triazol-5-ylidene) Ligands: Taming the MLCT Excited State of Iron(II). **2015**, *21*, 3628–3639.
- (24) Cannizzo, A.; van Mourik, F.; Gawelda, W.; Zgrablic, G.; Bressler, C.; Chergui, M. Broadband Femtosecond Fluorescence Spectroscopy of [Ru(bpy)<sub>3</sub>]<sup>2+</sup>. *Angew.* **2006**, *45*, 3174–3176.
- (25) Gawelda, W.; Cannizzo, A.; Pham, V.-T.; van Mourik, F.; Bressler, C.; Chergui, M. Ultrafast Nonadiabatic Dynamics of [Fe<sup>II</sup>(bpy)<sub>3</sub>]<sup>2+</sup> in Solution. *J. Am. Chem. Soc.* **2007**, *129*, 8199–8206.
- (26) Damrauer, N. H.; Cerullo, G.; Yeh, A.; Boussie, T. R.; Shank, C. V.; McCusker, J. K. Femtosecond Dynamics of Excited-State Evolution in [Ru(bpy)<sub>3</sub>]<sup>2+</sup>. *Science* **1997**, *275*, 54–57.
- (27) Yeh, A. T.; Shank, C. V.; McCusker, J. K. Ultrafast Electron Localization Dynamics Following Photo-Induced Charge Transfer. *Science* **2000**, 289, 935–938.

#### **Chapter 6: Future Work**

#### 6.1. Introduction

The work in this dissertation has spanned numerous transition metals, electronic configurations and ligand scaffolds in an effort to understand and manipulated ultrafast excited state dynamics in a variety of chemical systems. Coherent vibrational dynamics have been used in several ways ranging from an aid in characterizing the excited state dynamics to a tool with which to synthetically redesign the chromophore around. Although the results described here have expanded what is known about the excited state dynamics of several transition metal systems and the role of coherent vibrational dynamics, there are still numerous questions to be answered or additional research paths to be pursued. In what follows, we will provide a brief outlook for future work stemming from the work in each chapter of this dissertation.

## 6.2. Detailed Kinetic Modeling of Cr(acac')<sub>3</sub> Excited State Dynamics

The results of chapter 2 of this dissertation had shown that the excited state dynamics of  $Cr(acac')_3$  systems involve an initial ultrafast  ${}^4T_2 \rightarrow {}^2E$  ISC followed by a thermally activated  ${}^2E \rightarrow {}^4T_2$  bISC and subsequently by  ${}^4T_2 \rightarrow {}^4A_2$  IC to recover the ground electronic state. Kunttu and coworkers developed a kinetic model to describe the observations of their visible pump IR probe TA experiments shown in equation 2.1. However, because they fit applied their model to the recovery of the ground state bleach as opposed to decay of the excited state absorption signal (which is composed of a superposition of absorption from the  ${}^2E$  and  ${}^4T_2$  states), they were able to simplify their kinetic model to describe only the net  ${}^2E \rightarrow {}^4T_2$  bISC as opposed to the rates of both forwards and backwards reactions. Thus, the kinetic model developed by Kunttu and coworkers cannot describe the delayed  ${}^4T_2 \rightarrow {}^2E$  ISC after dissipation of some of the thermal energy in bulkier members of the  $Cr(acac')_3$  series such as  $Cr(TMHD)_3$ . To describe these dynamics more completely, a modified kinetic model is outlined in equation 6.1 in which an additional thermally activated ISC term has been added to the differential equation describing the concentration of the  ${}^4T_2$  state. The remainder of the parameters are identical to what was describe in equation 2.1 with the exception the time dependent effective temperature which is rewritten in equation 6.2 to include a generic bath temperature,  $T_{bath}$ , to allow for variable temperature measurements.

$$\frac{d\left[{}^{2}E\right]}{dt} = -\left(k_{bISC} + k_{p}\right)\left[{}^{2}E\right] + k_{ISC}\left[{}^{4}T_{2}\right] = -\left(A_{bISC}\exp\left(\frac{-E_{a,bISC}}{k_{b}T(t)}\right) + k_{p}\right)\left[{}^{2}E\right] + A_{ISC}\exp\left(\frac{-E_{a,ISC}}{k_{b}T(t)}\right)\left[{}^{4}T_{2}\right]$$
6.1a

$$\frac{d\left[{}^{4}T_{2}\right]}{dt} = k_{bISC}\left[{}^{2}E\right] - \left(k_{ISC} + k_{IC}\right)\left[{}^{4}T_{2}\right] =$$

$$A_{bISC} \exp\left(\frac{-E_{a,bISC}}{k_{b}T(t)}\right)\left[{}^{2}E\right] - \left(A_{ISC} \exp\left(\frac{-E_{a,ISC}}{k_{b}T(t)}\right) + k_{IC}\right)\left[{}^{4}T_{2}\right]$$
6.1b

$$\frac{d\left[{}^{4}A_{2}\right]}{dt} = k_{IC}\left[{}^{4}T_{2}\right] + k_{p}\left[{}^{2}E\right]$$
6.1c

$$T(t) = T_{bath} + (T_x - T_{bath}) \exp(-k_{VC}t)$$
6.2

Application of the kinetic model of equation 6.1 to the TA data of each of the Cr(acac')<sub>3</sub> series would allow for the most detailed description of the excited state dynamics of this class of compounds to date and would allow for an intricate view of how each synthetic modification employed in chapter 2 physically affects the excited state dynamics. The implementation of such a kinetic model will likely be somewhat difficult due to the large number of parameters to fit for. To make the situation easier, three types of experiments could be used to gain useful thermodynamic information on each compound. First, since it was insinuated by Kunttu and coworkers<sup>1</sup> that ground state recovery of Cr(acac)<sub>3</sub>, even at longer timescales, involves thermally activated bISC to the quartet manifold, then variable temperature ground state recovery measurements would afford the activation energy and preexponential factor for bISC. Additionally, variable temperature measurements could be employed to monitor the early time dynamics as the temperature of the bath plays a role in the time dependent effective temperature in equation 6.2. Finally, variable excitation wavelength measurements while monitoring at the same wavelength across the experiment set would vary the initial effective temperature,  $T_x$ . The combination of each of these experiment types may allow for a fit to equation 6.1, and in turn, an extremely detailed view of the excited state dynamics in this class of compounds.

#### 6.3. Excited State Dynamics of Six-Coordinate Cobalt(III) Compounds

Chapter 3 of this dissertation discussed the excited state dynamics of a series of Co(acac')<sub>3</sub> type complexes. A lot of the ambiguities from these results arose from assignments of spin states. Since visible TA experiments are not particularly sensitive to spin state, it is recommended that a complementary experiment be used to extract such information such as ultrafast kß fluorescence measurements which are highly sensitive to the spin state on the metal center. However, given that the such a measurement technique requires instrumentation that is difficult to get timely access to, alternative methods may be more practical for future endeavors. One method which could be used to confirm that ground state recovery occurs on a 2 ps timescale in these systems (as opposed to  $\sim$ 2 ps formation of the  $^5T_{2g}$  state) would be to perform full spectrum measurements while monitoring more in the UV. This may afford relatively larger signals for the  $^5T_{2g}$  state as the  $\pi \to \pi^*$  bands shift. This was not performed in the present work for two reasons. First, the low extinction coefficients of the ligand field bands necessitated a very high sample concentration which effectively makes the UV portion of the spectrum completely opaque. A remedy for this could be to use higher energy excitation using a band that has higher extinction coefficients so a lower concentration could be used. Second, the white light continuum generated in the sapphire window in the current experiment does not generate sufficient UV light to perform the experiment in question. Replacement of the sapphire window with a CaF<sub>2</sub> window on a translation state (to prevent damage) may allow for high enough UV output to perform the desired experiment.

Additionally, we know that cobalt(III) compounds of significantly higher ligand field strength than the Co(acac')<sub>3</sub> compounds studied show much longer ground state recovery lifetimes (presumably because they populate the  ${}^5T_{2g}$  state). It may be interesting to systematically alter the ligand field strength of six-coordinate cobalt(III) systems to monitor the onset of this extended lifetime. This could be achieved in numerous ways such as using the homoleptic series of  $Co(acac)_3 \rightarrow Co(NacNac)_3 \rightarrow [Co(bpy)_3]^{3+}$ , or using a more modular approach of  $Co(acac)_3 \rightarrow [Co(acac)_2(bpy)]^+ \rightarrow [Co(acac)_2(CN)_2]^-$  (or some other strong field ligand set) similar to what was performed in chapter 5 of this dissertation, or simply adding

incrementally higher numbers of nitrogen donors such as  $Co(acac)_3 \rightarrow [Co(acac)_2(en)]^+ \rightarrow [Co(acac)(tren)]^{2+}$ . Each of these series has the benefit of a  $\pi$ -system to tap into for high intensity charge transfer transitions from the excited state so that a signal can be seen in TA measurements.

## 6.4. Coherence as an Indicator and Constrained Iron(II) Compounds

The main point of chapter 4 of this dissertation was to illustrate that coherence information could point the investigator towards synthetic modifications that could alter photophysical properties. Future work in this regard would involve using this same process towards tuning the photophysics of a different chemical system. This would require that the system undergoes an ultrafast transformation that is driven by large amplitude nuclear motion. Although short dephasing times were used as an indicator for specific modes to target, the reliability of this indicator is still somewhat in question given the rapid dephasing times observed for some solvents or the quartz cuvette or even the broad range of dephasing times observed in the Cr(acac')<sub>3</sub> series which each had seemingly identical photophysical properties. However, regardless of the meaningfulness of individual dephasing times, excited state coherences relay important information about the nuclear motion upon photoexcitation which, when coupled with other information as well as chemical intuition, could provide important insights with regards to tuning the excited state dynamics of a chemical system.

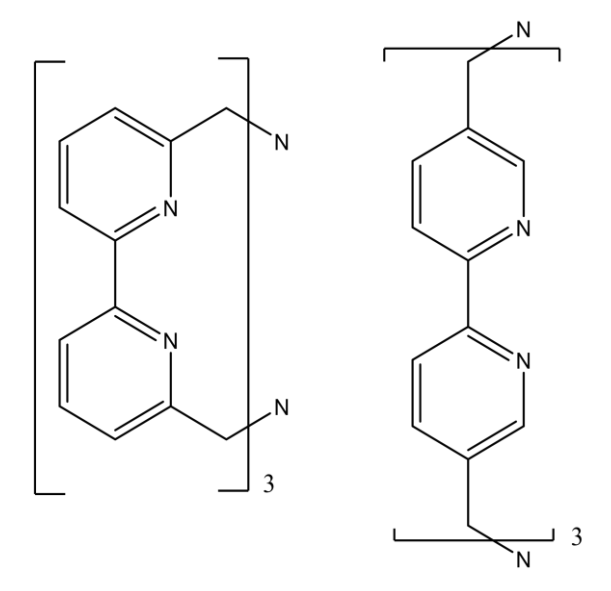


Figure 6.1. Structures of proposed condensed macrocyclic cage ligands.

An additional important insight that this work has brought forth is that highly strained iron(II) polypyridyls have much longer MLCT lifetimes. This concept could be extended to other macrocylic cage ligands as well such as the ligands shown in Figure 6.1. Both of these ligand sets have the potential to make a highly strained iron(II) chromophore with extended MLCT lifetimes.

## 6.5. Modular Manipulation of Excited State Dynamics of Iron(II) Chromophores

The work in chapter 5 of this dissertation has shown that the photophysical properties of iron(II) polypyridyl type complexes can be systematically tuned via switching a single bidentate polypyridyl ligand with other ligands of varying ligand field strength thus providing enough tunability to alter the ground state recovery and MLCT lifetimes by over an order of magnitude. Future efforts in this area could probe how the excited state properties are further perturbed by substituents on the polypyridyl ligand or by swapping additional polypyridyl ligands with stronger field ligands such as the dicarbene ligand used in this work. Considering the substantial affect that a single dicarbene ligand has had on the MLCT lifetime, the addition of another such ligand has the potential to create a substantially longer lived MLCT excited state with spectral properties readily tunable by substituents on the remaining polypyridyl ligand. Furthermore, the carbene ligand used in this study has further room for synthetic modifications that can potentially result in dramatic changes to its ligand field strength. By swapping out the peripheral methyl group with more electron donating or withdrawing groups one can, in theory, continue to significantly alter the electronic properties of the carbene carbon and, by extension, the metal center.

(1) Maçôas, E. M. S.; Mustalahti, S.; Myllyperkiö, P.; Kunttu, H.; Pettersson, M. Role of Vibrational Dynamics in Electronic Relaxation of Cr(acac)<sub>3</sub>. *J. Phys. Chem. A* **2015**, *119*, 2727–273.